



HAL
open science

Electrochimie & Nanoparticules magnétiques en laboratoire-sur-puce microfluidique pour le diagnostic médical. Détection du miARN-122.

Marie-Charlotte Horny

► **To cite this version:**

Marie-Charlotte Horny. Electrochimie & Nanoparticules magnétiques en laboratoire-sur-puce microfluidique pour le diagnostic médical. Détection du miARN-122.. Chimie analytique. Sorbonne Universités, UPMC University of Paris 6, 2017. Français. NNT : . tel-03980015

HAL Id: tel-03980015

<https://hal.science/tel-03980015>

Submitted on 9 Feb 2023

HAL is a multi-disciplinary open access archive for the deposit and dissemination of scientific research documents, whether they are published or not. The documents may come from teaching and research institutions in France or abroad, or from public or private research centers.

L'archive ouverte pluridisciplinaire **HAL**, est destinée au dépôt et à la diffusion de documents scientifiques de niveau recherche, publiés ou non, émanant des établissements d'enseignement et de recherche français ou étrangers, des laboratoires publics ou privés.

THÈSE DE DOCTORAT DE L'UNIVERSITÉ PIERRE ET
MARIE CURIE

Spécialité

CHIMIE-PHYSIQUE

Ecole Doctorale 388 : Chimie-Physique, Chimie Analytique de Paris Centre

présentée par MARIE-CHARLOTTE HORNY *sur le sujet*

**ELECTROCHEMISTRY & MAGNETIC NANOPARTICLES ON A
MICROFLUIDIC LAB-ON-CHIP FOR MEDICAL DIAGNOSIS.
DETECTION OF THE MICRORNA-122.**

Doctorat soutenu le 5 octobre 2017

devant un jury composé de :

Pr R. FERRIGNO, rapporteur
Pr L. MOTTE, rapporteur
Pr C. MÉNAGER, examinateur
Pr A. KUHN, examinateur
Dr C. SELLA, examinateur
Dr M. LAZERGES, invité
Dr J.-M. SIAUGUE, encadrant
Dr J. GAMBY, directeur de thèse

Paris, UPMC
2017



Remerciements

Je tiens à remercier tout d'abord, Mme Rosaria Ferrigno et Mme Laurence Motte qui ont accepté de lire et d'évaluer ce travail de thèse en tant que rapporteurs, ainsi que tous les membres du jury d'avoir accepté d'y prendre part.

J'adresse particulièrement mes remerciements à mes trois encadrants de thèse pour la confiance qu'ils m'ont accordée pour mener à bien ces travaux et le temps qu'ils m'ont consacré : Mathieu Lazerges pour ses conseils sur les biocapteurs, Jean-Michel Siaugue pour la synthèse des particules, d'avoir pris la patience de corriger mes erreurs de dilution et surtout Jean Gamby, pour son accompagnement, son soutien, sa disponibilité, et son optimisme pendant ces trois années.

Je souhaite remercier ensuite chacun de mes quatre laboratoires d'accueil et leur directeur : l'UTCBS à Chimie Paris, le PHENIX (UPMC), le LISE (UPMC) et le C2N anciennement LPN (Marcoussis) pour m'avoir chacun à leur tour, intégrés chaleureusement dans leurs équipes. Impossible de citer tout le monde ! Mais quand même : Daniel Rose pour ses doigts de fée pour la réalisation des connecteurs sur puce, Florence pour les dépôts de a-CN_x sur ce Plassys capricieux, Aude pour la synthèse de nanoparticules et son inébranlable bonne humeur, Vincent pour l'expertise en hyperthermie magnétique, Yasmine et Nadia, FX, Caro, Sébastien et Olivier pour les conseils moto, Anne-Claire, Guillaume, Abdu pour avoir fait de la salle blanche un endroit haut en couleurs où il fait bon vivre, mes collègues de course à pied, Frank, Stéphane pour l'entraînement et le juji tsu, ça forme la volonté ! Mes co-bureaux Simon, Julie, Mery, et ceux qui m'ont montré la voie, la paire inséparable Pierre et Marie, Clément, Nour, Adrien.

Tous ceux dont le soutien moral, à des moments clés de ma thèse, ont fait de ces trois ans une histoire inoubliable, Sara ma petite espagnole, Pierre, Quentin, Jean, Sylvain, Charles, Olivier, Ourania pour nos discussions au 3e et les immuables, Cake M, Babu, Quentin, Martin, Belaud, Melissa. Ma famille avec une impatience féroce pour les résultats et Antoine, pour avoir rendu les pics de Dirac si peu rationnels.

“La force du corps rend l'esprit plus fort, la force de l'esprit rend le corps plus fort”

Scientific publications

Speeches in international conferences

- The Electrochemical Society, San Diego 2016, USA, (5 days) DNA Electrochemical Hybridization Detection in Droplets Using Gold Ultramicroelectrodes in a Two-Electrode Configuration M.-C. Horny, M. Lazerges, J.-M. Siaugue, A. Pallandre, A.-M. Haghiri-Gosnet, and J. Gamby.

Speeches in national conferences or symposium

- Journées LabeX MiChem, Paris 2016, FRANCE, (1 day) Electrochemical detection of DNA hybridization & magnetic nanoparticles in a microfluidic Lab-On-Chip. M.-C. Horny, M. Lazerges, J.-M. Siaugue, C. Deslouis, F. Bedioui, A.-M. Haghiri-Gosnet, and J. Gamby.

Posters in national and international conferences

- French American Doctoral Exchange Seminar FADEX, Grenoble 2016, FRANCE (3 days) Microfluidic lab-on-chip for miRNA122 detection: a nanoplateform for DNA manipulation coupled to an ultrasensitive detection on ultra-microelectrodes.
- The 20th International MicroTAS, Dublin 2016, IRELAND (5 days) Increasing the efficiency of DNA electrochemical hybridization detection using microelectrodes in a two-electrode configuration in microfluidics. Marie-Charlotte Horny, Mathieu Lazerges, Jean-Michel Siaugue, Antoine Pallandre, Anne-Marie Haghiri-Gosnet, and Jean Gamby.

Peer-reviewed publications

1. M.-C. Horny, M. Lazerges, J.-M. Siaugue, A. Pallandre, D. Rose, F. Bedioui, C. Deslouis, A.-M. Haghiri-Gosnet, J. Gamby. "Electrochemical DNA biosensors based on long-range electron transfer: investigating the efficiency of a fluidic channel microelectrode compared to an ultramicroelectrode in a two-electrode setup" *Lab on a Chip*, Royal Society of Chemistry, 16, 2016, 4373-4381.
2. M.-C. Horny, M. Lazerges, J.-M. Siaugue, A. Pallandre, A.-M. Haghiri-Gosnet, and J. Gamby, (2016). "DNA Electrochemical Hybridization Detection in Droplets Using Gold Ultramicroelectrodes in a Two-Electrode Configuration", *ECS Transactions*, 72 (31) 1-6.

3. M.-C. Horny, J. Gamby, M. Lazerges, A. Michel, V. Dupuis, J.-M. Siaugue, and J. Gamby. "Magnetic hyperthermia on $\gamma\text{-Fe}_2\text{O}_3$ core-shell nanoparticles for DNA release " Nanoscale, Royal Society of Chemistry (*being finalised*).

Publications without peer-review

M.-C. Horny, M. Lazerges, J.-M. Siaugue, A. Pallandre, A.-M. Haghiri-Gosnet, and J. Gamby, (2016). "Increasing the efficiency of DNA electrochemical hybridization detection using microelectrodes in a two-electrode configuration in microfluidics" microTAS Proceedings, 2017, sous presse.

Accepted book chapters

1. Emmanuel Roy, Antoine Pallandre, Bacem Zribi, Marie-Charlotte Horny, François Damien Delapierre, Andrea Cattoni, Jean Gamby and Anne-Marie Haghiri-Gosnet., (2016). "Molecular Microfluidic Bioanalysis: Recent Progress in Pre-concentration, Separation, and Detection". In book: Applications of Microfluidics, Chapter: Molecular Microfluidic Bioanalysis: Recent Progress in Pre-concentration, Separation, and Detection, Editors: Intech Open Science, pp.In Press.
2. Emmanuel Roy, Antoine Pallandre, Bacem Zribi, Marie-Charlotte Horny, François Damien Delapierre, Andrea Cattoni, Jean Gamby and Anne-Marie Haghiri-Gosnet., (2016). "Overview of Materials for Microfluidic Applications". In book: Applications of Microfluidics, Chapter: Molecular Microfluidic Bioanalysis: Recent Progress in Preconcentration, Separation, and Detection, Editors: Intech Open Science, pp.In Press.

Ongoing CNRS invention declaration

- Dispositif micro-fluidique couplant hyperthermie magnétique et détection électrochimique sur puce (DI 10633-01) (dépôt prévu octobre 2017).

List of Abbreviations

| | |
|-------------------------|--|
| a-CN_x | amorphous-Carbon Nitride |
| AFM | Atomic Force Microscopy |
| AGO | Argonaute protein |
| ALT | Alanine Amino Transferase |
| AMF | Alternative Magnetic Field |
| cDNA | complementary Deoxyribonucleic Acid |
| CS | Core Shell particles |
| CE | Counter Electrode |
| CV | Cyclic Voltammetry |
| DLS | Dynamic Light Scattering |
| DNA | Deoxyribonucleic Acid |
| dsDNA | double-stranded Deoxyribonucleic Acid |
| EC | Electrochemical |
| EIS | Electrochemical Impedance Spectroscopy |
| EDC | 1-(3-dimethylaminopropyl)-3-ethylcarbodiimide hydrochloride |
| LET | Long-range Electron Transfer |
| LOC | Lab on Chip |
| LOD | Limit of Detection |
| MB | Methylen Blue |
| miRNA | micro Ribonucleic Acid |
| MNP | Magnetic Nanoparticles |
| mRNA | messenger Ribonucleic Acid |
| M_{sat} | saturation Magnetization |
| NHS | N-Hydro Succinimide |
| OGN | Oligonucleotides |
| PDMS | Polydimethylsiloxane |
| PEG | Poly Ethylen Glycol |
| RISC | RNA-Induced Silencing Complex |
| RT-PCR | Real Time - Polymerase Chain Reaction |
| SAM | Self-Assembled Monolayer |
| SPION | Super Paramagnetic Iron Oxide Nanoparticles |
| SQUID | Supra Quantum Interferometric Device |
| TEM | Transmission Electron Microscopy |
| S/N | Signal to Noise ratio |
| SLP | Specific Loss Power |
| ssDNA | single-stranded Deoxyribonucleic Acid |
| UME | Ultra-MicroElectrode |
| WE | Working Electrode |
| LISE | Laboratoire Interfaces et Systèmes Electrochimiques |
| PHENIX | Physicochimie des Electrolytes et Nanosystèmes Interfaciaux |
| UTCBS | Unité Technologique Chimie Biologie pour la Santé |

C2N Centre de Nanosciences et Nanotechnologies

Contents

| | |
|--|-----------|
| Scientific publications | ix |
| Introduction | xvi |
| Summary | xxxiv |
| 1 Bibliographic review | 1 |
| 1.1 miRNAs: the design of unique patterns of disease's state | 2 |
| 1.1.1 miRNAs: post-transcriptional regulators | 2 |
| 1.1.2 The miRNA-122 key regulator for numerous pathways | 6 |
| 1.1.3 DNA chips and miRNAs detection | 7 |
| 1.2 Electrochemical DNA biosensors. | 10 |
| 1.2.1 Principle | 10 |
| 1.2.2 Three key steps to master a DNA biosensor | 11 |
| 1.3 Microfluidics and Lab On a Chip | 15 |
| 1.3.1 Mass transport inside a microfluidic channel. | 15 |
| 1.3.2 Insight into microfluidics, toward the ideal LOC | 18 |
| 1.4 Magnetic manipulation of superparamagnetic nanoparticles | 20 |
| 1.4.1 Description and magnetic properties. Applications of mag- netic nanoparticles in biomedicine. | 21 |
| 1.4.2 Magnetic manipulation | 25 |
| 1.4.3 Core-shells particles | 26 |
| 1.4.4 Magnetic resonance imaging (MRI) contrast enhancement | 27 |
| 1.4.5 Drug delivery | 27 |
| 1.4.6 Magnetic separation | 28 |
| 1.4.7 Magnetic hyperthermia | 32 |
| 1.4.8 Biomedical sensors based on magnetic NP | 34 |
| 1.5 Devices using various coupling | 36 |
| 1.5.1 Ferguson, a microfluidic electrochemical chip | 36 |
| 1.5.2 Biomagnetic assays combining electrochemistry and magnetic particles | 37 |
| 2 DNA hybridization detection on Ultra-microelectrode | 39 |
| 2.1 Methodology | 42 |
| 2.1.1 DNA | 42 |
| 2.1.2 Long-electron transfer (LET) in DNA | 42 |
| 2.1.3 LET in $Fe^{II}/Fe^{III}/MB$ systems | 43 |
| 2.1.4 Ultra microelectrodes (UME) | 44 |
| 2.1.5 Electrochemical Methods | 48 |
| 2.2 Detection of DNA hybridization on gold UME in macrosystem | 52 |
| 2.3 Detection using microfluidics | 58 |
| 2.3.1 Microfluidic device | 58 |
| 2.3.2 Modeling with Comsol Multiphysics Finite Elements | 60 |

| | | |
|----------|---|------------|
| 2.3.3 | Transposing a gold UME on a microfluidic chip for DNA electrochemical hybridization detection in a two-electrode setup. | 61 |
| 2.3.4 | On the importance of the electrodes' geometry | 71 |
| 2.3.5 | Probe density | 72 |
| 2.3.6 | Detection on amorphous carbon nitride a-CN _x | 74 |
| 3 | γ-Fe₂O₃@SiO₂ core-shell nanoparticles, nanocarriers for DNA capture and release | 89 |
| 3.1 | Materials & Methods. | 92 |
| 3.1.1 | Materials | 92 |
| 3.1.2 | Synthesis of core-shell nanoparticles | 92 |
| 3.1.3 | Characterization of core-shell nanoparticles | 93 |
| 3.1.4 | DNA grafting | 94 |
| 3.2 | Synthesis and characterization of Core-shell Nanoparticles | 96 |
| 3.2.1 | Maghemite cores | 96 |
| 3.2.2 | Core-shell Nanoparticles | 102 |
| 3.3 | Capture and release of DNA targets | 126 |
| 4 | Towards a complete Lab-On-Chip | 133 |
| 4.1 | Materials and Methods | 134 |
| 4.1.1 | Microfluidic chip fabrication | 134 |
| 4.1.2 | Setup for performing on chip magnetic hyperthermia | 135 |
| 4.1.3 | DNA grafting, release and detection | 136 |
| 4.2 | Results and discussion | 136 |
| 4.2.1 | Magnetic hyperthermia on chip | 137 |
| 4.2.2 | Coupling of magnetic hyperthermia on chip and electrochemical detection | 141 |
| 4.3 | Perspectives | 147 |
| 4.3.1 | Optimizations | 147 |
| 4.3.2 | Miniaturization toward a portable equipment | 148 |
| 4.3.3 | Towards a capture/denaturation setup | 149 |
| A | Capture kinetics: Ultra-microelectrode vs Nanoparticles | 157 |
| A.1 | Diffusion dynamics of DNA targets on an Ultra-microelectrode | 157 |
| A.2 | Nanoparticles, nanomagnets for DNA capture | 159 |
| | General conclusion | 157 |
| | Bibliography | 163 |
| | Abstract | 189 |

Introduction

This work was done in collaboration between four laboratories: the laboratory Interfaces et Systèmes Electrochimiques, LISE (UMR 8235 CNRS/UPMC Paris) with Jean Gamby for the expertise in Electrochemistry in microfluidic systems, the laboratory Physico-Chimie des colloïdes et Nanosystèmes Interfaciaux, PHENIX (UMR 8234 CNRS/UPMC Paris) with Vincent Dupuis for the expertise in magnetism and Jean-Michel Siaugue for the expertise in design and fabrication of magnetic nanoparticles, l'Unité de Technologie Chimiques et Biologiques pour la santé, UTCBS (Chimie Paris Tech, INSERM, Université Paris Descartes) with Mathieu Lazerges for the expertise in DNA biosensors and le Centre de Nanosciences et de Nanotechnologies, C2N (UMR 9001 CNRS Univ.Paris-Sud) for the expertise in clean room micro- and nano-fabrication. This thesis was co-funded by the MiChem LabeX and the University Pierre et Marie Curie.

The challenge of the 21st century in molecular biology lies in the identification of new specific biomarkers for cancer or infectious diseases and to push the detection boundaries in order to treat patients even before the first symptoms of the disease appear. In this optic micro Ribonucleic acid (miRNA) are promising candidates for an early, rapid, precise and reliable diagnosis.

Powerful regulators of genetic expression with messenger RNA (mRNA) [1, 2], miRNAs allow a highly specific human cancer classification and thus the diagnosis of various cancers especially the diagnosis of liver diseases such as hepatitis C, B, metabolic disorders or drug abuse with miRNA-122 [3]. However in order to detect their in vivo change of molecular expression levels (under the femtomolar [4]) and that the detection meets both the quantitative and selective criteria, current techniques of detection (DNA chips, microarrays) need a previous amplification step usually done by Polymerase Chain Reaction (PCR) inducing an increase in the process frametime and quantification errors [5]. The selectivity of the detection is particularly crucial in the case of miRNAs as they are found in great number in the human organism and with comparable sequences [6].

The turning point of a highly sensitive detection is the direct transformation of a biologic event into an electric signal which will avoid the PCR step, a non negligible obstacle. Electrochemistry lives up to this expectation by directly transducing hybridization into a physical signal without labeling or further transformation. Voluminous literature exists on hybridization-based biosensors for the detection of specific oligonucleotides sequences that tends to optimize the limit of detection especially by playing on dimensions.

Not only the detection has to be quantitative and sensitive but also the detection device has to be portable, cost per test must be low enough to be done routinely, they have to integrate sample pre-treatment and parallel detection to meet needs and specifications of clinicians. Indeed, in the miRNAs case, it is the determination of the relative proportion of multiple miRNAs that will allow a reliable diagnosis. A

number of unmet needs can be fulfilled by microfluidic devices due to their portability, short sample processing time and flexibility. A non negligible advantage of miniaturization is the reduction of analysis time coming near the minute. Confinement and flow circulation favor targets' collision with the sensor and thus decrease limits of detection. Contamination by human manipulation are avoided between the injection of the sample to the analysis result. Reagents consumption are decreased (80% of analysis costs in bio-detection [7]).

Key points for performance efficiencies in biosensors are the transport of target molecules to the sensor and the chemical reaction itself. It is thus desirable to quantify surface binding within small fluids volumes (for precious samples or to get a large number of measurements from one single sample). Miniaturized sensors especially fluidic sensors are appealing for efficient hydrodynamics kinetics to transport targets [8] and automation [9]. But unraveling competing effects of diffusion convection and reaction (especially with microfluidic and even more with nanofluidic devices that have high surface to volume ratios and are thus sensitive to interfaces and diffusion issues) seems essential. To know if with the sensor size and concentration used, detection can take place and if at least one molecules is collected on the sensor's surface.

The coupling of a strong separation with a specific detection on a fully integrated Lab On Chip for early detection of ultra-low concentration analytes remains up until now the only way to conduct a complex analysis. Magnetic manipulation is a core component of miniature biological sampling and an "easy" way to prepare and separate biomolecules from their biological matrix. Superparamagnetic nanoparticles are, for that goal, appealing, due to their tunable magnetic properties. The challenge is to incorporate the magnetic separator on chip and still to keep a high magnetization with small objects and overcome fluid convection.

This manuscript is detailing the above mentioned scientific developments. It was split into 4 chapters:

- Chapter 1 is introducing the healthcare context around miRNAs justifying the research effort of this thesis. A panorama of electrochemical, microfluidic and biomagnetic sensors will be presented as well as the introduction of the concepts of mass-transport and magnetic manipulation on chip to allow the reader to get an insight into the objectives of this thesis.
- Chapter 2 is devoted to the transposition into microfluidics of an electrochemical hybridization-based biosensor and its optimization combining the expertise of the UTCBS, LISE and C2N laboratories. This sensor lies on the principles of long-range electron transfer in DNA and Ultra-microelectrodes. This microfluidic biosensor is a response to the needs of a rapid, highly specific, portable detection. It allowed especially to characterize hydrodynamics and mass-transport toward an electrode in microchannels. It also permitted to see the influence of the electrode material used and probe density issues on the efficiency of hybridization detection.
- Chapter 3 copes with the fabrication and characterization of a nanoplatform for DNA capture and release via magnetic hyperthermia, a PHENIX expertise.

The not so trivial influence of shape and size of particles on increased heat dissipation will be approached. A proof of concept of the release of DNA targets with magnetic hyperthermia will be given.

- Chapter 4 focuses on the transposition of DNA release with magnetic hyperthermia on a microfluidic chip with the challenge of the microfabrication of the chip to meet magnetic field application criteria. The influence of hydrodynamic conditions and channel geometries on experimental time scale and release efficiencies will be investigated. The coupling between the detection and the release module on the same microfluidic chip will be discussed. This multidisciplinary (physical, chemical and biological) chapter is the result of intensive collaborations between PHENIX, LISE, UTCBS and C2N laboratories and precisely reflects the interdisciplinary aspect of this thesis.

In order to make the reading of this manuscript easier, detailed calculations were organized in Appendix A. As the chosen language for this manuscript is English, a french summary was added, following this introduction, according to ED 388's specifications.

This work thesis resulted in four scientific publications under reading committee and one ongoing invention declaration (DI) to the CNRS . Two articles are already published, the two others are in the writing phase. These scientific works were presented to three international and one national conference (two orals and two posters) except for the results obtained in the frame of the CNRS DI.

French summary

Electrochimie & Nanoparticules magnétiques en laboratoire-sur-puce microfluidique pour le diagnostic médical. Détection du miARN-122.

Le challenge du 21^e siècle en biologie moléculaire repose d'une part sur l'identification de nouveaux marqueurs spécifiques pour le cancer et les maladies infectieuses, et d'autre part de repousser les limites de détections de ceux-ci afin d'établir un diagnostic précoce, peu coûteux, précis, fiable et rapide de la maladie avant même que les premiers symptômes n'apparaissent. Les acides micro-ribonucléiques (miARNs) sont des candidats de choix, en particulier le miARN-122.

Régulateurs puissants de différents processus cellulaires (pathologies, remodelage tissulaire)¹ en modulant l'expression des gènes, les miARNs sont des petits ARN non codants d'une vingtaine de nucléotides qui sont sécrétés hors des cellules, dans le plasma, à la mort de celles-ci. Les miARN permettent une classification hautement spécifique des cancers humains et donc leur diagnostic. C'est en particulier le cas du miARN-122, sur lequel se concentre ce travail de doctorat, qui permet le diagnostic de maladies du foie comme l'hépatite C, B et de maladies liées à l'action de médicaments.

Afin d'être capable de détecter leurs changements de concentration *in vivo* du niveau moléculaire (sous le femtomolaire²), de manière quantitative et spécifique, les techniques de détection actuelles (puces à ADN, microarrays) nécessitent une étape d'amplification réalisée par Polymerase Chain Reaction (PCR). Cette dernière induit dans le cas du miARN une augmentation drastique du temps de réaction et d'erreurs de quantification³. La sélectivité de la détection est particulièrement cruciale dans le cas des miARNs car ils sont nombreux dans l'organisme, avec des séquences proches.

Afin d'éviter l'écueil de la PCR, une transformation directe de l'évènement biologique de reconnaissance de la molécule d'intérêt en signal électrique est le point clé d'une détection sensible et directe. L'utilisation de biocapteurs électrochimiques répond à cette attente en traduisant directement l'hybridation de la cible (à détecter) en signal physique sans marquage ni transformation supplémentaire. Une littérature conséquente est disponible quant aux biocapteurs basés sur l'hybridation pour la détection d'oligonucléotides spécifiques qui tendent à optimiser les limites de détection.

Accéder à une limite de détection optimale ne suffit pas pour répondre aux besoins des cliniciens. Le biocapteur doit être portable, le coût par test doit être suffisamment bas pour constituer un test de routine. Un pré-traitement et une détection en parallèle sont aussi souhaités. Ce dernier point est particulièrement crucial dans le cas des miARNs car, c'est la détermination de la proportion relative de plusieurs miARNs dans le sang qui va permettre un diagnostic fiable et localisé.

Un certain nombre de ces critères sont remplis par l'utilisation de la microfluidique. Les puces microfluidiques sont des puces portatives, avec un temps d'expérimentation court et une grande

¹Van Rooij, E. *Circ. Res.* **2011**, *108*, 219–234.

²Corn, R.; Goodrich, T. T.; Lee, H. J.; Corn, R. M. **2016**, No. March.

³Moldovan, L.; Batte, K. E.; Trgovcich, J.; Wisler, J.; Marsh, C. B.; Piper, M. J. *Cell. Mol. Med.* **2014**, *18* (3), 371–390.

flexibilité due aux techniques de microfabrication en salles blanches. Le confinement dans des canaux micrométriques et l'hydrodynamique optimisée favorisent les collisions de la cible avec le capteur et ainsi augmentent la limite de détection. Les possibilités de contaminations par manipulation sont diminuées entre l'injection de l'échantillon dans la puce et l'analyse du résultat. La consommation de réactif est drastiquement diminuée (80% des coûts d'analyses en biodétection).

Les points clés pour un biocapteur performants, sont le transport de molécules cibles sur le capteur et la réaction chimique elle-même. Les capteurs miniaturisés en particulier fluidiques sont attirants pour leurs cinétiques hydrodynamiques, leurs propriétés de transport de cible et leur possibilité d'automatisation. Mais décorrélérer les influences compétitives de la diffusion, convection et de la réaction elle-même est essentiel, notamment en microfluidique et d'autant plus en nanofluidique où capteurs ont des ratios surface sur volume élevés et sont donc extrêmement sensibles aux interfaces et problèmes de diffusion. En effet, savoir si en tenant compte de la taille du capteur et de la concentration utilisée, une détection peut être possible et si au moins une molécule atteint le capteur permet une vision cohérente sur les résultats expérimentaux.

Le couplage d'une séparation forte avec une détection spécifique sur un laboratoire sur puce complet constitue la seule méthode jusqu'à présent pour une détection précoce d'analyses de concentrations très faibles. La manipulation magnétique est au cœur de la préoccupation du prétraitement miniaturisé des échantillons biologiques et constitue une méthode « facile » pour préparer et séparer des molécules d'intérêt de leur matrice biologique. Le challenge est d'incorporer un séparateur magnétique sur la puce elle-même, de garder une aimantation suffisante pour des nanoparticules, et de surmonter l'effet du flux.

Ce manuscrit détaille les développements scientifiques cités ci-dessus en quatre parties. Le chapitre 1 introduit le contexte médical autour du sujet des miARNs justifiant l'effort de recherche de ce doctorat. Dans un premier temps, l'attention est portée sur notre cible d'intérêt, l'acide micro-ribonucléique (miARN) et en particulier sur le miARN-122. Un panorama des capteurs électrochimiques est dressé et plus particulièrement les biocapteurs électrochimiques basés sur la détection de l'hybridation d'ADN, le moyen usuellement considéré comme le plus simple pour détecter de l'ADN ; avant d'aborder l'apport de la microfluidique sur les limites de détection, le temps d'analyse et la miniaturisation. Une introduction aux concepts du transport de masse appuyé sur l'étude de Squires *et al.*⁴ est donnée. Finalement, la contribution des nanoparticules magnétiques et de la manipulation magnétique sur puce est discutée avec un panorama rapide des propriétés magnétiques et de leur application en biomédecine précédant un point clé sur la séparation magnétique et l'hyperthermie magnétique. Le chapitre 2 est dédié à la transposition en microfluidique d'un biocapteur électrochimique basé sur la détection de l'hybridation et son optimisation en combinant les expertises des laboratoires UTCBS et LISE. Ce capteur est basé sur le principe du transfert d'électrons longue-distance dans l'ADN et tire profit des propriétés des Ultra-microélectrodes. Ce capteur microfluidique répond aux impératifs d'une détection portable, rapide et hautement spécifique. Il permet notamment de caractériser l'hydrodynamique et le transport de masse vers une électrode dans un microcanal. Il a aussi permis de voir l'influence du matériau d'électrode et la problématique de la densité de surface en sonde sur l'efficacité de l'hybridation. Le chapitre 3 traite de la fabrication et de la caractérisation d'une nanoplateforme pour la capture et le

⁴Squires, T. M.; Messinger, R. J.; Manalis, S. R. *Nat. Biotechnol.* **2008**, 26 (4), 417–426.

relargage d'ADN via l'hyperthermie magnétique, une expertise du laboratoire PHENIX. Une approche de l'influence non triviale de la forme et de la taille des particules sur l'augmentation de la production de chaleur est donnée. Ce chapitre constitue une preuve de concept du relargage d'ADN cible par hyperthermie magnétique. Enfin le chapitre 4 se concentre sur la transposition en microfluidique du relargage d'ADN par hyperthermie magnétique avec le défi que constitue la microfabrication d'une puce adaptée pour la génération d'un champ magnétique adapté aux petits volumes. L'influence des conditions hydrodynamiques associées à la géométrie du canal sur la durée de l'analyse et l'efficacité du relargage sont étudiées. Le couplage entre le module de détection du chapitre 2 et ce module de relargage sur la même puce microfluidique sera discuté. Ce dernier chapitre purement multidisciplinaire (biologie, chimie, physique) est le résultat d'une collaboration intensive entre le PHENIX, le LISE, l'UTCBS et le C2N et reflète d'une manière pertinente les aspects interdisciplinaires de ce travail de doctorat.

De profondes disparités dans les signatures des miARN peuvent être remarquées et utilisées pour la détection selon le type de maladies infectieuses et de cancers, en particulier le diagnostic des maladies du foie comme l'hépatite C, B, les désordres métaboliques ou l'abus de médicaments avec le miARN-122⁵. Mais exploiter les miARN comme biocapteurs demande une rigueur méthodologique⁶ qui jusqu'à présent, était réalisé par la RT-PCR avec les erreurs d'amplification et le temps accru d'analyse qui en découle.

Un laboratoire-sur-puce, ou lab on a chip (LOC) en anglais, comme son nom le suggère, se veut être une plateforme intégrée où toutes les expériences de biologie moléculaire peuvent être réalisées en commençant par l'injection directe de sang sur la puce et non d'ADN pré-purifié. Gervais *et al.* donnent un aperçu de ce à quoi ressemblerait le LOC du futur⁷. Leur dispositif se présente comme un couplage entre plusieurs modules (préparation de l'échantillon, pré-concentration, détection) qui utilise un volume d'environ 1 μ L d'un échantillon non traité et qui peut traiter parallèle des centaines de molécules (protéines, acides nucléiques et leurs contrôles négatifs) pour une détection dans la minute. La limite de détection (LOD) serait sous le femtomolaire avec une large gamme dynamique, et une grande sélectivité pour éviter les faux positifs. Une large gamme dynamique est particulièrement importante pour la détection des miARN pour lesquels la détection s'effectue par le changement relatif de concentration de plusieurs miARN dans une gamme qui peut s'étendre sur 10^3 ordres de grandeur selon que l'organe soit sain ou malade.

L'extraction, l'isolation, la purification et la manipulation de biomolécules sont des paramètres clés dans chaque analyse biochimique. Les protocoles classiques incluent l'électrophorèse, l'ultrafiltration ou la chromatographie. La séparation magnétique basée sur les nanoparticules magnétiques présente une alternative attrayante pour la capture sélective de protéines spécifiques ou d'ADN en utilisant des matériaux peu coûteux et un procédé rapide et simple. La petite taille des nanoparticules en font des matrices attractives du fait que la diffusion est réduite entre réactifs. Cela entraîne des réponses plus courtes, une gamme de réponse plus large et la possibilité d'atteindre des seuils de détection moléculaires. Le schéma type d'une séparation magnétique repose sur la capture d'une molécule d'intérêt dans son sérum d'origine par une nanoparticule magnétique

⁵Wang, X. W.; Heegaard, N. H. H.; Orum, H. *Gastroenterology* **2012**, *142* (7), 1431–1443.

⁶Moldovan, L.; Batte, K. E.; Trgovcich, J.; Wisler, J.; Marsh, C. B.; Piper, M. J. *Cell. Mol. Med.* **2014**, *18* (3), 371–390.

⁷Gervais, L.; De Rooij, N.; Delamarche, E. *Adv. Mater.* **2011**, *23* (24), H151-H176.

fonctionnalisée et l'isolation du complexe formé par rétention magnétique (décantation, aimant). Cependant à cause de leur faible moment magnétique, le gradient magnétique d'un simple aimant permanent ou électro-aimant est rarement suffisant pour capturer les nanoparticules magnétiques. De nombreuses stratégies ont été proposées dans la littérature pour surmonter cet inconvénient.

Le magnétisme des nanoparticules sous champ appliqué est gouverné par la compétition entre deux énergies : l'énergie d'anisotropie et l'énergie de Zeeman. L'énergie d'anisotropie tend à attirer le moment magnétique selon l'axe de facile aimantation. L'énergie de Zeeman cherche à aligner les moments magnétiques selon le champ. Afin de passer d'une direction de facile aimantation à l'autre, la barrière K.V (K, constante d'anisotropie magnétocristalline ; V, le volume de la particule) doit être franchie. Les nanoparticules sont de faible volume, la barrière d'énergie est du même ordre de grandeur que l'agitation thermique. A 300 K, la probabilité que les moments magnétiques commutent n'est pas nulle et le système relaxe selon une certaine période, lorsqu'il est soumis à un champ magnétique alternatif, le système n'étant pas en phase avec ce champ⁸. Les ferro-aimants exhibent une résonance magnétique pour des fréquences de l'ordre du gigahertz (le kilohertz utilisé n'est qu'un optimum technologique).

Le calcul du temps de relaxation du système dépend de la rotation de la particule dans le solvant soit externe (Brown) soit interne (Néel). La relaxation de Brown vient de la rotation physique des nanoparticules dans le fluide porteur, le moment magnétique étant figé selon l'axe d'anisotropie cristalline. La relaxation de Néel est induite par la rotation du moment magnétique de la nanoparticule dans le réseau cristallin lorsque la barrière K.V est franchie. Comme les deux mécanismes de relaxation ont lieu en parallèle, le temps effectif de relaxation est une contribution des deux phénomènes de relaxation. Le temps le plus court étant déterminant. Fortin *et al.* ont montré que le processus de pertes pour les nanoparticules de maghémite de diamètres inférieurs à 16 nm était gouverné par la relaxation de Néel⁹.

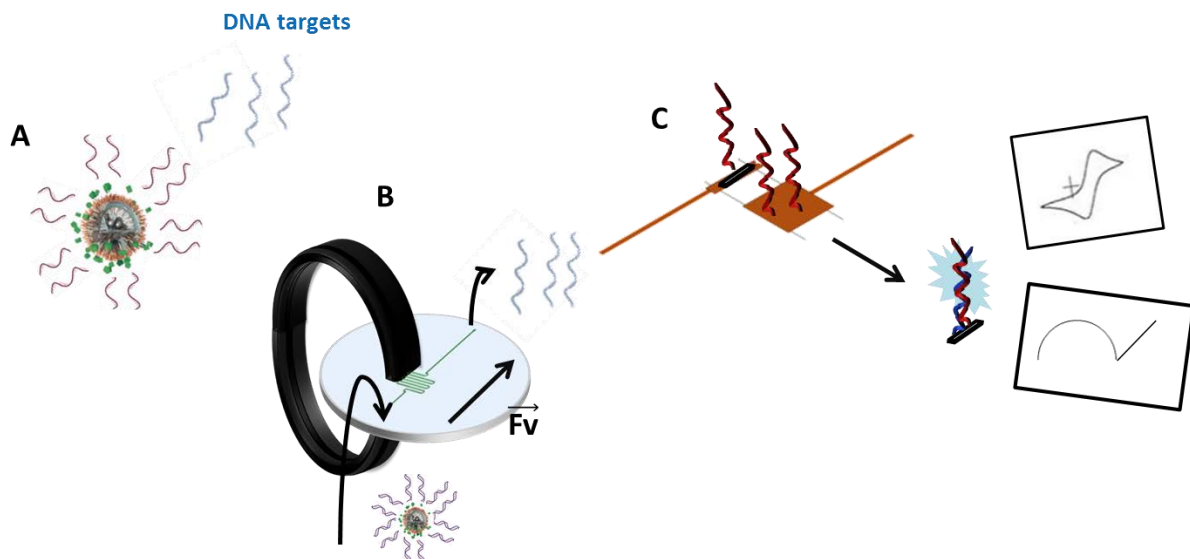
Les LOC sont des dispositifs intégrés qui cherchent à remplir les conditions du diagnostic clinique : haute sensibilité, spécificité, portabilité, rapidité, bas coût. Les LOC sont des candidats prometteurs pour détecter et quantifier les miARN. Mais la miniaturisation et le couplage de techniques très différentes sur une même puce (échantillonnage, séparation, détection) apportent leur lot de difficultés. Afin de remplir certaines spécificités du diagnostic clinique (rapidité, sensibilité, spécificité, semi-portabilité), nous avons réalisé un LOC avec un module de détection et de manipulation. Comme les miARN sont fragiles à manipuler, coûteux et facilement digérés par les protéines de la peau humaine, nous avons utilisé des sondes et cibles d'ADN synthétiques de la même séquence que celle du miARN-122 et son complémentaire. Ce LOC décrit sur la Figure ci-après est composé d' :

- Une nanoplateforme pour la capture d'ADN : des nanoparticules cœurs-coquilles avec un cœur de maghémite modifié et une coquille de silice fonctionnalisée avec groupements amines couplés aux ADN sondes de manière covalente ;
- Un module de relargage : une puce microfluidique contenant des nanoparticules cœurs-coquilles soumises à un champ magnétique alternatif radiofréquence concentré dans l'entrefer d'un électro-aimant (hyperthermie magnétique) ;

⁸Rosensweig, R. E. *J. Magn. Mater.* **2002**, 252, 370–374.

⁹Fortin, J.-P.; Wilhelm, C.; Servais, J.; Mé, C.; Bacri, J.-C.; Gazeau, F. *J. AM. CHEM. SOC.* **2007**, 129 (9).

- Un module de détection : un biocapteur électrochimique basé sur la détection de l'hybridation d'ADN composé d'une Ultra-microélectrode (UME) en or ou en carbone amorphe azoté (a-CNx) dans un canal microfluidique en configuration à deux-électrodes.



Vue artistique de notre LOC. A. Nanoplateformecœur-coquille magnétique pour la capture d'ADN. B. Module de relargage par hyperthermie magnétique sur puce. C. Biocapteur microfluidique pour la détection électrochimique par hybridation.

Détection de l'hybridation d'ADN sur Ultra-microélectrodes (UME)

Afin d'améliorer les chances de traiter les patients avec succès, la détection de maladies infectieuses ou de mutations génétiques à l'échelle moléculaire permet d'établir un diagnostic précis, fiable, rapide et peu coûteux avant même que les premiers symptômes de la maladie n'apparaissent. En combinant haute précision et rapidité, le diagnostic à l'échelle moléculaire est prometteur. Grâce aux avancées rapides en biotechnologies, le développement de méthodes rapides qui diminuent le temps d'analyse et offrent une sensibilité et une spécificité suffisante pour la détection d'ADN sont possibles par fluorescence, par microbalance à quartz (QCM) et par électrochimie. L'hybridation d'ADN est la méthode la plus prisée car la plus simple par rapport au séquençage direct. Il a été prouvé que l'ADN possédait un comportement conducteur même si aucune fonctionnalité biologique évidente ne requiert de l'ADN d'être un conducteur d'électrons. Ce phénomène peut être utilisé pour détecter une hybridation.

Lors de l'hybridation d'ADN, la séquence cible est identifiée avec un ADN sonde qui possède une séquence complémentaire à celle de la cible (règles de Watson et Crick's¹⁰). Un biocapteur est un dispositif composé d'une couche biologique active, qui agit comme un élément de reconnaissance et convertit l'interaction biologique en un signal qui peut être mesuré. Dans le cas de biocapteur à ADN, la couche biologique active est une couche d'ADN sonde. Plus précisément, le principe de la détection électrochimique de l'hybridation est la conversion de l'appariement des bases d'ADN en signal électrique. C'est là que l'électrochimie intervient. L'électrochimie est le seul moyen de traduire directement un événement biologique (l'hybridation d'ADN) en signal électrique sans autre transformation du signal physique.

¹⁰Watson, J. D.; Crick, F. H. C. *Nature*. 1953, pp 737–738.

Combinant une haute spécificité, un bas coût, une facilité d'utilisation, une portabilité et compatibilité avec les procédés de microfabrication, les biocapteurs électrochimiques font d'excellents candidats pour le diagnostic d'intérêt clinique et ainsi peuvent challenger la RT-PCR. Des travaux récents cherchent à optimiser les biocapteurs à ADN en termes de coût, de rapidité et de limite de détection.

Le choix de la technique d'immobilisation dépend de l'élément biologique (ADN), de la méthode de détection (l'électrochimie), du milieu dans lequel le biocapteur est plongé (aqueux, à température ambiante), de la stabilité mécanique et chimique de la matrice biologique. L'or séduit comme matériau d'électrode de par sa haute conductivité et ses nombreux procédés de fonctionnalisation (adsorption physique, impression microcontact, polymérisation, capture à l'intérieur d'un polymère conducteur). Des techniques plus spontanées sont préférées notamment l'adsorption physique car elle maintient l'activité biologique du biorécepteur. L'or permet d'immobiliser une monocouche d'ADN sonde bien définie et organisée, simplement et élégamment, via l'adsorption de fonctions thiol en deux heures¹¹.

Afin d'être efficace, trois étapes clés doivent être maîtrisées dans une biopuce à ADN : (i) l'immobilisation de la sonde sur son substrat solide, (ii) l'hybridation (ou reconnaissance) par le brin cible complémentaire, (iii) la conversion de l'évènement d'hybridation en signal physique.

Dans le chapitre 2, après un encart sur les ultra-microélectrodes et le transfert d'électrons longue-distance, une reconstitution d'un montage traditionnel à deux électrodes de Lazerges *et al.*¹² sur une UME en or est faite suivie de la comparaison avec son confrère intégré dans une puce microfluidique.

L'utilisation combinée d'une électrode microbande et d'un canal microfluidique offre : une réponse quasi-stationnaire rapide (autour de la milliseconde) grâce à une couche de diffusion très fine par rapport à la couche de convection ; une amélioration drastique de l'efficacité du capteur en termes de volume d'analyse et de dynamique du système (temps d'expérience) avec une manipulation aisée des échantillons¹³. Grâce aux temps de réponse de l'ordre de la microseconde, d'une résolution spatiale de la taille de l'électrode et une haute sensibilité de mesure en temps réel, l'utilisation d'UME permet l'accès à des milieux résistifs et l'étude de phénomènes très rapides.

Les mesures sont effectuées en voltammétrie cyclique, technique stationnaire bien connue et en spectroscopie d'impédance électrochimique. Cette dernière est une technique non stationnaire qui permet de séparer des réactions élémentaires si les constantes de temps sont suffisamment distinctes. En appliquant une faible perturbation au système électrochimique en dehors de son état stationnaire, les différentes réactions élémentaires n'évoluent pas à la même vitesse, permettant de disséquer le mécanisme électrochimique global. Dans notre cas, des réactions complexes hétérogènes interagissent avec le phénomène de transport de masse (hybridation, transport d'ADN, intercalation du bleu de méthylène), la voltammétrie cyclique n'est pas suffisante pour tout analyser.

Quand une interface est sortie de son équilibre, un flux permanent de charges et de matériaux est établi dû à des réactions électrochimiques, au transport de charges électriques entre les électrodes

¹¹Lucarelli, F.; Marrazza, G.; Turner, A. P. ; Mascini, M. *Biosens. Bioelectron.* **2004**, *19* (6), 515–530.

¹²Lazerges, M.; Tal, V. T.; Bigey, P.; Scherman, D.; Bedioui, F. *Sensors Actuators B Chem.* **2013**, *182*, 510–513

¹³Rossier, J. S.; Roberts, M. A.; Ferrigno, R.; Girault, H. H. *Anal. Chem.* **1999**, *71*, 4294–4299.

métalliques et l'électrolyte liquide. De plus, le transport d'espèces réactives vers l'interface est induit par des gradients électriques et des potentiels chimiques. Les lois élémentaires qui gouvernent les cinétiques de transport de masse et les réactions électrochimiques forment des couplages complexes générant des comportements non linéaires. Mais l'analyse locale de ce système non linéaire peut rentrer dans le cadre de la théorie linéaire. D'un point de vue expérimental, cela consiste en la mesure de l'impédance d'une cellule électrochimique en utilisant un signal de faible amplitude le long de la courbe de polarisation. L'impédance d'une électrode est fonction de la fréquence et du point de polarisation. Entre la limite haute fréquence et la limite basse fréquence, la dépendance en fréquence de l'impédance est due à une contribution capacitive de la double couche électrochimique et à une contribution faradique du transfert électronique à l'interface dû à la réaction électrochimique.

La détection est voltampérométrique. La rampe de potentiel est appliquée à l'électrode pour oxyder ou réduire les espèces électroactives d'intérêts. Le courant de transfert de charges (électrons) généré par la réaction faradique sera proportionnel à la concentration des espèces impliquées.

Un couple rédox de concentration connue et ayant une cinétique rapide de transfert de charge monoélectronique, le couple redox $[\text{Fe(III)(CN)}_6]^{3-} / [\text{Fe(II)(CN)}_6]^{4-}$, est utilisé comme référence de potentiel d'équilibre (0 V) et de courant du fait que les deux électrodes sont dans le même matériau (or). Ce dernier est donc utilisé dans les étapes de caractérisation du système électrochimique, d'immobilisation de la sonde, et d'hybridation de la cible.. L'hybridation d'ADN est suivie par voltammétrie cyclique et par Spectroscopie d'Impédance Electrochimique (SIE) permettant une analyse complémentaire de l'interface électrode/solution étant donné que la modification de surface fait suite à des événements de capture d'ADN cible à la surface du capteur.

Le comportement hydrodynamique de la puce est en adéquation avec la prédiction de Levich¹⁴ (ratio 1 entre le courant expérimental et le courant limite de Levich) sauf pour des valeurs de flux faibles, lorsque la diffusion radiale et les effets de bord deviennent non négligeables, un phénomène non pris en compte dans la théorie de Levich. Au contraire, lorsque le flux est plus élevé (supérieur à 0.01 $\mu\text{L/s}$), la couche de diffusion est réduite par la convection forcée et la contribution radiale des bords de l'électrode devient négligeable.

La géométrie des électrodes, particulièrement dans un dispositif couplant électrochimie et microfluidique, a une importance primordiale sur le comportement cité ci-dessus ainsi que sur le temps d'utilisation de la puce. Notre capteur est composé de 3 jeux de 2 couples d'électrodes, une électrode de travail et une contre-électrode avec une surface 70 fois plus grande. Cette configuration permet, d'une part d'utiliser la puce plus d'une fois si des électrodes sont endommagées et d'autre part, d'utiliser ce montage en configuration à deux électrodes. De plus, cette configuration rend possible la détection en parallèle et le suivi du profil de concentration des espèces le long du canal.

Un ADN sonde de 23 bases est auto-assemblé en une monocouche sur les microélectrodes d'or par adsorption de thiols dans un dispositif à deux électrodes classique et dans un dispositif intégré en microfluidique. L'immobilisation de la sonde résulte en une perte de signal sur les voltammogrammes, pertinent avec une couche dense chargé négativement (le squelette de

¹⁴Compton, R. G.; Fisher, A. C.; Wellington, R. G.; Dobson, P. J.; Leigh, P. a. *J. Phys. Chem.* **1993**, *97*, 10410–10415.

phosphate des ADN est chargé négativement) qui empêche la diffusion du complexe redox de référence aussi chargé négativement. Le transfert d'électron longue distance est choisi pour traduire l'évènement d'hybridation. Cette traduction directe est visible sur les voltammogrammes par un rétablissement du signal proportionnel à la concentration en cible introduite, dû à l'empilement des bases en π -stacking du duplex d'ADN, une configuration favorable au transport d'électrons. Le signal est d'autant plus augmenté par l'utilisation du bleu de méthylène, intercalant redox de l'ADN.

La quantification de la cible est déduite du signal électrique des courbes Intensité/Potentiel obtenues en soumettant le capteur à des concentrations décroissantes en cibles. La limite de détection pour l'hybridation d'ADN est de 0.1 fM sans flux et peut atteindre les 1 aM avec un flux de $0.5 \mu\text{Ls}^{-1}$, une valeur 10^4 fois plus faible que celle mesurée avec l'UME classique dans les mêmes conditions expérimentales. L'explication avancée repose sur l'apport accru de molécules vers l'aire de détection par la convection forcée. Un équilibre doit tout de même être conservé entre la vitesse de collection des cibles (volume d'échantillon utilisé) et le nombre de cibles qui atteignent le capteur. D'autant plus, que la couche de sonde adsorbée ne résiste pas à des flux trop élevés. Ces résultats ont été publiés dans Lab On Chip de la Royal Society of Chemistry¹⁵.

La densité de sondes immobilisées est calculée correspondant à un pourcentage de couverture de 80% soit 100 ADN cibles qui sont collectés sur un capteur avec 10^4 sondes, ce qui constitue une efficacité faible mais cohérente avec la littérature pour des couches denses sur or.

Plutôt que de nous pencher sur une stratégie de dilution de SAM, nous avons opté pour le choix d'un autre matériau, caractérisé de manière intensive au LISE et permettant une bonne réactivité électrochimique et des groupements amines de surface pour un greffage covalent.

Les films de carbone amorphe dope azote ($\alpha\text{-CN}_x$, $x=0.12$) sont des matériaux populaires d'électrode avec une large fenêtre de potentiel et une composition en chimie de surface flexible. La structure de surface peut être modifiée par des activations anodiques ou cathodiques afin de faire varier le nombre de groupements amines à la surface ainsi que la réactivité électrochimique en jouant sur le ratio sp^2/sp^3 .

Comme notre objectif est de pouvoir réaliser une hybridation d'ADN, donc de pouvoir différencier un simple brin d'un double brin, nous recherchons des groupements amines de surface et une réactivité chimique importante. Notre choix s'est porté sur le $\alpha\text{-CN}_x$ dopé à 3% d'azote (ratio C/N de 0.12) préparé par magnétron sputtering, activé en anodique dans du KOH (0.1M, 60s à 0.3 mA/cm^2).

L'activation anodique des électrodes en $\alpha\text{-CN}_x$ a permis d'augmenter la réactivité électrochimique, avec une action supposée sur la structure de surface et une diminution des sites isolants sp^3 et sur l'augmentation du nombre de fonctions amines de surface. Cette activation est visible sur les diagrammes de Nyquist par une réduction de la boucle de transfert de charge de 1.3 M Ω à 900 k Ω .

Soumis à des cycles d'immobilisation de sonde/hybridation de cycles, la réponse du capteur est conforme aux attentes. La couche immobilisée de sonde résiste parfaitement à un blanc dans NaCl

¹⁵Horny, M. C., Lazerges, M., Siaugue, J. M., Pallandre, A., Rose, D., Bedioui, F., ...& Gamby, J. (2016). Electrochemical DNA biosensors based on long-range electron transfer: investigating the efficiency of a fluidic channel microelectrode compared to an ultramicroelectrode in a two-electrode setup. *Lab on a Chip*, 16 (22), 4373-4381.

sans diminution de l'impédance. Des cibles avec une concentration de 10^{-18} M sont détectées avec une diminution de la boucle de résistance au transfert de charge indiquant le succès de l'hybridation *via* le rétablissement du transfert de charge dans la double structure de l'ADN.

Ceci constitue une preuve de concept de la détection d'hybridation de cibles à très faible concentration sur une électrode de α -CNx, une optimisation nécessaire serait de soumettre ce capteur à une mixture d'ADN de séquences et longueurs variables.

Dans l'optique de construire un LOC complet, l'étape suivante est de construire le module de manipulation d'ADN. Pour ce, il s'agit de synthétiser la nanoplateforme qui permet la capture et le relargage spécifique de l'ADN d'intérêt.

Nanoparticules cœurs-coquilles γ -Fe₂O₃@SiO₂, nanoplateforme pour la capture et le relargage d'ADN

Les billes magnétiques deviennent très populaires que ce soit pour des utilisations à l'échelle macroscopique ou nanométrique comme agent de transport, de manipulation, et de contraste¹⁶. Parmi elles, les nanoparticules magnétiques, en dehors de leur évident ratio élevé surface sur volume et d'une fonctionnalisation flexible, peuvent être manipulées aisément sans contact grâce à un champ magnétique. Afin d'être bien dispersées dans les fluides biologiques, la taille des nanoparticules doit être équilibrée entre un ratio élevé surface sur volume et une aimantation suffisante.

Rares sont les systèmes actuels de détection ou proches de la commercialisation, qui atteignent des limites de détection sensibles sans module de concentration ou d'amplification. La petite taille des nanoparticules en fait d'elles, une matrice attractive avec une barrière de diffusion réduite entre les réactifs. Cela conduit à des réponses plus courtes, des gammes de linéarité plus grandes et la possibilité d'atteindre des limites de détection moléculaires. Nous avons comparé et modélisé l'efficacité de capture d'une assemblée de nanoparticules de 80 nm en diamètre (TEM) à la capture sur une UME. Ces éléments justifient l'utilisation d'une matrice de nanoparticules en amont d'un module de détection sur UME. Le ratio entre les efficacités respectives est N, le nombre de nanoparticules, $N=10^{13}$ dans notre cas. Les nanoparticules sont des nano-aimants idéaux pour la capture d'ADN.

De nombreux systèmes magnétiques ont été proposés à travers la littérature¹⁷.

La stabilité colloïdale est la clé de nombreuses applications biomédicales. Grâce à leur petite taille, les nanoparticules ne sont pas ou peu soumises à l'attraction gravitationnelle. Sans champs appliqué, la stabilité des nanoparticules dépend de l'équilibre entre forces attractives (dipole-dipole de Van der Waals) et répulsives (forces stériques et électrostatiques). Le « design » de particules hybrides combinant composants organiques et non organiques est prisé avec des agents d'enrobage comme des polymères pour assurer la stabilité en solution aqueuse.

¹⁶Chen-Wen Lu, Yann Hung, Jong-Kai Hsiao, Ming Yao, Tsai-Hua Chung and Yao-Chang Chen. *Nano Lett.* **2007**, 7 (1), 149–154.

¹⁷Mauro Ferrari. *Nat. Rev.* **2005**, 5, 161–171.

La fonctionnalisation de nanoparticules magnétiques doit d'une part, conserver leurs propriétés magnétiques, et éviter l'agrégation, et d'autre part, en faire des plateformes biocompatibles pour la capture de biomolécules (ADN, enzymes, protéines, anticorps). Le type d'enveloppe détermine la taille et les propriétés physico-bio-chimiques des nanoparticules. Les agents d'enrobage peuvent être des molécules organiques fonctionnelles (aldéhydes, hydroxyles, carboxyles, ou amines) ou des polymères comme des polyéthylènes glycol (PEG) ou acides nucléiques peptidiques (PNA) qui assurent la stabilité de la particule via des répulsions stériques agissant comme des barrières contre les forces attractives.

La taille et la forme des nanoparticules sont des paramètres clés qui déterminent leur stabilité. La taille a un impact important sur le moment magnétique et la réponse à un champ magnétique appliqué. Pour une manipulation aisée avec un champ magnétique externe, l'aimantation totale doit être maximale. Les matériaux ferromagnétiques sont donc favorisés comme le fer, le nickel ou le cobalt. Les oxydes de fer sont particulièrement populaires sous leur forme maghémite- Fe_2O_3 ou magnetite Fe_3O_4 qui peuvent être synthétisés avec une bonne stabilité chimique contre l'oxydation et qui possèdent des propriétés électromagnétiques intéressantes. Un contrôle remarquable de la taille des objets est permis par l'utilisation de coquilles de silice amorphe via le procédé sol-gel. Les coquilles de silice, hydrophiles, sont particulièrement stables en milieu biologique ($\text{pH} < 9$) et peuvent être encore plus stabilisés avec des groupements fonctionnels. La fonctionnalisation avec des fonctions chimiques (amine, acides carboxyliques, thiols, époxydes) chargées à $\text{pH} 7.4^{18}$ et des chaînes de polymères PEG est bien connue et est particulièrement intéressante pour le couplage avec des biomolécules. De plus, une couche de silice écran les interactions dipolaires en écartant les particules magnétiques les unes des autres.

Une autre raison de choisir les nanoparticules magnétiques est leur comportement chauffant lorsqu'elles sont soumises à un champ magnétique alternatif radiofréquence. Dias *et al.* ont utilisé ce procédé pour évaluer la température au voisinage des nanoparticules, en chauffant leur nanoparticules d'oxyde de fer de 12 nm de diamètre fonctionnalisées avec de l'ADN de 10 à 12 paires de bases. Une élévation de température jusqu'à 8°C a été donnée par rapport à la température de la solution globale, à 5 nm de la particule. Cette élévation de température à l'échelle nanométrique est la clé de nombreuses applications dans le traitement de cancers¹⁹, d'activation de polymères thermosensibles ou de biomédecine pour le relargage ciblé de médicaments. En effet, le chauffage d'une solution biologique est un problème délicat dans une logique d'amplification et /ou détection d'une cible biologique. Outre, une dénaturation évidente des composants non compatibles avec les hautes températures, une boucle de rétrocontrôle est nécessaire pour prendre en compte les pertes thermiques et contrôler précisément la température.

L'hyperthermie magnétique des nanoparticules de maghémite, c'est-à-dire le chauffage local généré par la relaxation de Néel²⁰ des nanoparticules superparamagnétiques sous champ magnétique alternatif permet de s'affranchir de ces contraintes. Le voisinage de la particule devient plus chaud que la solution elle-même et refroidit à température ambiante en l'espace de quelques secondes après que le champ magnétique soit coupé.

¹⁸Georgelin, T.; Bombard, S.; Siaugue, J.-M.; Cabuil, V. *Angew. Chem. Int. Ed* **2010**, *49*, 8897–8901.

¹⁹Jordan, A. In *Hyperthermia in Cancer Treatment: A Primer*; Springer US: Boston, MA, 2006; pp 60–63.

²⁰Néel, L.; HEED, C. *Ann. Geophys. CNRS* **1949**.

Notre objectif est de coupler les propriétés magnétiques et la stabilité colloïdale sur le même nano-objet. Cela demande la fabrication d'objets pas trop petits pour conserver un moment magnétique suffisant et pas trop grand pour rester dans un régime efficace de diffusion.

Afin de répondre à ces spécifications et de continuer dans la tradition du laboratoire PHENIX, nous avons conçu des nanoparticules cœurs-coquilles avec un cœur de maghémite $\gamma\text{-Fe}_2\text{O}_3$, une coquille de silice et fonctionnalisées avec des chaînes de polymères PEG et des groupements amines ; la chaîne de polymère pour la stabilité par répulsion stérique, les amines pour les interactions électrostatiques et la possibilité d'un greffage covalent.

Les particules magnétiques silicatées constituent des agents de capture très efficace pour l'adsorption ou la capture de protéines ainsi que d'ADN à leur surface mais sont peu aisément manipulables avec leur petite taille. Une modification de leur structure en particulier de celle du cœur était nécessaire pour les manipuler plus facilement et augmenter leur pouvoir chauffant en hyperthermie magnétique.

Dans le chapitre 3, une technique aisée et flexible pour relarguer les brins d'ADN cibles hybridés, de la nanoplateforme est présentée. En utilisant l'hyperthermie magnétique sur des nanoparticules super paramagnétiques cœurs-coquilles qui combinent biocompatibilité et flexibilité, tous les atouts sont de notre côté pour atteindre une efficacité maximale. Notre objectif néanmoins n'est pas de créer les nano-objets les plus efficaces en terme de chauffage mais de présenter une méthode robuste et reproductible pour synthétiser une nanoplateforme avec des propriétés magnétiques et biologiques flexibles en solution aqueuse. La synthèse proposée est simple mais efficace pour l'hyperthermie magnétique.

La nanoplateformey- $\text{Fe}_2\text{O}_3@\text{SiO}_2$ synthétisée est stable à pH biologique et possèdent des propriétés nouvelles et flexibles. La synthèse et la fonctionnalisation est réalisée par condensation directe d'organosilanes sur les nanoparticules d'oxydes de fer citratées et triées résultant en une distribution de taille étroite (indice de polydispersité de 0.17) centrée autour de 11 nm.

En jouant sur la forme des particules, en agrégeant les cœurs de maghémite, et sur la taille de la particule cœur-coquille, leur pouvoir chauffant sont augmentés. Le pouvoir chauffant est évalué en terme de « specific loss power » (SLP) en soumettant les particules à un champ magnétique alternatif et en enregistrant l'évolution de la température en fonction du temps. Pour les grosses particules, (100 nm en diamètre TEM), la SLP est multiplié par 1.25 par rapport aux cœurs non enrobés.

Nos particules sont composées de plusieurs cœurs de maghémite monodomaine agrégés dans une coquille de silice formant des chaînes courtes plus ou moins bien définies. Dans une solution liquide, les relaxations de Néel et de Brown sont en compétition. L'anisotropie effective est fonction de la forme, du volume de la particule et des effets de surface. Pour de courtes chaînes comme les nôtres, l'augmentation de la SLP vient majoritairement de la géométrie en chaîne et d'un pseudo ordre magnétique lorsque la géométrie de l'ensemble prend la forme d'ellipses. Les boucles d'hystérésis sont plus rectangulaires pour les chaînes que pour les sphères²¹.

²¹Serantes, D.; Martínez-boubeta, C. **2014**, No. MARCH, 3–7.

Notre synthèse a l'avantage de combiner une simplicité expérimentale et une augmentation de la SLP correcte ($1.4 \text{ m}^2\text{nH/kg}$) par rapport à des systèmes optimisés mais difficile en procédé hydrothermal en bâtonnets par exemple ($0.68 \text{ m}^2\text{nH/kg}$).

Avec des diamètres physiques de 42 à 86 nm, les nanoparticules cœurs-coquilles synthétisées possèdent une charge positive après fonctionnalisation avec des groupements amines et des chaînes PEG permettant une stabilité colloïdale ainsi qu'un couplage avec des biomolécules. De 6 000 à 45 000 groupements amines sont disponibles, par particule, pour le couplage.

Une post-fonctionnalisation en greffant de l'ADN sonde, complémentaires à la cible, est réalisé afin de la capturer, avec une haute sélectivité. Avec la répulsion stérique due aux chaînes PEG et la répulsion électrostatique entre les brins d'ADN, un maximum d'environ 200 ADN sondes a pu être greffé par particule.

Un protocole modifié pour le greffage, immobilisation d'ADN duplex au lieu de brins séparés, a été effectué afin d'optimiser la quantité d'ADN sonde à la surface pour une meilleure efficacité de l'hybridation. Le relargage subséquent d'ADN cible par chauffage à 95°C de la solution dans son ensemble a permis de dénaturer 100 à 150 ADN cibles.

Soumis à un champ magnétique alternatif, les nanoparticules cœurs-coquilles de 80 nm de diamètre TEM, sont aussi efficaces en chauffage local par relaxation qu'en chauffant toute la solution à 95°C . La solution est ainsi maintenue à 27°C , un point crucial pour un milieu biologique ou une efficacité énergétique. Ce travail se veut une preuve de concept pour le relargage d'ADN à température ambiante.

Nos résultats demandent à être appliqués, pour une validation du procédé, à un schéma classique d'immobilisation de sonde, d'hybridation de cibles et de dénaturation. Afin de prouver la haute spécificité de capture de notre nanoplateforme, cette capture doit s'effectuer en milieu biologique complexe avec un mélange de séquences d'ADN de séquence et de longueur variable.

Nous avons donc construit avec succès une nanoplateforme efficace pour la capture et le relargage d'ADN, modèle du miARN-122. Transposer ce premier système en microfluidique, a permis de diminuer le temps d'expérience, la quantité d'échantillons utilisée. En effet, dans un canal de dimensions micrométriques, les collisions sont augmentées, amplifiant la dynamique des réactions. De plus, ce module de capture peut être couplé avec le module de détection du chapitre 2 afin de constituer un laboratoire-sur-puce complet et d'éviter une détection par fluorescence qui, d'une part perd des particules à cause des multiples filtrations hors puce et d'autre part est limitée en sensibilité (10^{-6} M).

Vers un laboratoire-sur-puce complet

Dans la chapitre 3, il est démontré que l'hyperthermie magnétique peut être utilisée pour relarguer de l'ADN cible hybridé à sa sonde elle-même greffée sur une nanoparticule magnétique. L'objectif du chapitre 4 est, grâce à la transposition de l'hyperthermie magnétique sur puce, de réduire d'une part le temps d'expérience dédié à l'extraction, la purification et d'autre part, de coupler sur la même puce microfluidique un module de manipulation de la cible d'intérêt avec son module de détection.

Il a été montré que la miniaturisation et le couplage de différents procédés de biologie moléculaire sur le même dispositif permettait de réduire le temps d'analyse, le volume de réactifs, de diminuer la contamination en limitant le nombre de manipulation humaine. On peut citer des dilutions, dosages, et quantification en parallèle²² ainsi que le couplage avec des captures magnétiques²³.

Le module de manipulation de la cible présenté dans le chapitre 4 se focalise sur le relargage de la cible par dénaturation thermique des brins d'ADN hybridés par l'hyperthermie magnétique sur puce. La transposition en microfluidique permet de confiner les nanoparticules dans un canal de 200 nL augmentant l'efficacité des cinétiques de réactions moléculaires. L'amplitude des champs magnétiques peut être diminuée ainsi que le volume d'échantillons. Cela ouvre aussi la porte à une détection directe de l'ADN relargué sur la même puce.

Dans le chapitre 4, plusieurs verrous technologiques sont franchis :

- La transposition de l'hyperthermie magnétique sur puce avec une optimisation du temps de résidence des nanoparticules sous champ pour un relargage de cibles augmenté.
- La fabrication d'un dispositif microfluidique pour réaliser une hyperthermie magnétique couplée à une détection électrochimique avec les points clés technologiques suivants : des électrodes encastrées dans un canal micrométrique gravé, un collage verre/PDMS très fin.

Ces résultats constituent les composantes d'un laboratoire-sur-puce complet pour le diagnostic médical. Ce dispositif est donc une réponse à la problématique du LOC tout intégré. Ce dispositif fluidique permettra une extraction sélective des cibles grâce à l'appariement entre la cible et la sonde. L'intégration sur la puce d'un module de détection électrochimique en aval du module de relargage rend possible la détection directe des cibles. La biocompatibilité et la fonctionnalisation par chimie de surface est fournie. Des nanoparticules magnétiques avec une fonctionnalisation flexible peuvent être intégrées de manière optimale pour l'extraction des cibles d'intérêts et leur relargage subséquent.

L'hyperthermie magnétique sur puce jette les bases pour de nombreux ajustements en termes de module d'extraction et de focus cellulaire ou moléculaire. Finalement la miniaturisation permet l'intégration d'une technique *in situ* de détection près des espèces relarguées permettant d'éviter le chauffage global de la solution et en réduisant le temps d'expérience en supprimant les étapes de filtration hors puce. Toutes ces optimisations vont d'autant plus augmenter l'intérêt de l'hyperthermie sur puce et l'efficacité de la détection microfluidique. Pour cette partie, l'intégration d'une microélectrode de type bande va permettre une quantification directe des espèces relarguées par électrochimie²⁴.

De nombreux systèmes pourraient bénéficier d'un chauffage local. En effet, le chauffage d'une solution biologique est un point délicat d'un processus d'amplification ou de détection de la cible d'intérêt. Un chauffage global nécessite l'utilisation d'une boucle de rétrocontrôle pour compenser

²²Ferrigno, R.; Lee, J. N.; Jiang, X.; Whitesides, G. M. *Anal. Chem.* **2004**, *76*, 2273–2280.

²³Saliba, A.-E.; Saias, L.; Viovy, J.-L. *Proc. Natl. Acad. Sci. U. S. A.* **2010**, *107* (33), 14524–14529.

²⁴Horny, M. C., Lazerges, M., Siaugue, J. M., Pallandre, A., Rose, D., Bedioui, F., ...&Gamby, J. (2016). Electrochemical DNA biosensors based on long-range electron transfer: investigating the efficiency of a fluidic channel microelectrode compared to an ultramicroelectrode in a two-electrode setup. *Lab on a Chip*, *16* (22), 4373-4381.

les pertes thermiques et peut induire la dénaturation des composants non compatibles avec les hautes températures.

Le chauffage locale sur ou en dehors d'une puce a déjà été utilisé dans la littérature pour des procédés cellulaires²⁵ ou moléculaires. La PCR, le protocole le plus utilisé pour amplifier des brins d'ADN avant détection nécessite un contrôle précis de la température sur une large gamme, à chaque cycle d'amplification (90°C, 55°C, 70°C et 37°C), induisant un temps long d'expérience.

Actuellement, la PCR en goutte, la PCR isothermale (LAMP, NASBA, RCA)²⁶ sont des alternatives à la PCR classique. Un dispositif industriel de contrôle de température Cherry Biotech fait état d'un chauffage et refroidissement le plus rapide du monde pour la microscopie mais uniquement dans une gamme de 5 à 45°C²⁷. Mais tous ces dispositifs sont couplés à un module de contrôle de température extérieur et à une chambre de thermalisation que ce soit pour un chauffage par effet Joule, Peltier, infrarouge ou microondes.

Notre dispositif est cohérent avec les innovations citées ci-dessus. Il permet la manipulation aisée de fluides biologiques sans interférence (sans fuite, ni adsorption démesurée). Le verre est biocompatible, transparent, non poreux ; le PDMS biocompatible, transparent et avec une adsorption réduite en biomolécules. La microfluidique permet un contrôle fin de la dynamique de l'environnement du microsystème (concentrations, flux, temps de résidence dans le canal) tout en gardant un volume de réaction adapté à l'utilisation d'échantillons biologiques précieux. L'utilisation de l'hyperthermie magnétique permet d'éviter l'utilisation de contrôleur de température extérieur ; l'inertie thermique n'est plus un paramètre limitant le temps de réaction.

Notre dispositif peut s'adapter aux technologies citées ci-dessus : les nanoparticules sont assez petites pour être assimilées par des cellules et le protocole PCR peut s'effectuer sur des brins d'ADN greffés à des nanoparticules.

Conclusion

Ce travail de doctorat s'inscrit dans le cadre des biocapteurs à ADN et des laboratoires-sur-puce pour le diagnostic précoce des miARNs. L'objectif est de challenger la RT-PCR, longue, avec des erreurs de quantification et des cycles thermiques à contrôler précisément. Ce travail cherche à aller au plus près des spécifications cliniques de spécificité, rapidité, portabilité porté par une citation de Whitesides : "In the future, it is certainly possible that healthcare will move from treating to anticipating disease." Whitesides, 2006.

La force et l'originalité de ce travail vient de la collaboration et la mise en commun de compétences de quatre laboratoires : le Laboratoire Interfaces et Systèmes Electrochimiques LISE (UMR 8235 CNRS/UPMC Paris) avec Jean Gamby pour l'expertise en Electrochimie et Microfluidique, le

²⁵Chen, T.; Gomez-Escoda, B.; Munoz-Garcia, J.; Babic, J.; Griscom, L.; Wu, P.-Y. J.; Coudreuse, D. *Open Biol.* **2016**, *6* (8), 160156.

²⁶Chang, C.-M.; Chang, W.-H.; Wang, C.-H.; Wang, J.-H.; Mai, J. D.; Lee, G.-B. *Lab Chip* **2013**, *13* (7), 1225–1242.

²⁷Heater Cooler for Microscopy | Cherry Biotech <http://www.cherrybiotech.com/heater-cooler-for-microscopy> <http://www.cherrybiotech.com/heater-cooler-for-microscopy> (accessed Apr 27, 2017).

Laboratoire Physico-Chimie des colloïdes et Nanosystèmes Interfaciaux PHENIX (UMR 8234 CNRS/UPMC Paris) avec Jean-Michel Siaugue pour le superparamagnétisme des nanoparticules, l'Unité de Technologie Chimiques et Biologiques pour la santé UTCBS (Chimie ParisTech, INSERM, Université Paris Descartes) avec Mathieu Lazerges pour l'expertise en biocapteurs à et le Centre de Nanosciences et de Nanotechnologies C2N (UMR 9001 CNRS Univ. Paris-Sud) pour les techniques de micro- et nanofabrication en salles blanches.

Ce travail a commencé par s'appuyer sur un état de l'art conséquent pour définir les avantages et inconvénients de l'énorme quantité de biocapteurs et de techniques de détection présents dans la littérature pour justifier le choix de biocapteurs électrochimiques et des nanoparticules magnétiques, tradition des laboratoires cités ci-dessus et la pertinence de la microfluidique pour la détection moléculaire. Le choix est un choix de simplicité : une détection basée sur l'hybridation plutôt que le séquençage directe pour détecter une séquence d'ADN, un capteur électrochimique pour convertir un événement de reconnaissance biologique en un signal électrique sans autre transformation du signal physique.

Des barrières technologiques et des verrous de procédés de fabrication ont été levés afin d'obtenir les composantes pour un laboratoire-sur-puce complet pour le diagnostic médical.

Premier verrou : la transposition en microfluidique d'un biocapteur électrochimique en configuration à deux électrodes et la détection d'ADN par hybridation. Cette transposition a mis en évidence l'importance de la géométrie des électrodes, du comportement hydrodynamique, des propriétés de transport de masse, du matériau de l'électrode et de la densité en sonde sur la détection de l'hybridation. L'utilisation d'une Ultra-microélectrode plane permet d'avoir une résolution spatiale et temporelle pour étudier des phénomènes rapides, avec une réponse quasi-stationnaire dans des petits volumes ; un capteur très local de concentration qui répond aux attentes de confinement pour l'augmentation des performances d'un couplage électrochimie et microfluidique. L'électrolyte support, un mélange équimolaire de ferro-ferricyanure avec du bleu de méthylène dans du NaCl, permet de différencier un simple brin d'un double brin résultant en une limite de détection proche de 1 aM sous flux avec un capteur robuste sur Ultra-microélectrode plane en a-CNx.

Deuxième réalisation : le design d'une nanoplateforme adaptée pour la capture et le relargage d'ADN. L'agrégation de cœurs de maghémite avant enrobage dans une coquille de silice fonctionnalisée et stable a résulté en un pseudo ordre magnétique sous forme de courtes chaînes favorable à un pouvoir chauffant suffisant pour induire un chauffage local (en laissant la solution à 27°C) et relarguer autant d'ADN cible attaché à la sonde qu'un chauffage global à 95°C de la solution. Un protocole modifié « double brin » a été développé pour optimiser la densité de surface en sonde pour limiter les étapes de filtration et quantifier directement le relargage. Ce protocole a été mis en place en réponse à la gêne électrostatique des brins d'ADN chargés négativement en surface de la particule en plus de la gêne stérique des chaînes de polymères fonctionnalisées pour la stabilité de la particule.

Troisième avancée technologique : la transposition de l'hyperthermie magnétique en microfluidique permet de confiner les nanoparticules dans un microcanal et d'y concentrer un champ magnétique alternatif radiofréquence via l'entrefer d'un électro-aimant. La caractérisation des paramètres hydrodynamiques a montré que la réaction limitante était la réaction de désybridation elle-même qui nécessitait un temps sous champ de dizaine de secondes. Ce microsystème est une preuve de

concept pour le relargage d'ADN sur puce, il permet de collecter un nombre comparable d'ADN par rapport à une stratégie de chauffage global à 95°C. Cette preuve de concept est l'objet d'une déclaration d'invention au CNRS (phase de dépôt).

Et enfin la conception d'un dispositif permettant le couplage de l'hyperthermie magnétique et d'une détection électrochimique sur la même puce, est l'objectif d'un LOC complet. Dans cette partie, nous avons été confrontés à l'utilisation de nouvelles technologies pour l'intégration d'une Ultra-microélectrode plane dans un canal profond gravé dans le verre et le collage de PDMS très fin sans fuite et résistant à de forts flux ($1 \mu\text{Ls}^{-1}$).

Ces réalisations et résultats constituent une avancée vers un laboratoire sur puce complet pour le diagnostic médical. Ce dispositif fluide permettra une extraction sélective de cible grâce à l'appariement spécifique des brins complémentaires. La miniaturisation permet l'intégration d'une technique de dénaturation de cibles en laissant la solution à température ambiante en amont d'un système de détection, une détection directe par électrochimie avec une haute sensibilité par rapport à la fluorescence. A noter que biocompatibilité et fonctionnalisation de surface sont compatibles avec le dispositif. La miniaturisation et la portabilité totale du dispositif sont possibles. On peut envisager des générations de flux par gravité par exemple ; la puissance nécessaire pour l'hyperthermie magnétique n'excédant pas celle d'un transformateur de téléphone portable.

L'objectif de ce travail de thèse n'était pas d'optimiser au maximum chaque brique du laboratoire-sur-puce mais plutôt de montrer l'influence de la transposition en microfluidique et son apport en termes de limites de détection optimisées, et temps d'expérimentations réduits. Le Chapitre 4 se veut une preuve de concept pour l'hyperthermie magnétique sur puce et devra être confronté à une solution biologique complexe d'ADN de longueurs et de séquences variables. On peut noter que le dispositif dans son ensemble possède une double barrière de spécificité, l'une à travers l'hybridation sur nanoparticules, et l'autre à travers les sondes couplées à l'UME.

Une stratégie a été proposée pour réaliser un module de capture complet (capture, immobilisation, purification, relargage) en couplant une géométrie fluide en coude avec des séquences magnétiques en champ statique et alternatif afin d'immobiliser les nanoparticules magnétiques taguées avec les molécules d'intérêt, de les séparer de leur matrice biologique avant de les relarguer par hyperthermie magnétique. Cependant dans la matrice d'origine des miARNs (sérum ou plasma), ces derniers sont encapsulés dans la protéine AGO ne laissant visible que 7 nucléotides sur 23 pour l'hybridation avec la sonde. Cela ne semble pas être suffisant pour un événement de reconnaissance spécifique, d'autant plus qu'une large portion de miARNs ont des séquences similaires. Une solution consisterait à fonctionnaliser les nanoparticules avec des anticorps spécifiques de la protéine argonaute du miARN à détecter mais ce genre d'anticorps, à notre connaissance, n'a jamais été synthétisé. Pour l'instant, le sérum et le plasma doivent être traités par un kit Qiagen mentionnée dans le chapitre 1 et c'est une mixture d'ARN qui serait injecté dans la puce.

Ce travail de thèse a été valorisé en quatre publications scientifiques et une déclaration d'invention en cours au CNRS. Deux articles ont déjà été parus, deux autres sont en phase d'écriture. Ces travaux scientifiques ont été présentés dans trois conférences internationales et une conférence nationale (deux oraux et deux posters).

Chapter 1

Bibliographic review

This opening chapter gives a general overview of this thesis work to justify the use of each technology.

In the first instance, the focus will be given to our targets of interest, micro ribonucleic acids (miRNAs) and in particular to the miRNA-122, to justify the research efforts devoted to DNA biosensors. We will then provide a detailed investigation of a particular class of DNA biosensors, electrochemical hybridization detection-base biosensors, commonly considered as the easiest way to detect DNA. Secondly the input of microfluidics on limit of detection, time of analysis and miniaturization will be discussed. The concept of mass-transport in fluidic channels and the competitive interactions of diverse phenomenon will be introduced. For this part we will rely on the intuitive study from Squires *et al.* that copes with diffusion, convection and reaction competition [10]. Finally, seeking the manufacture of a fully-integrated Lab-On-Chip, we will introduce the contribution of magnetic nanoparticles and magnetic separation. A brief overview of magnetic nanoparticles' properties and their applications in biomedicine will precede our focus on magnetic separation and magnetic hyperthermia.

This chapter will conclude on the coupling between all above mentioned techniques and the presentation of our platform for DNA hybridization detection.

1.1 miRNAs: the design of unique patterns of disease's state

1.1.1 miRNAs: post-transcriptional regulators

Powerful regulators of various cellular processes (pathologies, tissue remodeling) by modulating gene expression interference RNA (RNAi) can be decomposed in two groups: short interfering RNA (siRNA) and microRNA (miRNA). miRNAs are non coding RNA small from 20 basis or so. This special type of RNA, ribo-regulators are able to switch off a gene activity by acting directly on the gene or on messenger RNA (mRNA). It is a downregulation by either slicing mRNA or by a fixation on the 3'UTR area and blocking translation. Following we will start with the description of the structure, biogenesis and action of miRNA then its regulator role. Finally the detection will be discussed and the special case of our miRNA-122.

Primary structure of miRNA consists in a seed sequence from nucleotides 2 to 8. The seed gives the specificity of the miRNA target although supplementary nucleotides 13 to 16 play also a role in miRNA specificity. It is the seed that recognizes the 3'UTR mRNA area. A family of miRNA is a family with identical seed. Various sequences corresponding to the same seed are possible (isoform) with a divergence in the 3' area. The variation can be in the length of the sequence as well as in the sequence itself. These variations are coming from the maturation process.

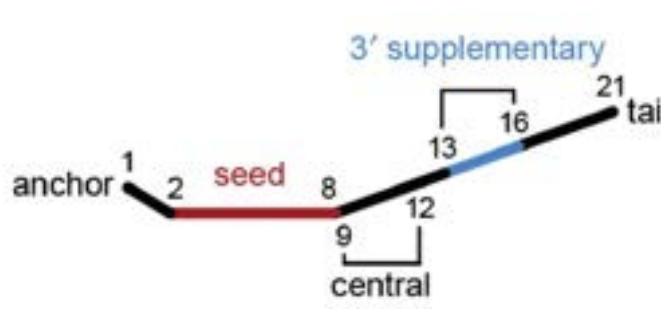


Figure 1.1: Primary structure of a miRNA [11].

miRNAs are acting as surveillance agents of the genome and transcriptome (all RNA generated from genome transcription) by targeting chromatin and transcripts. They act on several levels from chromatin formation to mRNA degradation and translation blocking [12].

miRNA are coming at 50% from intergenetic region of DNA (TU) or classe II genic area (dedicated to RNA) or even from mRNA intronic (not coding) areas. Human genome is composed at 5% of miRNAs *i.e.* more than 1000 different miRNAs regulating more than 30% of our genes. They control cellular growth tissues differentiation, heterochromatin formation and cellular proliferation [13].

miRNA biogenesis

miRNA is transcribed by a type II RNA polymerase into long primary transcripts (pri-miRNAs) either alone, from a unique gene, either in clusters (61% of miRNAs) giving a polycistronic organization. A polymerase is an enzyme that synthesizes a polynucleotide strand (DNA or RNA) from the 5' to the 3' end by using the complementary strand as a matrix and triphosphate nucleotides as monomers. Pri-miRNAs

fold into hairpin structures containing imperfect base pairing due to less stringent Watson and Cricks rules (G-U pairing for example). These loops are recognized by the Drosha ribonuclease III enzyme that slice around the pri-miRNA to yield precursor miRNAs (pre-miRNAs). A nuclease is an enzyme that cut phosphodiester links between nucleic acids and a ribonuclease is catalyzing RNA degradation in small strands. Transported out of the nucleus by the Exportin complex 5, the pre-miRNA is cut at the loop basis by another RNase III enzyme Dicer, to give a double-stranded precursor. Only one strand will be chose to give rise to the mature miRNA and to be placed in the Argonaute protein by a complex process, Figure 1.2.

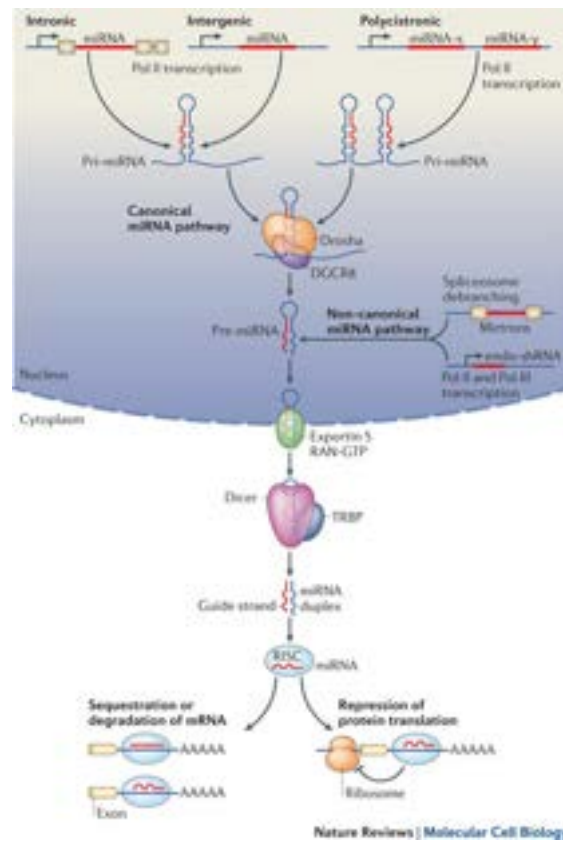


Figure 1.2: The miRNA biogenesis pathway.

Argonaute is part of a bigger complex, the RNA-induced silencing complex (RISC), Figure 1.3. miRNAs can only interact with their targets after their integration in the RISC complex.

When loaded with a guide strand (either siRNA or miRNA), it can inhibit mRNAs by two mechanisms as displayed on Figure 1.4.

If the miRNA is perfectly paired to the mRNA, it plays the siRNA role. Argonaute 2 (AGO-2) slices the mRNA resulting in its rapid decay. If the target and the strand are not completely complementary, miRNA through RISC initiates a cascade of events to block translation and degrade the mRNA [2].

The miRNA strand recognizes the target then GW182 [1] communicates with the PABP protein fixed on the adenylated tail of the mRNA. The miRNA is fixing itself on the non coding 3' area (3'UTR) of the mRNA. This fixation blocks translation and the further synthesis of proteins. Then mRNA is destabilize by disanylation and

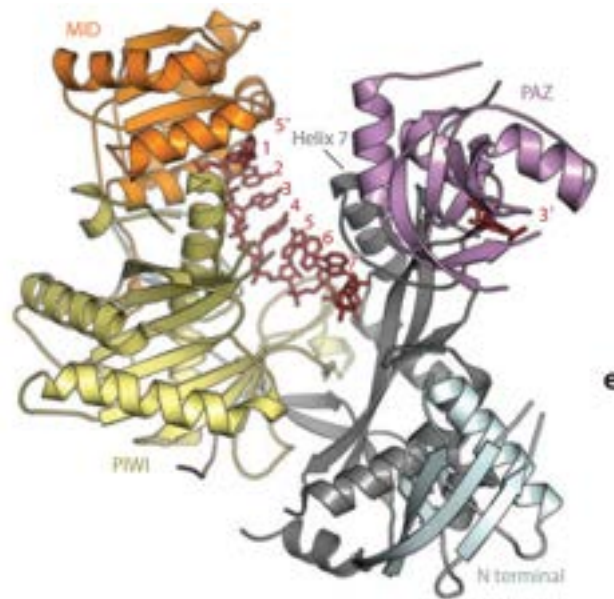


Figure 1.3: The RISC complex. The miRNA is numbered from its 5' to its 3' end.

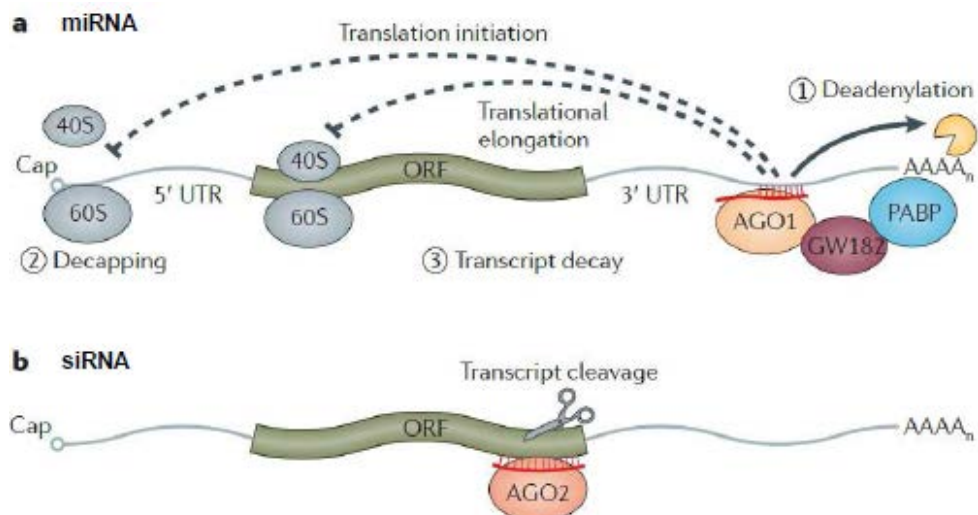


Figure 1.4: siRNA and miRNA action on mRNA as post-transcriptional regulators [14].

the expression profile of miRNA are highly specific on tumor type and gives a characteristic signature of each cancer [22].

| miRNA family/cluster | Tissue/cell type | Target mRNAs | Target processes | Oncogene/tumor suppressor | References |
|----------------------|--|---------------------------|---|---|-------------|
| let-7 | Ubiquitous | Lin-28, Hmga2, Igf2bp1 | Development, proliferation, organismal growth | Tumor suppressor | 36,38,47,48 |
| miR-1-133 | Cardiac and skeletal muscle | Hand2, Inx5, Ptbp1, Ptbp2 | Cell cycle, cardiac differentiation, splicing | Tumor suppressor | 22,49 |
| miR-15/16 | Ubiquitous | Bcl2, Cyclin D, Cyclin E | Apoptosis, cell cycle | Tumor suppressor | 50-52 |
| miR-17-92 | Ubiquitous/enriched in B cells | c-Myc, E2F, Bim | Proliferation, apoptosis | Oncogene | 53-56 |
| miR-22 | Ubiquitous/enriched in cardiac and skeletal muscle | Purb | Calcium homeostasis, stress response | Tumor suppressor | 57,58 |
| miR-34 | Ubiquitous/enriched in testis, brain, and lung | Sirt1, Snail, PNUMS | p53 pathway, EMT | Tumor suppressor | 59-69 |
| miR-122 | Liver | AldoA, Hfe2 | Cholesterol biosynthesis, lipid metabolism | Tumor suppressor | 70,71 |
| miR-124 | Neurons | Ptbp1 | Differentiation | Tumor suppressor | 72 |
| miR-143-145 | Ubiquitous/enriched in smooth muscle | Klf4, Elk-1, myocardin | Differentiation | Tumor suppressor | 73-76 |
| miR-181 | Immune cells | Shp1, Shp2, Dusp6, Tcf1 | Differentiation, TCR signaling | Unknown | 77-79 |
| miR-193b-365 | Brown adipocytes | Runx1t1 | Differentiation | Unknown | 80 |
| miR-200 | Epithelial tissue; olfactory bulb | Zeb1, Zeb2 | EMT | Context-specific oncogene or tumor suppressor | 81-83 |
| miR-203 | Epidermis | p63 | Cell cycle, proliferation, differentiation | Tumor suppressor | 84 |
| miR-223 | Myeloid cells | Mef2c | Differentiation | Tumor suppressor | 85 |
| miR-290-295 | ESCs | Lats2, Rbl2, p21, Casp2 | Cell cycle, proliferation, apoptosis, differentiation | Oncogene | 86-89 |
| miR-451 | Erythrocytes | 14-3-3z | Oxidant stress | Tumor suppressor | 90 |

Figure 1.6: Tissue/cell type-specific miRNAs [2].

1.1.2 The miRNA-122 key regulator for numerous pathways

First identified by Lee *et al.* in 1993 in *C. Elegans* [23], the miRNA-122's loci is localized on chromosome 18. It derives from a non coding liver specific RNA, transcribed from HCR gene. [24]. In order to be able to detect a liver injury e.g. a death a hepatic cells long before the liver death, specific markers for liver are needed in blood. Indicators that notably increases if the liver is suffering. Which is the case of enzymes ASAT or ALAT but muscles and heart are also releasing some. Only the miRNA-122 seems to keep up. Even if the concentration of circulating miRNAs are around the attomolar for a healthy liver. Compared to an increase in alanine aminotransferase (ALT) activity in blood (Figure 1.7) the changes in miRNA-122 concentrations appear earlier. Changes specific for liver injury directly correlated with liver histology. Its concentration return to baseline before ALT. The circulating miRNA-122 has a shorter circulating half-life which reflects dynamic changes in the histopathology state of the liver with more accuracy than ALT.

miRNA122 is a promising biomarker to detect among others drug-induced liver injuries (DILI) caused by obesity, alcoholism, HCV or HBV [26]. Indeed miRNA-122 is presenting a sequence mostly common between patients and its circulating level is affected when liver is in a pathological state. miRNA-122 is accessible in serum or plasma. It is highly liver specific and highly sensitive. Indeed, its level increases by a 100 to 400-fold factor in case of liver injury [27, 28]. It is generally dominant in liver up to 70% of the miRNAs population. It regulates lipids and cholesterol metabolism. It protects indirectly the liver against inflammation and fibrosis. It acts as hepatic tumor suppressor [26] and for hepatitis C (at the origin of cirrhosis, renal

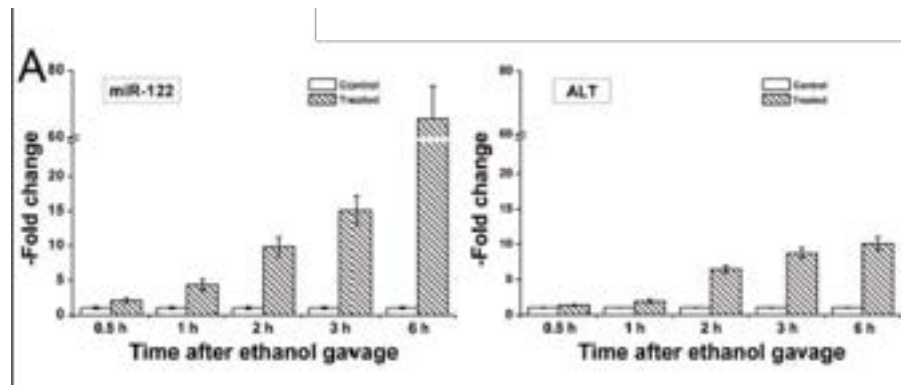


Figure 1.7: Comparison between alanine aminotransferase (ALT) and miRNA-122 responses to ethanol gavage [25].

insufficiency and HCC) plays an important function in virus replication.

In 2002, shortly after miRNA recognition, Calin *et al.* showed the correlation between miRNA abundance and human pathologies [29]. Five years later by suppressing Dicer, Chen *et al.* have caused a cardiac arrest [30]. miRNA was detected in serum and plasma with stable and reproducible levels: in 2009 Ji *et al.* detected a cardiac injury by finding miRNA biomarkers in plasma [31]. The same year the over-expression of miRNA 122 was proven to protect against liver cancer.

The incredible enthusiasm for miRNAs as a novel class of biomarkers comes also from the fact that miRNA levels can be modified *in vivo* and selectively targeted to regulatory pathways. Nevertheless side effects, stability of the strand *in vivo* and specific uptake by cells are not yet fully unraveled.

1.1.3 DNA chips and miRNAs detection

We will divide this section in two parts, the first short part focus on deep sequencing, Northern Blot Analysis and *In Situ* hybridization and the second on DNA chips current and future designs that could detect miRNAs. But first, we will address the issue of miRNAs extraction from blood.

miRNAs extraction

Extracellular miRNAs are stable in circulation [15, 32] reflecting tissue-and disease-specific miRNA signatures [33]. However exploiting them as biomarkers requires an extraction from the biological matrix. Indeed, in blood, miRNAs are associated with proteins such as argonaute or contained in exosomes [5]. Multiple extraction procedure with variable efficiencies are available [5]. Phenol:chloroform extraction takes one night to be performed, numerous silica-based methods can be partly automated with the Qiagen QiAcube [34], they all extract RNA. Extracellular miRNAs represent usually less than 1% of the total RNA recovered [17] yielding very low concentrations, thus the need of performant methods of detection.

Deep sequencing, Northern Blot Analysis and In Situ hybridization

Deep sequencing measures the absolute abundance and allow to discover new miRNA but the process is long and expensive. Only a few studies are reported due to the large amount of bioinformatic data generated [1].

Northern Blot Analysis is the most widely used technique although it's time consuming (two days) and requires large amounts of RNA (more than 8 μg) [1]. The process is composed of RNA isolation and fractionation by electrophoresis. The small fragments are transferred and fixed into a membrane and left to be hybridized on probes modified with a radio active ATP. The technique is specific up to 3 base-pairs.

In Situ hybridization reports of tissue specific expression patterns only with long RNA probes can be found [35].

DNA chips

Following electronic miniaturization, the increase of the number of components per unit area and the costs reduction, the miniaturization of DNA "chips" (so called by analogy with electronic chips) enabled the increase of analysis number notably crucial in gene sequencing. Automation, reduced amount of reagents and reasonable costs are promises arising from miniaturization.

The common ancestor macro-arrays are chips on which hundreds of probes (complementary DNA, cDNA) are dropped and analyzed by systems like BD-ClontechTM for example. The reduction in sizes and the increase in the number of probes gave rise to microarrays. In 2D geometry, or on more exotic templates, DNA chips and microarrays are micron-size inert (to decrease interferences and adsorption) substrate (plastic, glass or silicium less cheap) on which up to millions of probes are grafted. Their principle are based on the hybridization (more or less complementary pairing according to Watson and Cricks'rules) between the probe and the studied target. Target are prior to use amplified by PCR and labeled. One can cite some chips based on an original approach like MICAM^R (CEA LETI/CisBioTM) or NanoChip^R (NanogenTM). Their devices are composed of hundreds of electrodes engraved and individually addressable with a multiplex. The user can chose his probes before grafting via pyrrole electrically-induced polymerization (MICAM^R) or biotin-streptavidin linking (NanoChip^R). Sensibility is increased in the first case by the porous nature (high surface to volume ratio) of pyrrole. In the second case the electrical signal is used to attract and concentrate targets and probes on the detection area. One can also cite original geometries. IlluminaTM designed a millimetric bundle of optical fibers, each fibers modified with a microbead and a probe stuck at their extremity. The fluorescence of various labeled targets can be detected simultaneously. LuminexTM designed two batch of porous beads different in color. OGN are functionalized on their surface according to their color and left to hybridized with fluorescent targets. A cytofluorimeter qualitatively (fluorescence) and quantitatively (number of colored beads) analyzes the results that can be applied not only for OGN but also for antigenes, antibodies, ligands, proteins.

Microarrays were reported to be used for miRNAs extracted from tissues [36] and plasma [37] for the detection of heart disease [38].

All these setups have a common point they have a feeble sensibility that comes from their detection system. That is why they need to use amplified targets usually done by PCR. The principle is the repeated replication *in vitro* of a DNA strand with specific primers whose queen is the Polymerase Chain Reaction (PCR). Other techniques are available NASBA (Nucleic acid sequence based amplification), TM for isotherm target amplification, LCR (ligase chain reaction), Q β replication for probe amplification or bDNA for signal amplification. Their development are complex and their use is limited to commercial diagnostic kits. We will only describe PCR in the next part. For others techniques the reader can find complete descriptions in the book of Kaplan & Delpuch (Molecular Biology and Medicine) [22] and in the work of Chang *et al.* [39].

Filed in 1985, the patent for PCR of Mullis was in a short time used by all laboratories of molecular biology. Behind its easy realization and principle is hidden some traps that are susceptible to taint results with some errors. The principle lies on the DNA synthesis by a polymerase (Taq) from a synthetic primer that hybridizes on the sequence to be analyzed. Amplification is exponential as the number of DNA copies doubles after each cycle of denaturation/hybridization/elongation. First DNA is denatured at ca. 90°C to separate the two strands. Then after cooling to ca. 50°C the primer hybridizes on single-strand DNA. Finally around 70°C Taq replicates the DNA sequence from the primer. Usually 30 cycles of 6 minutes are needed to get 2³⁰ copies.

For RNA sequences a reverse transcription into cDNA is needed so that Taq can use it as a matrix [40]. In order to get a quantitative PCR, Real Time (RT)-PCR is used [41, 42]. RT-PCR is based on fluorescence resonance energy transfer (FRET, fluorescence quenching). A supplementary complementary sequence is introduced. Fluorescence is quenched as long as the target and the sequence are hybridized. The latter is destroyed as PCR goes on. The emitted fluorescence is proportional to the number of destroyed sequences and thus to the number of targets. The costs of RT-PCR can be reduced by using SYBR green that emits a green fluorescence when linked to a double strand but lacks in specificity.

First obvious limitation in PCR is the need for rapid variation of temperature with a 0.5 to 1°C precision that made PCR a long process (3 hours). To circumvent this drawback a nanoliter PCR is reported (CEA LETI). A small serpentine is etched on a silicium chip. Walls are doped so that the circulation of an electric current increases the heating of the silicium, controlled by sensors. The PCR is realized along the temperature gradients of the serpentine resulting in quicker thermic exchanges.

Above all the small size (around 22 nucleotides, the size of a PCR prime) of miRNAs makes PCR and all types of detection methods (out of deep sequencing) challenging. With their small size, probe design is limited and more importantly binding efficiencies are depending on temperature (melting temperatures T_m are determined by GC contents) on top of the sequence. Moreover miRNAs differ in sequence's length. Binding affinity is miRNA specific. Different binding kinetics on the same detection system make it difficult to perform quantitative measurements and furthermore to amplify with efficiency and without errors propagating along amplification cycles. Rather relative changes in concentrations between diseased or healthy state can be detected [37]. miRNA are closely related and differs only from a few basis making cross-linking with probes inevitable. The length of the probe can

be engineered thanks to a LNA (locked nucleic acid) yielding more accurate results.

In the 2007 revised Edition of *Molecular Biology and Medicine*, Kaplan & Delpech pinpointed the major challenge for highly sensible biosensors: transform a biological signal (hybridization) into an electrical signal directly readable by a small and portable near-patient equipment. Such a sensor would have an increased sensibility and would allow to get rid of the PCR step, a non negligible obstacle even integrated on a chip.

1.2 Electrochemical DNA biosensors.

1.2.1 Principle

Since the invention of the Clark Oxygen Electrode sensor, biosensors have demonstrated their increasing ability to detect pathogenic and physiologically relevant molecules for clinical use. Defined as "an independently integrated receptor transducer device, which is capable of providing selective or semi-quantitative analytical information using a biological recognition element" according to IUPAC [43], biosensors are composed of three key components: (i) the detector identifying the stimulus, (ii) the transducer converting the stimulus into a useful output, (iii) the signal processing system delivering the data in a readable format. A biological recognition element or bioreceptor consists of an immobilized component able to bind with the specific target (antibodies, nucleic acids, enzymes, cells). The transducer is converting the biochemical signal into an more or less as so readable signal. Usually biosensors are classified either by type of biological signaling either by type of transduction. Perumal *et al.* provides an extensive overview on both types to which the reader may refer [44].

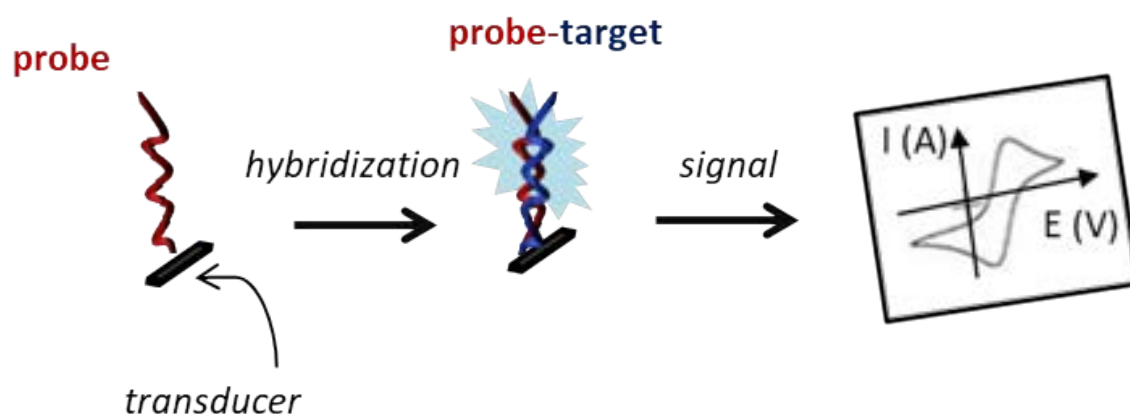


Figure 1.8: Schematic of DNA hybridization detection with voltamperometry.

We will not cover all the state of the art of all biosensors but following the above-mentioned consideration of Kaplan, electrochemical biosensors are compelling and literature offers an array of possibilities. Indeed electrochemistry is the only way

to directly transduce hybridization into an electric signal without further transformation of the physical signal and chemical modification of the target; an advantage over fluorimetric and optical sensors.

1.2.2 Three key steps to master a DNA biosensor

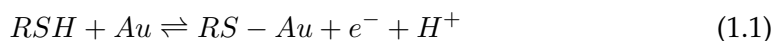
Because of its simplicity, DNA hybridization is more commonly used in the diagnostic laboratories than the direct sequencing method. DNA hybridization detection allies high efficiency and high specificity while the formation of the probe-target hybrid even in a mixture of many different, non-complementary nucleic acids. DNA biosensors are composed of a biological active layer (recognition element, the DNA probe) and converts the physical parameters of the biological interaction (hybridization) into a measurable analytical signal. Especially DNA biosensors are converting the base-pair recognition event into a useful electrical signal. The fabrication of an electrochemical biosensors is compatible with microfabrication technologies and consists in three key step: (i) immobilization of DNA probes, (ii) hybridization with target sequence, (iii) labeling and electrochemical investigation of the surface. The optimization of each step may conduct to an overall improvement in the device performance. The strategies to achieve probe immobilization, target recognition and detection are numerous. A plethora of biosensors can be found in the literature, which differ in the biological process followed, the choice of transduction exploited, and the electrode material used. We will subsequently detail each step and report particular achievements of the literature which conducted to an optimized LOD.

Probe immobilization

The strategy adopted in order to immobilize probes on a solid surface depends highly on the material used. We will focus on gold and carbon as they were reported to both provide different but both efficient approaches for probe immobilization.

Materials for electrodes: Gold versus Carbon

Electrode material is of crucial importance as currents have to be high enough to be able to distinguish between two hybridization state. Gold is of higher interest due to its conducting properties and it provides an elegant approach for well-defined and organized surfaces [45, 46, 47]. Direct chemisorption of thiol-modified DNA onto gold surfaces is the top of elegance. Sulfur coordinates strongly onto a variety of metals (gold, silver, platinum, gold is the most inert of them) following the equation:



Dense monolayer assemble in less than one hour [48] and even displace contaminants [46] avoiding the need to have a perfectly cleaned surface. SAM on gold were reported to be stable over -40 to 1400 mV (vs SCE) [49]. Full surface coverage by a monolayer of thiol dericativized DNA (HS-ssDNA) can be achieved in 2 hours with chemisorption enhanced at high salt conditions [50, 51, 52] hypothetically minimizing intermolecular electrostatic repulsions between DNA strands resulting in so dense layers that $[Fe(CN)_6]^{4-}$ was electrochemically silent [53].

Pan *et al.* used a gold electrode to detect oligonucleotides via a streptavidin/biotin binding [54]. To optimize the detection a mixed SAM of mercaptoundecanoic acid

(MAU) and mercaptoethanol (ME) or 6-mercaptohexanol (MCH) [55] to get a better coverage, a less dense SAM and higher difference of currents before and after hybridization yielding a 10^{-16} M LOD with LET.

Gold allows also the coupling between several techniques as considered by Manesse *et al.* with the coupling between Electrochemical Impedance Spectroscopy and SPR for single stranded DNA detection [56] on a SiO_x/Au surface. Au-SH links are the support of chemical and electrochemical reductions. SiO_x layer adds a notable stability that allows 20 hybridization/deshybridization cycles without degradation and a matrix for the immobilization of 10^{12} molecules per cm².

Carbon-based surfaces for DNA sensing have also received their fair chair of attention [57]: carbon paste [58], pencil lead [59], screen-printed [60], carbon fiber [61], glassy carbon [62].

Concerning the probe layer built step, carbon allow the control of surface chemistry and coverage. Potential-controlled adsorption [58, 63, 64] asks for oxidative pretreatment of carbon surface [65]. A positive applied potential enhances the stability of the probe through electrostatic attraction between the negatively charged phosphate DNA backbone and the positively charged electrode [66]. Nevertheless, adsorption does not resist stringent washing steps and favors dense layers that leave probes poorly accessible for targets. On the contrary covalent grafting provides a strong link to resist washing and regeneration steps. Among them, carbodiimide covalent binding is a prized method. On activated surface [62] of electrochemically oxidized glassy carbon surfaces, N-hydrosulfosuccinimide (NHS) and water soluble carbodiimide (EDC) reagents activate carboxylate groups [67]. Single-strand DNA covalently bind to these activated groups through deoxyguanosin residues. Optimized protocol involves modified carbon with steric acid and a DNA probe elongated with dG at the 3' end [68] or the direct immobilization of terminal amino groups through amide bounds formation. It is also applicable to avidin-coated surfaces [63] or polymer coated surfaces that offers conductivity properties [69, 61].

Independently of the kind of material used, the use of peptidic nucleic acids (PNA) probes instead of DNA showed enhanced selectivity and improved distinction between closely related sequences. PNA are DNA analogues but with uncharged pseudopeptide backbones resulting in less electrostatic interactions. This affirmation is leading to a key point for DNA probe immobilization enabling maximum hybridization efficiency. Probes have to be accessible for targets to hybridize, it's mainly going hand in hand with not to dense layers and favorable orientations. It is problematic for gold and its dense layers of thiol adsorbed probes. Mixed SAM were thus engineered with 2-mercaptoethanol (MCH) to increase target accessibility up to 100%.

Target hybridization

Once association of two complementary strands has begin, fast zippering enables formation of the duplex. Kinetics of hybridization reaction at solid surfaces are reported to be slower than in solution [70] due to the lower accessibility of the probe. Parameters such as ionic strength (salt conditions up to 3.2 M [71, 58, 72, 73], higher

concentrations favor non specific adsorption of the target [74] and stabilize mismatched duplex), temperature (with an optimum of 20-25°C below T_m [71]), contact time, length of the sequence play an important role.

The use of blocking agents to minimize non-specific adsorption has been proposed [69, 75]. Hybridization with an applied potential [58, 72, 73] was also reported to yield best results by bypassing the electrostatic repulsions between negatively charged DNA strands.

Numerous pathways for hybridization detection

In the domain of probes grafted on a solid substrate for direct hybridization with an unlabeled DNA target by using electrochemical transduction, a wide range of concentrations are reported in the literature from femtomolar to attomolar and even zeptomolar concentrations. We will further investigate the type of transduction used.

Direct DNA oxidation

Direct detection of DNA oxidation can be used per se [25, 76, 77, 78, 57, 79]. Indeed the faradic charge necessary for guanine oxidation is higher after hybridization, see Figure 1.9. Both on carbon electrodes or on conducting polymers the LOD reached is ca. 10^{-15} M for classical target DNA and nanomolar for single mismatch detection. For instance, Riccardi *et al.* [80] achieved a $2 \cdot 10^{-16}$ M limit of detection by monitoring the changes in oxidation of gold polypyrrole due to DNA hybridization. Differential pulse voltammetry (DPV) was used for direct DNA oxidation on a conducting polymer leading to a 10^{-17} M [81] and a 10^{-15} M limits of detection with genomic DNA on polydeoxycytidine [82]. However these biosensors can not be regenerated due to the irreversible nature of oxidation.

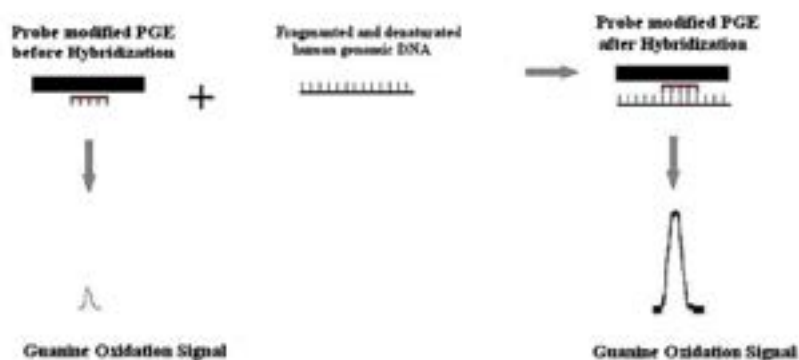


Figure 1.9: Oxidation based transduction [82].

Non-faradic biosensors

Another type of biosensors, the non-faradic biosensors [25, 76, 79] are based on the shift of impedance due to the increase of charge density after hybridization. Indeed DNA concentration and thus the concentration in counter-ions sodium shielding DNA according to the double-layer model increases. The precise measure of DNA hybridization via the impedance of the double layer is allowed thanks to this technique. Impedance measurements as they are dynamic contrary to voltammetric

techniques allow the double layer interfacial capacitance measurements and thus the screening of interfacial properties modifications of electrodes induced by charged molecules immobilization. Proof of the built of non faradic biosensors on carbon nanotubes conducting polymers or semi-conductors (with a higher variation of potential) can be found in literature. Their LOD reached atomic levels of detection. Non-faradic biosensors coupled with impedance techniques for screening the interface charge density have reached a 10^{-18} M limit of detection on GaN nanowires [83] (Figure 1.10) and a 10^{-20} M limit of detection on boron-doped diamond with a polyethyleneimine layer [84].

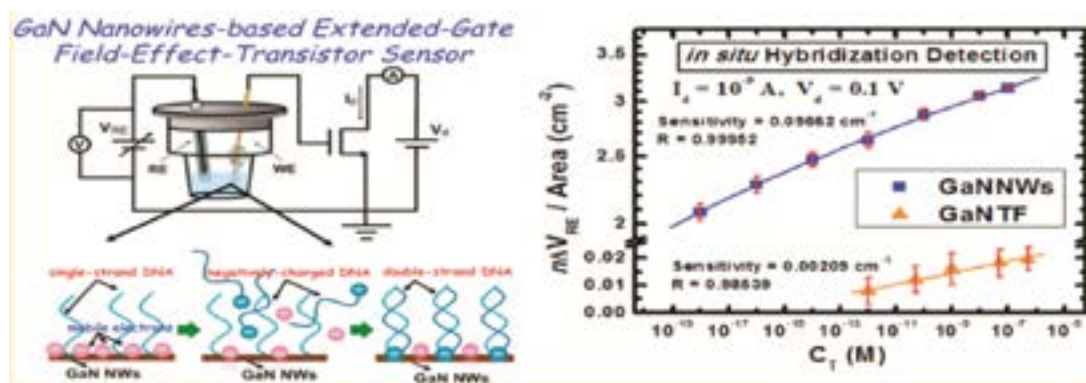


Figure 1.10: Ultrasensitive in situ label-free DNA detection using a GaN nanowire-based extended-gate field-effect-transistor sensor [83].

Long-range electron transfer toward a redox indicator

DNA, with its double-stranded structure is the seat of long-range electron transfer through the π -stacked aromatic cycles. A redox intercalator that increases electron transfer can be added as intercalant [57, 79, 85, 86, 87, 88, 89, 86, 90, 91]. Hybridization can be detected by an increase in current signal of an electroactive indicator that preferentially binds to the double-stranded DNA. This indicator can be a small electroactive DNA intercalating compounds that posses higher affinity for the hybrid than for single-strand DNA. The concentration of the intercalator increases at the electrode interface upon hybridization resulting in increased electrochemical signals.

$\text{Co}(\text{bpy})_3^{3+}$ was used for the detection of cystic fibrosis ΔF508 deletion sequence (3 base pairs mismatch with healthy sequence) [68] along with $\text{Co}(\text{phe})_3^{3+}$ in chronopotentiometry yealding a $0.05 \mu\text{g mL}^{-1}$ LOD. Daunomycin in linear sweep voltametry reaches a $0.01 \mu\text{g mL}^{-1}$ LOD. Dharuman et al. reported a 40% increase with the use of methylene blue, negatively charged and proflavine, positively charged, both redox intercalant [92]. Methylene blue has a strong association with free guanine bases of single strand DNA and was reported to have the ability to detect single mutation in short OGN [93, 94]. Chen *et al.* [95] have reported a 10^{-16} M limit of detection with their nanogap sensor with sandwich arrays of gold/ SiO_2 /gold using long-range electron transfer toward the redox indicator.

1.3 Microfluidics and Lab On a Chip

In the optic of always improving detection limits and reducing sample volume, microfluidic comes undoubtedly in mind. With microfluidics, volume of biological fluids needed is drastically decreased to the microliter or even nanoliter, automation is easier, kinetics are improved by flow circulation. But before diving into the ocean of papers on microfluidic devices, the improvement given by size reduction and in flow device are not that simple. Limits of detection hang on lots of variable obviously target concentration but also mass transport regime, probes densities, setup geometry.

1.3.1 Mass transport inside a microfluidic channel.

One can ask itself if feeble concentrations and small sensors can be mixed. Feeble target concentrations don't ask for a large area to catch them all? Divergent views are found in literature. Sheehan *et al.* have shown that diffusive transport of subpicomolar concentrations of targets would take hours to days to reach small sensors and that flow would not help [96] whereas on nanowires it takes minutes for a femtomolar target solution to be collected [97]. On a similar note Avila *et al.* define two regime for surface based sensors: a concentration limited regime (high volume samples, low affinity probes) and a ligand-depletion regime (high efficiency binding, feeble concentrations in target, small volumes). The latter highly dependent on probe densities yields an apparent K_D (equilibrium dissociation constant) that may lead to misinterpretation of observed affinity and possible discrepancies between LOD from two similar sensors [98].

Squires *et al.* provides an interesting intuitive approach to cope with competitive mass transport process [10]. Their model is the following: a target (with a diffusion coefficient, D) solution of uniform concentration C_0 is flowing through a fluidic channel of height, H , and width W_c ($W_c \gg H$) at a volumetric flow rate, Q . On the floor of the channel lies the sensor of width, W , and length, L , functionalized with a number of bm receptors per unit area (Figure 1.11).

Diffusion

Target molecules diffuse randomly and reach the sensor after a time $t \approx d^2/D$, d the distance to the sensor and D the diffusion coefficient of the molecule. The depleted zone grows thicker and thicker (with a $\delta \approx \sqrt{D \cdot t}$ thickness) and extent infinitely into the channel collecting targets at a j_D collection rate, adapted from Fick's law.

$$j_D = D \cdot \frac{c_0}{\delta} \quad (1.2)$$

When the depletion zone grows larger, diffusive flux gets smaller resulting in a slower collection of the targets. J_D depends on the shape of the sensor, the collection rate of sphere of radius L is given by $J_D^{(S)} = 4 \cdot \pi \cdot D \cdot c_0 \cdot L$ [99].

Convection

Convection transports targets along with the flow $Q/H \cdot W_c$. We are taking the pressure-driven Poiseuille flow case with a parabolic profile. Convection stops the growth of

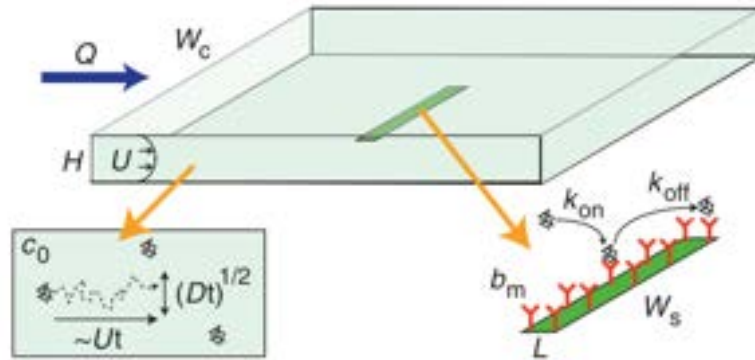


Figure 1.11: Squires' model [10] : a target (with a diffusion coefficient, D) solution of uniform concentration C_0 is flowing through a fluidic channel of height H and width W_c ($W_c \gg H$) at a volumetric flow rate, Q . On the floor of the channel lies the sensor of width, W_s and length, L , functionalized with a number of b_m receptors per unit area.

the diffusion layer. Equilibrium is reached at $j_D = Q \cdot c_0$ where the sensor collects every target injected. Diffusion dominates near the sensor, convection wins far away.

Two Peclet numbers can be defined to characterize mass-transport depletion zone around the sensor. The first Peclet number Pe_H [100] is used to distinguish the domination of diffusion versus convection.

$$Pe_H = \frac{Q}{D \cdot W_c} \quad (1.3)$$

For $Pe_H \ll 1$, the diffusion layer propagates and targets can be collected. For $Pe_H \gg 1$, convection shrinks the diffusion layer, targets are swept away before they can diffuse. Only a few enter the steady thin diffusion zone. The flow through the depletion zone is given by:

$$J_D \approx \frac{D \cdot c_0}{\delta} \cdot W_s \cdot L \quad (1.4)$$

The second Peclet number Pe_S tells if the depletion zone is thicker than the sensor or otherwise.

$$Pe_S = 6 \cdot \left(\frac{L}{H}\right)^2 \cdot Pe_H \quad (1.5)$$

The couple (Pe_H, Pe_S) gives the mass transport regime in which the (channel, sensor) of given dimensions operates. It is particularly important for scales as different as nano and microdevices. For example for a nanowire at a 10 fM target concentration, 3 hours have to be waited between binding events (the depletion zone is way bigger than the sensor). For a microsensor with a similar Pe_H binding events are happening every 7 s.

What about the chemical reaction?

In the first order Langmuir kinetics the surface concentration $b(t)$ of receptors bound by targets is the following [10]:

$$\frac{\partial b}{\partial t} = k_{on} \cdot C_b \cdot (bm - b) - k_{off} \cdot b \quad (1.6)$$

With $K_D = k_{on}/k_{off}$ the equilibrium dissociation constant so that the number of receptors bound in equilibrium is [10]:

$$N_R^B \approx \frac{bm \cdot A \cdot c_0}{K_D} \quad (1.7)$$

with A, the surface of the sensor.

Giving a critical concentration under which no targets bind [10]:

$$c^* = \frac{K_D}{bm \cdot A} \quad (1.8)$$

To continue with the example of the nanowire and the microsensor with a K_D of 1 nM, a c^* of 10^{-3} M is found for the nanowire whereas c^* reaches ca. 20 aM for a microsensor with an equilibrium time in the order of magnitude of inverse of the off rate k_{off}^{-1} .

Unraveling the mass-transport regime

To put in a nutshell, two regimes can be distinguish:

- If convection and diffusion deliver targets so slowly that reaction time is negligible, the regime is mass-transport limited and J_D is given by Equation 1.9.

$$J_D \approx D \cdot c_0 \cdot W_S \cdot F, F = 0.81 \cdot Pe_S^{1/3} \quad (1.9)$$

- If reaction time can't be neglected, it's the reaction limited regime and J_R is written as stated by Equation 1.10.

$$J_R \approx k_{on} \cdot bm \cdot c_0 \cdot L \cdot W_S \quad (1.10)$$

For efficient collection, diffusion must balance reaction flux. $J_R = J_D$ gives Equation 1.11.

$$c_s \approx \frac{c_0}{1 + k_{on} \cdot bm \cdot \frac{\delta}{D}} \quad (1.11)$$

Defining a third number, the Damkohler number Da:

$$Da = k_{on} \cdot bm \cdot \frac{\delta}{D} \quad (1.12)$$

If $Da \ll 1$, the system is reaction limited (nanowire), and if $Da \gg 1$, it is mass-transport limited. Sensor's saturation time is given by Equation 1.13.

$$\tau = Da \cdot \tau_R, \tau_R = \frac{1}{k_{off} + k_{on} \cdot c_0} \quad (1.13)$$

An extensive number of chemical and physical parameters can be modified in order to influence the mass transport regime. Electrostatic interactions between charges molecules can increase binding through pH or salt concentration [101, 102]

and thus reduce c^* . Mass transport increase by decreasing the depletion zone thickness. Mechanical/electrical/magnetic actions (stirring, mixing [103], waste channels, pumping [104], electroosmosis, Lab On CD where flow control is induced by rotation [105]) can also actively act in this direction, hence an advantage of using a microfluidic setup.

1.3.2 Insight into microfluidics, toward the ideal LOC

The advances in microfluidic technology are leading to more accurate and reliable immunoassays through four keys points:

- a higher degree of control of the flow of liquids and thus interfaces
- the possibility of miniaturization and automation
- improvements of assay conditions (mixers, less contamination)
- a flexibility needed for point of care diagnostics (often change of analytes, reagents and multiple operations with one sample).

From the willingness to detect in small volumes with high precision (gas/liquids chromatography [106], electrophoresis [107, 108]) to precisely controlling fluids (printing [109], micropumps, valves [110]) microfluidics emerged as an obvious and invaluable tool for analytical chemistry analysis. The panel of success is broad (Biosite Tirage System for pregnancy tests [111], CaliperTM (AgilentTM) with the commercialized Bioanalyser 2100^R for multiple analysis (electrophoresis, cell sorting, RNA, DNA, proteins separation and size detection)) and the methods are multiple. For a complete review the reader can refer to the work of Gervais *et al.* [112].

A Lab On Chip as its name suggests seeks to become a fully integrated platform on which all experiments needed in molecular biology could be performed starting by the direct injection of blood on the chip and not only pre-purified DNA. Gervais *et al.* provides a glimpse into the future of what should look like the ideal Lab On Chip, Figure 1.12. Presented as a coupling between multiple modules (sample preparation, concentration, detection) that uses a small volume of unprocessed sample taken directly from the patient (volume as low as 1 μL , lower than the 25 μL drop from finger prick). It should be a multiplex analysis of up to hundreds of analytes of a variety of proteins and nucleic acids and negative controls for a detection in the minute. The limit of detection (LOD) should be below the femtomolar with a large dynamic range with a great selectivity to avoid false positives. A large dynamic range is crucial for many detection scheme notably for miRNAs where a disease/injury is detected by the relative changes in concentration of multiple miRNAs with a dynamic range of 10^3 order of magnitude between the healthy and the diseased state [27, 28]. Parameters such as long shelf life, transparency of the sealing material, not temperature sensitive and easy to use by non-technical experts should also be kept in mind.

Finally the ideal LOC should be able to analyze, detect, calibrate, record and transmit wireless data for a one \$ test in order to be used as a routine test.

Among other parameters, we will take a moment to consider the materials used, crucial to participate to the efficiency of the test whether for flow control, sensitivity or adhesion of biomolecules.

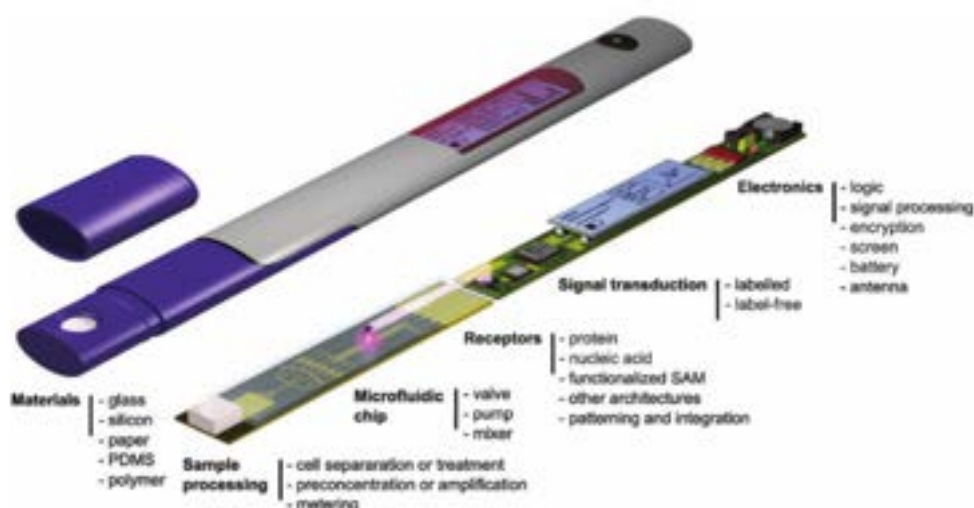


Figure 1.12: Futurist scheme of a lab on chip imagined by Gervais *et al.* [112].

Materials

Originally in silicon and glass [113], the latter was rapidly preferred to the first one for costs and transparency reason. Poly(dimethylsiloxane) PDMS makes currently the majority [114] due to its transparency, porous character and easiness to manufacture with its other counterpart PMMA (poly(methylmethacrylate)), PET (Polyethylene Terephthalate) [115, 116], COC (cyclic olefin copolymer), or teflon [117], paraffin [118], paper [119] patterned by photolithography and treated [120] to repel biomolecules, increase sealing properties (plasma, chemical vapor adhesion) or build self-assembled monolayers.

A one test chip ?

Most of the time, thermal or chemical try of regeneration results in desorption or severe decrease in hybridization efficiency [121]. That is why disposable strips that obviate the need for a regeneration step have currently the preference. Printed [122] or photolithographed [123, 124] electrodes allowing the parallel fabrication of multiple electrodes facilitate biosensing protocols as lots of electrodes are required for practical evaluation of real samples.

Pre-concentration of analytes

Detection biomarkers with extremely low abundance in pico-, femto- even attomolar levels can be challenging for biosensors. In order to increase sensitivity, biomolecules can be pre-concentrated prior to detection. Accumulation using electrokinetic trapping [125], filtration with porous silica membrane [126] or trapping at the intersection of perpendicular channels [127] can lead to 10^6 accumulation factors. As previously mentioned PCR and other on chip amplification systems (LAMP, loop mediated isothermal amplification or NASBA) also increase amount of targets prior detection.

Sample processing

Extraction [128], isolation, purification and biomolecules manipulation are key parameters in every biochemical analysis. Classical protocols include electrophoresis, ultrafiltration, precipitation and chromatography. Among available methods affinity chromatography is often preferred for its efficiency and selectivity. Nevertheless the use of a liquid chromatography is limited to pre-treated samples. Non-homogeneous solutions like protein mixtures are incompatible with experimental conditions of commercial columns that ask for medium without particles.

Magnetic separation based on MNP represents an attractive alternative for selective capture of specific proteins or DNA while using cheap materials and rapid and easy process. The small sizes of NPs make them attractive matrix as diffusion is reduced between reagents. It generates shorter responses, a wider linear response range and the possibility to reach biological detection limits. The principle of magnetic separation is the following: tagged MNP with a biological probe are mixed with serum (cells, blood, plasma). After a necessary time of incubation target species binds with a preferably strong link to probe molecules attached to MNP, the complex are isolated with various magnetic devices (decantation, magnetic pillars, electro-magnets...). Volumes are low thanks to a high surface to volume ratio, specialized equipments such as spinner of chromatography are avoided. Automated systems for nucleic acids separation are already available for nanoliter samples [129].

However due to their small magnetic moment, the magnetic gradient of a single permanent or electro-magnet is rarely enough to trap MNPs. Various strategies have been proposed in literature to overcome this drawback. In the following section the manipulation of SPM particles and their use as separating agents will be discussed. As a start a reminder of the magnetic properties of magnetic particles will be given as well as a large overview of MNP capabilities in biomedicine.

1.4 Magnetic manipulation of superparamagnetic nanoparticles

Precise control of synthesis and functionalization pathways is crucial as size and shape of NPs are key parameters for stability and biological purpose. Size plays a crucial role in magnetic moment and on the response to an applied magnetic field. Magnetization is directly proportional, in a first approximation, to the volume. For an easy manipulation with an external field total magnetization of the material should be maximum. Ferromagnetic materials are thus favored as iron, nickel or cobalt especially iron oxides under its magnetite Fe_3O_4 or maghemite $\gamma\text{-Fe}_2\text{O}_3$ form that can be easily synthesized with a better chemical stability against oxidation and posses interesting electro-magnetic properties. MNP with corresponding properties have been used for a wide range of applications such as drug delivery, hyperthermia, magnetic resonance imaging (MRI), tissue engineering and repair, biosensing and biochemical separation.

In this section structural data for maghemite will be given as well as magnetic properties. Finally the modifications generated from the dimensions changes to the nanoscale will be discussed. We won't describe here the various existing synthesis pathways of MNP as it will be discussed in Chapter 3.

1.4.1 Description and magnetic properties. Applications of magnetic nanoparticles in biomedicine.

Ferrites are characterized by a spinel crystalline structure. Oxygen ions are defining a cubic network where Fe^{2+} cations are located at the interstices. Fe_3O_4 magnetization comes from its antiferromagnetic coupling (superexchange through oxygen) between Fe^{3+} cations in octahedral and tetrahedral sites leaving the magnetic moment of Fe^{2+} cations (in octahedral sites) responsible for magnetization.

Magnetic properties of the iron oxide are defined by their purity and crystallinity characterized by XRD (X-Ray Diffraction), AT, Mössbauer and Infrared spectroscopy in solid phase or SAXS, SANS, EDX in liquid phase.

Magnetic materials with a permanent magnetic moment

The magnetic properties of a material are the result of local arrangements of magnetic moments. These local magnetic moments are commonly called spin and can be viewed as little magnets. The interactions between atomic magnetic moments of a same material generate a possible magnetic order below a certain critical temperature.

All materials are magnetic to some extent depending on their atomic structure and temperature. A magnetic material placed in a magnetic field of strength \mathbf{H} sees its individual atomic moments contribute to the overall response, they are modifying their orientation to be along the field and the material is acquiring a magnetization \mathbf{M} in $\text{m}^2 \text{A kg}^{-1}$ or emu g^{-1} if normalized by magnetic mass in Equation 1.14:

$$M = \chi \cdot H \quad (1.14)$$

with the volumetric magnetic susceptibility χ [130] (for homogeneous and linear materials).

For quasi non existing interactions between atoms and crystalline network the arrangement is not ordered, spontaneous macroscopic magnetization is zero, as for:

- Diamagnetism (intrinsic property of matter): Electrons are paired, there is no permanent magnetic moment, a small moment is induced by the field ($\chi = -10^{-6}$ - 10^{-1}).
- Paramagnetism: electrons are not paired, there is a resulting permanent magnetic moment and magnetic moments perfectly align in the direction of an applied field for a positive magnetization ($\chi = 10^{-6}$ - 10^{-3}).

For a spontaneous magnetic order, with no applied field, due to exchange electrostatic interactions leading to a 10^4 times larger M , three behavior can be distinguished [131]:

- Ferromagnetism: exchange interactions are favoring parallel alignment of magnetic moments. Under a T_c temperature (Curie temperature), interactions are higher than thermal motion and a spontaneous magnetization is present without an applied field.
- Antiferromagnetism: below a Neel temperature (T_N), magnetic moments align with spins pointing in opposed and equal way resulting in a zero total magnetization. Above T_N , the antiferromagnetic behavior become similar to paramagnetism due to thermal motion.

- Ferrimagnetism: antiparallel spins with different force vector resulting in a spontaneous magnetization below T_c (typically the case of a solid with a crystalline order characterized with multiple sub-networks).

Nanomagnetism

The transition to nanoscale modifies various properties. Contrary to bulk materials where magnetic order is confined in multiple magnetic domains (Bloch walls), under a critical size D_c , the creation of walls become adverse. Bloch walls vanish to minimize magnetostatic energy and particles tend to be composed of a single domain [132]. The critical diameter is ca. 10-100 nm for maghemite [133, 134].

The permanent magnetic moment of monodomain particles is the sum of all atomic magnetic moments constituting the particle.

Surface effects are also affected by size reduction. The reduction of the number of atoms results in an increased contribution of surface atoms that do not have the same environment than in volume generating surface spins with supplementary interactions. The maximum magnetization for nanoparticles that can be reached under field e.g. saturation magnetization M_{sat} is lower than bulk values due to these increased surface effects [135]. 60 emu g^{-1} is the agreed value for nanometric maghemite, 74 emu g^{-1} for bulk maghemite.

Magnetism of nanoparticles under an applied magnetic field \mathbf{H} is governed by the competition between two energies: anisotropy energy [136] and Zeeman energy as written in Equation 1.15.

$$E = K.V.\sin^2\theta - \vec{\mu}.\vec{H} \quad (1.15)$$

The first term refers to magnetocrystalline anisotropy energy which tends to attract the magnetic moment μ ($\mu = \mu_0.M_s$) along the easy magnetization axis. For monodomain nanoparticles, anisotropy energy is generally uniaxial. K is the uniaxial anisotropic constant, V the volume of the particle and θ the angle between magnetization and the easy magnetization axis as pictured in Figure 1.13. The anisotropy energy possesses two minimum ($\theta=0$ and π) split with a $K.V$ energy barrier.

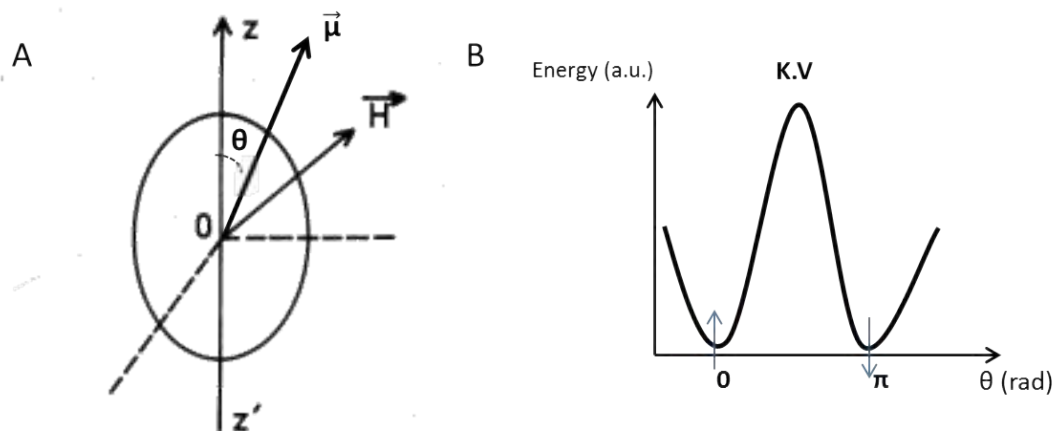


Figure 1.13: A. Uniaxial particle ; the easy axis of magnetization is $z'Oz$. B. Representation of the barrier energy to be crossed to go from a spin up to a spin down state.

Anisotropy energy is in competition with Zeeman energy (second term of Equation 1.15) which tends to align the magnetic moment along the field \mathbf{H} . To go from one direction of easy magnetization to another, the barrier energy $K.V$ has to be given to the system. In view of the small size of the particles, the barrier energy is small and can be of the same order of magnitude of thermal motion, $k_B.T$ [137].

Quasi-static magnetic properties

The alignment type of magnetic moments with applied field depend on anisotropy energy and temperature.

- For $k_B T \gg K.V$ (high temperature behavior), particles are called superparamagnetic. Thermal fluctuations are too high to maintain a stable magnetic order. Superparamagnetic particles follow the Langevin model. The particle does not possess a magnetic moment in the absence of an external field. However under an applied field and for monodispersed particles, the magnetization curve $M-H$ can be described by Langevin function:

$$M = M_s \cdot M(x) = M_s \left[\coth(x) - \frac{1}{x} \right] \text{ with } x = \frac{\mu_0 \cdot \mu \cdot H}{k_B \cdot T} \quad (1.16)$$

μ is the magnetic momentum of the single domain particle, μ_0 free space permeability ($\mu_0=4\pi \cdot 10^{-7}$), M_s saturation magnetization, k_B the Boltzmann constant and T the temperature. x is the ratio between magnetic energy, $\mu_0 \cdot \mu \cdot H$, and thermal motion energy, $k_B \cdot T$.

Figure 1.14 displays the increase in magnetization with the applied field until saturation magnetization M_s . This magnetic study does not show any memory or magnetic remanence, characteristic of superparamagnetic objects.

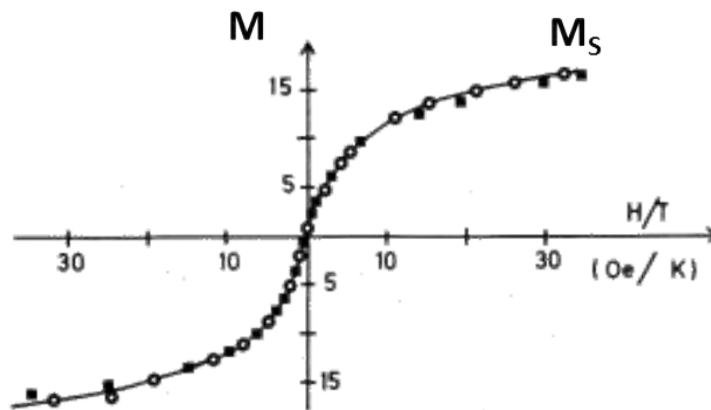


Figure 1.14: Magnetization curves of 45 Å diameter iron particles in mercury [136].

Various information can be extracted from the magnetization curve. From the low and high field approximation of the Langevin model, the magnetic diameter can be assessed. Ferrofluid samples e.g. a colloidal suspension of magnetic monodomain particles of typical size 10 nm [138] are never completely monodisperse and a log-normal distribution P is usually assumed [139]. For the diameter, d , of

spherical magnetic particles, a median diameter, d_0 , and a polydispersity index, σ , the log-normal distribution is written according to Equation 1.17.

$$P(d) = \frac{1}{\sqrt{2\pi}\sigma d} \cdot e^{-\frac{\ln(d/d_0)^2}{2\sigma^2}} \quad (1.17)$$

The maximum of $P(d)$ corresponds to a diameter d_{TEM} :

$$d_{TEM} = d_0 \cdot e^{-\sigma^2} \quad (1.18)$$

- For $k_B \cdot T \ll K \cdot V$, particles are in a blocked state, thermal motion is not sufficient to overcome $K \cdot V$. Particles follow the Stoner-Wolffarth model.

Magnetization depend on the history of the material. The magnetic response to an applied external magnetic field is characterized with an hysteresis loop as displayed on Figure 1.15.

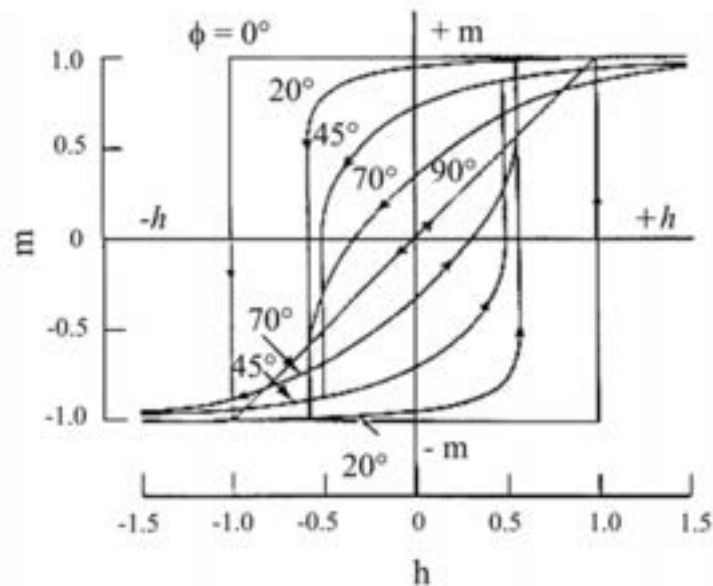


Figure 1.15: Theoretical hysteresis loops of a single domain particle for various ϕ angle between the easy magnetization axis and the applied field ($m = M/M_s$, $h = H/H_c$) [136].

At the application of an external field, H , the magnetic flux density increases until a saturation value, B_{sat} . When H decreases the material keeps a remanent flux B_r at $H=0$ and a coercive field H_c at $B=0$. It is the needed field to apply in order to demagnetize the material. The competition between anisotropic energy and Zeeman energy gives rise to the hysteresis loop. The opening of the loop is function of the angle between the easy magnetization axis and the applied field. For parallel (zero angle) and antiparallel (π angle) situations, the hysteresis cycle has a rectangular shape.

Dynamic magnetic properties

For $T=300$ K, the probability of commutation of magnetic moments from one direction of easy magnetization to another is not zero, the system will relax with a certain period τ . The consequence on magnetic measurements done in a time

varying field will depend on the time of measurements $1/f$. Thus, due to thermal motion of the particle magnetic moment, the magnetization is not in phase with the time varying magnetic field \mathbf{H} [140].

- For $f \ll 1/\tau$, the thermal equilibrium may be achieved and the sample exhibits an intrinsic superparamagnetic behaviour. The magnetization curve may be described by a Langevin formalism.
- For $f \leq 1/\tau$, the moment is locked to the particle and aligns along \mathbf{H} in very high fields. As the field is decreased, a remanent magnetization subsists and the magnetization curve exhibits hysteresis (i.e. dissipation) [138].

Ferromagnets exhibit magnetic resonance at frequencies around 10^9 Hz [140], thus a GHz-frequency should constitute a theoretical optimum, the kHz-frequency fields (100 kHz) is a technological optimum. The calculation of magnetization relaxation time depends on the way the particle are rotating in the solvent of dispersion, either external (Brown relaxation) or internal (Néel relaxation).

Brown relaxation comes from the physical rotation of nanoparticles in the carrier fluid, the magnetic moment being locked onto the crystal anisotropy axis with a characteristic time, τ_B , given by [141]:

$$\tau_B = \frac{3 \cdot \eta \cdot V_{hydro}}{k \cdot T} \quad (1.19)$$

where η is the viscosity of the carrier fluid, k the Boltzmann constant, T the temperature, and V_{hydro} the hydrodynamic volume of the particle.

Néel relaxation is induced by the rotation of the magnetic moment of NP within the crystalline network which occurs when the anisotropy energy barrier $K \cdot V$ (for an uniaxial crystal) is overcome. The released energy by the spin relaxation is dependent on the anisotropy energy of the NP *i.e.* the energy that imposes the direction of the magnetic moment within the crystalline network. The characteristic time, τ_N , for Néel relaxation is written as:

$$\tau_N = \tau_0 \cdot e^{Ea/kT} \quad (1.20)$$

where τ_0 is of the order of 10^{-9} s and $Ea = k_B T$, the thermal energy.

As the two relaxation mechanisms take place in parallel, the effective relaxation time τ is given by the relationship: $1/\tau = 1/\tau_N + 1/\tau_B$. The shorter time determines the dominant mechanism of relaxation. Fortin *et al.* determined by using different solvent viscosities (restriction of the particle orientation) that the loss process for maghemite particles with diameters below 16 nm in water was governed by Néel relaxation [142].

1.4.2 Magnetic manipulation

A magnetic field gradient is required to exert a force at distance on a magnetic moment. A uniform field only generate a torque. Magnetic force acting on a point-like magnetic dipole, m , is given by:

$$F_m = (m \cdot \nabla) B \quad (1.21)$$

For a weakly diamagnetic medium as water, $m=V.M$ with, m , the total moment of the particle. The volumetric magnetization is:

$$M = \Delta\chi H \quad (1.22)$$

with $\Delta\chi=\chi_m-\chi_w$, the effective susceptibility relative to water. It should be kept in mind that, for nanoparticles, $\chi=\chi(H)$. For dilute suspensions of nanoparticles in pure water. The system NPs+water can be approximate by

$$B = \mu_0 \cdot H \quad (1.23)$$

So

$$F_m = \frac{V_m \cdot \Delta\chi}{\mu_0} \cdot (B \cdot \nabla) \cdot B \quad (1.24)$$

With $\nabla \times B=0$, Maxwell equation without time varying electric fields or currents

$$\nabla(B \cdot B) = 2Bx(\nabla x B) + 2(B \cdot \nabla)B = 2(B \cdot \nabla)B \quad (1.25)$$

$$F_m = V_m \Delta\chi \nabla \left(\frac{1}{2} B \cdot H \right) = V_m \Delta\chi \nabla \frac{B^2}{2\mu_0} \quad (1.26)$$

With B^2/μ_0 , the differential of the magnetostatic field energy density. For $\Delta\chi > 0$, the magnetic force acts in the direction of steepest ascent of energy density scalar field. This is the basis toward magnetic separation and drug delivery.

Examples of magnetic manipulation will be given in section 1.4.6.

1.4.3 Core-shells particles

When a core-shell particle is composed of several magnetic cores the particle has also a superparamagnetic behavior. If interaction between magnetic cores are negligible, magnetic moment of the particle is in first approximation the sum of each core's magnetic momentum divided by the volume of the core-shell. A large susceptibility could be expected when a core-shell is saturated with many cores. Currently the trend is ca. 70% of filling for maghemite without losing its superparamagnetic properties. An example of micrometer core-shells is given on Figure 1.24.

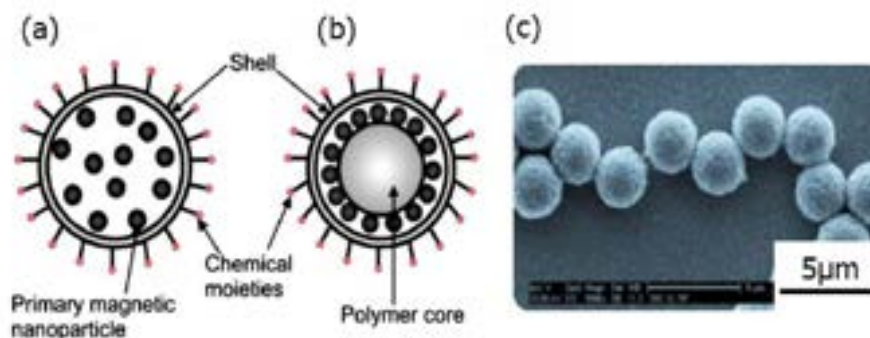


Figure 1.16: Dynabeads core-shells: (a) and (b) their structure, (c) SEM picture, physical diameter: 2.8 μm

If all magnetic particles have reached their saturating magnetization the magnetic moment of the core-shell is given by:

$$m = M_{sat} \cdot \frac{4}{3} \cdot \pi \cdot d \cdot R^3 \quad [A \ m^{-2}] \quad (1.27)$$

with M_{sat} saturation magnetization (when every spin vector of each domain are colinear), R is the core-shell radius, d represents the volumic fraction of iron oxide. Under an applied magnetic field moments align as for paramagnetic materials but with a 10^4 times higher magnetization as each moment of each NP is aligning. This property and the absence of remanent magnetization after the application of an external field allow MNPs to keep their colloidal stability and avoid aggregation. Well-dispersed particles are crucial for biomedical applications. On the shell of MNP relies particle stability. The latter is possible if electrostatic repulsion, hydrophilic particle-particle interactions and steric repulsion compensate [143].

1.4.4 Magnetic resonance imaging (MRI) contrast enhancement

MRI is a non invasive imaging technique providing high-resolution anatomical images. It can provide the diagnosis of soft tissues cartilage allowing the differentiation between malignant and healthy cells.

Iron oxide NPs are the most commonly used SPM contrast agents because of their enhanced proton magnetization relaxation at their sites of accumulation providing better contrast [143]. They are also in most cases taken up by the reticuloendothelial system (RES). MRI contrast relies on the differential permeation and uptake kinetics of healthy and tumorous tissue. [144] The delineation of a tumor by particles relies on the fact that a malignant tumor does not show any uptake of iron oxides because a malignant tumor does not have an intact RES. RES uptake depends on the size and surface charge of the particles. On the basis of these studies, specific magnetic iron oxide particles have been designed that can escape uptake by the RES of liver and spleen, and thus have a longer blood half-life. SPM particles have been used to visualize the vascular system [145], the nervous system [146], lymph nodes [147] liver tumors [148], brain tumors [149] as relaxation times of tumor cells are not altered by contrast agents. Iron oxide NPs lend themselves to encapsulation into target specific agents such as liposome to localize bone marrow [150].

1.4.5 Drug delivery

MNP use in drug delivery decreases side effects in non-specific therapies (chemotherapies) by targeting specific sites (cancer related) [151] generating a reduced amount of drugs used and a reduced dosage. Drugs can be attached to a biocompatible magnetic carrier usually a ferrofluids (NPs' small sizes allow to cross physiological barriers) injected into the patient blood. External high gradient magnetic fields concentrate the complex at a specific site. Drug is released via either enzymatic activity, pH, osmolality or temperature changes [152] to be taken up by tumor cells. Efficiency depends on field strength, size and concentrations of particles, blood flow rate, circulation time and distance from the magnetic source [153]. Larger particles around $1 \mu\text{m}$ as agglomeration of SPM particles are more effective with higher magnetization.

The optimization of drug carriers go through coatings. Magnetic component usually magnetite, maghemite or more exotic iron, cobalt, nickel, yttrium aluminum

iron garnet [154] are coated with a biocompatible polymer (PVA, dextran) or inorganic silica. Coatings are a shield from surroundings environment and a matrix for functionalization (carboxyl groups, biotin, avidin, carbodiimide... [155]) and further linking with drugs or biomolecules. Or either way a drug carrier can also be a porous polymer with magnetic NP inside the pores [156]. Metallic coatings has also been considered notably for immunosensing platform, SERS, as contrast agent for imaging and photothermal ablation [157, 158].

Not only drugs can be linked to magnetic NPs but also radionucleide that remain permanently attached to the particle avoiding the several limitations in terms of accumulation in cells. Radionucleide doesn't need to penetrate the cell to act effectively [159].

Great promise in the domain of gene therapy should also be cited. Holding a viral vector carrying the therapeutic gene thanks to its magnetic carrier near a tissue increases the efficiency of gene transfection and expression [160, 143].

1.4.6 Magnetic separation

Magnetic separation is a two step process. Firstly, the desired biomolecules have to be labeled with magnetic material. Secondly, the labeled biomolecules have to be carried away thanks to fluid based techniques. Labeling requires a chemical modification of the NP surface usually a coating with biocompatible molecules [161, 162, 163] with two advantages. The link between particles and target site and an increase in colloidal stability.

The separation itself consists in the immobilization of labeled material by a field gradient with the force $F_m^{\vec{}}$ that needs to overcome hydrodynamical drag force acting on NP in flow [164].

$$F_d = 6.\pi.\eta.R_m.\Delta v \quad (1.28)$$

With η the viscosity (water), R_m the radius of the NP, and $\Delta v = v_m - v_w$ the difference in velocity of NP and water [165]. From Equation 1.26,

$$V_m = \frac{4}{3}.\pi.R_m^3 \quad (1.29)$$

The velocity of the NP relative to the carrier fluid is:

$$\Delta v = \frac{R_m^2.\Delta\chi}{9.\mu_0.\eta}.\nabla(B^2) = \frac{\xi}{\mu_0}.\Delta(B^2) \quad (1.30)$$

With ξ the magnetophoretic mobility the measure of how manipulable a magnetic particle is. Obviously a bigger NP has a higher ξ than a smaller one.

Now, talking about the separator itself. The application of a permanent magnet on the side of an eppendorf and the removal of the supernatant is a basic separator. But efficiency will be increased by the use of high field gradients to capture magnetic NP as they flow. The general scheme of magnetic separation is the following. The magnetically tagged entities are flowing through a column where magnetic wires/beads are packed and magnetized with an external magnetic field. The tagged entities are trapped, the untagged matrix flow through. The labeled material can be

recovered by retrieving the applied field. Optimizations focus on avoiding adsorption of tagged material on the magnetic matrix.

Alternatives can be found by the manufacture of specific design field gradients systems like quadrupolar arrangement [166], fluid flow fraction with a spatially varying magnitude field gradient [167], or by playing on magnetophoretic mobilities with an applied magnetic field with a static flow and a permanent magnet [168].

Seeking to reach the maximum sampling capabilities literature report the use of combined magnetic materials. Magnetic separation is generally only the first step before a subsequent detection.

In this optic, as previously mentioned Teste *et al.* [169] trapped 35 nm in diameter MNPs with an enhanced field gradient. Micrometric iron ferromagnetic NPs concentrate magnetic field lines from a permanent magnetic immobilized on top of their setup, Figure 1.17. Magnetic force to capture and manipulate the MNPs to the wanted location is made easier. A 1 ng mL^{-1} limit of detection for immunoglobulin E was reached only consuming $5 \mu\text{L}$ of reagents in 20 minutes on a fully integrated chip.

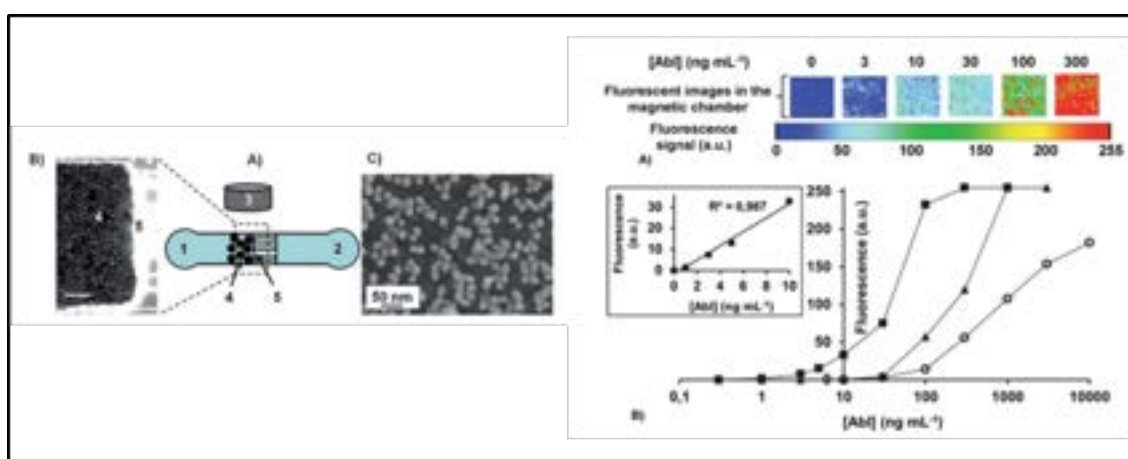


Figure 1.17: Teste *et al.* on chip immunoassays with 35 nm MNP [169].

Choi *et al.* used a planar electromagnet with a serpentine coil and a semi encapsulated Ni/Fe permalloy to immobilize superparamagnetic micrometer beads in a dynamic flow, Figure 1.18. The uniform field generates a 71 pN magnetic force allowing the enhanced capability of capture and separation to perform a double antibody/antigene recognition [170].

Rida *et al.* locally manipulated micron size ferromagnetic particles with an oscillating magnetic field transverse to the microfluidic channel and generated by soft magnetic iron tips, Figure 1.19. This magnetic coupling build up open column structures that allows strong interactions with the fluid flow [171]. Similarly Lacharme *et al.* achieved a complete on-chip immunoassay by using trapped self-assembled magnetic NP chains (Figure 1.20) and reached a 1 ng mL^{-1} LOD for murine monoclonal antibodies [172].

Smistrup *et al.* preferred to use a passive separation with array of soft magnets to create several capture points for fluorescent magnetic beads, Figure 1.21. The use of passive structures magnetized by an external magnetic field provides larger fields and generate gradients inside the channel allowing to overcome a 5 mm s^{-1} flow

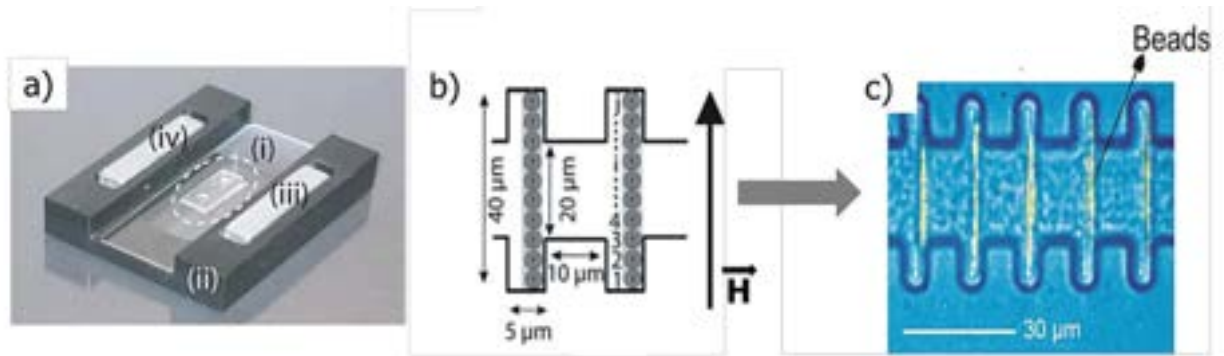


Figure 1.20: Lacharme lab-on-chip's device. (a) Schematic view of magnetic elements. Geometrically trapping of beads, schematic view (b) and fluorescent view (c) [172].

with a 50 mT field. An advantage of their setup is that beads can be further released and are not stuck [173].

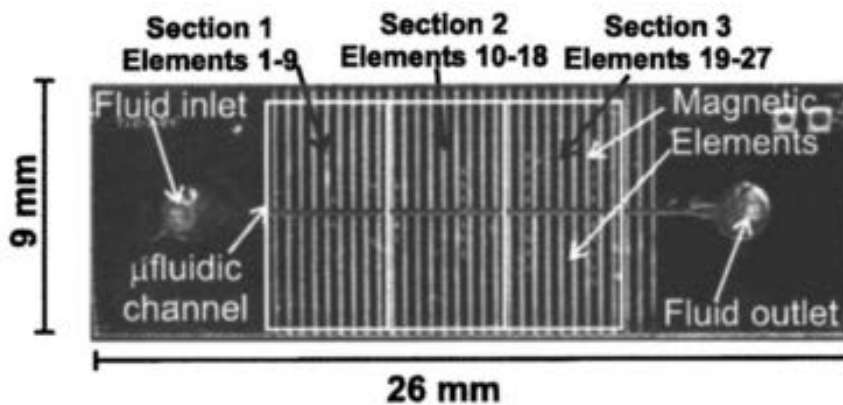


Figure 1.21: Smistrup's magnetic separation chip showing the position of the microfluidic channel and the passive soft magnetic elements. The external homogenous magnetic field is applied vertically in the plane of the paper [173].

Ramadan *et al.* showed, with a computation and then confirmed it with experiments, that the optimized geometry for planar electromagnets (better than magnetic fields generated by a coil as limited by Joule heating) is a spiral design. Spiral designs generate up to five times stronger fields even if they are complicated to realize (need an insulating layer and two layers of metal) [174].

With their dense dynamical fluidized bed, Tabnaoui *et al.* reached a 1 pM LOD with two magnets in a 30° orientation on each side of a microfluidic channel [175]. Kim *et al.* performed a dual analytes detection on chip immunoassay with fluorescent beads conjugates with superparamagnetic NPs. They detected simultaneously IgG of rabbit and mouse over different range of detection (from pg mL^{-1} to ng mL^{-1}) by playing on beads concentration [176].

As the objective of a Lab-On-Chip is to perform a complete sampling of a biologic

sample, synthesis of the magnetic NP can also be incorporated on chip as did Cabrera *et al.*. On a three layers natural rubber based microfluidic device the decoration of magnetite with a gold coating in aqueous media is done as well as magnetic separation with an incorporated permanent magnet [158]. On a similar note Digigow *et al.* designed a microreactor to functionalize SPION (superparamagnetic iron oxide nanoparticles) with PEG and amine groups. Their microreactor is composed of a permanent magnet and a mesh to immobilize and separate SPION from the unbound molecules [177].

For instance, separation of specific biomolecules from their native environment has been used for selection of tumor cells from blood leading to enhanced detection of malarial parasites [178] or for cell counting [179]. Usually magnetic separation is the first step in a more complex chain of detection that needs sample preparation. We can cite pre-processing technology for PCR [180], localization of labeled material for further detection [181] or the combination with sensing techniques (optical [182], electrochemical (See Section 1.5.2)). Indeed the mobility of magnetic NPs allows a shorter reaction time and a greater volume of reagent to be processed compared to standard immunoassays.

1.4.7 Magnetic hyperthermia

Inducing malignant cell death by heating while keeping healthy tissues at biological temperatures has led to new possibilities in cancerous treatments [183]. The procedure involves the application of an AC magnetic field of sufficient strength and frequency to cause the heat of dispersed particles in target tissue. For clinical purpose the challenge is to chose adequately the right amount of nanoparticles to heat. Not to many otherwise the legal toxic levels are reached, not to few as efficiency will be lost. The first papers on magnetic NP as hyperthermia mediator were published as soon as 1957 by Gilchrist [184] and shortly after followed their effect on biological systems especially to induce necrosis in cancer cells by increasing their temperature [185, 186, 187]. Clinical trials of this method are underway in Germany in patients with brain and prostate cancers [188].

Heating locally is not only a way to kill cancerous cells but can also be used for a wide range of applications like triggering molecular or cellular process [189].

Therefore underlying physical mechanisms for heat generation by small NP under alternative magnetic fields have to be understood. Not only the heat dissipation rate in surrounding media (blood, tissues) has to be taken into account [190] but also the intrinsic contributions of particle properties to heat induced mechanism has to be discussed.

Under a radiofrequency alternative magnetic field (AMF) magnetic moment of iron oxide nano-crystals oscillate and produce a local heating of the medium [191] e.g magnetic friction. The AMF induces a dephasing between the applied field and the magnetic momentum of the nanoparticle's domain yielding dynamic hysteresis. The excited magnetic spins release energy in the form of heat while relaxing. The heating effects are due to several types of loss processes (hysteresis losses, Néel

and Brown relaxation), the relative contributions of which depend strongly on particle size. Nanoparticles with a core diameter less than 30 nm are supposed single-domain particles. Their magnetization is thus governed by the combined effects of the rotational external (Brownian) and internal (Néel) diffusion of the particle magnetic moment [192].

Ferrofluids are good candidate for hyperthermia. Indeed, from the first law of thermodynamics applied to ferrofluids, the magnetic work is converted into internal energy U when magnetization lags the field H according to the following integral, expressed per unit of volume, [140]:

$$\Delta U = -\mu_0 \cdot \int M \cdot dH \quad (1.31)$$

with M the magnetization and μ_0 , the permeability of free space. Following this, the volumetric power dissipation P , is proportional to :

$$P \propto \chi'' \cdot H^2 \cdot f \quad (1.32)$$

with χ'' the out-of-phase component of the complex ferrofluid susceptibility χ . The highest heating rates are found for magnetite and maghemite, as shown on Figure 1.22.

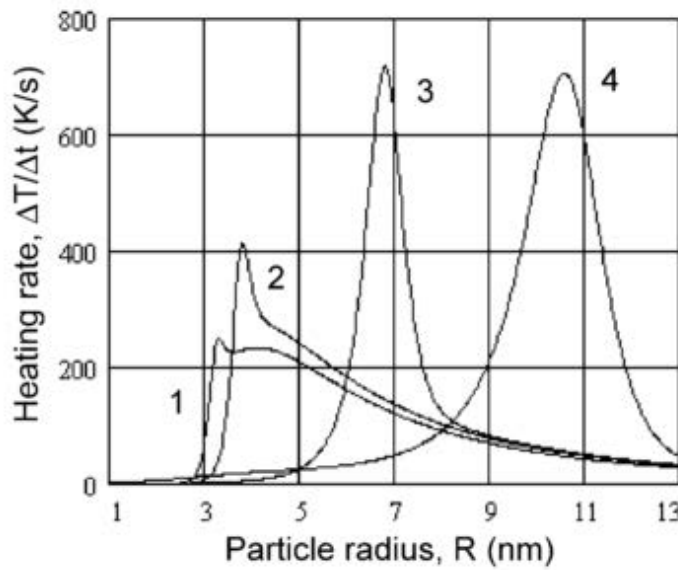


Figure 1.22: Comparative heating rate for various ferrite: **1.** Barium ferrite, **2.** Cobalt ferrite, **3.** Magnetite, **4.** Maghemite. $F=300$ kHz, $B=0.09$ T, $\phi=0.07$, $\tau_0=10^{-9}$ s in tetradecane [140].

As showed by Equation 1.31 the maximum reachable heating phenomenon should involve a rectangular hysteresis loop. This could only be achieved with an ensemble of uniaxial particles perfectly aligned with H , a difficult configuration to achieve as such, experimentally. With the advent of ferrofluids e.g. SPM NPs suspended in water [193, 194] new roads for increased hyperthermia are open.

The heating capacity of NP is described thanks to the specific loss power SLP (also called specific adsorption rate SAR) in $W g^{-1}$ according to the following equation

$$SLP = \frac{\text{Dissipated power}}{\text{Magnetic mass}} = \frac{c_p \cdot m_{tot}}{m_{mag}} \cdot \frac{dT}{dt} \quad (1.33)$$

where c_p is the specific heat capacity of the sample, m_{tot} the sample's mass, and $m_{mag} = \Phi \cdot \rho_{mag} \cdot V$ is the mass of magnetic material in the sample (Φ , the fraction of magnetic material and $\rho_{mag} = 5.07 \text{ g cm}^{-3}$, the volumic mass of iron oxide).

Multiplying SLP by the density of the particle yield P, the volumetric power dissipation, for comparison with magnetic particles covering all size ranges [195, 194, 196]. Most real ferromagnetic particles require high applied fields (ca 100 kA m^{-1}) to generate saturated loops. In contrast, superparamagnetism in ferrofluids were reported to give rise to more efficient heating properties. Hergt *et al.* reported a 200 W g^{-1} SLP at 14 kA m^{-1} [197].

It has been shown that SLP for monodispersed particles of maghemite increases with frequency (see Figure 1.23).

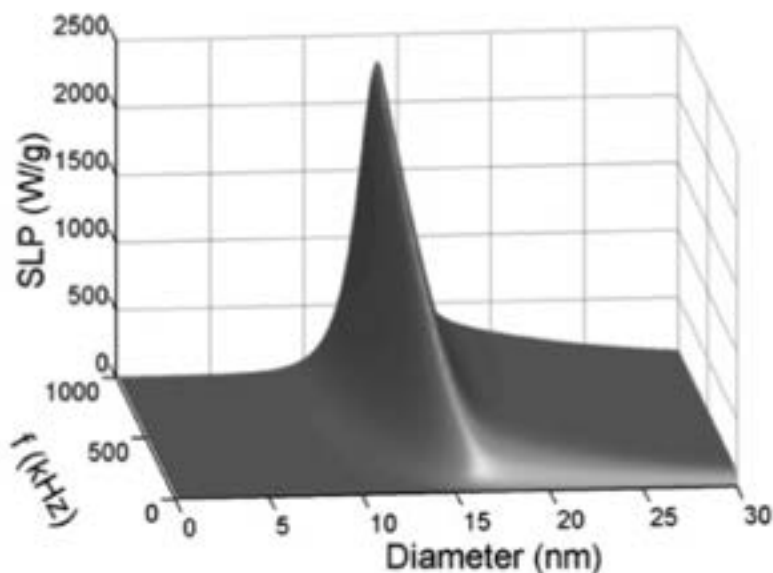


Figure 1.23: SLP of monodispersed particles of maghemite as a function of particle diameter and magnetic field frequency [142].

Arising from the interaction between magnetic NPs and a static or time varying external magnetic field a lot of others applications are reported. To cite a few: magnetic twisting cytometry to relate to mechanical properties of cell membranes [198], tissue engineering for mechanical growth of cells [199] or magnetic biosensing where a NP is coupled to analyte specific molecules to detect target molecules which will be discussed in the following section.

1.4.8 Biomedical sensors based on magnetic NP

Ideal iron oxide MNP diameter for biomedical applications lies between the superparamagnetic threshold at room temperature e.g. 10 nm and the size of a magnetic domain ca. 70 nm. MNP coating is a key element for specific binding of biomolecules

or to avoid agglomeration but magnetic properties may or may not be affected depending on the type of coating. Biological molecules exploit highly specific interactions between molecular pairs for a mutual recognition and the trigger of signalization pathways. If a biomolecular entity is immobilized on a MNP, the complex can specifically bind to the biomolecular partner. Monitoring the selected target localization by applying a magnetic field gradient and isolate the target is thus possible. Magnetic particles used in analytical biochemistry are composed of embedded nanoparticles (cores) in a polymer glass or silica matrix (shell) with a core-shell, shell-core or matricial design as displayed on Figure 1.24. The iron oxide MNP functionalization have to on one hand keep magnetic properties and on the other hand made them biocompatible platform of biomolecules (DNA, enzymes, proteins, antibodies) capture.

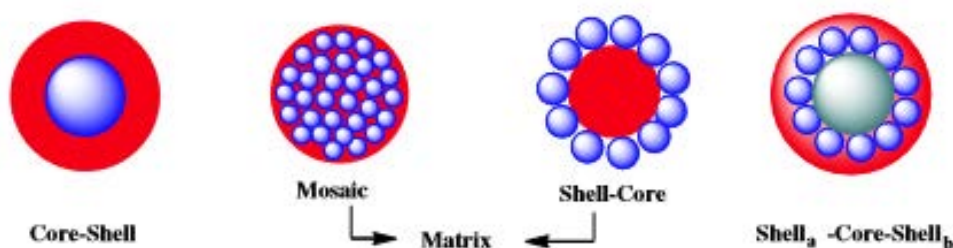


Figure 1.24: Various design of core-shells [200].

By coupling a click chemistry, enzyme-free, chain amplified (CCLCR) on gold nanoparticles with a magnetic separation, Kato *et al.* proposed an ultra-sensible colorimetric technique to detect 20 nucleotides long DNA and RNA [201].

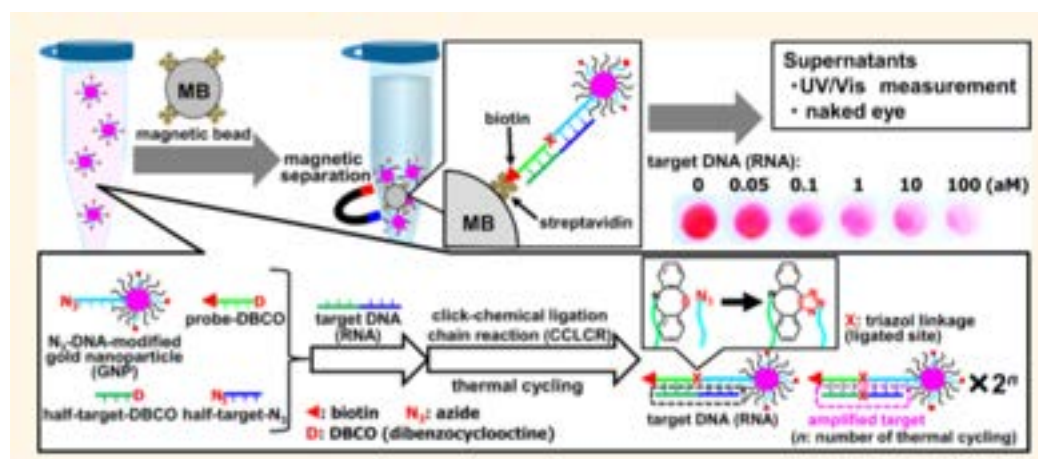


Figure 1.25: CCLCR [201].

Target DNA is hybridized on its probe attached on a gold nanoparticle of 15 nm in diameter reaching a 13 to 120 DNA strands coverage per NP. Targets are then exponentially amplified via hybridization thermal denaturation and purification cycles. Purification is done by magnetic separation on MNP beads functionalized with streptavidin (targets are modified with biotin). Detection is done par spotting the change in intensity of the 525 nm plasmonic band with a UV-Vis or visually. A zeptomolar 10^{-21} M LOD is reached after 40 thermal cycles. Single mismatch detection is possible.

There is also demonstration of hybridization detection on magnetic beads [202, 203]. The latter are used for magnetic isolation of the DNA-probe-target duplex (removal of non hybridized DNA and mismatched sequences) usually to make up for the fact that unmodified electrodes are used.

1.5 Devices using various coupling

1.5.1 Ferguson, a microfluidic electrochemical chip

Following miniaturization progress, electrochemistry adapted rather easily to the micrometric scale thanks to standard photolithographic technologies and Ultra-microelectrodes (UME) to fit into microfluidic devices [204, 205]. The coupling between electrochemistry e.g. an interfacial reaction, with microfluidics e.g. a microvolume issue [206] rely on the control of geometries and hydrodynamical conditions to be performant [207].

Ferguson *et al.* reported an Integrated Microfluidic Electrochemical DNA (IMED) sensor coupling two biochemical functions on chip e.g. PCR and electrochemical detection with an enzyme digestion in between to get a single-strand DNA. The PDMS/glass chip is composed of a PCR chamber that perform 38 cycles of amplifications in 1h40min (with the enzyme digestion) controlled by a temperature controller regulating a platinum resistive temperature detector mounted onto a custom thermofoil pad. Their device demonstrated a 10 aM LOD for non-purified genomic DNA (17-basis) with a mixed probe layer on gold composed of a thiol adsorbed MB redox labeled probe and 6-mercapto-1-hexanol [208].

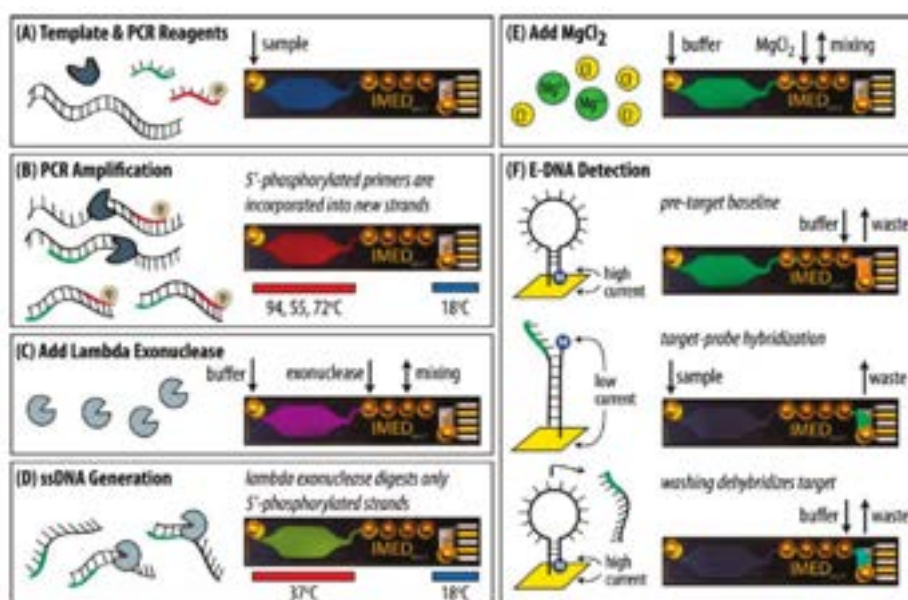


Figure 1.26: Assay overview with IMED sensor: (A) Template DNA with primers. (B) PCR amplification with temperature control. (C and D) Enzyme digestion to get a single-strand DNA. (E) Salt concentration adjustment with MgCl_2 (50 mM) for optimized hybridization conditions. (F) ACV hybridization detection: baseline current, target hybridization, probe regeneration.

1.5.2 Biomagnetic assays combining electrochemistry and magnetic particles

Not many devices were reported to couple the advantages of both electrochemistry and magnetic separation. A few examples are reviewed below.

Wang *et al.* coupled a detection approach to magnetic separation. The capture of the target was realized by magnetic spheres, unbound material was eliminated by magnetic separation. The target was released and detected with oxidation detection reaching a $0.01 \mu\text{g mL}^{-1}$ LOD [202]. They also linked with a streptavidin-biotin link beads with probes and detected BRCA1 with a $0.01 \mu\text{g mL}^{-1}$ LOD [209]. By monitoring silver precipitation on gold nanoparticles BRCA 1 was detected with a 0.2 ng mL^{-1} LOD. Palecek *et al.* reached a 5 ng mL^{-1} LOD by using paramagnetic beads coupled with guanine oxidation [203, 210].

Significant changes of miRNAs' signatures occur in various diseases especially cancers [211, 212, 213] especially the diagnosis of liver diseases such as hepatitis C, B, metabolic disorders or drug abuse with miRNA-122 [3]. But exploiting miRNAs as biomarkers requires methodological thoroughness [5] that was until now completed by RT-PCR, with all the limitations of amplification errors and long time of analysis that comes with it.

Lab On Chips are fully integrated devices that seek to meet clinical diagnosis specifications: specificity, increased sensitivity, portability, rapidity, cheapness, making them promising candidates to detect and quantify miRNAs. But the miniaturization and the coupling of various techniques (sampling, separation, detection) don't come without issues and surprises. In order to meet quite a few specifications (rapidity, sensitivity, specificity), cited in this first chapter, we realized Lab-On-Chip devices for a detection module and a capture module. miRNAs are fragile to manipulate, are easily digested by human proteins and expensive. We thus used synthesized DNA probes and targets matching the miRNA-122 sequence and its complementary.

Following scheme 1.27 describes the platform:

- Nanoplatfrom for the capture of DNA: Magnetic core-shell nanoparticles with a modified magnemite core and a silica shell functionalized with amines anchoring groups linked to DNA probes.
- Release module : Microfluidic chip filled with the magnetic CS nanoparticles subjected to a radiofrequency alternative magnetic field concentrated in the gap of an electromagnet to perform magnetic hyperthermia.
- Detection module: Electrochemical DNA hybridization detection-based sensor: UME in gold or nitrogenated amorphous carbon in a microfluidic channel in a two-electrode setup.

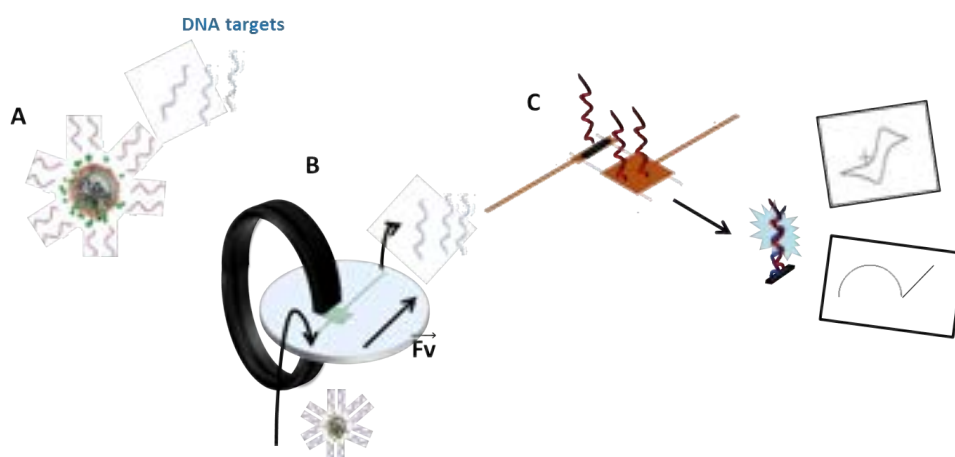


Figure 1.27: Artistic view of our Lab-On-Chip device. **A.** Magnetic core-shell nanoplatform for DNA capture, **B.** Magnetic hyperthermia release module, **C.** Electrochemical hybridization detection-based sensor.

Chapter 2

DNA hybridization detection on Ultra-microelectrode

In order to improve the chances of successfully treating patients, the detection of infectious diseases or genetic mutations at the molecular scale allow to establish a cheap, precise, fast and reliable diagnosis even before the appearance of the first symptoms. Combining high precision and speed, the diagnosis at molecular scale is promising. Thanks to the fast breakthroughs in biotechnologies, the development of fast methods that reduce the time of analysis and offer sensibility and specificity for DNA detection were made possible in fluorescence [214], Quartz Crystal Microbalance [215] and electrochemistry [78]. DNA hybridization is the most prized method as the simplest regarding a direct sequencing. Even more now that it was recently proven that DNA base stack exhibits "wirelike" behavior even if there is no obvious biological function that requires DNA to be a conduit for electron tunneling. This phenomenon can be used to detect hybridization.

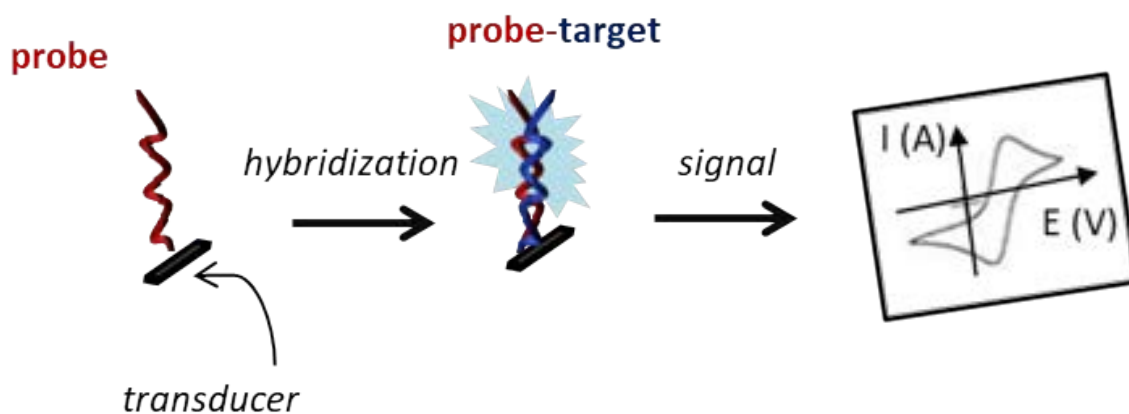


Figure 2.1: Schematic of DNA hybridization detection.

During DNA hybridization, the target sequence is identified with a DNA probe which possesses complementary sequences to the one of the target DNA (Watson and Crick's rules [216]). A biosensor is a device composed of a biological active layer acting as a recognition element and converting the biological interaction into a signal that can be measured. In the case of a DNA biosensor an immobilized DNA layer is the biological layer. More precisely the principle underlying DNA electrochemical biosensors is the conversion of the matching of DNA base pairs into an electrical signal. This is where electrochemistry takes action. Electrochemistry is the only way to directly transduce a biological event (e.g. DNA hybridization) without any other

transformation of the physical signal.

Combining high specificity, cheapness, easiness to use, portability and compatibility with microfabrication processes, electrochemical biosensors are excellent candidates for diagnosis of clinical interest and so to challenge RT-PCR. Recent works seek to optimize DNA biosensors in terms of cost rapidity and limit of detection.

The choice of the immobilization technique depends on the biological element (DNA) the transducer (electrochemistry) the medium in which the biosensor will evolve (aqueous medium at room temperature) the mechanical and chemical stability of the matrix. Gold is widely used as electrode material due to its high conductivity and numerous techniques of functionalization (physical adsorption, microcontact impression, polymerization, trapping inside a conducting polymer). Spontaneous techniques are the most valued especially physical adsorption as it maintains the biological activity of the bioreceptor. Gold provides an easy and elegant way to immobilize a probe DNA well-defined and organized monolayer via thiol adsorption in two hours [57].

In order to be efficient, three key steps have to be mastered in a DNA biochip:

- probe immobilization on a solid substrate,
- hybridization (or recognition) of the complementary target strand,
- conversion of the hybridization event into a physical signal (*i.e.* transduction).

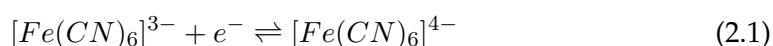
In this chapter, after an insight on Ultra-microelectrodes and long-range electron transfer a reconstitution of the traditional two-electrode configuration setup of Lazerges *et al.* [77] on gold UME will be done followed by its comparison with its counterpart integrated into a microfluidic system.

The combined use of a microband electrode and a fluidic channel termed a channel microelectrode offers:

- a fast steady state current response (around one millisecond) due to a very thin diffusion layer limited by the convection regime,
- a drastic improvement in the efficiency of the sensor in terms of the volume of the analytes and system dynamics (time of experiment) with easy manipulation of samples [115, 217, 218, 219, 220, 221, 222].

The detection is voltamperometric. A potential ramp is applied to the electrode to oxidize or reduce electroactive species of interest. As a result, the charge (electrons) transfer current generated by the faradic reaction is proportional to the concentration of the specie of interest.

An electroactive species is thus needed: we used the $[\text{Fe}^{III}(\text{CN})_6]^{3-} / [\text{Fe}^{II}(\text{CN})_6]^{4-}$ redox couple associated with the one electron transfer Equation 2.1 on a channel microelectrode during the immobilization and hybridization steps.



The equilibrium potential was set at 0 V as both microelectrodes are in gold. DNA hybridization is followed by cyclic voltammetry (CV) as well as Electrochemical Impedance Spectroscopy (EIS) with the redox couple allowing surface property analysis, such as surface modification, when binding events of target DNA occur on the sensor surface. The selectivity of the electrochemical DNA biosensor using

an UME was already verified in a previous study using the same protocol scheme where a double-stranded DNA (miRNA-122) had a single mismatch in the sequence [223]. Finally a last improvement will be done by changing the electrode material into amorphous carbon nitride for reasons that will be explained along the way.

2.1 Methodology

2.1.1 DNA

The DNA used mimics the fragments of interest miRNA-122 and its complementary. First DNA are used because of RNA's fragility. Indeed the RNase presents on our fingers is sufficient to destroy miRNAs asking thus for precautionary measures such as specialized material. DNA-DNA hybridization or DNA-RNA hybridization are similar due to their close association constants DNA/RNA hybrids are slightly more stable [?].

2.1.2 Long-electron transfer (LET) in DNA

Electron with their feeble mass can tunnel through high electron volts and nanometer wide barriers in less than a second leading to wide applications from semiconductors to respiratory chains. Semi-classical theory for chemists (*Marcus* [224] and *Levich* [225]) unraveled electron transfer through the following Equation 2.2 [226] for two weakly interacting redox centers at fixed distance and orientation (described by the standard free-energy change ΔG°).

$$k_{ET} = \sqrt{\frac{4.\pi^3}{\hbar^2.\lambda.k_B.T}} \cdot H_{AB}^2 \cdot \exp\left(-\frac{(\Delta G^\circ + \lambda)^2}{4.\lambda.k_B.T}\right) \quad (2.2)$$

Nuclear reorientation and reorganization are described by the parameter λ . Electronic coupling strength between reactions and products is described by H_{AB} and H_{AB}^2 is the probability of electron tunneling from donor to acceptor. For biologists evidence of LET was proven by measures of intramolecular ET in protein crystals [227].

In 1953, the discovery of the double structure of DNA not only reveals its role of support of the genetic information but also its unique physical and electronic properties. The heart of the double helix of DNA is composed of cyclic aromatic base pairs stacked and wrapped in a negatively charged phosphate backbone. Double stranded DNA structure is a π stacking as an aromatic crystal. A structure enabling a conductive behavior [228, 229] particularly efficient ($\beta < 10 \text{ nm}^{-1}$ [226], $k_{ET} \approx 10^{10} \text{ s}^{-1}$ [230]). The high concentration of aromatic bases stacked in the double helix facilitates ET due to smaller tunneling energy gaps than in proteins [231].

Indeed it has been demonstrated thanks to photochemical and photophysical methods that the double structure of DNA is in fact the efficient support of charge transfers. These studies uses the quenching in fluorescence. Figure 2.2 shows a donor and an acceptor trapped inside the DNA duplex. The fluorescence of an intercalator, here ethidium (red), is quenched by the rhodium intercalator (yellow) localized 20 Å away. Double stranded DNA is perfectly ordered and basis overlap thus red and yellow are in position of quenching. The quenching of ethidium is inhibited in the case of a perturbation in the π -stacking inducing less overlapped basis (here a pink mismatch). From photochemical and pulse radiolytical measurements the efficiency of LET can be described by a rate constant at close contact k_{ET} and β the exponential distance decay constant in the following relation:

$$k_{ET} = k_{ET}^\circ \cdot e^{-\beta \cdot (r-r_0)} \quad (2.3)$$

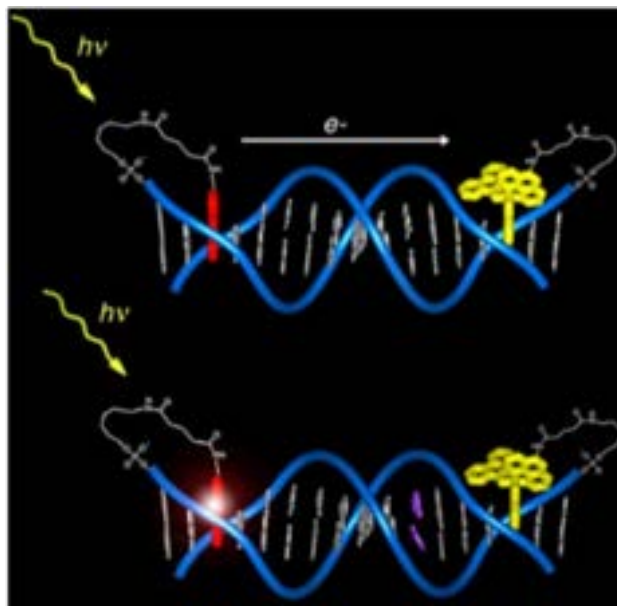


Figure 2.2: Photochemical studies of quenched fluorescence.

Biochemical studies of which ultra fast spectroscopy have shown that charge transport happens at the femtosecond time scale and is very sensitive to changes in the conformation of DNA and to the orientation of base pairs. The fluorescence quenched studies have shown that the charge transport has an oscillating behavior with a period of 4 base pairs (altered by temperature). Barton has proposed a model in which the charge is transiting through the delocalized π domains [232, 233] and highlights the importance of intra-strands H-bonding contacts for long range reactivity. Harriman *et al.* checked with high resolution time resolved fluorescence spectroscopy that DNA is an effective pathway for electron transfer by looking at the fluorescence lifetime of intercalated EB^+ and DAP^{2+} [229].

2.1.3 LET in $Fe^{II}/Fe^{III}/MB$ systems

Barton *et al.* [53] designed for the first time a DNA biosensor based on the principle of charge transfer through DNA. A monomolecular self-assembled layer of DNA of 15 base pairs is immobilized on a gold electrode of 200 μm in diameter. Thanks to thiol adsorption DNA forms a dense monolayer with DNA helices in the upright direction on a height of 45 \AA [234]. In order to improve the sensibility of the electrochemical cell, Barton has associated to the electrocatalytic process a redox intercalant, methylene blue (MB). MB is an organic intercalant with a $k \approx 10^6 \text{ M}^{-1}$ affinity constant. Its reduction is reversible with a 0 V redox potential (vs NHE) lower than the one of $[Fe^{III}(CN)_6]^{3-}$.

Electrons are transiting from the gold electrode to the intercalated MB and are accepted by the ferrocyanate in solution. The oxidized MB is again available for electrochemical reduction. The cycle goes on until the gold electrode potential is sufficiently negative to reduce MB. The $Fe(CN)_6^{3-}$ reduction eases the diffusion of the complex along the helix while the intercalator takes part to the electron transfer through the base stacking.

MB allows to increase the sensitivity of the signal measurement. Inserted inside the base pairs the structure of DNA becomes more open and thus more accessible

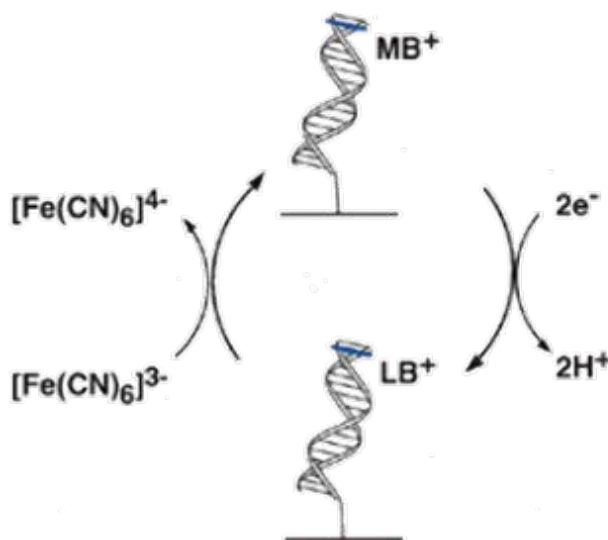


Figure 2.3: Electron transfer with oxido-reduction of ferrocyanate and MB intercalant [232].

to ions in solution [55]. The influence of the location of the intercalator has been investigated [232] resulting in a lack of dependency. With a negative global charge $\text{Fe}(\text{CN})_6^{3-}$ is electronically inactive at the DNA monolayer surface, itself negatively charged. A single-stranded probe DNA in thus hindering the electron transfer between gold and electrolyte. An other intercalant Daumyocine (organic intercalant covalently linked to G bases of DNA) has a better affinity with DNA than MB. The exchange dynamic would be slower which would hinder the electron crossing. A unique non complementary base do not affect the general structure of the helix but disturb subtly the electronic structure of the stacking. With a mismatch, less molecules of MB are catalyzed, the concentration of catalysis is decreased.

In double stranded DNA the basis are perfectly arranged in parallel plans with a partial overlap. An helix well stacked has shown to exhibit fast electron transfer [235]. On the contrary single-stranded DNA does not have an ordered structure. This difference in structure has been verified by measuring the optical density at 260 nm. The extinction coefficient of single stranded DNA is higher due to its lack of structure thus lack of quenching due to the overlap [?].

We have chosen the principle of gold electrode with an organized monolayer via alkanethiols which efficiency was proven many times and with a possible regeneration [236]. Now a coupling with the benefits of the UME is described in the next section.

2.1.4 Ultra microelectrodes (UME)

This UME description was largely inspired from the courses from Frederic Lemaître, doctor in the P.A.S.T.E.U.R Laboratoire, Department of chemistry in Ecole Normale Supérieure, Paris.

In the fifties and the sixties, electrochemical detection methods flourish including voltammetry and techniques probing small signals. Twenty years later, the discovery of the original properties of Ultra-microelectrodes [237, 238, 239] opens the gate to novel possibilities of analysis. The modifications of mass transport conditions give rise to high current densities at the surface of these UME while the current itself is kept very low. These characteristics allow electroanalytical analysis impossible until now with classical electrodes especially for low electrolyte concentrations. Multiple factors allow to study fast process: the spatial resolution that offers the possibility to study concentration changes in micrometer volumes, the change in time scale and the decrease of the effects of the ohmic drop due to the reduction in the UME's size [207].

Faradic and capacitive currents

During a classical electrochemical analysis, a current is flowing through an electrode dipping into a solution generating a polarization of the electron/solution interface with a particular organization of charges at the interface. With electroactive species and a potential $E \gg E_{ox/red}^{\circ}$, the current flowing through the electrode is a contribution of two process. The faradic current is associated with the redox reaction and the capacitive current is generated by the reorganization of charges at the electronic double layer.

The faradic current (due to the electrochemical process), I_F reflects the transport of electroactive species in solution towards the electrode if a sufficient potential is applied. This transport can be achieved by diffusion (the electrochemical reaction induces a concentration gradient), migration (electrical field) and convection (solution movement). When a potential $E_{applied} \gg E_{Ox/Red}$ is applied the oxidation process is limited by transport especially the diffusion of electroactive species.

The double layer, in the *Gouy and Chapman* model [240, 241], is composed of counter-ions organized in the *Debye* layer. The potential at the electrode surface is decreasing exponentially with the distance. The electronic double layer is behaving like a capacitor with a capacitive current i_C :

$$i_C = \frac{\Delta E}{R_S} \cdot e^{-\frac{\Delta t}{R_S \cdot C_d}} \quad (2.4)$$

Diffusion regime

For millimetric planar electrodes, the thickness of the diffusion layer is very low compared to the size of the electrode. The transport of the species is described by a semi infinite linear diffusion (no radial diffusion). Currents and concentrations are predicted by *Cottrell's* Equations 2.7 solution to *Fick's* laws.

$$\vec{J} = -D \cdot \vec{grad}C$$

and

$$\frac{\partial C}{\partial t} = D \cdot \Delta C \quad (2.5)$$

with D , the diffusion coefficient.

The concentration profile is given by:

$$C_R(x, t) = C_R^* \cdot (1 - \operatorname{erfc}(\frac{x}{2\sqrt{D_R \cdot t}})) \quad (2.6)$$

$$i(t) = \frac{n.F.A.C_R^*\sqrt{D_R}}{\sqrt{\pi.t}} \quad (2.7)$$

with n the number of electron exchanged, F , the Faraday constant and A the area of the electrode.

Cottrell's equation predicts high current for short times thus inaccessible as the maximal measurable current is limited by instrumentation. Moreover a capacitive current is added to the faradic current. For a longer timescale the diffusion layer is ruined by convection.

For Ultra-microelectrodes (from 1 to 25 μm in radius), the establishment of a stationary regime and a spherical symmetry is expected. A change in the regime of diffusion near the electrode is induced by the transition from millimetric to micrometric sizes. The diffusion layer thickness and the size of the electrode are now around the same order of magnitude with non negligible border effects (radial diffusion).

Four types of UME can be differentiated: spherical, cylindrical, disk or band. Current and concentrations can only be calculated analytically for the spherical electrode.

Fick's laws give the following current prediction:

$$i = nFAD_R C_R^* \left[\frac{1}{r'_0} + \frac{1}{\sqrt{\pi D_R t}} \right] \quad (2.8)$$

For short times, $t \ll \frac{r'_0{}^2}{D_R}$, Cottrell's equation is still relevant:

$$i \approx nFAD_R \frac{C_R^*}{\sqrt{\pi D_R t}} \quad (2.9)$$

The diffusion layer thickness $\delta = \sqrt{\pi D_R t}$ is small compared to the radius of the electrode making the edge effects negligible and the regime of diffusion planar. Diffusion layer thickness and current are time varying, this is a transitional regime.

For long times, $t \gg \frac{r'_0{}^2}{D_R}$, the current is stationary:

$$i \approx nFAD_R \frac{C_R^*}{r'_0} \quad (2.10)$$

The typical duration of an electroanalysis experiment goes from a few seconds to hundred of seconds. The spherical regime would be never reached for a millimetric electrode contrary to a UME (around 30 ms for a radius, r'_0 , of 1 μm).

Even if the experiment will be lasting several thousand of seconds the steady state would never be established because of the convection layer. On the contrary, the thickness of the diffusion layer is far larger than the one of the convection layer for UME. The small size of the latter is allowing thus to reach a spherical regime of diffusion and a stationary current rapidly (around few milliseconds). The thickness of the diffusion layer is a few times r'_0 . Gradients of concentration generated by the disturbance are located near this value. The UME is only sensitive to changes in concentration near its active surface making UME great local concentration probes.

Time constant, ohmic drop and signal to noise ratio

The electrical double layer is the source of the electrical noise. From the Equation 2.4, it is proportional to C_d . An electrode in a solution of resistance R_S can be modeled with a RC circuit with a $R_S.C_d$ time constant. The latter acts as a filter which is limiting the electrode potential variations. The capacitor is charged for ca. ten times the time constant e.g. 30 μs for a millimetric electrode.

Faradic and capacitive currents flow are generating a ohmic drop $(i_C+i_F).R_S$ introducing a dephasing between the real potential and the measured/imposed value.

The signal on noise ratio (S/N) is proportional to i_F/i_C .

As the surface of the counter electrode is larger than the surface of the working electrode (S_{WE}), current lines are contained in a conic volume and the following relations are deduced for UME:

$$R_S \propto \frac{1}{r'_0} \quad (2.11)$$

$$C_{dl} \propto S_{WE} \quad (2.12)$$

$$\tau \propto r'_0 \quad (2.13)$$

$$S/N \propto \frac{1}{r'_0} \quad (2.14)$$

Contrary to the case of the millimetric electrode where S/N is independent of the size. From Equation 2.14, it is thus possible to detect very small currents (up to 0.1 pA [242]). The experimental setup is also simplified as there is no need of a reference electrode to decrease the ohmic drop.

The case of the planar microband UME

For planar electrodes the situation is identical to the spherical ones, at short time scales, the current is becoming quasi-stationary and is proportional to the width L.

$$i = \frac{2nF_R C_R^*}{\ln(64 \frac{D_{R,t}}{\omega^2})} . L \quad (2.15)$$

$$R_S \propto \frac{1}{L} \quad (2.16)$$

$$C_d \propto L \quad (2.17)$$

The ohmic drop is thus minimal and independent from the size of the electrode. If L decreases, τ is dropping and S/N is increasing.

Thanks to their microsecond time of response, a spatial resolution around the size of the electrode, a spherical regime of diffusion, high sensitivity measurements in real time, UME allow the access to highly resistive media and the study of fast phenomenon. We will finish this section with a quote of C. Amatore on the UME name:

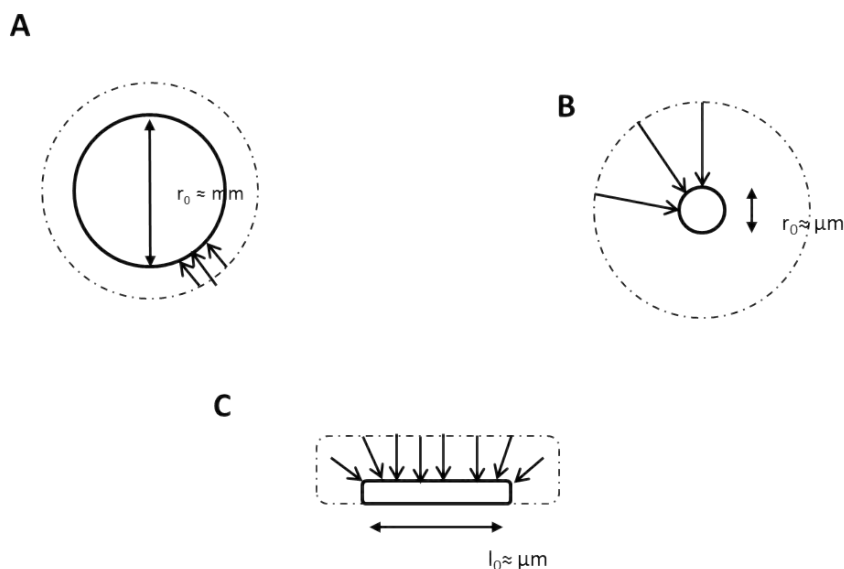


Figure 2.4: Diffusion layer behavior: **A.** Spherical millimetric electrode, **B.** Spherical UME, **C.** Planar UME. Dotted line are displaying the diffusion layer.

"The electrochemical behaviors of the electrodes not only are related to their dimensions but also depend on the time scale of the experiment and the thickness of the convection-free layer. It stresses once more the futility of trying to propose an absolute definition of ultramicroelectrodes based on the objects themselves. Indeed, the same electrode may behave as a microelectrode or an ultramicroelectrode, depending on these parameters."

C. Amatore *et al.* in *Analytical Chemistry* **2010**, 82, 6933-6939.
Differences between ultramicroelectrodes and microelectrodes.

We will use and describe our own UME in the following sections.

2.1.5 Electrochemical Methods

The manufacture of such a sensor asks for a stable and specific surface chemistry and thus the understanding of molecular interactions of the electrode/liquid interface. The use of both Electrochemical Impedance Spectroscopy and Cyclic Voltammetry, the main electrochemical methods used in this work, allows to describe precisely the interface.

Cyclic Voltammetry (CV)

CV is well described in literature [243]. It is a simple technique to study reactions occurring as a function of a potential. It can be used as a preliminary method in order to obtain a quick overview of the relevant potentials. Also it can be used to be sure to deal with a reversible response and to measure reaction kinetic parameters.

For this technique a triangular sweep potential $E(t)$ is imposed on the WE resulting in an oxidant and reductive current. As a convention a positive current (anodic) fits to an oxidation and a negative current (cathodic) fits to a reduction. For a reversible nernstian reaction (peaks separated by $2.22 RT/nF$) the intensity I_P of the

peak current as a function of the sweep speed ν is given by the following Equation [244]:

$$I_P = 0.4463.n.F.C^0.S.D^{1/2}.\left(\frac{F.\nu}{R.T}\right)^{1/2} \quad (2.18)$$

with, n , the number of exchanged electrons, C^0 , the concentration of electroactive species, F , the Faraday constant ($96\,485\text{ C mol}^{-1}$), D , the diffusion coefficient ($\text{m}^2\text{ s}^{-1}$), T , the temperature in K, S , the surface of the electrode (cm^2) and, R , the perfect gas constant ($8.3144\text{ K}^{-1}\text{ mol}^{-1}$).

Electrochemical Impedance Spectroscopy (EIS) [245]

EIS is a non-stationary technique that allows to separate the elementary reactions when the time constants are sufficiently distinct. By inducing a small perturbation of the electrochemical system outside its stationary state, the diverse elementary processes do not evolve at the same rate. The global electrochemical process can thus be dissect. In our case complex heterogenous reactions interact with mass transport (hybridization, electrolyte consumption, transport of DNA, redox reduction and intercalation of MB).

Under flow, the effect of diffusion can be avoided at the potential of equilibrium. An as important point is this possibility to only look at a feeble δE decreasing the time of measurement whereas CV needs to sweep a large potential range.

For linear systems, in the sinusoidal regime, the relation between current and potential can be expressed by a Z ratio between effective value of current and tension and its ϕ dephasing. The impedance $Z(\omega)$ of an electrochemical interface is a complex number that can be displayed either in polar ($|Z|$, ϕ (module, argument)) either in Cartesian coordinates ($\text{Re } Z(\omega)$, $\text{Im } Z(\omega)$):

$$Z(\omega) = |Z| \exp j\phi = \text{Re } Z + j \text{Im } Z \quad (2.19)$$

With $|Z|^2 = (\text{Re } Z)^2 + (\text{Im } Z)^2$, $\phi = \arctan(\text{Im } Z / \text{Re } Z)$, Z real part $\text{Re } Z = |Z| \cos \phi$ and Z imaginary part $\text{Im } Z = |Z| \sin \phi$. Two types of graphs, Nyquist diagram or Bode plots, can be used to describe these relations as displayed on Figure 2.5 for an electrical equivalent circuit:

$$Z(\omega) = R_e + \frac{1}{\frac{1}{R_i} + jC_d\omega} \quad (2.20)$$

The behavior of an electrochemical interface which current is limited both by the electrochemical reactions speed and mass transport is described by differential equations for the kinetics and partial equations for mass transport.

When an interface is brought out of its equilibrium a permanent flux of charges and matter is established due to electrochemical reactions for electrical charges transport between metallic electrodes and the liquid electrolyte. Moreover the transport of reactive species toward the interface is driven by gradients of electrical and chemical potentials. Elementary laws governing the kinetics of mass transport and the electrochemical reactions with complex couplings between these laws generate a non linear behavior of the electrochemical system. But the local analysis of a non linear system can be limited to the linear theory. From an experimental point of view, it consists of the measure of the impedance of the electrochemical cell by using a disturbance signal of feeble amplitude along the current-tension polarization curve.

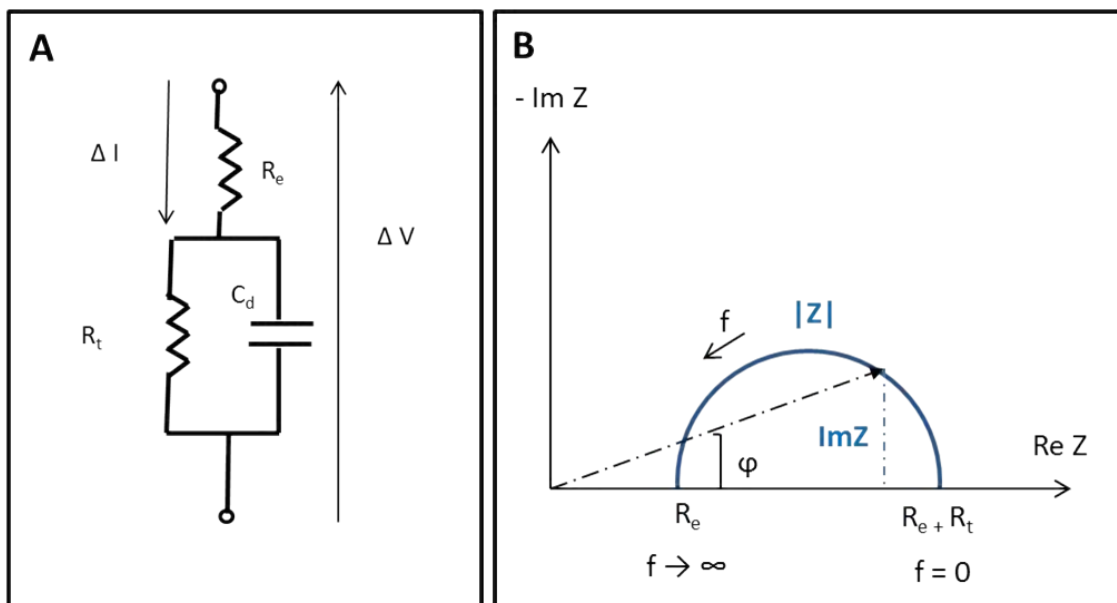


Figure 2.5: Representations of the impedance Z in the complex plane (Nyquist graph B.) and equivalent electrical circuit (A). R_e stands for the electrolyte resistance, R_t the charge transfer resistance and C_d the double layer capacitance.

The behavior at the interface can be resolved in linear regime. As displayed on Figure 2.6 a sinusoidal tension of feeble amplitude $V(t) = \Delta V \cdot \sin \omega t$ is superimposed to the continuous tension V_S of polarization. A sinusoidal current of feeble amplitude $I(t) = \Delta I \cdot \sin(\omega t - \phi)$ is added to the continuous current I_S resulting in a Lissajous ellipse on X-Y. The measure of Z along the polarization curve allow a complete description of the interface.

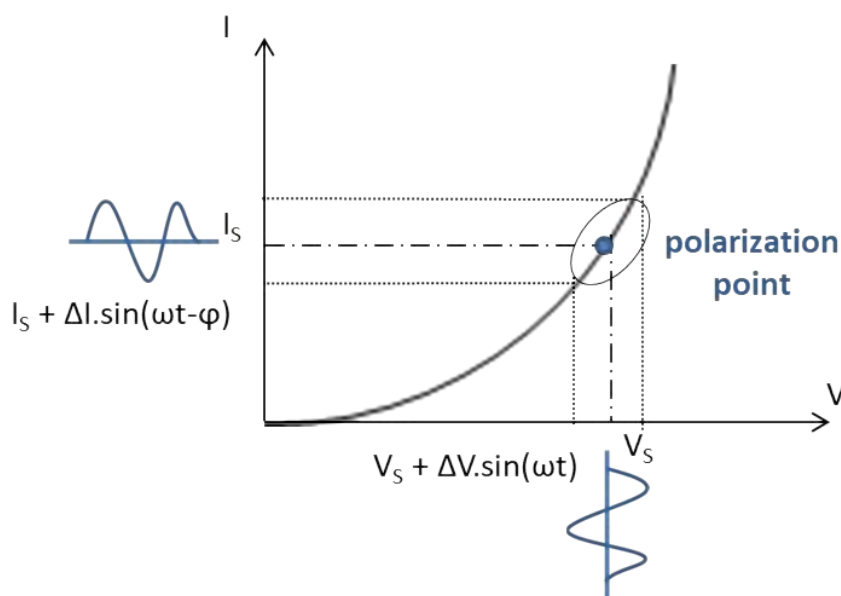


Figure 2.6: Principle of the analysis of a non linear system.

This technique is measuring the response of the system when a small sinusoidal

current or potential perturbation is applied. In order to induce a potential perturbation, a DC potential is set until a steady response is reached. The potential perturbations are run at a given amplitude for a given set of frequencies. If the potential perturbation is of the form:

$$E(t) = E_0 + \delta E(t)$$

with

$$\delta E(t) = |\delta E| \sin(\omega t) \quad (2.21)$$

with ω the pulsation in rad s^{-1} .

The electrochemical impedance is linked to the response in current with

$$Z(\omega) = \frac{\widetilde{E}(\omega)}{\widetilde{I}(\omega)} = |Z| \cdot e^{j\cdot\phi} \quad (2.22)$$

with $j^2 = -1$ and δE and δI the complex amplitude of $\delta E(t)$ and $\delta I(t)$.

$|Z|$ is the module and ϕ the argument of the impedance.

As I and E are ω dependant, Z is a function of frequency. Z can be expressed with a real and an imaginary part with the following equation:

$$Z(\omega) = Z'(\omega) + j \cdot Z''(\omega) \quad (2.23)$$

Z' and Z'' expressed in ohms.

Thus Z can be plotted in the complex plane by a vector with Z' and Z'' Cartesian coordinates. This plot is called Nyquist diagram. It can also be plotted by a Bode diagram $|z|$ as a function of $\log f$.

With

$$|Z| = \sqrt{Z'(\omega)^2 + Z''(\omega)^2} \quad \text{and} \quad \phi = \arctan\left(\frac{Z''}{Z'}\right) \quad (2.24)$$

The impedance of an electrode is a function of both the frequency and of the polarization point $P(I_0, E_0)$. The high frequency limit of the diagram gives the ohmic resistance R_e . As for the low frequency limit, it matches $(R_e + R_p)$, R_p the polarization resistance. R_p is defined as a slope $R_p = dE/dI$ at the polarization point corrected by the ohmic drop.

Between these two limits, the dependency according to the frequency of $Z(\omega)$ comes from its non-resistive behavior:

- the capacitive contribution of the electrochemical double layer. The charges are lacking or in excess (electrons on the electrodes or ions in the electrolyte). It modifies the repartition of charges at the interface.
- the faradic contribution linked to the electron transfer at the interface coming from the electric current and the electrochemical reaction. The analysis of impedance data can be either fitted with equivalent electrical elements giving parameters with more or less electrochemical significance or the whole system can be modeled and the EIS derived from it.

The double layer capacitance is represented by a capacity C_d (in F cm^2). As for the faradic process it is described as a faradic impedance $Z_F(\omega)$. If capacitive and faradic currents are supposed added, the interface metal/electrolyte is represented

with an electrical equivalent circuit named the Randles circuit. In the complex plane, the impedance of the electrode can be calculated, as follows:

$$Z(\omega) = R_e + \frac{Z_f(\omega)}{1 + j\omega C_d \cdot Z_f(\omega)} \quad (2.25)$$

The faradic impedance is a mix of several impedances. It comprises a resistive term called charge transfer resistance, R_t , and impedance of concentrations of electroactive species in solution (diffusion-convection) and adsorbed.

Experimentally the impedance measurements are done on two setups. The first is a setup comprising a frequency response analyzer (FRA 1255) coupled to a dielectric interface Solartron (DI1296). The dielectric interface is controlled by the SMART software. The dielectric interface is characterized by a large frequency range from 1 mHz to 20 MHz. The second, is a Biologic potentiostat equipped with a low current module.

The measure of impedance depends on several physical and chemical parameters. Thus the nature of the surface on which impedance is measured will have an effect on the global response of the studied system notably on the dependence in frequency of the double layer capacitance.

2.2 Detection of DNA hybridization on gold UME in macrosystem

Materials and Methods

Electrochemical measurements were done with a mini portable ammeter. The 25 μm ultra-microelectrode (UME) was homemade using 99.99% pure Goodfellow gold wire sealed in glass capillaries as sketched on Figure 2.7. The counter electrode was a 2 mm diameter gold wire sealed in a Teflon cylinder (Metronic, France). The gold UME was polished with 3 μm silicon carbide disks and rinsed with deionized water. Methylene blue (MB, Sigma-Aldrich), $\text{K}_3\text{Fe}^{\text{III}}\text{CN}_6$ (NormaPur), $\text{K}_2\text{Fe}^{\text{II}}\text{CN}_6$ (Sigma-Aldrich) and NaNO_3 (NormaPur) composed the electrolyte and are used as purchased. The composition of the electrolyte is detailed in Table 2.1.

Table 2.1: Electrolyte composition.

| Component | Concentration |
|-------------------------|---------------|
| MB | 10^{-8} M |
| ferri/ferrocyanide | 3 mM |
| NaCl or NaNO_3 | 0.5 M |



Figure 2.7: Schematic representation (not to scale) of the conventional working UME ($\phi = 25 \mu\text{m}$) dipping into $\text{Fe}^{II}/\text{Fe}^{III}$ and methylene blue (MB) electrolyte on top of the counter electrode ($\phi = 2 \text{ mm}$).

DNA probes, (P), DNA complementary targets, (T), and mismatched DNA (M) 23 basis long were purchased from Eurogentec (France). Their structures are described in Table 2.2.

Table 2.2: Sequences of Oligonucleotide Strands

| Oligonucleotide | Sequence (5' to 3') |
|-----------------|--|
| Probe (P) | 5'-Thiol C6-CAA ACA CCA TTG TCA CAC TGC-3' |
| Target (T) | 3'-G TTT GTG GTA ACA GTG TGA CG-5' |
| Mismatch (M) | 3'-G TTT GTG GTA AGA GTG TGA CG-5' |

Probe (P) immobilization

After rinsing the UME is dipped into a 500 μL probe solution at $10 \mu\text{g mL}^{-1}$ in 0.5 M NaCl for 2 hours then the UME is rinsed for 10 seconds under ultra pure water (18 M Ω). Before the measure the UME is dipped into an eppendorf containing 1 mL of the electrolyte for 30 seconds. Each measurement (-0.1 V, 0 V and 0.1 V) is done after 1 minute of stabilization.

Hybridization with the target (T)

After the measurement the UME is rinsed 10 s with ultra pure water and dipped into a 500 μL target solution at $10 \mu\text{g mL}^{-1}$ in 0.5 M NaCl for 30 minutes. After hybridization the UME is rinsed three times with 1 mL of 0.5 M NaCl.

Results

First, the diameter of the home-made UME was checked by comparing the current from a commercial platinum UME of 15 μm in diameter as sketched in Figure 2.8. By following the path of equations below the diameter, D_{Au} , has been deduced.

$$\frac{I_{Au}^{lim}}{I_{Pt}^{lim}} = \frac{D_{Au}}{D_{Pt}} \quad (2.26)$$

So

$$D_{Au} = D_{Pt} \cdot \frac{I_{Au}^{lim}}{I_{Pt}^{lim}} \quad (2.27)$$

For the platinum I_{Pt}^{lim} and gold I_{Au}^{lim} currents, the stationary currents of diffusion were taken. I_{Pt}^{lim} is equal to 7 nA and I_{Au}^{lim} is equal to 13 nA giving a diameter of D_{Au} equal to 28 μm which is near the 25 μm value sought.

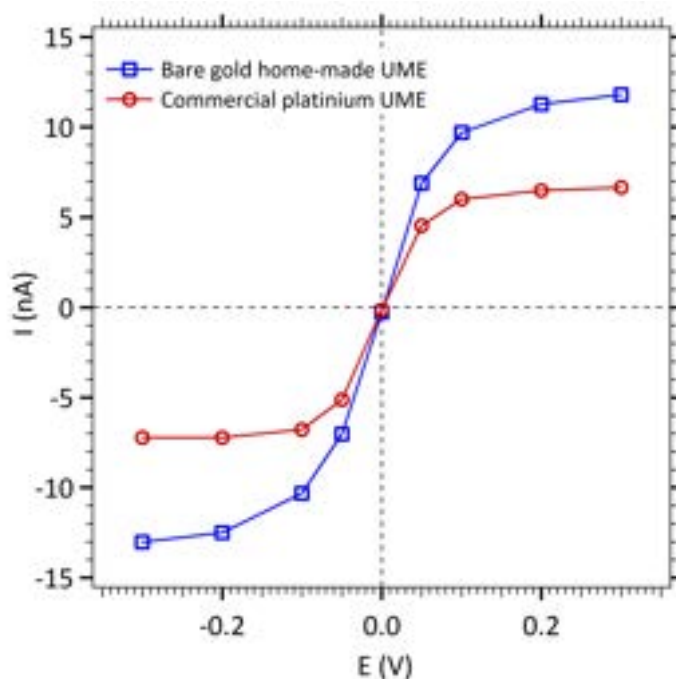


Figure 2.8: Electrochemical responses of our home-made gold UME and a commercial platinum UME of 15 μm in diameter dipping in the electrolyte solution.

Figure 2.9 compares the current intensity before and after hybridization and on a bare gold electrode (without any DNA probe immobilization). Electrochemical measurements are done on a narrow potential range (from -0.1 to 0.1 V) to avoid any unwanted faradic reaction from the biological matrix, on one hand, and to reach the maximal meaningful current for currents differentiation on the other hand.

As described above, DNA detection is based on LET through the π stacking of double stranded DNA. The redox couple $\text{Fe}^{II}/\text{Fe}^{III}$ is used as it prevents electron transfer before hybridization. Negatively charged, it can not diffuse through the layer of probe DNA due to electrostatic repulsions with the negatively charged phosphates from the DNA backbone. MB is catalyzing $\text{Fe}^{II}/\text{Fe}^{III}$ oxido-reduction both

redox specie and DNA intercalant. However, current before hybridization is not equal to zero due to leakage current coming from UME edge effects.

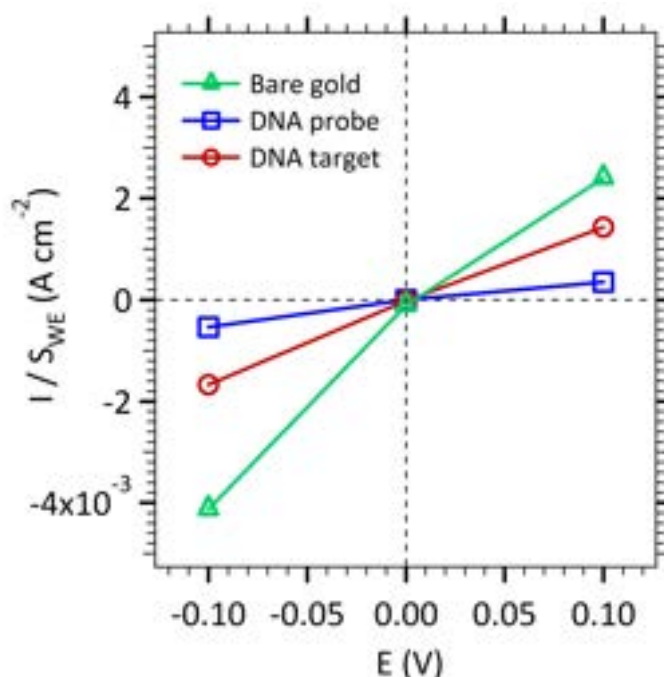
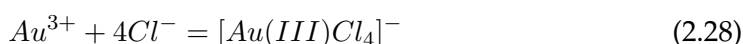
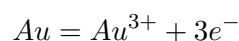


Figure 2.9: Electrochemical response of the biosensor in NaCl 0.5 M of the bare UME (green triangles) of the UME covered with single stranded DNA probes (blue squares) and double-stranded DNA target at 1.5 M (red dots).

After hybridization we observe a net increase in current, sign of the success of hybridization.

The stability of the SAM in NaCl is then probed. Figure 2.10, layout A, depicts the electrochemical response to a biosensor after 30 minutes in NaCl compared to its response before and after hybridization.

A large increase in current after dipping into NaCl should be noted. The SAM is breaking down and leaving holes in it. It can be explained by the attack of the gold electrode by chlorides. Equations governing the reaction between gold and chloride anion are the following with a standard redox potential of 1.0 V [246]:



A change in electrolyte is needed. NaNO₃ will replace NaCl. Na⁺ cations of NaNO₃ are shielding, as well, the negative charges of DNA phosphate backbone. Hybridization and probe immobilization remain in NaCl, as it is the condition to obtain a dense SAM, crucial for reproductibility and biosensor efficiency (dense films prevent the intercalators diffusion inside the monolayer).

Figure 2.10, layout B, shows the electrochemical response before and after hybridization and after extended immersion in NaNO₃ to test the stability of the SAM

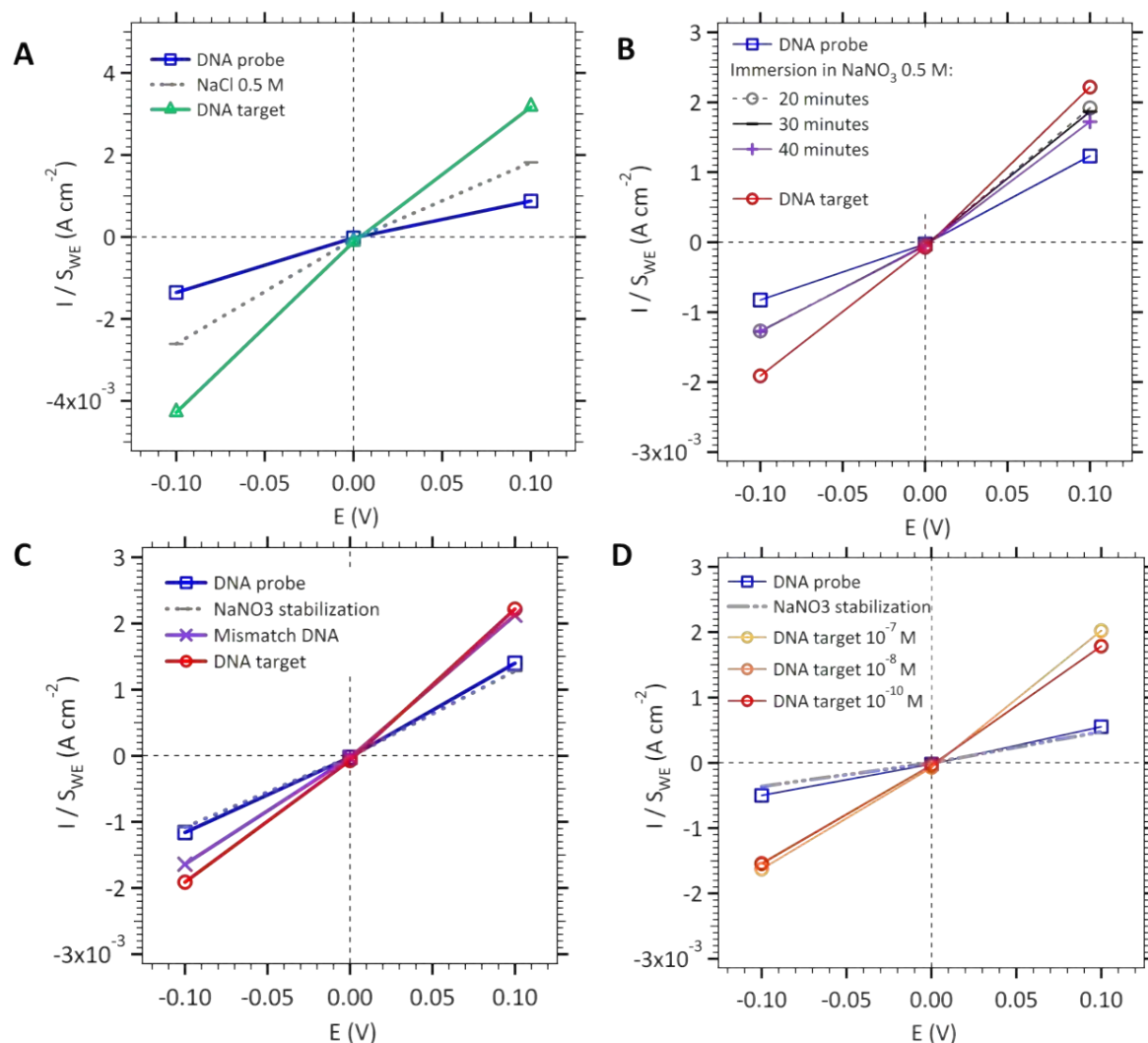


Figure 2.10: A. Electrochemical response of the biosensor after probe immobilization (blue squares) after a 30-minutes immersion in NaCl 0.5 M (grey dotted lines) and after DNA hybridization with the target at 1.5 M (red dots). B. Electrochemical response of the biosensor after probe immobilization (blue squares) after a 20 (grey dotted line) 30 (black line) and 40-minutes (pink crosses) immersions in NaNO_3 0.5 M and after DNA hybridization with the target at 1.5 M (red dots). C. Electrochemical response of the biosensor after probe immobilization (blue squares) after a 30-minutes immersion in 0.5 M NaNO_3 (grey dotted lines) after detection of a DNA with one mismatch M (pink crosses) and after DNA hybridization with the target at 1.5 M (red dots). D. Electrochemical response of the biosensor after submission to decreasing concentrations of DNA targets.

after the change of electrolyte. No SAM damage can be noticed, current is even decreasing after immersion in NaNO_3 . The choice of NaNO_3 is validated.

Mismatch detection

Figure 2.10, layout C., shows the electrochemical response after the hybridization of a target DNA with a mismatch in the middle of its sequence. A large decrease in current compared to the fully complementary DNA can be noted. Indeed the mismatch is a rupture in the stacking of DNA bases preventing the electron transfer. The detection of the mismatch is more precise for Fe^{II} oxidation (e.g. $E=+0.1$ V). Indeed the mismatch current is closer to the current before hybridization implying that there is no electron transfer through DNA structure.

Figure 2.10, layout D, shows the response of the biosensor submitted to decreasing concentration of DNA target solution.

The detection limit reached for now on is 10^{-10} M for an hybridization current still near its initial value for $1.5 \mu\text{M}$.

We immobilized a DNA monolayer of 23 bases on a gold UME of $25 \mu\text{m}$ in diameter and we detected the hybridization of a DNA target thanks to LET in an electrolyte of $\text{Fe}^{III}/\text{Fe}^{II}$ redox complex, Methylene Blue redox intercalant and NaNO_3 electrolyte. Our biosensor thanks to charge transfer is very sensitive to base disruption (mismatch) allowing to detect down to one unique mismatched DNA basis. The LOD reached the 0.1 nM. This simple biosensor with its rapid, cheap and precise detection is a promising candidate for the follow-up of our project.

The results on the detection of DNA hybridization on this sensor outside microfluidics were presented during a speech at the Meeting of the Electrochemical Society, May 2016 in San Diego and documented into a ECS paper [247].

Reported LOD with this "classical" UME setup lies around 10^{-9} - 10^{-10} M [77]. It is clearly not low enough to detect miRNAs in basal concentrations and to challenge RT-PCR with its below 10^{-18} M LOD (See Chapter 1 Section 1.5.1). This is where microfluidics comes in.

The association between an UME and microfluidics provides a good temporal and spatial resolution as well as a confined environment effect increasing the local concentration. A microfluidic setup implies the use of microfabrication techniques and clean room facilities. The electrodes will be design using optical lithography which will ensure that the UME will be manufacture in a well-controlled system with a perfect reproducibility. Minute sample volumes decreasing costs and reduced contamination are valid advantages for a microfluidic setup.

In the following section, the description of our microfluidic device and a comparison with the "classical" setup will be done in a Lab On Chip (HORNY, M.-C., LAZ-ERGES, Mathieu, SIAUGUE, J.-M., et al. Electrochemical DNA biosensors based on long-range electron transfer: investigating the efficiency of a fluidic channel micro-electrode compared to an ultramicroelectrode in a two-electrode setup. Lab on a Chip, 2016, vol. 16, no 22, p. 4373-4381.) article from the Royal Society Chemistry

Journal included.

To be thorough in the comparison, I used the same apparatus (Biologic potentiostat with low current module) for the setup outside and inside the microfluidic chip (measurements of Section 2.2 were reiterate using the potentiostat instead of the ammeter).

As opening for the LOC article, I am proposing a more detailed process for the microfluidic device fabrication and a Comsol modelling of the electrochemical process on a gold electrode in a microfluidic channel.

2.3 Detection using microfluidics

2.3.1 Microfluidic device

The microfluidic device (Figure 1C in the LOC article) was made in the clean room facilities of the Center of Nanosciences and Nanotechnologies (C2N, Marcoussis, France). The key steps of the microfabrication are sum up in Figure 2.11. To get more details on the fabrication techniques please refer to Appendix B.

All lithographic masks were designed using L-Edit software (Tanner EDA, Figure 2.12). The device was microfabricated by assembling an upper PDMS part with a microchannel and a lower part containing gold microelectrodes patterned on a glass substrate.

The electrodes were prepared on clean glass slides, cleaned in a piranha solution (H₂SO₄/H₂O₂, 1:1) and rinsed in water, acetone and then isopropanol and finally dried in N₂ gas. The AZ-5214 photoresist was spin-coated (30 s, 1000 rpm, 250 rpm s⁻¹) and baked for 90 s using a hot plate (125°C). Subsequently, the photoresist was exposed to UV light (10 mW, Süss MicroTec MJB4) baked for 90 s and flood for 30 s and developed for 45 s. Afterward, the slides were rinsed in water, and cleaned by using a reactive ion etching (RIE Nextral NE100, 180 s, 50% O₂, 10 W) to remove all resin residues. An evaporator (Pfeiffer Vacuum Classic 500) was used to deposit a 20 nm titanium layer for contact and 200 nm of gold followed by a classic lift-off process in acetone.

The PDMS channels were made from a channel master made of SU-8 on a Si wafer. The master was fabricated by applying photoresist SU8-2002 as adhesive layer (MicroChem Corp.) by using a spin-coater (30 s, 1500 rpm s⁻¹, 200 rpm s⁻²). After spin coating, the wafer was baked on a hot plate (65°C for 3 min, then 95°C for 5 min) and finally 2 h at 110°C.

Then a 16 μm thick layer of SU8-2050 was applied using a spin-coater (30 s, 3700 rpm s⁻¹, 200 rpm s⁻²). The photoresist was baked on a hot plate (65°C for 3 min, then 95°C for 5 min) exposed to UV light (25 s, 16.5 mW), developed using SU-8 developer for 120 s and baked on a hot plate (65°C for 2 min, then 95°C for 7 min).

The PDMS was fabricated by mixing silicon elastomer base and silicon elastomer curing agent in a 10:1 proportion. A 1 cm thick layer of PDMS is poured onto the SU-8 master mold to obtain a negative replica after degassing and curing the fluidic network at 70°C overnight. The channels were cut out with a scalpel and the holes for the inlets and outlet tube (0.75 mm diameter) were made by a hole punch.

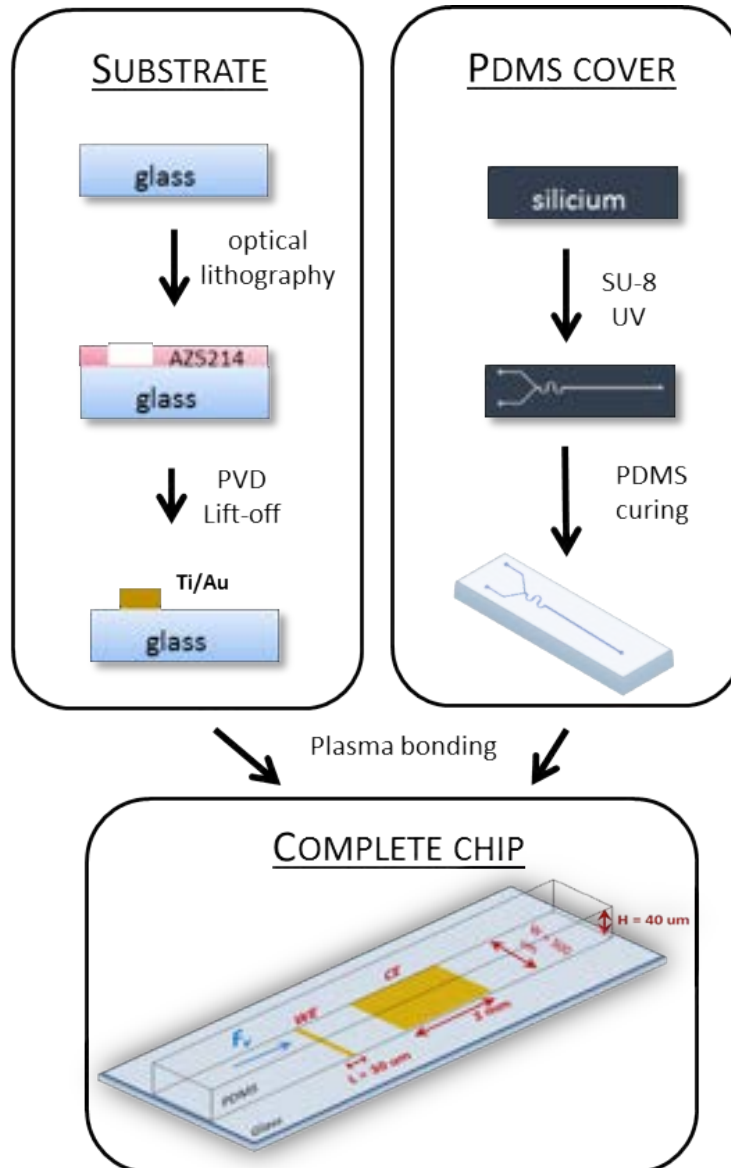


Figure 2.11: Microfabrication key steps: inverted optical lithography, Ti/Au metallization, PDMS fabrication and bonding.

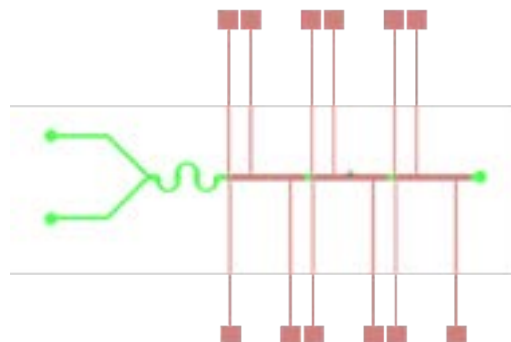


Figure 2.12: L-edit drawing of the channel mask (green) and the electrodes mask (red) at their rightful place.

The PDMS and the glass substrates with the electrodes are washed with isopropanol and dried with nitrogen. The electrode slides and the PDMS channel were mounted together by activating the PDMS and the glass surface with a plasma cleaner (Nanonex Ultra-100, 60 s, 100% O₂, 20 W) to favor adhesion. The manual alignment of the PDMS and electrodes is performed under binocular conditions for the correct electrode alignment on the microfluidic channel (see Figure 2.12). This was followed by a heat treatment step for 15 min (95°C). For the electrical connections to the electrochemical equipment either wires were soldered onto the gold electrodes either a home-made wafer carrier as drawn on Figure 2.13 was used. The cells produced have three sets of (WE, CE) couples.

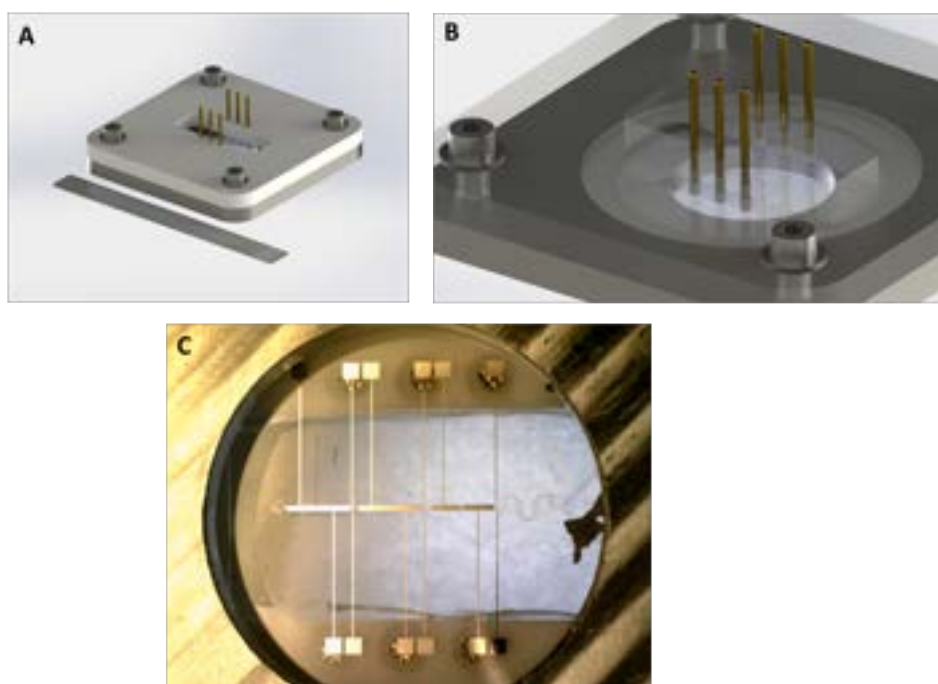


Figure 2.13: The home-made wafer carrier. **A.** Artistic global picture of the wafer carrier. **B.** Zoom on the contacts with the electrodes (artistic view). **C.** Picture of the electrodes and the channel inside the wafer carrier (bottom view).

2.3.2 Modeling with Comsol Multiphysics Finite Elements

By using the transport of diluted species module of Comsol Multiphysics modeling the hydrodynamical behavior of our sensor allows to get some current values and thickness of the diffusion layer. The model used is widely inspired from the work of Faure *et. al.* [248] and adapted for our geometry and material.

M_F is the mass flow density on the WE. That corresponds to the number of moles arriving on the WE per surface unit per time unit.

$$M_F = C_{ox} \cdot K_f - C_{red} \cdot K_b \quad (2.29)$$

$$K_f = k_{het} \cdot e^{\frac{\alpha a n F \eta}{R T}} \quad (2.30)$$

$$K_b = k_{het} \cdot e^{\frac{\alpha_c n F \eta}{R T}} \quad (2.31)$$

with, η , the surtension, k_{het} , the constant of standard rate of electron transfer (taken equal to 0.007 cm s^{-1}), α_a and α_c the anodic and cathodic charge transfer coefficients. The flow on WE are respectively, $-M_F$, for C_{red} and, $+M_F$, for C_{ox} . The current is calculated from the mentioned flows by integration on the surface. The flow on the counter electrode is the current divided by the surface of the counter electrode the Faraday constant, for C_{red} . For C_{ox} , the current is multiplied by (-1). The conditions inside the microchannel are the following:

- a convection along x axis due to the flow,
- a zero flow on all domains except on electrodes,
- an initial value of the concentrations C_{red} and C_{ox} on all domains,
- a flow of increasing value starting from static: $0.08, 0.2, 0.5 \mu\text{L s}^{-1}$,
- a 10 mV s^{-1} sweep rate.

The diffusion coefficients for Fe(III) and Fe(II) were respectively 6.0 and $5.7 \cdot 10^{-6} \text{ cm}^2 \text{ S}^{-1}$ [249]. And the mesh was chosen finer on the WE.

Figure 2.14 shows the concentration of redox species in the channel. At the inlet, concentration is maximal. In the vicinity of the electrode, oxidative specie is consumed (blue) by the WE and produced by the CE (green yellow orange). The trail is due to the flow that brings the species. The diffusion layer thickness (blue green) can be estimated and compared between a no flow situation and a $0.5 \mu\text{L s}^{-1}$ flow.

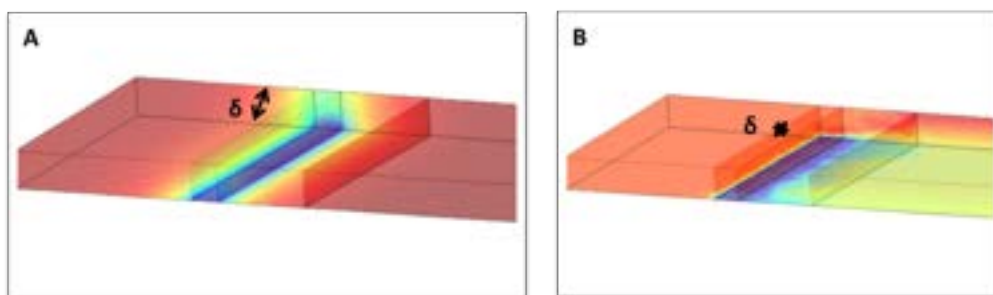


Figure 2.14: Simulated Fe(II) flow and display of diffusion layer. **A.** Static conditions (no flow). **B.** Dynamic conditions ($0.5 \mu\text{L s}^{-1}$ flow rate). The maximum (red) and minimum (blue) concentrations of Fe (II) corresponds to the minimum and maximum respective concentrations of Fe (III) with δ the thickness of the diffusion layer.

2.3.3 Transposing a gold UME on a microfluidic chip for DNA electrochemical hybridization detection in a two-electrode setup.

We chose to keep the article and present it in its integrity as its structure reflects with consistency the parallel between the classical and microfluidic setup, parallel we want to pinpoint in order to shine lights on the input of microfluidics. (i) the characterization of hydrodynamics, (ii) hybridization schemes, and (iii) the quantification of the number of targets reaching the sensor will be presented and discussed.



Cite this: DOI: 10.1039/c6lc00869k

Electrochemical DNA biosensors based on long-range electron transfer: investigating the efficiency of a fluidic channel microelectrode compared to an ultramicroelectrode in a two-electrode setup†

 M.-C. Horny,^{ad} M. Lazerges,^b J.-M. Siaugue,^c A. Pallandre,^d D. Rose,^a F. Bedioui,^b C. Deslouis,^a A.-M. Haghiri-Gosnet^d and J. Gamby^{*ad}

Here, we describe the transposition of an ultramicroelectrode (UME) setup into a microfluidic chip configuration for DNA biosensors. The hydrodynamic properties of the fluidic channel microelectrode were screened with an $[\text{Fe}(\text{III})(\text{CN})_6]^{3-}/[\text{Fe}(\text{II})(\text{CN})_6]^{4-}$ redox couple by cyclic voltammetry to provide a basis for further biological processes. A 23-base DNA probe was self-assembled into a monolayer on gold microelectrodes both in classical configuration and integrated in a microfluidic setup. Special interest was focused on the DNA target mimicking the liver-specific micro-ribonucleic acid 122 (miRNA122). Long-range electron transfer was chosen for transducing the hybridization. This direct transduction was indeed significantly enhanced after hybridization due to DNA-duplex π -stacking and the use of redox methylene blue as a DNA intercalator. Quantification of the target was deduced from the resulting electrical signal characterized by cyclic voltammetry. The limit of detection for DNA hybridization was 0.1 fM in stopped flow experiments, where it can reach 1 aM over a $0.5 \mu\text{L s}^{-1}$ flow rate, a value 10^4 -fold lower than the one measured with a conventional UME dipped into an electrolyte droplet under the same analytical conditions. An explanation was that forced convection drives more biomolecules to the area of detection even if a balance between the speed of collection and the number of biomolecules collected has been found. The latter point is discussed here along with an attempt to explain why the sensor has reached such an unexpected value for the limit of detection.

 Received 8th July 2016,
Accepted 22nd September 2016

DOI: 10.1039/c6lc00869k

www.rsc.org/loc

1. Introduction

A key consideration for biosensors is the limit of detection imposed by the molecular level changes in the expression of biomolecules to be able to perform reliable diagnostics before symptoms of a disease appear. In the context of a new genera-

tion of cheap and portable biosensors, biomolecules present *in vivo* at physiological levels have to be detected quickly while maintaining high specificity.

In recent years, research studies have focused on micro-ribonucleic acids (miRNAs) as they have been detected in serum and plasma of humans at stable and reproducible levels.¹ Indeed, being specific regulators of gene expression under baseline conditions, miRNAs have more pronounced functions in case of stress or disease, decreasing or increasing their levels in serum and plasma,² thus opening the possibility of using miRNAs as diagnostic biomarkers of various diseases.^{3–5} They have also been shown to allow precise differentiation and classification of cancers.^{6,7} For instance, miRNA122 is only produced by liver cells in case of injury (hepatitis, alcoholism, obesity).⁸ Commonly, miRNA detection studies use real-time PCR (polymerase chain reaction).⁹ Although PCR is a powerful technique, it has limitations due to protocol times, cost, accurate quantification, and the need for complete fine tuning of the temperature during multiple

^a Sorbonne Universités, UPMC Univ Paris 06, CNRS, Laboratoire Interfaces et Systèmes Electrochimiques, 4 place Jussieu, F-75005, Paris, France.

E-mail: Jean.gamby@lpn.cnrs.fr

^b UTCBS, U 1022 INSERM, UMR 8258 CNRS, Paris Sciences Lettres University, Ecole Nationale Supérieure de Chimie de Paris, 11 rue Pierre et Marie Curie, 75005 Paris, France; Sorbonne Paris Cité, Université Paris Descartes, Faculté de Pharmacie de Paris, 4 avenue de l'observatoire, 75006 Paris, France

^c Sorbonne Universités, UPMC Univ Paris 06, CNRS, UMR 8234, Laboratoire Physico-chimie des Electrolytes et Nanosystèmes Interfaciaux (PHENIX), 4 place Jussieu, F-75005, Paris, France

^d Centre de Nanosciences et de Nanotechnologies, CNRS, Univ. Paris-Sud, Université Paris-Saclay, C2N – Marcoussis, 91460 Marcoussis, France

† Electronic supplementary information (ESI) available. See DOI: 10.1039/c6lc00869k



stages of hybridization/denaturation; thus it still requires further development to improve its robustness.^{2,8,10}

DNA hybridization is more and more chosen as the most prized method compared to direct sequencing due to a better understanding of the long range electron transfer mechanism through DNA duplex π -stacking.¹¹ The electronic coupling within its inner core of a stacked array of heterocyclic aromatic base pairs is very sensitive to local disruptions such as mismatches, making a DNA biosensor particularly sequence specific. In a DNA biosensor, the target sequence is recognized by a complementary DNA probe and hybridized. The hybridization of two basis according to Watson and Crick's rules¹² is converted into an electrical signal.

In order to be efficient, three key steps have to be controlled in a DNA biochip: (i) probe immobilization on a solid substrate, (ii) hybridization (or recognition) of the complementary target strand and (iii) conversion of the hybridization event into a physical signal (*i.e.* transduction). The strategies to achieve probe immobilization, target recognition and detection are numerous. A plethora of biosensors can be found in the literature, which differ in the biological process followed, the choice of transduction exploited, and the electrode material used. The literature has a significant number of papers that classify and compare different kinds of biosensors. In the domain of probes grafted on a solid substrate for direct hybridization with an unlabelled DNA target by using electrochemical transduction, a wide range of concentrations are reported in the literature from femtomolar to attomolar and even zettomolar concentrations. For instance, Riccardi *et al.*¹³ achieved a 2×10^{-16} M limit of detection by monitoring the changes in oxidation of gold polypyrrole due to DNA hybridization. Differential pulse voltammetry (DPV) was used for direct DNA oxidation on a conducting polymer leading to 10^{-17} M (ref. 14) and 10^{-15} M limits of detection with genomic DNA on polydeoxycytidine.¹⁵ Non-faradic biosensors coupled with impedance techniques for screening the interface charge density have reached a 10^{-18} M limit of detection on GaN nanowires¹⁶ and a 10^{-20} M limit of detection on boron-doped diamond with a polyethyleneimine layer.¹⁷ Chen *et al.*¹⁰ have reported a 10^{-16} M limit of detection with their nanogap sensor with sandwich arrays of gold/SiO₂/gold using long-range electron transfer toward the redox indicator.

In this work, a traditional two-electrode configuration setup comprising a gold ultramicroelectrode (UME) and a large counterelectrode inspired by the work of Lazerges *et al.*¹⁸ is compared to its counterpart integrated into a microfluidic system. The combined use of a microband electrode and a fluidic channel termed a channel microelectrode offers (i) the obtention of a fast steady state current response (around one millisecond) due to a very thin diffusion layer compared to the convection layer and (ii) a way to drastically improve the efficiency of the sensor in terms of the volume of the analytes and system dynamics with easy manipulation of samples.^{19–25} These aims are achieved by the use of an [Fe(III)(CN)₆]³⁻/[Fe(II)(CN)₆]⁴⁻ redox couple in a chan-

nel microelectrode during the immobilization and hybridization steps in order to set an equilibrium potential at 0 V as both microelectrodes are in gold. DNA hybridization is followed by cyclic voltammetry (CV) with the redox couple allowing surface property analysis, such as surface modification, when binding events of target DNA occur on the sensor surface. The selectivity of the electrochemical DNA biosensor using an UME was already verified in a previous study using the same protocol scheme where a double-stranded DNA (miR122) had a single mismatch in the sequence.²⁶

2. Materials and methods

2.1. Chemicals

Sodium chloride (NormaPur), methylene blue (Alfa Aesar), potassium ferricyanide(III), and potassium hexacyanoferrate(II) (Sigma-Aldrich) were used in the experiments without further purification. The thiol-labeled DNA probe (P) and complementary target (T) were purchased from Integrated DNA Technologies (Belgium). Their sequences are shown in Table 1. The target DNA used mimics the fragment of interest miRNA-122 for the diagnosis of liver cells in case of injury (hepatitis, alcoholism, obesity).

2.2. Microfluidic chip fabrication

All lithographic masks were designed using L-Edit software (Tanner EDA). The device was microfabricated by assembling an upper PDMS part with a microchannel and a lower part containing gold microelectrodes patterned on a glass substrate. Glass substrates were cleaned with a piranha solution (H₂SO₄/H₂O₂, 1:1) prior to use. The glass slides were then spin-coated with AZ5214 resin followed by inverted lithography on an MJB4 aligner. Substrates were then cleaned by a reactive ion etching (RIE) process to remove all resin residues and then metallized with a 200 nm layer of gold on top of a 20 nm titanium layer followed by a classic lift-off process.

The fluidic circuit is obtained from a master mold made of SU-8. Fabrication of the mold starts with the cleaning of the silicon wafer and lithography of a 16 μ m thick layer of SU-8. A 1 cm thick layer of PDMS is poured onto the SU-8 master mold to obtain a negative replica after curing the fluidic network at 70 °C overnight. The PDMS and the glass substrates with the electrodes are washed with isopropanol and dried with nitrogen. Then, the PDMS part is treated with nitrogen plasma to favor the adhesion of the PDMS onto the glass slide. The manual alignment of the PDMS and electrodes is performed under binocular conditions for the correct electrode alignment on the microfluidic channel (see Fig. 1C).

Table 1 Thiol-labeled DNA probe (P) and target (T) sequences

| Name | Sequence |
|------|--|
| P | 5'-thiol C6-CAA ACA CCA TTG TCA CAC TGC-3' |
| T | 5'-GCA GTG TGA CAA TGG TGT TTG-3' |



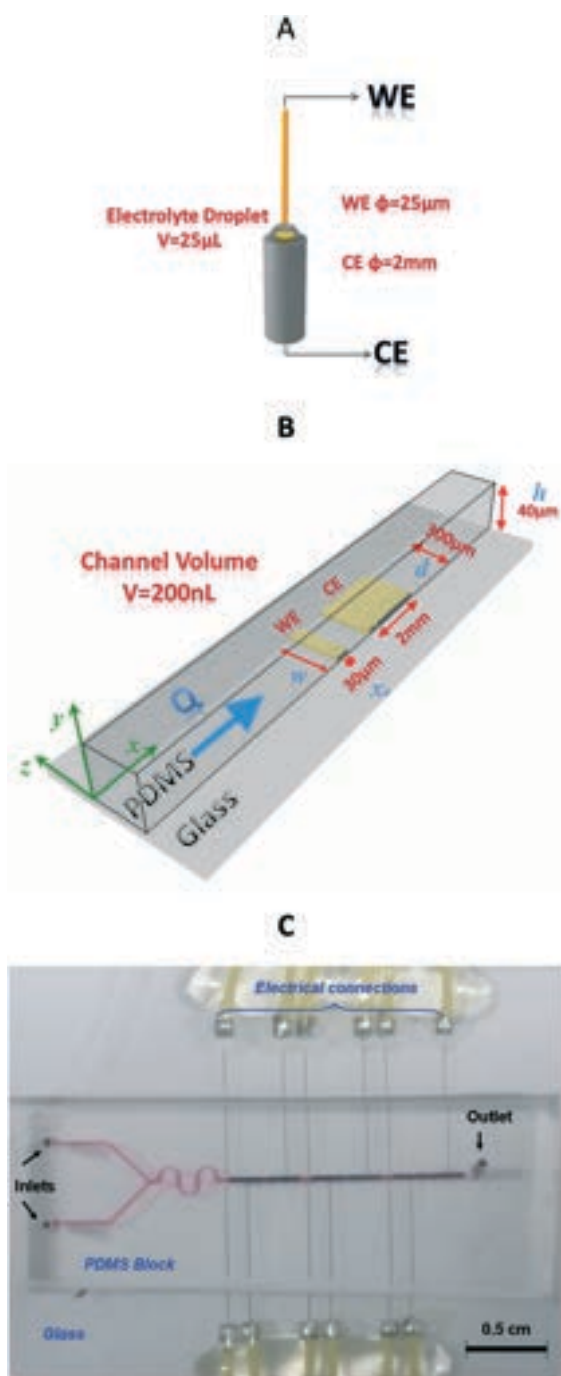


Fig. 1 Schematic representations (not to scale). A. Conventional working UME ($\phi = 25 \mu\text{m}$) dipped into $\text{Fe}^{\text{II}}/\text{Fe}^{\text{III}}$ and methylene blue (MB) electrolyte on top of the counterelectrode ($\phi = 2 \text{ mm}$). B. Microchannel electrode configuration. Detection area and fluidic channel microelectrodes with their dimensions. WE stands for working electrode (width, $w = 300 \mu\text{m}$, length $x_e = 30 \mu\text{m}$), CE stands for counterelectrode ($w = 300 \mu\text{m}$, $x_e = 2 \text{ mm}$), and h and d represent the fluidic channel height and width, respectively. Note that here $w = d$. C. Global picture of the microfluidic device comprising several pairs of two-microelectrode networks for multi-detection possibility. The fluidic microchannel (filled with a red colour dye) with two inlets allows the injection of the sample and the redox couple.

2.3. Ultra-microelectrode fabrication

The $25 \mu\text{m}$ ultra-microelectrode (UME) was home-made using 99.99% pure Goodfellow gold wire sealed in glass capillaries. The counterelectrode was a 2 mm diameter gold wire sealed in a Teflon cylinder (Metronic, France). The gold UME was polished with $3 \mu\text{m}$ silicon carbide disks and rinsed with de-ionized water.

2.4. Probe immobilization and target hybridization

The DNA probe immobilization was performed by incubating the UME electrode for two hours in a $500 \mu\text{L}$ volume of $10 \mu\text{g mL}^{-1}$ DNA probe diluted in 0.5 M NaCl. Then the UME electrode was rinsed with deionized water. Between probe immobilization and target recognition, the UME is in contact for 30 minutes with 0.5 M NaCl to test the stability of the self-assembled monolayer (SAM). Target hybridization was performed in a $500 \mu\text{L}$ solution of DNA target of decreasing concentration in 0.5 M NaCl solution for 30 minutes followed by rinsing with 0.5 M NaCl solution. An $[\text{Fe}(\text{III})(\text{CN})_6]^{3-}/[\text{Fe}(\text{II})(\text{CN})_6]^{4-}$ redox couple and a methylene blue (MB) redox catalyst were added to a 0.5 M NaCl solution for electrochemical detection.

ss-DNA probe immobilization in a microfluidic chip was performed by circulating a $0.15 \mu\text{M}$ DNA probe in 0.5 M NaCl and then stopping the flow for two hours. The flushing and the test of stability of the SAM are the same as for the UME. High frequency electric impedance spectroscopy (HFEIS) measurements were performed to estimate the probe density (see the ESI†). A value of $1.1 \times 10^{-11} \text{ mol cm}^{-2}$ SAM coverage was found to roughly match the $4.47 \times 10^{-10} \text{ mol cm}^{-2}$ experimental value found for close-packed short-thiol SAM on gold by Rouhana *et al.*²⁷

Hybridization was performed under various flow conditions with samples of target DNA of increasing concentrations in 0.5 M NaCl for 30 minutes.

2.5. Electrochemical detection

For the electrochemical measurement, the UME was immersed in a $25 \mu\text{L}$ electrolyte drop, while for the microfluidic chip, a flow of $0.2 \mu\text{L s}^{-1}$ was selected.

Cyclic voltammetry was performed using the two-electrode setup displayed in Fig. 1A. For simplicity, this design will be called the conventional UME setup (Fig. 1A) in contrast to the microfluidic setup (Fig. 1B and C).

Please note that the thiol-gold bond is formed spontaneously on the surface of both the WE and CE, and thus both electrodes are functionalized with ss-DNA probes. However, for several reasons, the measured current at each step (bare gold, ss-DNA immobilization or ds-DNA hybridization) will be mainly attributed to the WE current response (see Fig. 2). First, the CE was intentionally positioned after the WE (*vs.* flow), in order to favour DNA-probe immobilization and then DNA-target hybridization on the WE. Second, as the counterelectrode ($6 \times 10^{-3} \text{ cm}^2$ surface area) in the fluidic channel is about 66-fold larger than that of the working microelectrode ($9 \times 10^{-5} \text{ cm}^2$), it can be considered as a pseudo reference



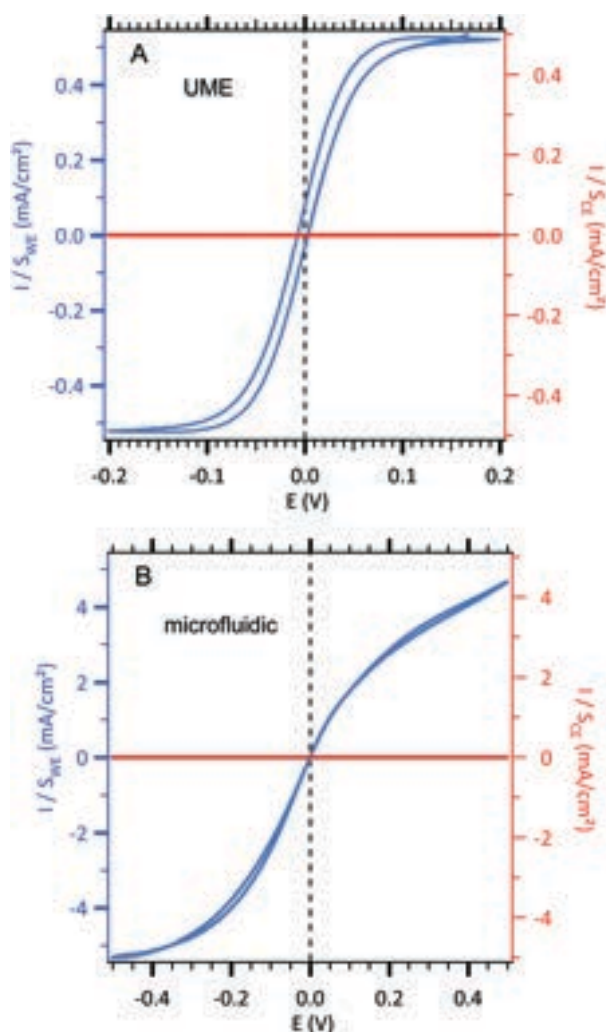


Fig. 2 Sigmoidal voltammograms of an equimolar solution of 3 mM $[\text{Fe}(\text{III})(\text{CN})_6]^{3-}/[\text{Fe}(\text{II})(\text{CN})_6]^{4-}$ and 0.5 M NaCl centred at zero potential with the two configurations (see Fig. 1). The current densities of the working electrode (WE, left axis in blue) and the counterelectrode (CE, right axis in red) are normalized according to each electrode area. (A) Conventional UME set-up as illustrated in Fig. 1A. Cyclic voltammetric response of an UME as a WE electrode using 10 mV s^{-1} as the scan rate. (B) Microfluidic setup as illustrated in Fig. 1B. Cyclic voltammetric response of a WE microband electrode using $0.05 \mu\text{L s}^{-1}$ as the fixed value of the flow rate and 10 mV s^{-1} as the scan rate.

since its current density variation is lower compared to that of the working microelectrode.

2.6. Apparatus

Cyclic voltammetry measurements were performed using EC-lab software from Biologic SP-300 electrochemical station. Both setups have a two electrode configuration. The scan rate was set to 10 mV s^{-1} for the microfluidic setup to obtain quasi-identical forward and backward waves. For the conventional configuration, a scan rate of 25 mV s^{-1} was selected.

High frequency electric impedance spectroscopy (HFEIS) measurements were performed by coupling a frequency re-

sponse analyser (Solartron FRA 1255B) with a dielectric interface (Solartron DI 1296A) to the apparatus. The frequency range used for measurements was varied from 1 MHz to 0.1 Hz. The sinusoidal AC signal excitation between microelectrodes is set to 100 mV peak to peak, since DC was fixed at 0 V.

The microfluidic setup was connected to a programmable syringe pump allowing a flow rate in the range from $0.01 \mu\text{L s}^{-1}$ to $5 \mu\text{L s}^{-1}$.

3. Results and discussion

3.1. Hydrodynamic conditions in the microfluidic channel and mass transport to the microelectrode

The high aspect ratio (d/h) of the fluidic channel (h and d are the height and width of the channel, respectively) ensures a quasi one-dimensional Poiseuille flow. The only velocity component is v_x in the flow direction, which depends on y , the coordinate orthogonal to the two parallel planes with a well-known developed parabolic profile, as follows:

$$v_x = \frac{1}{2\mu} \frac{\partial p}{\partial x} \left(\frac{h^2}{4} - y^2 \right) \quad (1)$$

where y varies between $-h/2$ and $+h/2$, $\partial p/\partial x$ is the pressure gradient along the flow direction, and μ is the dynamic viscosity.

One can define the volumetric flow rate Q as follows:

$$Q = d \int_{-h/2}^{+h/2} v_x dy = \frac{d}{2\mu} \frac{\partial p}{\partial x} \frac{h^3}{6} \quad (2)$$

and the wall velocity gradient S as follows:

$$S = \left. \frac{\partial v_x}{\partial y} \right|_{y = \pm h/2} = \frac{1}{\mu} \frac{\partial p}{\partial x} \frac{h}{2} \quad (3)$$

This results in the following relation between Q and S :

$$Q = \frac{h^2 d S}{6} \quad (4)$$

The concentration distribution of a solute obeys the mass transport equation:

$$\frac{\partial c}{\partial t} + \mathbf{v} \cdot \nabla c = D \Delta c \quad (5)$$

The diffusion-convection term is reduced to $v_x \frac{\partial c}{\partial x}$ and the diffusion term to $\frac{\partial^2 c}{\partial y^2}$.

The solution of eqn (4) when the electrode acts as an ideal mass sink is obtained with the boundary conditions $c = 0$ on the electrode and $\partial c/\partial y = 0$ on the insulating areas.



Given these conditions, L. P. Reiss and T. J. Hanratty²⁸ have predicted the limiting diffusion current to a thin rectangular microelectrode of width w and length x_e placed cross-wise to the flow direction:

$$I_{\text{lim}} = 0.807nFc_{\infty}D^{2/3}x_e^{2/3}wS^{1/3} \quad (6)$$

where n is the number of electrons exchanged, F is the Faraday constant (96485 C mol^{-1}), c_{∞} is the concentration of electroactive species (mol cm^{-3}) and D is the diffusion coefficient of the electroactive species ($\text{cm}^2 \text{ s}^{-1}$). x_e , w , h and d are the dimensions (μm) shown in Fig. 1B.

Eqn (6) implies that the diffusion layer thickness is small enough with respect to h so that v_x within is approached by its linear approximation, as follows:

$$v_x = v_x(y=0) + y\left(\frac{\partial v_x}{\partial y}\right)_y=0} + \dots = y\left(\frac{\partial v_x}{\partial y}\right)_y=0} \approx y \cdot S \quad (7)$$

For consistency, y is taken here as a local orthogonal coordinate from the wall (*i.e.* y and v_x are null at the wall).

Compton²⁹ has proposed an equivalent expression as a function of the volumetric flow rate (see eqn (1)):

$$I_{\text{lim}} = 0.925nF c_{\infty} D^{2/3} x_e^{2/3} w \left(\frac{4Q}{h^3 d}\right)^{1/3} \quad (8)$$

Note that here $w = d$.

Therefore, for both eqn (6) and (8) to be valid, it is required that the diffusion layer which develops from the leading edge of the microelectrode (*i.e.* for $x = 0$) remains very small at its leaving edge, *i.e.* for $x = x_e$.

The local diffusion layer thickness is defined as follows:^{30,31}

$$\delta_x = 3^{1/3} \Gamma(4/3) \left[\frac{Dx}{S} \right]^{3/4} \quad (9)$$

where Γ , the Gamma function, is the factorial function.

In Nernst layer approximation and using Fick's law, eqn (6) or (8) can be obtained from eqn (9) by a straightforward integration.

Therefore, from eqn (9) and (4), one can also check whether the used microelectrode fulfills the condition of a sufficiently small diffusion layer thickness at $x = x_e$.

As an example, for $Q = 10^{-3} \text{ cm}^3 \text{ s}^{-1}$ corresponding to the higher imposed volumetric flow rate, and with $D = 10^{-5} \text{ cm}^2 \text{ s}^{-1}$, $x_e = 30 \mu\text{m}$, $h = 40 \mu\text{m}$ and $d = 300 \mu\text{m}$, one obtains $\delta_{x_e} \sim 2.5 \mu\text{m}$.

This value corroborates the above assumption of a linear velocity profile within the diffusion layer. For much lower Q values, this assumption could not be justified.

In a first step, a test experiment was conducted with a fast redox system. To this end, an equimolar solution of 3 mM $[\text{Fe}(\text{m})(\text{CN})_6]^{3-}/[\text{Fe}(\text{n})(\text{CN})_6]^{4-}$ and 0.5 M NaCl was introduced into our designed microchip flow channel containing the

two-microelectrode setup under laminar flow conditions. The results are displayed in Fig. 2.

Sigmoid shape voltammograms are observed as expected for a laminar flow. They are centred at zero potential. Indeed, in this two-electrode setup, the working electrode and the counterelectrode are made from the same metal and are immersed in the same electrolyte containing the redox couple. Indeed, the 2 mm gold counterelectrode (very high area compared to the 30 μm gold working electrode) can be considered as a pseudo-reference electrode allowing a feeble potential drift during measurements.

In order to compare the currents from the conventional setup and the microfluidic setup, the obtained current curves, I_{WE} , were normalized with the surface of each working electrode ($S_{\text{conventional}} = 1.96 \times 10^{-5} \text{ cm}^2$ and $S_{\text{microfluidic}} = 9.0 \times 10^{-5} \text{ cm}^2$) resulting in a comparable current density, J_{WE} , at a given potential (in mA cm^{-2}) as shown in Fig. 2. Moreover, in each configuration, the current density, J_{WE} , on the working electrode is compared to the one on each counterelectrode, J_{CE} , which is negligible. The scan rate was optimized at 10 mV s^{-1} to obtain a steady state current response and to minimize the gap between the forward and backward current curves. Moreover, the qualitative difference in the fluidic voltammogram (non-symmetric), where the reduction current is slightly higher than the oxidation current, is due to the difference between the diffusion coefficients of $[\text{Fe}(\text{m})(\text{CN})_6]^{3-}$ ($D = 6.6 \times 10^{-6} \text{ cm}^2 \text{ s}^{-1}$) and $[\text{Fe}(\text{n})(\text{CN})_6]^{4-}$ ($D = 5.6 \times 10^{-6} \text{ cm}^2 \text{ s}^{-1}$) in NaCl as supporting electrolytes. For instance, the theoretical ratio between the diffusion coefficients ($(D_{\text{Fe}(\text{m})}/D_{\text{Fe}(\text{n})})^{2/3}$) is equal to 1.12 that is close enough to the 1.15 experimental ratio between the limiting current in reduction ($I_{\text{lim,reduction}}$ at -0.4 V) and the limiting current in oxidation ($I_{\text{lim,oxidation}}$ at $+0.4 \text{ V}$) according to eqn (6).

To analyse the hydrodynamics in the fluidic channel microelectrode, a flow rate of increasing value was imposed. The results are shown in Fig. 3. The limiting current plateau is flow dependent as the diffusion layer near the microelectrode is controlled by the forced convection. While the voltammogram of the UME (Fig. 2A) shows the expected S-shape, the one corresponding to the fluidic channel microelectrode (Fig. 2B) indicates an apparent more sluggish reaction. The cathodic plateau current for example is attained below -0.4 V , whereas this is achieved at -0.1 V for the UME. The more plausible explanation is the larger value of the ohmic drop between the WE and CE in the fluidic channel. High frequency electric impedance spectroscopy (HFEIS)³² measurements were performed to estimate the ohmic resistance (see eqn S2 in the ESI†).

In Fig. 4, the intensity of the reduction plateau current that has been normalized with eqn (6) is plotted against the volumetric flow rate, $(Q)^{1/3}$. It can be observed that the deviation with respect to the value given by eqn (6) in the low flow rate range is significant. A similar behaviour was observed by Ordeig *et al.*³³ in their simulation with a gold microelectrode. They ascribed this low flow rate behaviour to the effect of



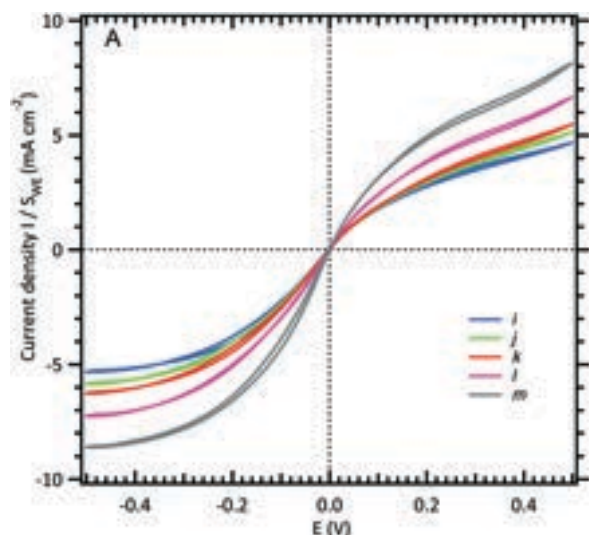


Fig. 3 Limiting current intensity response of a WE microchannel electrode vs. volumetric flow rates (see Fig. 1B). The channel is filled with an equimolar solution of 3 mM $[\text{Fe}(\text{III})(\text{CN})_6]^{3-}/[\text{Fe}(\text{II})(\text{CN})_6]^{4-}$ and 0.5 M NaCl. The scan rate is fixed at 10 mV s^{-1} , and five flow rates are shown here: (i) 0.05, (j) 0.08, (k) 0.1, (l) 0.2, and (m) $0.5 \mu\text{L s}^{-1}$.

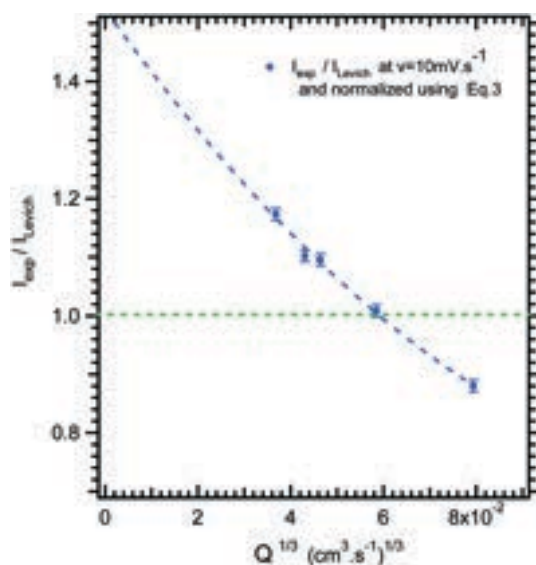


Fig. 4 Limiting current ratio between experimental current, I_{exp} , and Levich equation current, I_{Levich} , as a function of the $1/3$ volumetric flow rate for the microfluidic setup.

edge diffusion at the microelectrodes and channel wall effects which were not taken into account in eqn (6) or (8) at lower flow rates.

3.2. DNA hybridization protocol with the conventional UME

Thiols adsorb on gold substrates building self-assembled monolayers (SAMs) according to eqn (10).²¹



The use of thiol micromolar concentrations minimizes the contributions of any added impurities to the adsorption kinetics²¹ onto which reproducibility and stability of the measurements are critically dependent. Moreover, with a micromolar concentration, a full monolayer is built within two hours.²⁷ A value of $1.1 \times 10^{-11} \text{ mol cm}^{-2}$ SAM coverage was found (see the ESI†). DNA hybridization detection is based on long range electron transfer through the DNA double strand *via* π -stacking as described previously. The $[\text{Fe}(\text{III})(\text{CN})_6]^{3-}/[\text{Fe}(\text{II})(\text{CN})_6]^{4-}$ redox couple was used to discriminate a single strand DNA immobilized from a double strand hybridized. Indeed, DNA is wrapped within a negatively charged sugar phosphate backbone which prevents diffusion of the also negatively charged redox complex inside the SAM. However, the current density before hybridization (red curve, Fig. 5A) is not zero probably due to edge effects and holes in the SAM. After hybridization (blue curve, Fig. 5B), the current-voltage slope is steeper indicating that hybridization occurred. The DNA hybridization response sensitivity was obtained with the use of a MB redox intercalator. In brief, methylene blue (MB) is used as both a redox catalyst and a DNA-duplex organic intercalator having an affinity constant of 10^6 M^{-1} . The MB reduction step is reversible with a redox potential of 0 (vs. NHE) that is lower than that of $[\text{Fe}(\text{III})(\text{CN})_6]^{3-}$ reduction. The electrons jump from the gold electrode to the intercalated MB and are then accepted by the ferrocyanate in solution. The MB oxidized form is

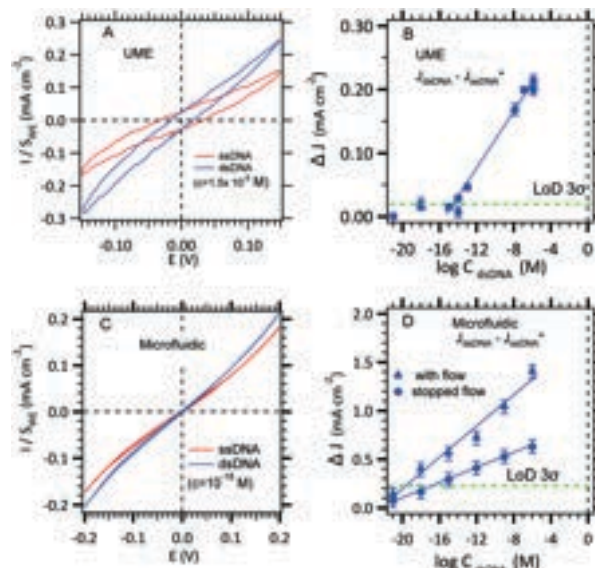


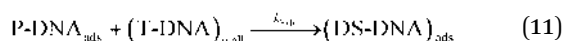
Fig. 5 Effect of hybridization on cyclic voltammetry current with the two configurations. A. Two electrodes in the UME configuration where the kinetic current on a $25 \mu\text{m}$ diameter microelectrode is obtained for $\text{Fe}(\text{II})/\text{Fe}(\text{III})$ (3 mM) MB (10^{-8} M) in 0.5 M NaCl in the absence and in the presence of a DNA target. B. LOD determination using the conventional UME set-up (see Fig. 1A) recorded at -0.1 V (see panel A). C. Effect of increasing hybridization target concentrations on the microchannel electrode sensor for a working flow rate of $0.5 \mu\text{L s}^{-1}$. D. LOD determination using the microfluidic set-up (see Fig. 1C) with several pairs of microelectrodes (blue circles) recorded at -0.2 V (see panel C).



regenerated for a further electrochemical reduction. The LOD determination and standard deviation on measurements will be discussed in section 3.3.1.

3.3. Hybridization detection in the microfluidic setup

3.3.1. Modelling and theoretical calculations. In order to clarify the mass transport competition between convection diffusion and reaction kinetics, the rules of thumb established by Squires *et al.*³⁴ from Newman's works³⁵ were revealed to be very useful in parallel with Comsol Multiphysics modelling. The description of hybridization reaction relies on a simple chemical kinetics: DNA targets (T) can hybridize on DNA probes (P) immobilized on the gold surface according to eqn (11).



The hybridization rate is expressed as follows:

$$r_{\text{hyb}} = k_{\text{hyb}} \Gamma_{\text{P}} [T]_0 \quad (12)$$

where $[T]_0$ and Γ_{P} (b_{m}/Na) are the concentration of T-DNA at the wall and the surface concentration of P-DNA on the sensor.

As shown in eqn (11) and (12), the partial order of reaction for each reactant is one and the global order is two. As a consequence, the observed hybridization rate, r_{obs} , between T-DNA and P-DNA can be viewed as a second order reaction, with r_{obs} in M s^{-1} and k_{obs} in $\text{M}^{-1} \text{s}^{-1}$ representing the observed hybridization kinetic rate constant.

We consider, from time $t = 0$, the concentration of T at the wall which is lower than the concentration of T in the bulk, *i.e.* $0 < [T]_0 \leq [T]_{\text{bulk}}$, because the hybridization reaction is considered as slow. However, at infinite time t_{∞} (*i.e.* 30 minutes at least for the hybridization time step in our experiments), the concentration at the wall tends to the bulk concentration, $[T]_0 = [T]_{\text{bulk}}$, and because any P was hybridized ($\Gamma_{\text{P}}=0$), the hybridization rate tends to zero.

As a consequence, the concentration of DS at infinite time, $[DS]_{t=\infty}$, is equal to the initial concentration of ($\Gamma_{\text{P}})_{t=0}$, and then the measured current corresponding to the hybridization step at infinite time becomes proportional to the initial concentration, $(i)_{t=\infty} \propto (\Gamma_{\text{P}})_{t=0}$.

The dehybridization rate of DS, r_{des} , is proportional with the double stranded DNA concentration and it is considered as a zero order reaction since the amount of the adsorbed DS-DNA on the gold microelectrode can be considered as unchanged:

$$r_{\text{des}} = k_{\text{des}} \quad (13)$$

with k_{des} in M s^{-1} representing the dehybridization kinetic rate constant.

As a consequence, the ratio ($k_{\text{des}}/k_{\text{hyb}}$) is defined as the equilibrium dissociation constant, K_{D} , which is given in M.

We also consider that the dehybridization rate is negligible in comparison with the hybridization rate, as follows:

$$r_{\text{des}} \ll r_{\text{hyb}} \quad (14)$$

The transport of target T is described in the analyte stream according to eqn (5) with the obtained value for the diffusion coefficient of T-DNA being around $10^{-11} \text{ m}^2 \text{ s}^{-1}$ which is much lower than that of the redox probe, that is in accordance with an expected thin diffusion layer ($D_{\text{T-DNA}} \ll D_{\text{Fe(m)}}$).

The flow entrance on the sensor is described as a radial velocity vector. At the outlet, the outflow condition used is given as follows:

$$n \cdot (-D\nabla C) = 0 \quad (15)$$

The hybridization of target DNA at the functionalized surface gives rise to a net flux at the corresponding boundaries as follows:

$$N_{\text{T}} = -r_{\text{hyb}} + r_{\text{des}} = -r_{\text{hyb}} \quad (16)$$

The hybridization rate depends on the target concentration in the stream and it was taken into account in numerical calculations where two Comsol Multiphysics modules were coupled (surface reaction and transport of diluted species). In other words, hybridization of targets on the probe creates a concentration gradient which permits the diffusion of species to the surface. Indeed, diffusion dominates near the sensor while convection predominates further. The analytical resolution of this problem gives a diffusion layer thickness for $x = x_{\text{e}}$ that varies with the flow rate using eqn (9) and (4) as follows.

The calculation reveals that the depletion zone is thinner than the sensor surface, as follows:

$$\delta_{\text{x}} = 3^{2/3} \Gamma \left(\frac{4}{3} \right) \left[\frac{D_{\text{N}} b^2 d}{6Q} \right]^{1/3} \quad (17)$$

As listed in Table 2, the δ_{x} value corresponding to each imposed volumetric flow rate can be deduced.

Finally, the flow through the depletion zone can be approximated as follows:

$$J_{\text{D}} = -D\nabla C \approx \frac{Dc_{\text{N}}}{\delta_{\text{x}}} \cdot x_{\text{e}} \cdot w \quad (18)$$

An example of calculation is tested below for 10 fM as initial concentration, $0.2 \mu\text{L s}^{-1}$ as flow rate, a binding-site density, b_{m} , equal to $6.7 \times 10^{12} \text{ sites cm}^{-2}$ calculated from the value of SAM's coverage given in section 3.2 and, the equilibrium dissociation constant of DNA at room temperature that is taken equal to $K_{\text{D}} = k_{\text{off}}/k_{\text{on}} = 10^{-11} \text{ M}$.³⁶ Consequently, one can estimate that 4.1 molecules per second will reach the



sensor surface at this working concentration and this flow rate. In other words, 0.24 seconds between binding events can be estimated. As the dehybridization rate constant was supposedly negligible due to the strongly bound DNA duplex at room temperature,³⁷ the expected number of target molecules to be bound to the sensor is given by eqn (19).

$$N_B = J_D \cdot t \quad (19)$$

with t being the hybridization time step.

By taking into account these data, a number of molecules (7.6×10^3) can be estimated during a hybridization time step of 30 minutes. Moreover, the target molecules collected are only those in the thin diffusion layer. The goal is to select an accurate flow in our device configuration that will allow a sufficient number of DNA targets to be captured and sensed in 30 minutes reaction time. Although taller channels enable faster flows and quicker measurements, they reduce the relative fraction of biomolecules collected and thus increase the volume of reaction (V) needed. It is obvious that the detection limit imposed by the sensor is related to the local concentration at which one molecule will be bound to the sensor. To this aim, the theoretical number of targets for different initial concentrations and various flow rates are calculated and then listed in Table 2.

As shown in Table 2, it is necessary to strike a balance between a slow flow where all target molecules could be collected and a fast flow where target molecules are swept away before they can enter the diffusion layer and be collected. It is obvious that a fast flow increases the volume of solution discarded which is a disadvantage when expensive biological samples are used. Another reason for the choice of an intermediary flow rate is that the SAM on gold (thiol-Au) is a fragile system. Indeed, the risk of SAM degradation could increase and distort the probe current measurement. As a consequence, for the next experiments, a flow rate of $0.5 \mu\text{L s}^{-1}$ was selected because it discards less than 1 mL of solution with an expected theoretical LOD between 1×10^{-18} and 1×10^{-16} M.

3.3.2. Experimental LODs and comparison. According to the previous calculation, hybridization run experiments were performed for an optimized flow rate of $0.5 \mu\text{L s}^{-1}$. The immobilized SAM of single-stranded DNA results in a low current level (red line, Fig. 5C) for which the slope increased with the working concentration of its complementary strand

Table 2 Theoretical estimation of the number of targets bound to the sensor (N_B), volume of solution (V) discarded, and thickness of the diffusion layer (δ_x) for various flow rates (Q) and initial concentrations (C_0)

| Q ($\mu\text{L s}^{-1}$) | δ_x (μm) | V (μL) | N_B (number of targets) | | |
|---------------------------------|---------------------------------|--------------------------|---------------------------|-------------------|--------------|
| | | | 10^{-14} M | 10^{-16} M | 10^{-18} M |
| Static | 31.2 | 0.009 | 4.2×10^4 | 4.2×10^2 | 4.2 |
| 0.2 | 0.91 | 360 | 1.4×10^5 | 1.4×10^3 | 14 |
| 0.5 | 0.67 | 900 | 1.9×10^5 | 1.9×10^3 | 19 |
| 0.8 | 0.57 | 1440 | 2.3×10^5 | 2.3×10^3 | 23 |

Table 3 Comparison of the limits of detection (LODs) according to the setup (conventional or microfluidic) and flow rate (Q)

| Setup | Conventional UME | Microfluidic stopped flow | Microfluidic with flow |
|------------------------------|------------------|---------------------------|------------------------|
| Q ($\mu\text{L s}^{-1}$) | — | — | 0.5 |
| LOD (M) | 10^{-14} | 10^{-16} | 10^{-18} |

(blue lines, Fig. 5C). When working with thiolated SAM absorbed on gold substrates, the risk of SAM's desorption must be taken into account. The control experiment has to be periodically recorded because the measured current increases after a 30 minute immersion in the background electrolyte. This deterioration of the SAM might come from the gold substrate attacked by the chlorides. For this reason, the probe immobilization and target recognition were preferentially conducted in saline solution (0.5 M NaCl solution) in order to reach a dense and compact SAM to ensure reproducibility and biosensor efficiency (to prevent diffusion of redox species through the DNA monolayer).

To gain confidence with the experimental results, the standard deviation (SD) on each experimental point was calculated using the definitions established by Armbruster *et al.*³⁸ In our case, blank current density measurements, J_{ssDNA} , were recorded (30 minutes in the presence of single-stranded DNA in 0.5 M NaCl without target DNA). Then, the current density, J_{dsDNA} , was measured after the hybridization of the double stranded DNA (30 minutes in 0.5 M NaCl with target DNA). Finally, the difference between J_{dsDNA} and J_{ssDNA} was plotted with the DNA target concentration, and the LOD was estimated by taking the intersection between the linear section of the experimental data and 3-fold of the SD line. As shown in Fig. 5B and D, the error bars were generated using the standard deviation of the means of the difference between the ssDNA current density and the blank current density obtained with the conventional and microfluidic configurations. The obtained experimental LODs are summarized in Table 3 where a subfemtomolar and an attomolar concentration can be reached as it was theoretically estimated for stopped flow and with flow, respectively (see Tables 2 and 3).

Conclusions

We describe here the transposition of a conventional two-electrode set-up into a microfluidic one allowing the increase in the system's dynamics and thus the increase in the number of DNA targets hybridizing on the sensor achieving 1 aM as the LOD. This unexpected LOD is due to a forced convection which diminishes the diffusion layer thickness and results in a faster collection of the DNA targets toward the sensor. Thus, more targets are collected and contribute to the increase of the hybridization signal.

The advantages of the microfluidic setup in comparison with the UME conventional setup are an easy to use two-electrode configuration for fast screening and a more



efficient control of the distance between electrodes. Indeed, there is less risk of damage to the SAM of single-stranded DNA by manipulating the microelectrode, thus decreasing the standard deviation of blank measurements. Another advantage of the electrobiochip described here is the possibility of multi-detection for parallel analysis of numerous miRNAs especially relevant in the case where a cancer manifests through multiple miRNAs, generating a map of miRNA concentration changes.

Acknowledgements

This work was supported by the LabEx MiChem part of French state funds managed by the ANR within the Investissements d'Avenir programme under reference ANR-11-IDEX-0004-02. The authors would also like to thank the "Centre de Nanosciences et de Nanostructures" for its financial support through the clean room facilities in Marcoussis, France.

References

- Q. Shi, X. Yang and D. L. Mendrick, *Biomarkers Med.*, 2013, 7, 307.
- E. Van Rooij, *Circ. Res.*, 2011, 108, 219.
- T. Adachi, M. Nakanishi, Y. Otsuka, K. Nishimura, G. Hirokawa, Y. Goto, H. Nonogi and N. Iwai, *Clin. Chem.*, 2010, 56, 1183.
- X. Ji, R. Takahashi, Y. Hiura, G. Hirokawa, Y. Fukushima and N. Iwai, *Clin. Chem.*, 2009, 55, 1944.
- G. A. Calin, C. D. Dumitru, M. Shimizu, R. Bichi, S. Zupo, E. Noch, H. Aldler, S. Rattan, M. Keating, K. Rai, L. Rassenti, T. Kipps, M. Negrini, F. Bullrich and C. M. Croce, *Proc. Natl. Acad. Sci. U. S. A.*, 2002, 99, 15524.
- A. M. Gurtan and P. A. Sharp, *J. Mol. Biol.*, 2013, 425, 3582.
- A. Lujambio and S. W. Lowe, *Nature*, 2012, 482, 347.
- L. Moldovan, K. E. Batte, J. Trgovcich, J. Wisler, C. B. Marsh and M. Piper, *J. Cell. Mol. Med.*, 2014, 18, 371.
- B. S. Ferguson, S. F. Buchsbaum, J. S. Swensen, K. Hsieh, X. Lou and H. T. Soh, *Anal. Chem.*, 2009, 81, 6503.
- X. Chen, S. Roy, Y. Peng and Z. Gao, *Anal. Chem.*, 2010, 82, 5958.
- S. O. Kelley, E. M. Boon, J. K. Barton, N. M. Jackson and M. G. Hill, *Nucleic Acids Res.*, 1999, 27, 4830.
- J. D. Watson and F. H. C. Crick, *Nature*, 1953, 171, 737.
- C. D. S. Riccardi, H. Yamanaka, M. Josowicz, J. Kowalik, B. Mizaikoff and C. Kranz, *Anal. Chem.*, 2006, 78, 1139.
- K. Arora, N. Prabhakar, S. Chand and B. D. Malhotra, *Sens. Actuators, B*, 2007, 126, 655.
- E. Alipour, M. H. Pournaghi-Azar, M. Parvizi, S. M. Golabi and M. S. Hejazi, *Electrochim. Acta*, 2011, 56, 1925.
- C. P. Chen, A. Ganguly, C. Y. Lu, T. Y. Chen, C. C. Kuo, R. S. Chen, W. H. Tu, W. B. Fischer, K. H. Chen and L. C. Chen, *Anal. Chem.*, 2011, 83, 1938.
- J. Weng, J. Zhang, H. Li, L. Sun, C. Lin and Q. Zhang, *Anal. Chem.*, 2008, 80, 7075.
- M. Lazerges, V. T. Tal, P. Bigey, D. Scherman and F. Bedioui, *Sens. Actuators, B*, 2013, 182, 510.
- J. S. Rossier, M. A. Roberts, R. Ferrigno and H. H. Girault, *Anal. Chem.*, 1999, 71, 4294.
- K. Stulik, C. Amatore, K. Holub, V. Marecek and W. Kutner, *Pure Appl. Chem.*, 2000, 72, 1483.
- C. Amatore, C. Sella and L. Thouin, *J. Electroanal. Chem.*, 2006, 593, 194.
- I. Streeter, N. Fietkau, J. Del Campo, R. Mas, F. X. Munoz and R. G. Compton, *J. Phys. Chem. C*, 2007, 111, 12058.
- D. Suwatchara, M. C. Henstridge, N. V. Rees and R. G. Compton, *J. Phys. Chem. C*, 2011, 115, 14876.
- H. Wang, Y. Liu, C. Liu, J. Huang, P. Yang and B. Liu, *Electrochem. Commun.*, 2010, 12, 258.
- M. Faure, A. Pallandre, S. Chebil, I. Le Potier, M. Taverna, B. Tribollet, C. Deslouis, A.-M. Haghiri-Gosnet and J. Gamby, *Lab Chip*, 2014, 14, 2800.
- A. Nassi, F. X. Guillon, A. Amar, B. Hainque, S. Amriche, D. Maugé, E. Markova, C. Tsé, P. Bigey, M. Lazerges and F. Bedioui, *Electrochim. Acta*, 2016, 209, 269.
- L. L. Rouhana, M. D. Moussallem and J. B. Schlenoff, *J. Am. Chem. Soc.*, 2011, 133, 16080.
- L. P. Reiss and T. J. Hanratty, *AIChE J.*, 1963, 9, 154.
- R. G. Compton, A. C. Fisher, R. G. Wellington, P. J. Dobson and P. A. Leigh, *J. Phys. Chem.*, 1993, 97, 10410.
- M. A. Lévêque, *Ann. Mines*, 1928, 13, 283.
- S. C. Ling, *J. Heat Transfer*, 1963, 85, 230.
- M. Faure, B. Sotta and J. Gamby, *Biosens. Bioelectron.*, 2014, 58, 61.
- O. Ordeig, N. Godino, J. Del Campo, F. X. Muñoz, F. Nikolajeff and L. Nyholm, *Anal. Chem.*, 2008, 80, 3622.
- T. M. Squires, R. J. Messinger and S. R. Manalis, *Nat. Biotechnol.*, 2008, 26, 417.
- J. Newman, in *Electroanalytical Chemistry*, ed. Bard A., Dekker, New York, 1973, vol. 6.
- P. W. Stevens, M. R. Henry and D. M. Kelso, *Nucleic Acids Res.*, 1999, 27, 1719.
- T. E. Ouldrige, A. A. Louis and J. P. K. Doye, *J. Chem. Phys.*, 2011, 134, 085101.
- D. A. Armbruster and T. Pry, *Clin. Biochem. Rev.*, 2008, 29(Suppl 1), S49.



Following this article that highlights the advantages of transposing UME in a microfluidic chip, I propose below a discussion on the importance of the geometry of electrodes on hydrodynamical properties and a discussion on the probe density for hybridization efficiency.

2.3.4 On the importance of the electrodes' geometry

The geometry of the electrodes especially in a device coupling electrochemistry with microfluidics has a crucial importance in terms of electrodes' integration inside the fluidic channel, hydrodynamical behavior and ratio time of manufacture versus life time of the chip. The principle of channel-electrode was described by Reiss and Hanratty [250] and was then exploited by Compton leading to a limiting diffusion current as a function of the volumetric flow rate [251]:

$$I_{lim} = 0.925nFc_{\infty}D^{2/3}x_e^{2/3}w \left(\frac{4Q}{h^2d} \right)^{1/3} \quad (2.32)$$

The two-electrode setup.

Traditionally, detection setups are designed with three electrode using millimetric electrodes. Such systems are not well-adapted to DNA detection in microliter samples and to miniaturization. In section 2.1.4 the benefits of using UME have been extensively justified. Moreover, the manufacture and the integration inside a microfluidic channel is made easier.

Our setup is composed of multiple planar pairs of 30 μm working electrodes and 2 mm counter electrodes. The counter-electrode of 2 mm in width can be considered as a pseudo-reference electrode as its area is high (70 times higher) compared to the 30 μm of the working UME yielding to a small current density variation and so on to a small potential drift during potential sweep.

Without a reference electrode the signal in CV is centered at the axes origin as displayed on Figure 2, explained in the LOC article.

Levich prediction

The location of one electrode from another has also its importance .

The hydrodynamic behavior of our chip matches the Levich prediction with a good adequacy (ratio 1) except for small flows ($<0.01 \text{ uL s}^{-1}$). Indeed Levich equation does not take into account either channel edge effect or radial diffusion on the edge of microelectrodes. When the flow is increasing, the diffusion layer is shrinking, radial contribution of microelectrodes' edges become negligible [252, 253].

But, other similar systems reported a smaller ratio (around 0.3), see Figure 2.15, layout B even if the hydrodynamical conditions put the sensor in a pure Levich regime ($X_e/Pe < 0.04$ and $X_e \cdot Pe > 15$, Pe the Peclet number, $X_e = x_e/h$) [222]. The difference comes from the location of the working electrode in relation to the counter electrode. Indeed when using a two-electrode setup, there is a generator collector effect with small gaps between electrodes [205]. With an inserted WE inside a T

counter electrode (layout A), the upstream CE may collect the redox species and decreasing their concentration in the surroundings of the WE. Plateaus with smaller intensity are thus obtained. On the contrary, with our geometry, the WE is located upstream of the CE, and may have the role of generator. Our electrodes are also separated with gaps higher than 100 .

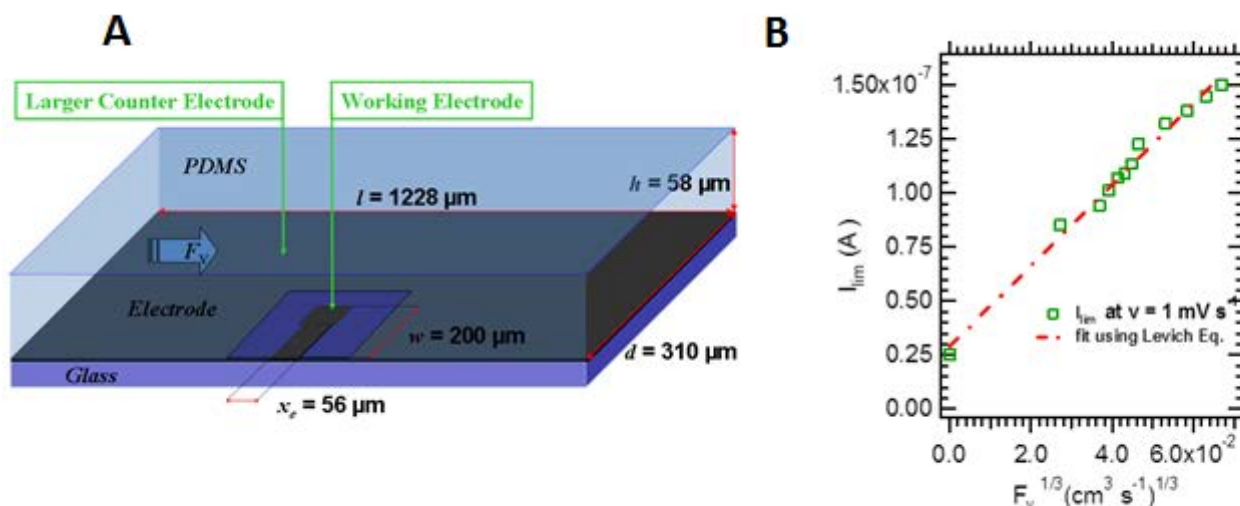


Figure 2.15: Geometry (A) and Levich curve (B) of Faure *et al.* setup [222]

Electrode arrays

The sensor is composed of 3 sets of 2 pairs of electrodes, a working electrode and its 70-fold larger counter electrode. This configuration allows the use of the same microchip more than once and to have always a working (WE, CE) couple even if an electrode is damaged. Moreover it was planned to perform parallel detection at different location on the chip to follow mass-transport inside the channel. Arrays of electrode have higher performance due to increased mass-transport [205].

2.3.5 Probe density

High frequency electric impedance spectroscopy (HFEIS) measurements were performed to estimate the probe density and the ohmic resistance in the microdevice. The instruments used are a frequency response analyser (Solartron FRA 1255B) coupled with a dielectric interface (Solartron DI 1296A). The frequency range used for EIS measurements was varied from 1 MHz to 0.1 Hz. The sinusoidal AC signal excitation between the two microelectrodes is set to 100 mV peak to peak, since DC was fixed to 0 V.

One can supposed that defects in a thiolated ss-DNA monolayer (ss stands for single stranded) allow electroactive molecules to reach the gold electrode surface. Assuming that all the current is passed by holes on the SAM electrode, the electrode coverage can be estimated by measuring the charge transfer resistance (R_{ct}) and by

comparing the R_{ct} ratio between a bare gold surface and the surface blocked by the ss-DNA thiol immobilized.

The probe density was determined from the percentage of the coverage surface θ , as follows

$$1 - \theta = \frac{R_{ct,t=0}}{R_{ct,t}} \quad (2.33)$$

with, $R_{ct,t=0}$, is the charge transfer resistance of the bare gold electrodes and, $R_{ct,t}$, is the charge transfer resistance of the surface blocked by the SS-DNA thiol immobilized.

The charge transfer resistance, can be estimated as the difference on the real-axis between the asymptotic resistance limit at low frequency, R_{LF} , and that as frequency tends towards ∞ , R_{HF} , (Figure 2.16). As one can observe on real-axis, R_{HF} , traditionally name the ohmic resistance, Re , is negligible in comparison with R_{LF} .

$$R_{ct} = R_{LF} - Re \quad (2.34)$$

From data displayed on Figure 2.16, the ohmic resistance is estimated around 4.1 k Ω , the charge transfer resistance for the bare Au electrode and for the thiolated ss-DNA electrode over 2 hours are found equal to $R_{ct,t=0} = 210$ k Ω and $R_{ct,t=2h} = 1.1$ M Ω , respectively.

According to Equation 2.33, a total coverage of 80% of the electrodes with ss-DNA probes was obtained. By taking into account that the surface of the WE and the CE gold electrodes is $S_{tot} = 6.09 \cdot 10^{-3}$ cm², we deduce that the surface covered by ss-DNA is $A_{ss-DNA} = 4.9 \cdot 10^{-3}$ cm². Moreover, if we assume that the DNA strands are in upright position [234] the DNA head surface, A_{head} , can be calculated as follows,

$$A_{head} = \pi \cdot d_{head}^2 \quad (2.35)$$

With, d_{head} , the diameter of a DNA head estimated around 2 nm.

As a consequence, the number of DNA probes, N_{ss-DNA} , immobilized is estimated around $3.92 \cdot 10^{10}$ molecules and thus the binding site density ($6.44 \cdot 10^{12}$ sites cm⁻²) can be calculated as follows:

$$bm = \frac{N_{ss-DNA}}{A_{tot}} \quad (2.36)$$

Similarly, Γ_p , the surfacic concentration ($1.07 \cdot 10^{-11}$ mol cm⁻² is given by bm/Na , with Na being the Avogadro's number. This value of $1.1 \cdot 10^{-11}$ mol cm⁻² SAM coverage was found to roughly match the $4.47 \cdot 10^{-10}$ mol cm⁻² experimental value found for close-packed short-thiol SAM on gold by Rouhana *et al.*[254]. Lazerges *et al.* found a 67 to 69% of coverage with disulfide bounds using quartz crystal microbalance [255, 256].

These close packed DNA probe layers are not an optimal strategy for hybridization. Indeed if we compare the 10^{10} DNA probes grafted on the sensor and the 1400 target molecules evaluated to be bound to the sensor (Table 2 in LOC, $0.2 \mu\text{L s}^{-1}$ flow, $C^0 \cdot 10^{-16}$ M) it is rather low. Accordingly around 40% of hybridization ratio can be found in literature [256, 255]. Lazerges *et al.* achieved to increased this value up to

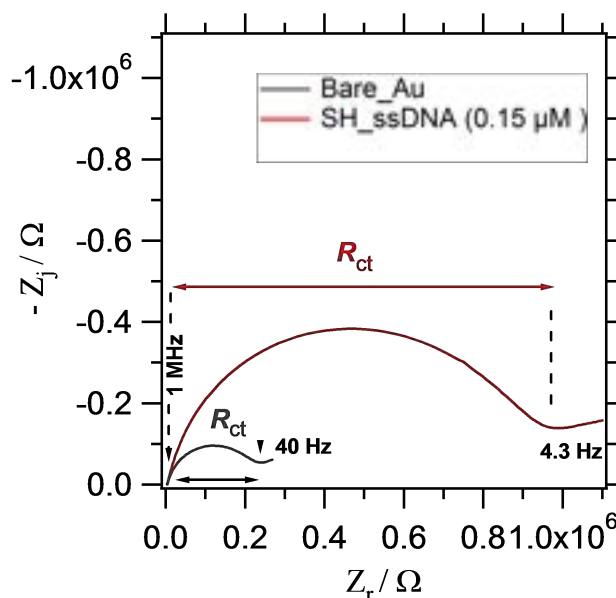


Figure 2.16: Nyquist representation of HFEIS data between the two microelectrodes filled with 3 mM equimolar concentration $[\text{Fe}^{\text{III}}(\text{CN})_6]^{3-} / [\text{Fe}^{\text{II}}(\text{CN})_6]^{4-}$ in 0.5 M NaCl. The applied potentials are $V_{DC} = 0$ V and $V_{AC} = 100$ mV for frequencies from 1 MHz to 0.1 Hz. The diameter loop allows a quick estimation of ohmic resistance, $R_e \approx 4.1$ k Ω , and of the charge transfer resistances, $R_{ct} \approx 210$ k Ω and 1.1 M Ω for bare gold and thiolated ss-DNA electrode (after 2h), respectively.

90% with a diluted monolayer by decreasing the repulsive interactions between the negatively charged DNA strands. They used a modified probe by adding a non complementary sequence [255]. Other strategies prescribe to use a mixed SAM such as the addition of 6-mercaptohexanol [257]. Mixed thiols with various terminal groups and chain length are more stable and more reactive by limiting sterical hindrance [258].

Multiple solutions are reported to both dilute the SAM and fill the holes left by thiol desorption. Regarding thiol reductive desorption under a negative potential: the stability of the SAM not only depends on the thiol chosen (short long alkyl-thiols [259], aromatic thiols [260] or thiolated DNA [261]) but also on the metal surface crystallinity [262] and the adsorption site [263]. For more information on the fate of thiols after desorption see the work of Casanova *et al.* [264].

Confronted to thiol desorption, another material widely investigated in the LISE laboratory was under our attention for covalent grafting. Amorphous carbon nitride was used as protective coating for many hard disks or read heads bears promising properties. Carbon surfaces have been exploited for molecular architectures for biosensors molecular electronics or coatings [265, 266].

2.3.6 Detection on amorphous carbon nitride a-CN_x

a-CN_x films are popular electrode materials with a large potential window (3 V-4 V [267]) interesting electrochemical reactivity [268] and chemical surfacic composition [269]. The surface structure, surface properties, number of grafting sites available

are tunable according to the atomic percentage of nitrogen in the a-CN_x. What's striking is that this grafting sites are also reactive sites for electrochemical reactivity. High surface reactivity are highly dependent on the surface state and can be affected by synthesis (by varying the sp³/sp² ratio), pretreatment (electrochemical or plasma) and dopant.

Diamond like carbon, boron nitrogen doped diamond show this kind of properties (rate constant of electron transfer, k_0 around 10⁻⁴-10⁻² cm s⁻¹) as well as amorphous carbon nitride [270]. The latter has been used for a wide range of applications, from the covalent grafting of heparin [271] to the detection of heavy ions in cancerous therapies [272] or metallic ions detection [273] with increased sensitivity compared to boron doped diamond.

Materials and Methods

Microfabrication

The microfluidic device for sensing on amorphous carbon nitride is roughly the same as described in section 2.3.1. Instead of a gold layer, a platinumium layer is used for a-CN_x, x=0.12, adhesion and conductivity. Above the working electrode, an a-CN_x, x=0.12, layer of 220 nm (checked in SEM) is deposited (mask on Figure 2.17 with DC magnetron sputtering (MP300s Plassys, t=20 min, 200 W, P<2.10⁻⁷ Torr) with a graphite target (ϕ =75 mm, e=5 mm, 99.99% of purity), 7 cm far from the sample under a flow of nitrogen (%N₂=3%, P_{Ar+N₂}=0.4 Pa). The main steps of the microfluidic device fabrication are summarized on Figure 2.18.

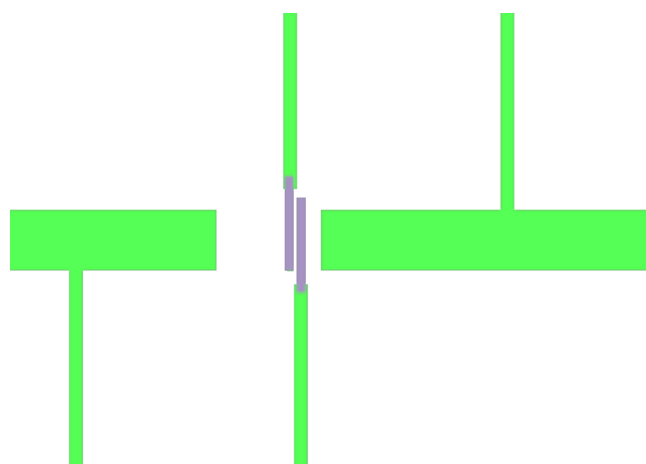


Figure 2.17: L-edit mask for second layer fabrication (purple) on top of the first one (green).

Conducting AFM characterization

AFM observations were carried out in air using a Molecular Imaging instrument in the contact mode. For this purpose, silicon nitride triangular cantilevers bearing pyramidal silicon nitride tips and possessing a 0.38 N m⁻¹ spring constant were used.

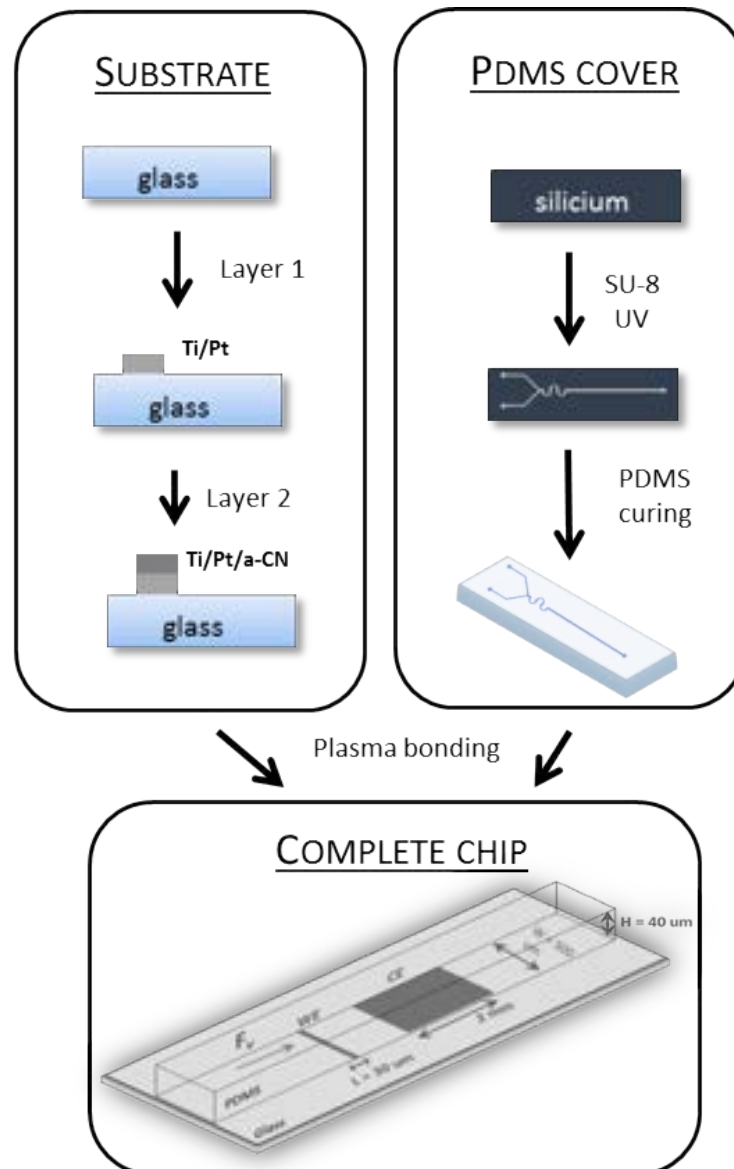


Figure 2.18: Microfabrication key steps: inverted optical lithography, Ti/Pt metallization, a-CN_x magnetron sputtering, PDMS fabrication and bonding.

Potentials between -10 and 10 V (up) and 10 and -10 V (down) were imposed. Saturation currents were imposed at -10 and 10 nA.

Apparatus

The apparatus used are a frequency response analyser (Solartron FRA 1255B) coupled with a dielectric interface (Solartron DI 1296A) or a potentiostat Gamry (reference 600+). The frequency range used for EIS measurements was varied from 1 MHz to 0.1 Hz. The sinusoidal AC signal excitation between the two microelectrodes is set to 100 mV peak to peak, since DC was fixed to 0 V.

Pretreatments

a-CN_x substrates were electrochemically activated either with a potential cycling at 50 mV s⁻¹ between -1.0 V and 0 V/Pt (10 cycles) in a 0.5 M H₂SO₄ with 10⁻² M HCl solution (cathodic activation) or in a 0.1 M KOH solution (galvanostatic, I=2.7.10⁻⁵ mA, 0.5 μL s⁻¹ flow) cathodic activation.

Probe grafting and target hybridization

ss-DNA probe immobilization in a microfluidic device was performed via a two-step protocol. First carboxyl groups on the a-CN_x surface were activated by pouring a 2.10⁻⁷ M EDC and NHS solution inside the chip for 20 minutes. Then by circulating a 0.15 μM DNA probe in 0.5 M NaCl and stopping the flow for three hours. The flushing was done with deionized water and the test of stability of the SAM is done in 0.5 M NaCl, 0.5 μL s⁻¹ flow for 30 minutes. Hybridization was performed under various flow conditions with samples of target DNA of increasing concentrations in 0.5 M NaCl for 30 minutes.

Surface characterizations

Interfaces between a-CN_x and electrolyte were screened in our two-electrode setup (Pt/aCN_x, x=0.12, 30 μm working electrode and Pt 2 mm counter electrode, Figure 2.19) in the electrolyte made of an equimolar (3 mM) mixture of Fe(II) and Fe(III) in 0.5 M NaCl and 10⁻⁸ M MB with the use of Electrochemical Impedance Spectroscopy (EIS) and Cyclic Voltametry (CV).

Carbon electrode materials

Regarding the surface state

In amorphous carbon nitrides deposit, multiple configurations of the a-CN_x bond are possible. Carbon possess four valence electrons, nitrogen five. Nitrogen stands in the donor position e.g. a type n dopant. Three types of sp³ bonds, five types of sp² bonds and one type of sp¹ bond (See Figure 2.20).

Sp² bounded networks are delocalized π bondings. N favor interlayer bondings. N in sp² C breaks π bonds to get an unpaired electron disposable for σ bonds [274]. N₄⁺ bears an unpaired electron for doping. N induces π bonds and sp² clustering in C [274]. a-CN_x films with high fractions of sp² are obtained by radiofrequency

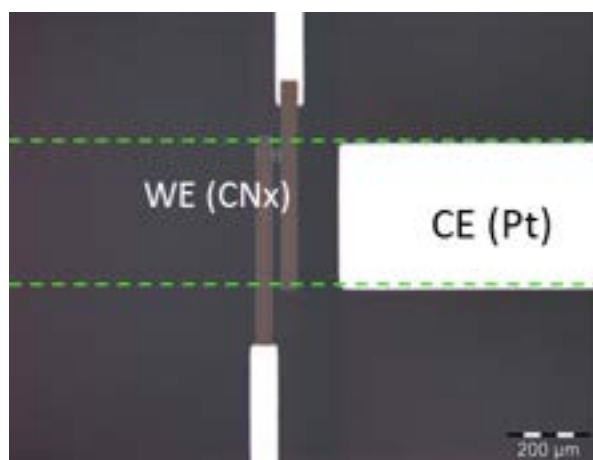


Figure 2.19: Optical microscopic image of the a-CN_x WE with the CE platinum electrode.

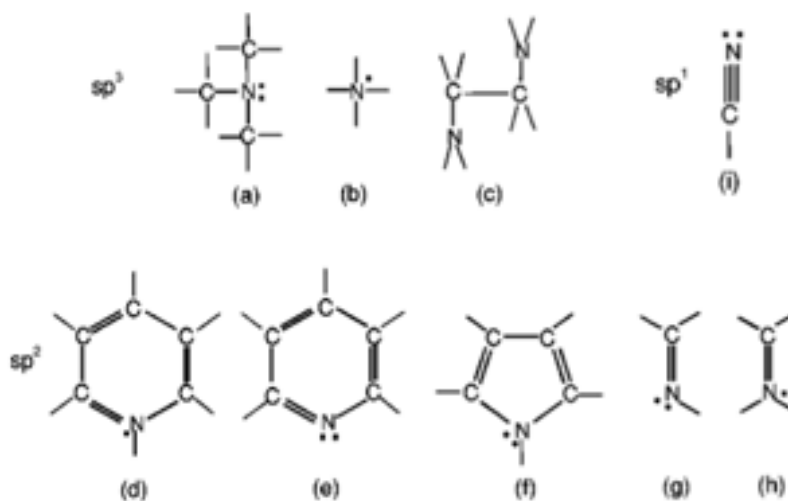


Figure 2.20: The main bonding configurations of nitrogen in carbon nitrides. Lines represent a covalent bond, dots represent unpaired electrons.

sputtering.

Ferrari *et al.* compared the properties of a-CN_x films according to the technique of deposit [274]. They can be classified in two families: chemical deposit in the vapor phase (CVD) and physical deposit in the vapor phase (PVD).

- For CVD, the chemical deposits are enhanced with a plasma thanks to a radiofrequency generator with methane and nitrogen as precursor gas. A graphite target and N₂ as precursor gas can be used as well both at room temperature and at higher temperatures [275, 276].
- Regarding PVD, a wide range of techniques are available from photoablation to laser pulses under a nitrogen pulse or cathodic pulverisation in radiofrequencies at 13.56 MHz [277, 267].

According to the synthesis, various surface properties can be obtained. The type of nitrogenated deposit has to be chosen according to the presence of absence of hydrogen and according to the percentage of sp²/sp³ sites. For a-CN_x films, lots of sp² are present, tetrahedral (t)-a-CN, above 80% in sp³ and a-CH_xN_y and ta-CH_xN_y obtained by chemical deposit.

Electronic conductivity and electrochemical reactivity are linked but not in an obvious way. Electrochemical reactivity, which can be enhanced by pre-treatments (H₂SO₄, ΔE_p=72 mV, k₀=1.1.10⁻² cm s⁻¹ [278, 279]) is depending on the surface composition and thus on the percentage of atomic N at the surface which is linked to the nitrogen bulk contents tuned during the thin film deposition. It was showed that (C, N) compositions changed from (87%, 13%) to (91%, 9%) respectively after anodic pretreatment [280].

Jribi *et al.* compared the influence of bulk nitrogen contents, x, on the percentage of superficial nitrogen atoms and electrochemical reactivity in a-CN_x films [278] by grafting a fluorocarbonyl terminated ferrocene based redox probe on various amorphous carbon nitride (a-CN_x, x=0.12 ≤ x ≤ 0.27) samples. By using spectroscopic and voltammetry techniques, they proved the spontaneous formation of surface amine groups and they showed that the lower the atomic nitrogen content in the bulk of the film, the higher is the corresponding surface coverage from 1.1% (x=0.27, P_{N₂}=30%) to 6.5% (x=0.12, P_{N₂}=3%). These amine sites could partly result from the presence of residual hydrogen or be produced from the dissociation of water as an impurity in sputtering gas. Amines sites are rare, they concluded that further amination was necessary.

Concerning electrochemical reactivity, low N₂ contents are expected to produce higher amounts of sp²/sp³ type. They noticed that ΔE_p values were lower for x=0.19 and x=0.12. The increase of electrochemical reactivity with reduced nitrogen content can be partly explained by the varying charge carrier in a-CN_x samples [281].

As our aim is to immobilize DNA and distinguish a single strand from a double strand, we seek both amines anchoring groups (for covalent grafting of the probe) and a high electrochemical reactivity. Thus we chose an amorphous carbon nitride with a 3% of nitrogen content (x=0.12) prepared by magnetron sputtering technique that will be activated to increase surface amination.

Characterizations

XPS were not used in this study as it was done before [222, 279]. Moreover XPS are screening ca. 10 nm of the surface yet the modifications of surface reach only a few nanometers. Atoms surfacic contribution to XPS spectrum are small compared to the volumic contribution and a-CN_x, contrary to other materials like diamond, have around the same composition (C, N, O) as the grafted moieties.

The material chosen as substrate (here platinum) is relevant. Figure 2.21 shows an increased conductor behavior between a-CN_x, x=0.12, deposited on platinum (Ti/Pt, black curve) compared to a-CN_x deposited on bare glass (gray curve) illustrated by steeper curves. This behavior was consistent with previous observations [268].

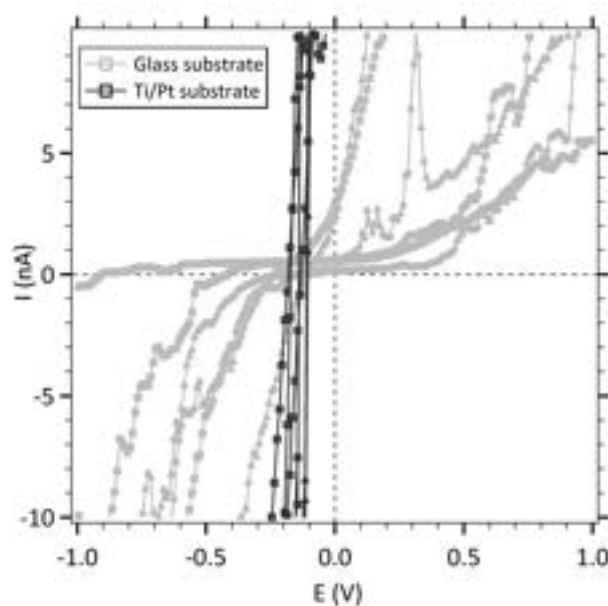


Figure 2.21: AFM conducting measurements on a-CN_x, deposited directly on glass (grey curves) or with a Ti/Pt adhesion layer (black curves).

Potential window

A large potential window is required for biological applications of a-CN_x films. A potential window is characterized by the application of an overpotential which differs from the equilibrium potential that does not induce a change in the interface chemical composition, no faradic current is flowing through, no oxidation or reduction potential will be seen.

On Figure 2.22, the potential window of the deposited a-CN_x film can be seen, without a redox couple, with a 3.5 V range consistent with literature [280]. In practice, a small faradic current comes from residual O₂ dissolved in the buffer. The potential window is limited by H₂O reduction and H₂O or Cl⁻ oxidation.

Surface activation

a-CN_{0.12} films prepared by magnetron sputtering techniques show moderate reactivity as prepared but can be electrochemically activated to finally work towards

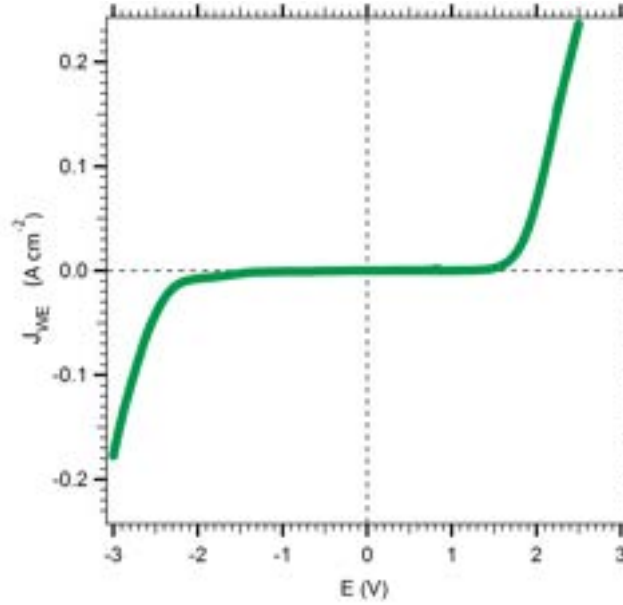


Figure 2.22: Potential window of an a-CN_x, x=0.12, film in 0.5 M NaCl.

a metallic behavior [280]. Usually cathodic pre-treatments consist in a 0.5 M H₂SO₄ cycling, but we preferred to use an anodic activation in 0.1 M KOH, reported to result in increased electrochemical reactivity and increased oxygen amounts at the interface, especially under the carboxyl groups form [282].

Figure 2.23 shows cyclic voltammograms performed on the as-grown electrode (layout A) and after their electrochemical activation (layout B) in a 3 mM Fe(CN)₆⁴⁻ / Fe(CN)₆³⁻ solution. In both cases, the steady-state current given by the Levich equation, Equation 2.37 for each flow reaches the same value.

$$I_{lim} = 0.925.n.F.C^0.D^{2/3}.x_e^{2/3}.\omega.\left(\frac{4.Q}{h^2.d}\right)^{1/3} \quad (2.37)$$

where, n , is the number of electron exchanged, F the faraday, D and C^0 the diffusion coefficient and the bulk concentration of electroactive species, ω and h , the width and height of the channel, x_e the width of the WE and Q the flow rate. ω is equal to d , in our case.

The analysis of steady-state voltammograms according to the Mirkin *et al.* procedure [283] allows extraction of the standard rate constant, k^0 . The activation procedure increases the standard rate, displayed by straightened slopes. Before activation k^0 is equal to $5.6.10^{-4}$ cm s⁻¹ and after activation k^0 reaches $1.3.10^{-3}$ cm s⁻¹ consistent with previous observation in anodic activation [279].

As for the variation of the limiting current, I^{lim} , versus flow rate, it matches rather well the Levich prediction (layout C). The ratio between experimental current value and limiting current versus flow rate 1/3 is yielding a ratio of 1, for medium and high flow rates, consistent with the shrinking of the diffusion layer under convection. At lower flow rates, edge and wall effects are not taken into account in Equation 2.37.

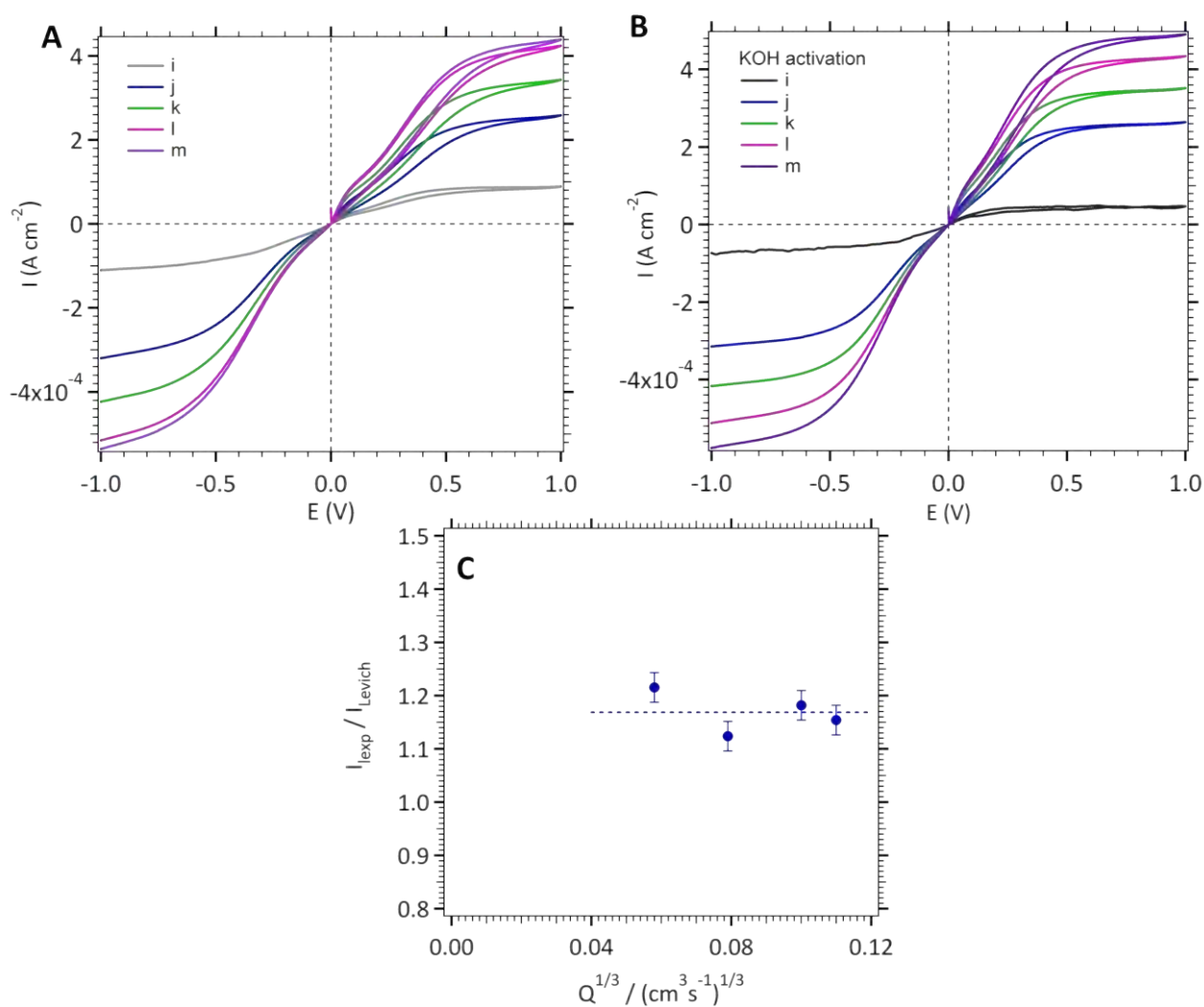


Figure 2.23: CV curves (10 mV s^{-1}) of the a-CN_x microelectrode in $\text{Fe}(\text{CN})_6^{4-} / \text{Fe}(\text{CN})_6^{3-}$ (3 mmol L^{-1})+NaCl (0.5 mol L^{-1}) under various flow rates (static (i), 0.2 (j), 0.5 (k), 1.0 (l), 1.5 (m) $\mu\text{L s}^{-1}$) before (A.) and after (B.) activation. C. Limiting current ratio between experimental current, I_{exp} , and Levich equation current, I_{Levich} , as a function of the 1/3 volumetric flow rate. The dotted line displays the mean of experimental values.

Figure 2.24 shows EIS diagrams in Nyquist representation on an as-grown electrode (red circles) and after its electrochemical activation (black squares) in an equimolar ferri/ferrocyanide solution at the equilibrium potential. The flattened semi-circles are generally explained by a distribution of interfacial reactivity. Before activation, the charge transfer resistance is about 1.3 M Ω whereas after activation its value drops to 900 k Ω indicating an increased electrochemical reactivity.

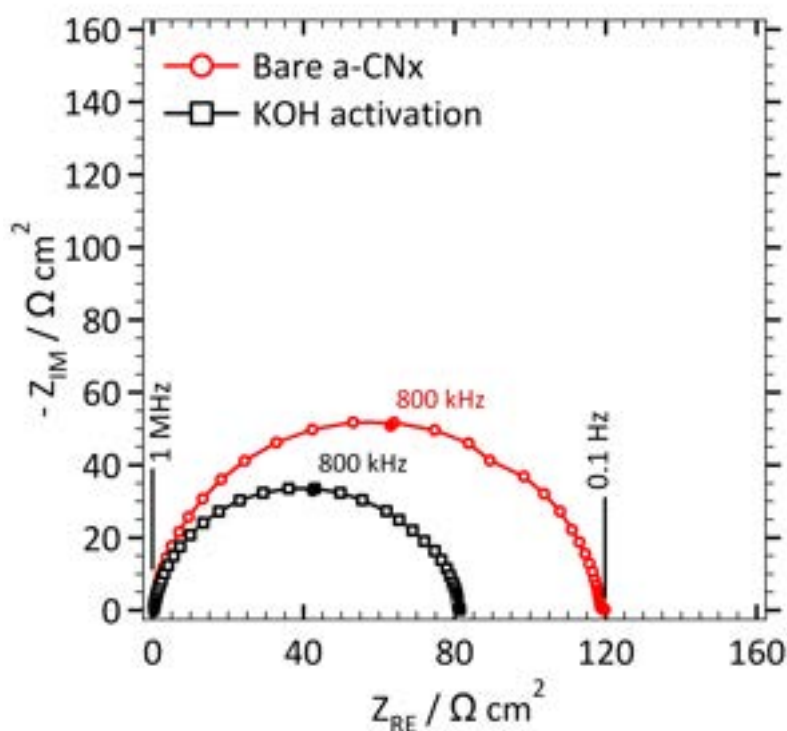


Figure 2.24: Nyquist EIS diagrams of the impedance response of the a-CNx microelectrode in $\text{Fe}(\text{CN})_6^{4-} / \text{Fe}(\text{CN})_6^{3-}$ (3 mmol L^{-1}) + NaCl (0.5 mol L^{-1}) before (red circles) and after (black triangles) activation.

At the equilibrium potential, the kinetic constant k^0 value can be deduced from the measurement of the charge transfer resistance R_{ct} , that displays electron transfer at solution/a-CNx interface, as written in Equation 2.38.

$$k_0 = \frac{R.T}{F^2.S.R_{ct}.C^0} \quad (2.38)$$

where R is the molar gas constant ($8.314 \text{ J mol}^{-1} \text{ K}^{-1}$), T the thermodynamic temperature (K), F the Faraday constant ($96,485 \text{ C mol}^{-1}$), S the area of the electrode, C the redox species concentration (3 mM), and R_{ct} the charge-transfer resistance (Ω).

Amorphous carbon nitride electrodes without pretreatments give kinetic constant between 1.6 and $5.4 \cdot 10^{-4} \text{ cm s}^{-1}$. Those activated with anodic KOH pretreatment yield kinetic constant values between 2.3 and $9.4 \cdot 10^{-4} \text{ cm s}^{-1}$ according to several electrodes tested. KOH anodic pretreatments are undoubtedly increasing electrochemical reactivity. The variability in the electrochemical reactivity may come from the deposition process of a-CNx thin films. Indeed, it is difficult to precisely tune such a low flow of nitrogen (0.27 sccm) and this flow is varying during the

magnetron sputtering leading to slightly different nitrogen contents for each chip.

A more thorough investigation with XPS shows that activation decreases the content of superficial N atoms involved in C-N sp^3 bonds [280, 270]. The influence of activation on the microstructure of a-CN_x films [284] results in a substitution of C atoms in the graphite clusters by N generating a clustering of sp^2 sites. N-C sp^3 and N=C sp^2 increases whereas C=C sp^2 decreases. C contents goes from 87% to 91% and N contents from 13% to 9% (removal in C-N bonds into NH₃). This is in good agreement with higher reactivity as C sites are the preferred sites for electron exchange.

These results are in good agreement with cathodic pretreatment that reveals electrophilic terminations that increase ET for most scanarii [285, 286, 287] whereas anodic pre-treatment reveals carbonyl and carboxyl endings. As they are nucleophilic they decrease ET for redox couples.

DNA hybridization detection on a-CN_x by EIS

DNA hybridization detection is based on long range electron transfer through the DNA double structure via π stacking. Figure 2.25 shows the EIS response of the biosensor subjected to a DNA-target solution.

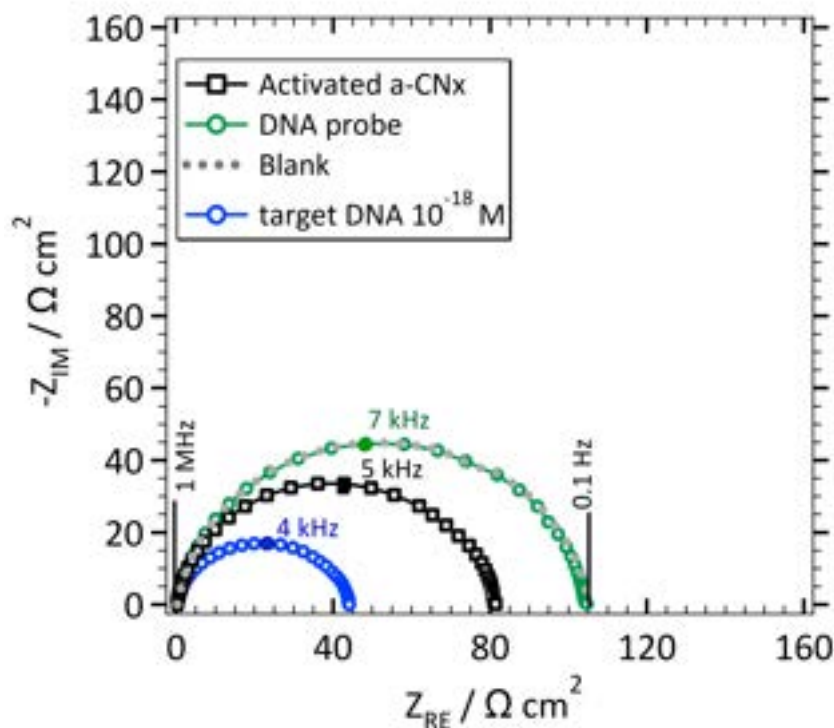


Figure 2.25: DNA hybridization detection (EIS). Probe immobilized (black curve), target hybridization (green curve).

The DNA probe layer (DNA modified with a -NH₂ ending) is covalently grafted to the a-CN_x carboxyl groups activated with EDC/NHS [288]. It is a repulsive layer

for the negatively charged $\text{Fe}(\text{CN})_6^{3-}$ complex. DNA is also negatively charged hindering the diffusion of the complex inside the probe layer. The result is an increase in the impedance loop up to a R_{ct} of 600 $\text{k}\Omega$ (green circles on the graph).

The stability of the grafted monolayer was checked by flushing a blank solution in hybridization conditions (0.5 M NaCl at $0.5 \mu\text{L s}^{-1}$ for 30 minutes). No deterioration of the probe layer can be seen as indicated by an unchanged Z value (grey dotted line). This observation is consistent with a covalent grafting. It is obviously an optimization with respect to the results of probe immobilization on gold.

The hybridization with target DNA reestablishes the electron transfer via LET increased by the use of MB indicated by a decrease in impedance (blue squares) up to 157 $\text{k}\Omega$, a value lower than the one of bare a-CN \times (black curve, 300 $\text{k}\Omega$) showing the success of hybridization.

Such an high electrochemical reactivity value after hybridization could be explained by the insertion of ions inside the a-CN \times structure. Insertion of cation inside indium tin oxide (ITO) was reported when performing electrochemical reduction leading to Na^+ insertion and a drastic morphological change decreasing, in that case, electrode conductivity [289]. Ions insertion were also reported in graphene [290].

Electrochemical reactivity after hybridization may also come from the self-assembly of double-strand DNA on a-CN \times electrode. Ciesielski *et al.* reported the self-assembly of G-based structures on flat surfaces generating highly ordered nanostructured materials inspired from the self-association of natural nucleobases. These structures constituted building blocks for electrically/optically active units [291].



Figure 2.26: Chemical grafting and DNA hybridization detection scheme.

Concerning the critical density of probes on the surface.

One can calculate the number of immobilized DNA probes on the UME with a similar calculation as in Section 2.3.5 except that DNA probes are only grafted on a-CN \times working electrodes and are rather in a lying position than in an upright position (SAM on gold are more dense). The ratio between the ss- R_{ct} and R_{ct} of bare a-CN \times (Figure 2.25, with a $100 \mu\text{g mL}^{-1}$ probe concentration introduced) is giving a 50% surface coverage giving $3 \cdot 10^8$ DNA probe grafted and yielding a $4 \cdot 10^{12}$ groups cm^{-2} density ($6 \cdot 10^{-12} \text{ mol cm}^{-2}$) compared to the $2.2 \cdot 10^{14}$ available grafting sites [278]. We assume that those amine sites obey a random and even distribution [292].

Figure 2.27 displays the impact of increasing concentrations of DNA probes from 10 to $10\,000 \mu\text{g mL}^{-1}$ introduced on the grafting density. The curve reaches a plateau that may indicate the saturation of the amines groups available for grafting. We took for the optimum value the half high of the plateau e.g. $500 \mu\text{g mL}^{-1}$ for further grafting. We believe that it will result in a medium density of probes on the surface, that will leave enough space to targets to approach [56].

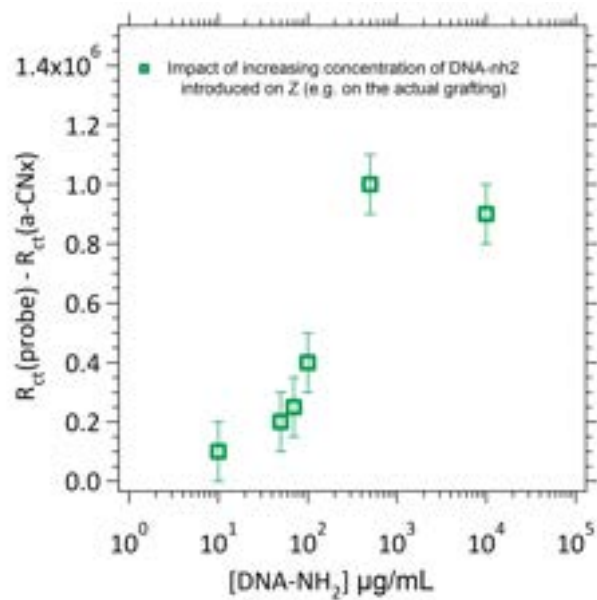


Figure 2.27: Biosensor response in EIS subjected to increasing concentrations of DNA probe solution.

Limit of Detection

Limit of detection curves were plotted on Figure 2.28 to determine the behavior of the sensor submitted to target solution of decreasing concentration.

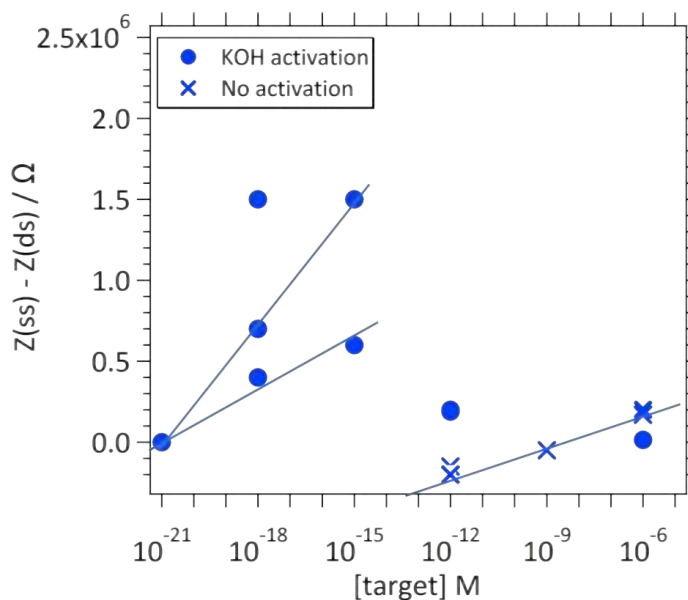


Figure 2.28: Biosensor response in EIS subjected to decreasing concentrations of target solution.

The sensor's response for non activated a-CN_x (crosses) is smaller even non existing in regard to the activated electrodes (circles). It may come from the number of amines sites available for grafting with the probes and thus the number of probes available for target hybridization. Negative values for $Z(ss) - Z(ds)$ come from experiments that resulted in larger loops after hybridization (larger than the loop corresponding to the probe grafting) perhaps an influence on single strand adsorption on the surface rather than hybridization. These values were kept anyway for accuracy.

For small concentrations of targets e.g. 10^{-21} - 10^{-15} some linearity in the sensor's response can be found resulting in a pseudo limit of detection of 1 aM. The sensor based on a-CN_x electrodes is able to detect concentrations down to the attomolar range. Variations in linear slopes may come from the variability found in electrochemical reactivity, electrodes with higher reactivity tend to better detect, in terms of impedance, double-stranded DNA compared to single-stranded DNA in that case.

Conclusion

Here, we described the transposition of an ultramicroelectrode (UME) setup into a microfluidic chip configuration for DNA biosensors. First the behavior of a gold UME in a two electrode setup was studied with the $[\text{Fe(III)(CN)}_6]^{3-} / [\text{Fe(II)(CN)}_6]^{4-}$ redox couple outside a microfluidic chip. Hybridization detection schemes were performed taking advantage of the spatial and temporal resolution of UME allowing the study of molecular phenomenon in microvolumes with a S/N optimized ratio and the detection of small currents with a high sensitivity (ohmic drop is kept minimal).

Seeking reproducible measures with precise positioning of the electrodes and higher dynamics due to confinement, this first biosensor was integrated in a microfluidic channel. The hydrodynamic properties of the fluidic channel microelectrode were screened by cyclic voltammetry matching the Levich predictions.

A 23-base DNA probe was self-assembled into a monolayer on gold microelectrodes both in classical configuration and integrated in a microfluidic setup. Special interest was focused on the DNA target mimicking the liver-specific micro-ribonucleic acid 122 (miRNA122). Long-range electron transfer was chosen to transduce hybridization. This direct transduction was indeed significantly enhanced after hybridization due to DNA-duplex π -stacking and the use of redox methylene blue as a DNA intercalator. Quantification of the target was deduced from the resulting electrical signal characterized by cyclic voltammetry. The limit of detection for DNA hybridization was 0.1 fM in stopped flow experiments, where it can reach 1 aM over a $0.5 \mu\text{L s}^{-1}$ flow rate, a value 10^4 -fold lower than the one measured with a conventional UME dipped into an electrolyte droplet under the same analytical conditions. An explanation was that forced convection drives more biomolecules to the area of detection even if a balance between the speed of collection and the number of biomolecules collected has been found.

The switch to a-CN_x material for working electrode was a response to the instability of the DNA layer along with a high density of probes. A strong grafting with a stable DNA probe layer of $3 \cdot 10^8$ strands (against $4 \cdot 10^{10}$ on gold UME) that allowed thorough water rinsing at $2 \mu\text{L s}^{-1}$ was obtained yielding successful hybridization down to 1 aM.

In this chapter we achieved successful electrochemical microfluidic biosensors taking advantage of electrochemistry and microfluidic coupling and the extensive properties of UME. The optimized electrochemical microfluidic sensor on a-CN_x allow quantification measurements in a 30-minutes protocol.

Without losing sight of the overall ideal goal to test a mixture of DNA in a fully integrated LOC, the following step is to design a capture platform to separate our target DNA of interest from the biological matrix.

Chapter 3

$\gamma\text{-Fe}_2\text{O}_3@SiO_2$ core-shell nanoparticles, nanocarriers for DNA capture and release

Magnetic beads are becoming very popular both in the nanometric and the microscopic range as carriers, manipulating agents or contrast agents [293]. Magnetic nanoparticles beside their obvious high surface to volume ratio and a flexible functionalization can be easily handled without any contact thanks to a magnetic field. To be well dispersed in biological fluids, the size of nanoparticles has to be balanced between a high surface to volume ratio and a high magnetization.

All current detection systems or soon to be commercialized ones do not reach sensitive limits of detection without a concentration or amplification module. The small size of NP make them an attractive matrix as the barrier of diffusion is reduced between reactants. It leads to shorter responses, increased linear range and the opportunity to reach molecular limits of detection. We compared the uptake efficiency of an assembly of nanoparticles of 80 nm in diameter to the uptake on an electrode of 30 μm (see Annexe A for the detailed demonstration). These elements justify the use of an assembly of nanoparticles upstream to a module of DNA detection via an Ultra-microelectrode. The ratio between the respective efficiencies is N , the number of nanoparticles, $N = 10^{13}$ in our case, making nanoparticles ideal nano-magnets for DNA capture.

Lots of magnetic systems were proposed through the years [294, 295, 296, 297, 298]. However the challenge is to keep an homogeneous magnetic fluid without limitation of the mass transfer and the particles needs to have a sufficient magnetization to be handled and to be able to perform various grafting.

Colloidal stability is the key for biomedical applications. Thanks to their narrow size nanoparticles are little or not at all submitted to gravitational pull. Without any field the nanoparticles' stability depend on the balance between attractive forces (dipole-dipole Van der Waals interactions) and repulsion forces (sterical and electrostatical forces). Hence the design of hybrid particles combining organic with inorganic [299, 300] and the need of coating agents like polymers for stability [301, 302, 303].

Magnetic nanoparticles' functionalization has to maintain their magnetic properties to avoid any aggregation and to make them biocompatible platforms for the capture of biomolecules (DNA, enzymes, proteins, antibodies). The type of envelope determines the size and the physico-bio-chemical properties of the NP. Coating agents can be functional organic molecules (aldehydes, hydroxy, carboxy or amines)

or polymers such as PEG, PNA [304] or PEI that ensure the stability of the particle via steric and electrostatical repulsions acting as a fence against attractive forces.

Size and shape of nanoparticles are key parameters to determine their stability. Size has an heavy impact on magnetic moment and the response to an applied magnetic field. For an easy manipulation by an external field the overall magnetization has to be maximum. Ferromagnetic materials are thus favored as iron, nickel or cobalt. Particularly popular is the iron oxide under its magnetite Fe_3O_4 or maghemite $\gamma\text{-Fe}_2\text{O}_3$ form that can be synthesized with the best chemical stability against oxidation and possess the interesting electro-magnetic properties. A remarkable control of the size of the objects is allowed with amorphous silica shells via the sol-gel process. The silica coating, hydrophilic, is especially stable in biological media (pH < 9) and can be even more stabilized with functional groups: the functionalization with chemical functions (amine, carboxy acid, thiol, epoxy) charged at pH 7.4 [305] and polymer PEG chains is well-known and interesting for a coupling with biomolecules. Moreover a silica layer shields dipolar interaction by taking away magnetic particles from one another [306].

Another reason why choosing MNP is their local outstanding heating behavior subjected to a radiofrequency alternative magnetic field (AMF). Dias *et al.* achieved by heating iron oxide nanoparticles functionalized with DNA under an AMF to assess roughly the temperature in the vicinity of a magnetic nanoparticle. They assessed an increase of 8°C compared to the bulk solution at 5 nm of a nanoparticle [189]. This increase of temperature at the nanoscale is the key of many applications in cancer treatment [307, 308] using thermosensible polymers or biomedecine for targeted drug delivery [309]. Indeed the heating of a biological solution is a tricky issue in an amplification and / or detection of a biological target. Beside an obvious denaturation of the parts non compatible with high temperature, a feedback loop is needed to take into account the thermal losses and precisely tune the temperature [39].

Magnetic hyperthermia on maghemite nanoparticles *e.g.* local heating by Néel relaxation of a super paramagnetic nanoparticle under an alternative magnetic field overcome these constrains. The interior of the nanoparticles becomes much hotter than the macroscopic solution and cools to the temperature of the ambient fluid on a time scale of seconds after the magnetic field is turned off [310].

Our aim is to couple magnetic properties and colloidal stability on the same nano-object. This asks for not to small objects to obtain sufficient magnetic moment [311] and not to big to stay in an efficient regime of diffusion.

To complete all the needed specifications and to continue with the PHENIX laboratory tradition, we designed core-shell nanoparticles with a maghemite $\gamma\text{-Fe}_2\text{O}_3$ core, a silica shell and functionalized with polymer chains and amine groups ; polymer chains for NP stability *e.g.* steric interactions, amines for electrostatic interactions and covalent grafting [312, 313].

Magnetic silica particles are very efficient in adsorbing/capturing proteins and DNA on their surface but are very hardly available with a small size distribution and an ideal spherical shape. A modification of their structure and shape particularly their core was needed to handle them more easily and to perform higher magnetic hyperthermia.

In this chapter, an easy and flexible way to release hybridized DNA targets from their nanocarrier module is presented. By using magnetic hyperthermia on superparamagnetic core-shell nanoparticles that combine biocompatibility and availability all the odds are in our favor to reach the maximum efficiency. Our focus is not on creating the most powerful nanoheaters but to present a robust and reproducible way to synthesise a nanopatform with flexible properties both magnetic and biologic in aqueous solution. This synthesis is simple although efficient for magnetic hyperthermia.

First in this chapter, we will describe and characterize our synthesized maghemite core-shell nanoparticles as stable and magnetic efficient particle. Then the nanoparticles will be characterized in terms of surface properties as a capture unit for DNA. Finally an original and efficient way of releasing the DNA mimicking miRNA-122 captured, with magnetic hyperthermia, will be described.

3.1 Materials & Methods.

3.1.1 Materials

N-(3-Dimethylaminopropyl)-N-ethylcarbodiimide hydrochloride (EDC); N-Hydroxy-sulfosuccinimide sodium salt (NHS); 3-(N-Morpholino)propanesulfonic acid sodium salt (MOPS); tetraethoxyorthosilicate (TEOS); 3-(aminopropyl)triethoxysilane (APTS) were purchased from Sigma–Aldrich (St Quentin Fallavier, France). Citric acid was purchased from Merck (Nogent sur Marne, France). 2-[Methoxy(polyethyleneoxy) propyl]-trimethoxysilane (PEOS), containing 3-6 ethylene oxide groups, was purchased from Gelest (Morrisville, PA, USA). 30% H₂O₂, HCl and NaOH solutions were obtained from VWR (Strasbourg, France). The oligonucleotides were purchased from Integrated DNA Technology (Belgium). The probe is 21-basis long and is modified with a carboxy-end. The target is an unmodified DNA sequence of 20 basis as written in Table 3.1.

Table 3.1: Sequences of Oligonucleotide Strands

| Oligonucleotide | Sequence (5' to 3') |
|-----------------|--|
| Probe (P) | 5'-Carboxy C6-CAA ACA CCA TTG TCA CAC TGC-3' |
| Target (T) | 5'-GC AGT GTG ACA ATG GTG TTT G-3' |

3.1.2 Synthesis of core-shell nanoparticles

γ -Fe₂O₃ cores synthesis.

Maghemite γ -Fe₃O₄ nanoparticles were synthesized following the Massart co precipitation synthesis [314]. First, weight 180 g FeCl₂ with 100 mL of HCl and 500 mL of distilled water. Weight 715 mL of FeCl₃ in the latter preparation with 3 L of distilled water under agitation. Add 1 L of NH₃ 22.5%. The washes are done in distilled water under magnetic decantation. Add HNO₃ 52.5% to pass in acidic medium. Then in order to oxidized the NPs synthesized weight 323 g of Fe(NO₃)₃ in 800 mL of water and bring to boil. Add to the latter preparation and heat until change of color. Add 360 mL of HNO₃ 52.5% diluted in 2L of water to pass in acidic medium. Three cycles of washes in acetone and two cycles in ether are needed. The final nanoparticles are dispersed in 1L of ultra-pure water.

NPs' sorting

To size-sort the biggest MNP, 5 mL of HNO₃ 68% was added to induce destabilization [315]. The dense phase (floculate) with the bigger particules is separated from the supernatant by magnetic decantation. Keep the floculate and repeat this cycle with 5 mL then 3 mL of HNO₃.

Citration

To stabilize the MNPs by electrostatic repulsion in aqueous medium at pH 7, they are citrated to give them negative charges. Add citrate with a 0.13 ratio against number of iron moles. Heat at 80°C for 30 minutes and wash with magnetic decantation using acetone and ether. Disperse in ultra-pure water.

Silica shell synthesis and functionalization

Classical synthesis of NPs A

This classical synthesis stems from a procedure developed and optimized by the PHENIX group [312, 313, 316].

For 700 μL of sorted citrated ferrofluid ($[\text{Fe}]=1.02\text{ M}$), add 50 mL of water, 100 mL of ethanol 99%, 900 μL of TEOS, 1.88 mL of NH_3 30% and leave to react under agitation for two hours.

For the functionalization add 300 μL of TEOS, 350 μL PEOS and 150 μL APTS and leave to react 24 hours. Wash in ethanol and ether with a 15:1 ratio and disperse in 50 mL of a sulfonic acid (MOPS) pH 7.4 buffer. The suspension is stable for months.

Modified synthesis (NPs B, C, D).

Before their coating within the silica shell, increasing concentrations of a NH_4Cl salt ($[\text{NH}_4\text{Cl}]=2.5 ; 4 ; 5\text{ mM}$) were added to the solution in order to more or less agglomerate the cores. Then proceed to the adding of coating agents and redispersion as described for the classical synthesis.

3.1.3 Characterization of core-shell nanoparticles

Iron concentrations

Precise iron concentrations in the samples were needed for later magnetic and grafting experiments. Atomic adsorption spectrometry was performed to access the iron concentration. Previously the samples were allowed to incubate in HCl 37% and diluted in distilled water.

Transmission Electron Spectroscopy (TEM)

TEM examinations were obtained after placing a single drop (6 μL) diluted 1/1000 of the aqueous solution of MNPs onto a copper grid coated with a carbon film. The grid was left to dry in air for several hours at room temperature. TEM analysis was carried out in a Jeol 100cx electron microscope model working at 100 keV. Transmission Electron Spectroscopy allow the observation of the surface morphology with a deep field. TEM gives a good resolution up to the 10^{th} of nm.

Dynamic Light Scattering (DLS)

DLS and ζ -potential measurements were performed on a Zetasizer 3000 HS Malvern at room temperature. Each sample was diluted in MOPS at pH 7 and was measured three times, combining 10 runs per measurement.

Magnetostatic SQUID measurements.

Magnetostatic measurements were performed on a SQUID magnetometer. SQUID measurements on liquids were done on 10 times concentrated solutions and on powders (dehydration in an oven at 70°C).

AMF assays

The AMF assays were performed on the Magnetherm from Nanotherics with a frequency around 535 kHz and a field of 10.56 kA m^{-1} . The ferrofluid sample ($V=500 \mu L$) is introduced into a copper coil, which is part of a resonant RLC circuit producing an AC magnetic field in the frequency range 300-550 kHz and with amplitudes up to 10.56 kA m^{-1} . The coil is cooled by a water circulation to get rid of the influence of thermal gradients. The bulk solution temperature was measured with a nonmetallic optical fiber (Fluoroptic, Luxtron Corp.) placed in the center of the sample. The rise in temperature was approximated by a linear increase as a function of time dT/dt . The Specific Loss Power of the nanoparticles was calculated according to Equation 3.1.

$$SLP = \frac{m_{total}}{m_{mag}} \cdot c_p \cdot \frac{dT}{dt} \quad (3.1)$$

with c_p the specific calorimetric capacity of water and m_{total} and m_{mag} the total mass of the sample and the mass of magnetic material, respectively.

Quantitative measurements of the NH_2 groups functionalized

The NH_2 coverage was quantified with the fluorescamine test in fluorescence. The fluorescamine solution was prepared with 5.6 mg of fluram in ethanol 99%. The standards were prepared with 0.56 g of APTS in ethanol 99%. The five standards respectively made with 0, 20, 80, 160 and 260 μL of the APTS solution in 10 mL graduated flask and then 20 μL was withdrawn in each, poured in all transparent spectrophotometer cuvettes and completed with the stock solution. The standards were then allowed to incubate 2 h in the dark.

Amino concentrations were measured with a fluorescence spectrophotometer Cary Eclipse ($\lambda_{excitation}=390 \text{ nm}$; $\lambda_{emission} = 480 \text{ nm}$).

3.1.4 DNA grafting

Single strand protocol

Our DNA probe to be loaded has been modified with a carboxy tail in order to be coupled to the NH_2 NPs via a peptidic EDC/NHS coupling. The chosen process was a two step process after optimization. First, in a total 1 mL MOPS/NaCl 0.5 M solution, CO_2H -DNA were activated in a 100 equivalent of EDC and NHS solution for 20 minutes (0.05 g of each were dissolved in 5 mL of dionized water and a volume corresponding to 100 equivalent of the introduced amount of DNA-probe was withdrawn and introduced in the reacting medium). Then 78 μL of NPs were introduced in the medium and left to react overnight. Separation between loaded nanoparticles and ungrafted DNA was done using Miltenyi MS Columns with a double MOPS/NaCl washing.

Double-strand protocol

First the target DNA was put to hybridize with the probe during 30 minutes in a 1 mL MOPS buffer with 0.5 M NaCl. Then 100 equivalent of EDC and NHS was poured into the solution during 20 minutes to activate the carboxy functions of the probe DNA. Finally the nanoparticles were added and left to react overnight. Separation between loaded nanoparticles and ungrafted DNA was done using Miltenyi MS Columns.

DNA quantitation measurements

All DNA quantitation measurements were done using fluorescence spectroscopy performed on a Cary Eclipse fluorimeter ($\lambda_{excitation}=480$ nm, $\lambda_{emission}=520$ nm) with the Quant-iT Oligreen ss DNA Assay Kit from Invitrogen [317]. Calibration curve of Quant-iTTM Oligreen was realized with standards of our own DNA as shown on Figure 3.1 for the probe and target calibration. Samples in 4mL cuvettes were excited at 480 nm. The fluorescence emission intensity was measured at 520 nm using a Cary Eclipse Spectrofluorometer and plotted as a function of oligonucleotide concentration.

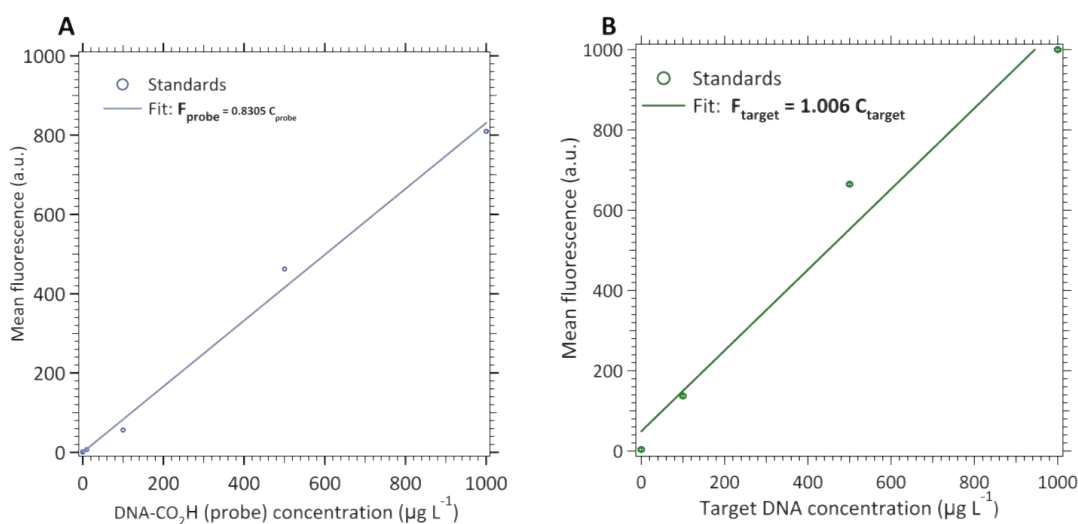


Figure 3.1: Linear quantitation of our DNA probe (A) and target (B) using the Quant-iT Oligreen ssDNA reagent.

3.2 Synthesis and characterization of Core-shell Nanoparticles

3.2.1 Maghemite cores

Numerous iron oxide MNP process roads

Numerous synthesis processes allow a precise control over size and shape of iron oxide NPs in solution. Some physical methods exist as gas phase decomposition or electronic lithography but can not control any sizes at the nanoscale. Chemical methods (sol-gel, oxidation, co-precipitation, nanoreactors) have proven their value to produce NP under 15 nm in diameter in terms of easiness to control the shape and the composition. To obtain bigger NP (30 to 100 nm) for easy magnetic manipulation or heating power literature is less prolific. The most interesting methods are reported in Table 3.2.

Table 3.2: Various iron oxide MNP process roads.

| Method | Conditions | Time | Solvent | Size (distribution) | Reference |
|------------------|------------|---------|---------|-----------------------|-----------|
| Co-precipitation | Easy | Minutes | water | <20 (+) | [314] |
| Thermal decay | Difficult | Days | organic | \leq 20(++) | [318] |
| Microemulsion | Difficult | Hours | organic | \leq 50(+) | [319] |
| Polyol | Easy | Hours | organic | <10(++) | [320] |
| Hydrothermal | Easy | Days | water | <10 ³ (++) | [321] |

In the lights of this rapid overview chemical precipitation of Fe^{2+} and Fe^{3+} cations is without doubt the easiest and quickest way to synthesized NP according to our expectations (size below the SPM barrier 50 nm and below the monodomain critical value 18 nm, high yield, synthesis in water, flexible post functionalization).

Co-precipitation benefits are numerous. We can cite cheap reactants, mild conditions possible in water, final concentrated solutions in iron and a flexible synthesis both for size and surface properties of the NP. Two of the few limitations stands on the number of parameters and the relatively large size distribution that can be compensated with a sorting.

Maghemite NP synthesis via co-precipitation

The reaction is done in an aqueous single phased liquid allowing to control germination and growth of iron hydroxide seeds. The synthesis consists in iron oxide precipitation by adding a base in Fe^{II} and Fe^{III} . The precipitate is isolated with magnetic decantation and stabilized by adding concentrated acid and base. Size shape composition and reproducibility depends on the type of salt used (chlorates, sulfates, nitrates), on the Fe^{2+}/Fe^{3+} ratio, the temperature of the reaction, the pH value, the ionic concentration of reactants and the nature of the base. Massart and Cabuil [314] were among the first to precisely determine the key parameters to control the yield and the size of magnetite or maghemite NP (between 3 and 20 nm) by

playing among other parameters on pH and the nature of the base. Conversion in maghemite is easily realized by chemical oxidation of magnetite.

Figure 3.2 describes the different steps of the synthesis of maghemite nanoparticles $\gamma\text{-Fe}_2\text{O}_3$ from colloidal magnetite obtained by co-precipitation in a ferric and ferrous basic chloride solution.

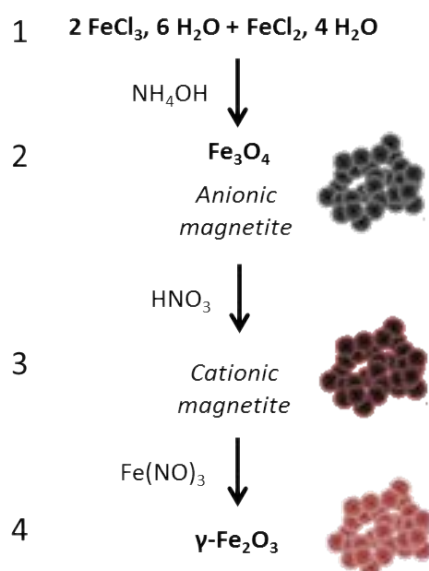


Figure 3.2: Scheme of the maghemite synthesis (inspired from Mornet *et. al.* [191]).

The synthesis starts with an inorganic polycondensation resulting in the formation of two precursor $\text{Fe}_2(\text{OH})_4$ and $\text{Fe}_3(\text{OH})_6$. The molar fraction in Fe^{2+} leading to the best yield in maghemite is the one of the stoichiometric conditions e. g. 0.33. When the precursor concentration reaches a limit value, magnetite germs are formed (nucleation) and grow according to the Oswald mechanism (germs growth). The germs formation is controlled by the precursor concentration that blocks nucleation when reaching an inferior limiting value and leading to maturation and ageing of germs. This process in four steps (precursor, nucleation, growth and ageing) was described by La Mer in 1950 [322].

Size and shape are tuned by the ratio of $\text{Fe}^{II}/\text{Fe}^{III}$, temperature, pH and the nature of the base. For small and monodispersed particles, a high speed of nucleation and a low speed of growth is needed. Magnetite nanoparticles are oxidized in acid medium leading to the formation of maghemite $\gamma\text{-Fe}_2\text{O}_3$.

Magnetic properties of fine particles are size dependent and influenced by the polydispersity of the sample [323]. Size sorting with nitric acid destabilization allows to separate the dense phase (where all the biggest nanoparticles are) from the supernatant [315].

For biological applications, nanoparticles need to be dispersed in a pH 7.4 with an ionic strength of 100 nM. At pH 7, maghemites are at their zero charge point (ZCP) and thus foculate due to the lack of electrostatic repulsions. That is why they are citrated to give rise to nanoparticles charged between pH 4 and 10. They are negatively charged at pH 7.

Characterizations of the synthesized maghemite superparamagnetic nanoparticles

After synthesis, we obtain a batch of size-sorted maghemite nanoparticles, which polydispersity will be assessed by Transmission Electron Microscopy (TEM) in this section, with an iron concentration of 1.0 M, determined by atomic adsorption spectroscopy (see section 3.1.3).

Two techniques are widely used to characterize the size and the aggregation state of nanoparticles as well as their surfacic charge: Dynamic Light Scattering (DLS) and Transmission Electron Microscopy (TEM). The latter gives information on the size and the morphology of the particles. The principle of this technique is based on the interactions electron-material. An incident beam of electrons is sweeping the surface of the sample. The inelastic diffusion of these electrons through the material brings out the emission of secondary electrons from the core levels of the atoms. The emitted quantity is function of the surface topography and the atomic number of the atoms. The image reflects the composition of the surface. However TEM does not reflect their dispersion state as particles are dried out. DLS is complementary to TEM insofar as it informs on the size distribution of the particles dispersed in aqueous medium. The mean hydrodynamic diameter measured differs from the physical diameter as it reflects the solvated particles with their double layer and changes strongly with the flocculation state of the system.

Size distribution

Ferrofluid samples e.g. a colloidal suspension of magnetic monodomain particles of typical size 10 nm [138] are never completely monodisperse and a log-normal distribution P is usually assumed [139], see Chapter 1 Section 1.4.1. The mean diameter d of spherical magnetic particles and polydispersity index σ from the log-normal distribution can be extracted from the log-normal fittings as shown on Figure 3.3.

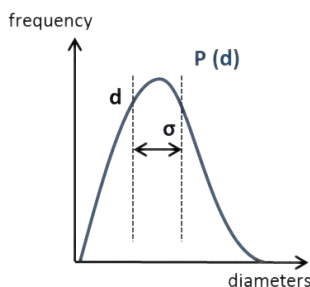


Figure 3.3: d_0 and σ parameters extraction from log-normal fitting curves.

First a comparison was made between sorted and non sorted MNP as shown on Figures 3.4 and 3.5. A histogram $P_{obs}(d)$ of the size distribution is realized by particles' counting on TEM images by Image J on about 200 particles. Size numbering were fitted (red line) with the log-normal distribution. The aggregation state of the particles were investigated in the form of DLS measurements (green sticks).

Figure 3.4 displays polydispersed particles with a mean physical diameter d_{TEM} of 7 nm ($\sigma=0.27$). Particles are well dispersed according to the measurement of their mean hydrodynamic diameter (green stick) of d_{hydro} 13.5 nm. The hydrodynamic

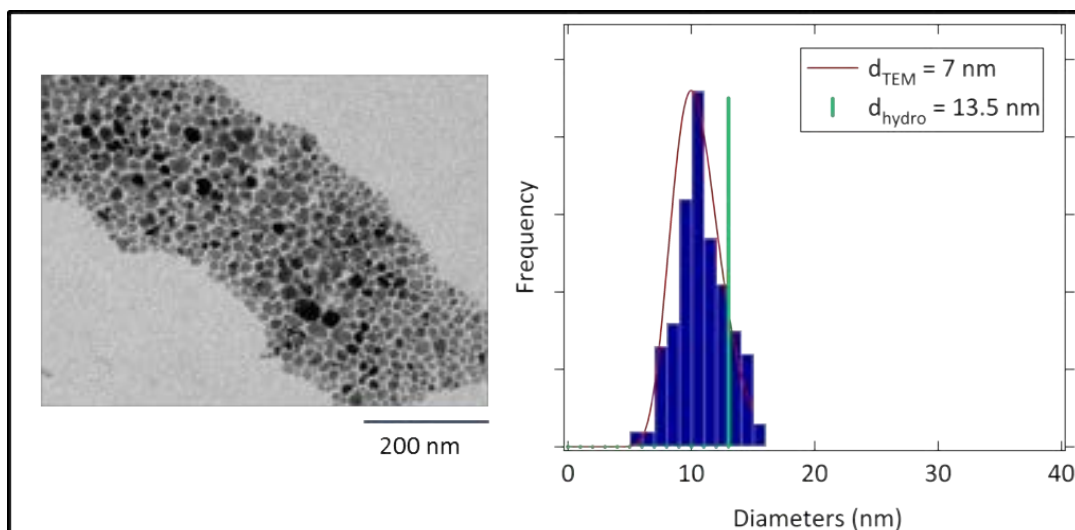


Figure 3.4: Initial MNPs obtained by a classical Massart Synthesis in Transmission Electron Microscopy and size numbering fitted with the Langevin model. Particles counting was done by Image J on 200 particles

diameter differs from the physical diameter as it reflects the solvated particles with their double layer.

In order to have more efficient particles regarding their magnetic properties, cores were sorted to retain the biggest particles in order to decrease the polydispersity index. Indeed particularly for magnetic hyperthermia, it has been observed that size dispersion strongly weakens the heating efficiency of samples between 12 and 17 nm diameters [142]. Size selection with nitric acid to induce destabilization is causing larger particles to precipitate and leaving smaller and nearly monodisperse particles in the supernatant. Results are shown on Figure 3.5.

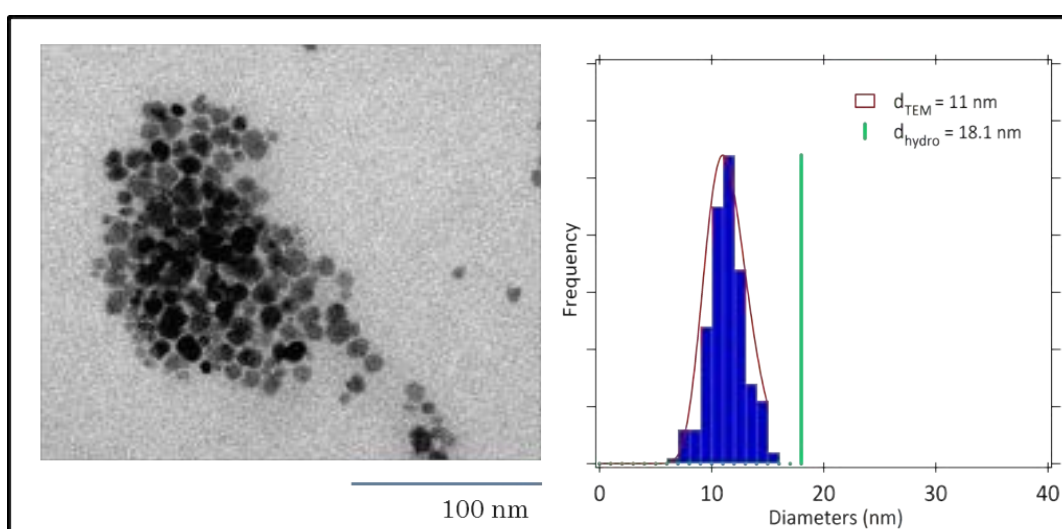


Figure 3.5: Sorted MNPs of 11 nm in diameter obtained by a Massart Synthesis and sorting in Transmission Electron Microscopy and size numbering fitted with the Langevin model. Particles counting was done by Image J on 200 particles

3.5 TEM image displays spherical particles with no sign of aggregation corroborated with a DLS diameter of 18.1 nm in diameter indicating well dispersed particles. The size histogram show a narrower distribution with a mean physical diameter of 11 nm ($\sigma=0.17$) indicating the success of our sorting.

Following is a magnetic characterization of sorted cores to provide a basis for further magnetic investigations of the future encapsulated system.

Magnetostatic measurements

As discussed in Chapter 1 section 1.4.1, one striking characteristics of the ferrofluids is their superparamagnetic behaviour. On Figure 3.6 the magnetization curve of both MNP in powder and in liquid state are displayed. Their magnetization curves show no hysteresis cycle at 290 K, a superparamagnetic characteristic. As far as the ferrofluid solution is diluted (magnetic interactions between grains are negligible) and that the suspension is monodisperse, magnetization can be described as a symmetric sigmoid described by Langevin:

$$M = M_{sat} \left(\coth x - \frac{1}{x} \right) \quad (3.2)$$

with

$$x = \frac{\mu_0 \cdot m_s \cdot V \cdot H}{k \cdot T}$$

μ_0 the vacuum magnetic permeability, M_{sat} the saturation magnetization of the solution is equal to $m_s \cdot \phi$, m_s the saturation magnetization of the magnetic material, ϕ the volume fraction of particles in suspension and $k \cdot T$ the thermal motion energy.

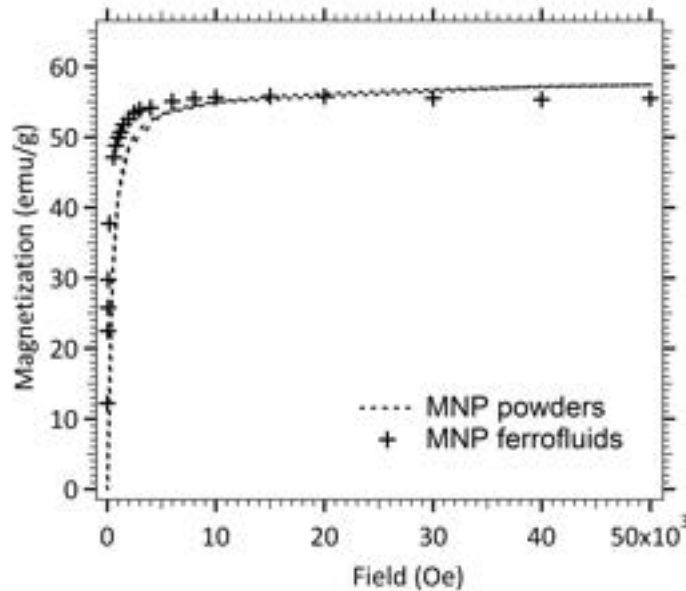


Figure 3.6: Magnetostatic measurements on sorted bare cores MNP in powder (dotted line) and ferrofluid state (black crosses).

On 3.6, the saturation magnetization of MNP in liquid state and powder state yield around the same saturation magnetization M_{sat} value 57 emu g^{-1} . $m_s = M_{sat} / \phi$ (ϕ the volumic fraction of magnetic material) can be compared to $\overline{m_s}$ the saturation

magnetization of bulk γ -Fe₂O₃ (85 emu g⁻¹). These values are lower compared to the bulk maghemite but reach the reported value for nanometric maghemite (60 emu g⁻¹) due to surface effects.

The measurement of the saturation magnetization M_{sat} of powders allows to extract the M_{sat} value and the magnetic concentration through ϕ , the volumic fraction of particles in suspension, yielding a 0.077 M iron concentration. This value differs from the 0.1 M concentration determined by atomic adsorption spectroscopy, the difference may come from a titration imprecision. We will keep the 0.077 M value for the following analysis. From the sigmoid of fluids a magnetic stability can be noted and the magnetic size of the particles and their polydispersity can be assessed [324].

Measurements under an alternative magnetic field (AMF)

As discussed in Chapter 1, magnetic hyperthermia on maghemite nanoparticles e.g. local heating by Néel relaxation of a superparamagnetic nanoparticle under an alternative magnetic field exhibit heating properties.

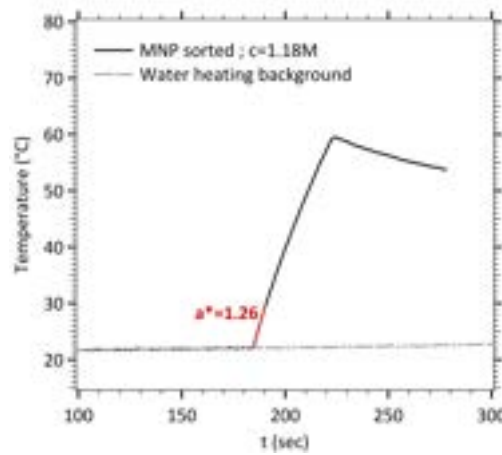


Figure 3.7: Magnetic hyperthermia on sorted bare cores MNP against water heating due to heating of the coil.

Figure 3.7 displays the increase in temperature of the sorted MNP of 11 nm (physical diameter). The rise in temperature is not a straight line due to thermal losses of the non adiabatic chamber. We thus took only the 30 first second to calculate the dT/dt from which we subtracted the initial slope corresponding to the water heating (dotted line) yielding a a^* corrected slope. With the massic specific heat capacity of water c_p (4185 J kg⁻¹ K⁻¹) and m_{mag} (Equation 3.4, V_{tot} is the total volume of the suspension, ρ_{mag} their volumic mass, equal to 5.07 g cm⁻³, ϕ their volumic fraction in suspension), the SLP is given by Equation 3.3.

$$SLP = \frac{m_{tot}}{m_{mag}} \cdot c_p \cdot \frac{dT}{dt} \quad (3.3)$$

$$m_{mag} = \phi \cdot V_{tot} \cdot \rho_{mag} \quad (3.4)$$

Equation 3.3 can be simplified in

$$SLP = \frac{\rho_0}{\phi \cdot \rho_{mag}} \cdot c_v \cdot \frac{dT}{dt} \quad (3.5)$$

by replacing m_{mag} by its expression from Equation 3.4 and m_{tot} by $\rho_0 \cdot V_{tot}$ with ρ_0 the volumic mass of the sample, diluted. The volumic fraction of magnetic material can be further expressed in:

$$\phi = \frac{V_{mag}}{V_{tot}} \quad (3.6)$$

with the volume of magnetic material V_{mag} equals to m_{mag} / ρ_{mag} . The mass of magnetic material m_{mag} can be expressed with the molar concentration in iron in solution $c(\text{Fe})$:

$$m_{mag} = c(\text{Fe}) \cdot V_{tot} \cdot \frac{M_{\text{Fe}_2\text{O}_3}}{2} \quad (3.7)$$

with $M_{\text{Fe}_2\text{O}_3}/2$ the molar mass of magnetic material. Equation 3.7 is leading to:

$$\phi = \frac{V_{mag}}{V_{tot}} = c(\text{Fe}) \cdot \frac{M_{\text{Fe}_2\text{O}_3}}{2 \cdot \rho_{mag}} \quad (3.8)$$

Numerical application in Equation 3.8 can lead to further simplification:

$$\phi = \frac{160}{2.5070} \cdot c(\text{Fe}) = 0.0158 \cdot c(\text{Fe}) \quad (3.9)$$

with $2 \cdot M_{\text{Fe}_2\text{O}_3}$ equals to 160 g mol^{-1} and ρ_{mag} equals to 5070 g L^{-1} .

Finally the volumic fraction of magnetic material in percent is given by:

$$\phi(\%) = 1.5 \cdot c(\text{Fe}) \quad (3.10)$$

with $c(\text{Fe})$ the iron concentration of the solution in mol L^{-1} .

Our sorted cores reach the value of 57 W g^{-1} consistent with the reported 60 W g^{-1} value of maghemite for our experimental conditions (535 kHz, 10.56 kA/m).

3.2.2 Core-shell Nanoparticles

The use of nanoparticles for manipulation and loading purposes are conditioned by their hydrodynamical size, morphology and magnetic size. Once our core-shell nanoparticles were fully characterized with Transmission Electron Spectroscopy (TEM), Supra Quantum Interferometric Device (SQUID) and Diffusion Light Scattering (DLS) their heating efficiency were assessed with magnetic hyperthermia.

Encapsulation, a modified synthesis with pre-aggregation

Even if it has not been clearly demonstrated that an increase in magnetic material induces an increase in heat dissipation observations tend to point in that direction. In any case, an increase in size comes with an increase in DNA loading. We thus turned our focus on increasing the cores' sizes of our particles and along with it the size of the global particle with its coating. The simplest way to increase core size is to put together several maghemite cores together thanks to an aggregation with a NH_4 salt by playing on the destabilization of the nanoparticles induced by an increase in

ionic strength i.e. screening of electrostatic repulsion. It should be noted that, so far, no one reported the increase of SLP through core aggregation.

Before encapsulation, the agglomerated cores were screened by DLS to be seen on Figure 3.8.

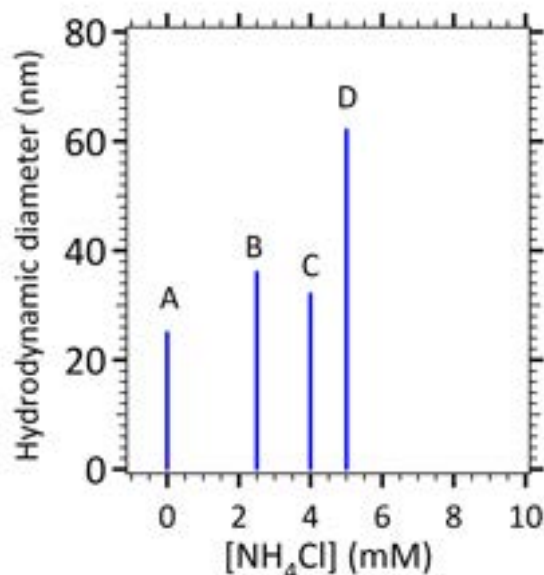


Figure 3.8: DLS of agglomerated cores vs the concentration of NH₄Cl salt introduced.

Nanoparticles functionalization

Protection of the iron oxide nanoparticles with a silica shell remains a classical process in the context of biologic applications. Chemically stable in aqueous medium (pH < 9), silica is easily functionalizable with various chemical functions (amines, carboxy acids) allowing a covalent grafting of the molecules of biological interest. Finally silica allows to shield dipolar interactions by pulling away the magnetic cores one from another.

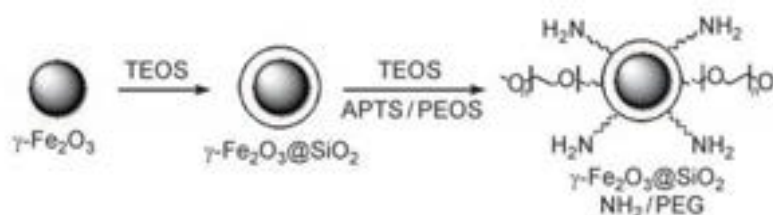


Figure 3.9: Scheme of the maghemite encapsulation with silica and subsequent functionalization with PEG chains and amine groups.

Two main synthesis roads are available for silica functionalization of nanoparticles. Sol-gel [325] and microemulsion in a micellar microreactor [326]. For this work, the sol-gel process was chosen as it is easy, without surfactants and allows high scale synthesis.

The sol-gel process starts with the condensation of a silica monomer (RSi(OR)_3 alkoxy silane) on the surface of iron oxide nanoparticles. Follows a two-step process: hydrolysis and condensation initiated in an acid or basic medium in a mixed medium water/ethanol [325]. During hydrolysis, silanol are formed and give rise to siloxane by intermolecular condensation. Siloxane condense on hydroxyl sites on the surface of iron oxides resulting in a silica layer as pictured on the Figure 3.10 of our maghemite cores encapsulated in a silica shell of ca. 15 nm. pH, temperature, solvent, alkoxy silane are sensitive parameters to play on in order to tune the silica shell [306, 312]. The grafting of functionalized organosilane to introduce covalently a reactive chemical function on the silica surface is preferred to the alternative of chloration (no secondary toxic products) [327].

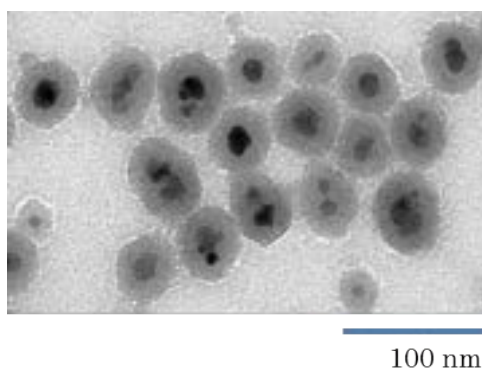


Figure 3.10: TEM picture of encapsulated cores in a silica shell.

Silanol groups then condense on silica and reticulate to give rise to the silica network. TEOS, first to be added, start the reticulation of the silica network and facilitate condensation of APTS and PEOS. APTS is introduced lastly as its autocatalytic properties make its condensation speed higher than the one of the PEOS and so let it condensate on silica germs. The reaction is stopped by ether that precipitate nanoparticles by decreasing the dielectric constant of the medium. The liquid phase and organosilanes that have not reacted can thus be eliminated. Final redispersion is realized in MOPS pH7.4.

Colloidal stability

The colloidal state is characterized by a large specific surface compared to the volume. The particles chemical behavior is thus governed by the surface properties. Colloidal interactions are particularly crucial for nanoparticles as they overcome gravity. Two types of interparticular interactions can be distinguish: the forces describe by the DLVO theory and sterical repulsions.

Van der Waals attractive forces are issued from the electronic charge fluctuation around atoms. It is mostly an induced dipole-induced dipole interaction in r^{-6} (r , atomic radius) with an action area from 0.2 to 10 nm.

Two types of repulsive interactions are at work: electrostatic forces and steric hindrance. Electrostatic repulsion corresponds to the net charge at the surface of the particle (adsorption of charged ions, dissociation or ionisation of surface groups). It is described by the double layer model (Figure 3.11).

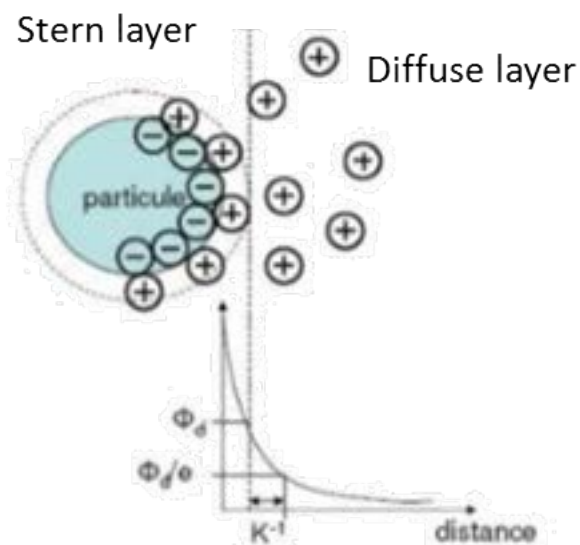


Figure 3.11: Scheme of the Stern and diffuse layer around a particle.

The internal Stern layer is composed of counter ions strongly adsorbed and solvent molecules. The external layer of diffuse layer is composed of counter ions subjected to the electronic potential of the surface and to thermal motion. Internal radius of this layer corresponds to the hydrodynamical radius (electronic potential $\Phi d \approx \zeta$, potential zeta) and is delineated by the shearing plane of the solvent when the particle is in motion. When two charged particles are interacting, their diffuse layers are interpenetrating. Local concentrations in counter ions are locally increasing, leading to a repulsive potential. For short and long distances, Van der Waals interactions are dominating but for a distance near the Debye-Huckel shielding length, electrostatic repulsion prevails. Debye-Huckel length imposes an energy barrier which depends on surfacic charges and ionic forces and have to be compared to the thermal motion energy $k_B T$.

To conclude, more ionic forces are weak and surfacic charges high, more the particles are stable in solution.

A third type of interaction to note is steric hindrance. The presence of organic molecules adsorbed or chemically linked allows to decrease the approach distance between molecules (higher than the action field of Van de Waals forces).

Colloidal stability is an interaction game (attractive and repulsive) between particles in solution [328]. Magnetic dipolar interactions and Van der Waals forces tends to aggregate the particles. Steric (PEG) and electrostatic (presence of ionisable groups) repulsions maintain the balance.

Number of objects in solution

A spectrometric dosage of atomic adsorption gives an iron concentration of the final suspension of 15 mM.

Using the volumic mass of iron oxide $\rho_{mag} = 5.07 \text{ g cm}^{-3}$ and its molar mass $M_{FeO_{1.5}} = 80 \text{ g mol}^{-1}$, the volumic fraction of nanoparticles in suspension can be written according to Equation 3.11.

$$\phi(\%) = 1.5.c(Fe) \quad (3.11)$$

From the volume filled by the nanoparticles in $700 \mu\text{L}$ of maghemite

$$V_{mag} = \phi.V_{tot} \quad (3.12)$$

and the volume filled by one nanoparticle:

$$V_p = \frac{4}{3}\pi R_{mag}^3 \quad (3.13)$$

The number of maghemite nanoparticles in $700 \mu\text{L}$ is obtained by:

$$N_{mag} = \frac{V_{mag}}{V_p} \quad (3.14)$$

And by counting the number of cores in each silica shell N_{core} , the number of core-shell N_{CS} is obtained by dividing N_p by the number of cores.

$$N_{CS} = \frac{N_{mag}}{N_{core}} \quad (3.15)$$

From an iron concentration of 15 mM , a value of ca. $2.6 \cdot 10^{16}$ Core-shell nanoparticles can be deduced.

TEM measurements: From spherical to elliptical morphology

The size distribution of both core and core-shell particles are following a log normal law. Particles are defined as A, B, C and D for reading clarity as their diameter is increasing.

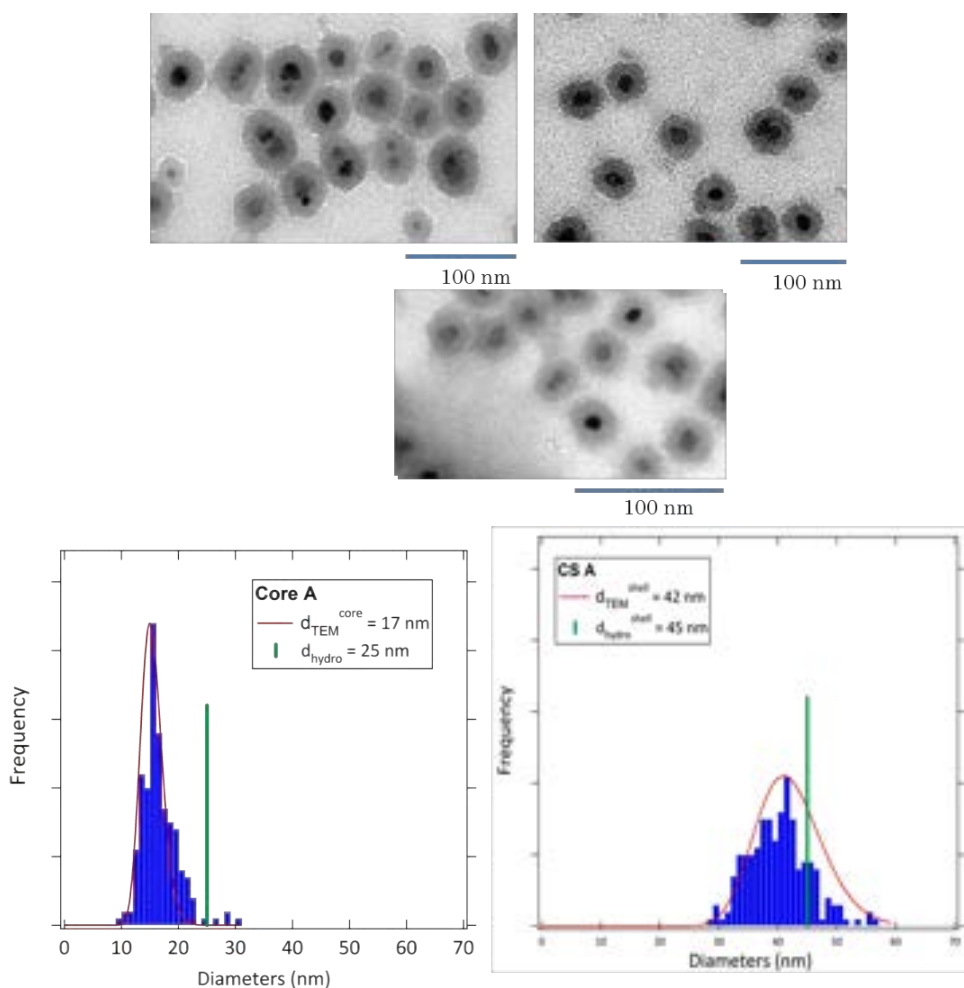


Figure 3.12: Transmission Electron Microscopy pictures of CS A. Size numbering fitted with the Langevin model and DLS measurements.

CS A are spherical particles as depicted on Figure 3.12. A majority of one encapsulated cores per silica shell can be seen.

The red line corresponds to the best fit of log-normal distribution $P(d)$ yielding a physical diameter of $d_{phys}^{CS} = 42$ nm for the total core-shell ($\sigma = 0.19$) and 17 nm ($\sigma = 0.17$) for the cores. Particles counting was done by Image J on 200 particles. Particles are well-dispersed both as MNP and encapsulated particles indicated by their hydrodynamic diameters (25 and 45 nm respectively).

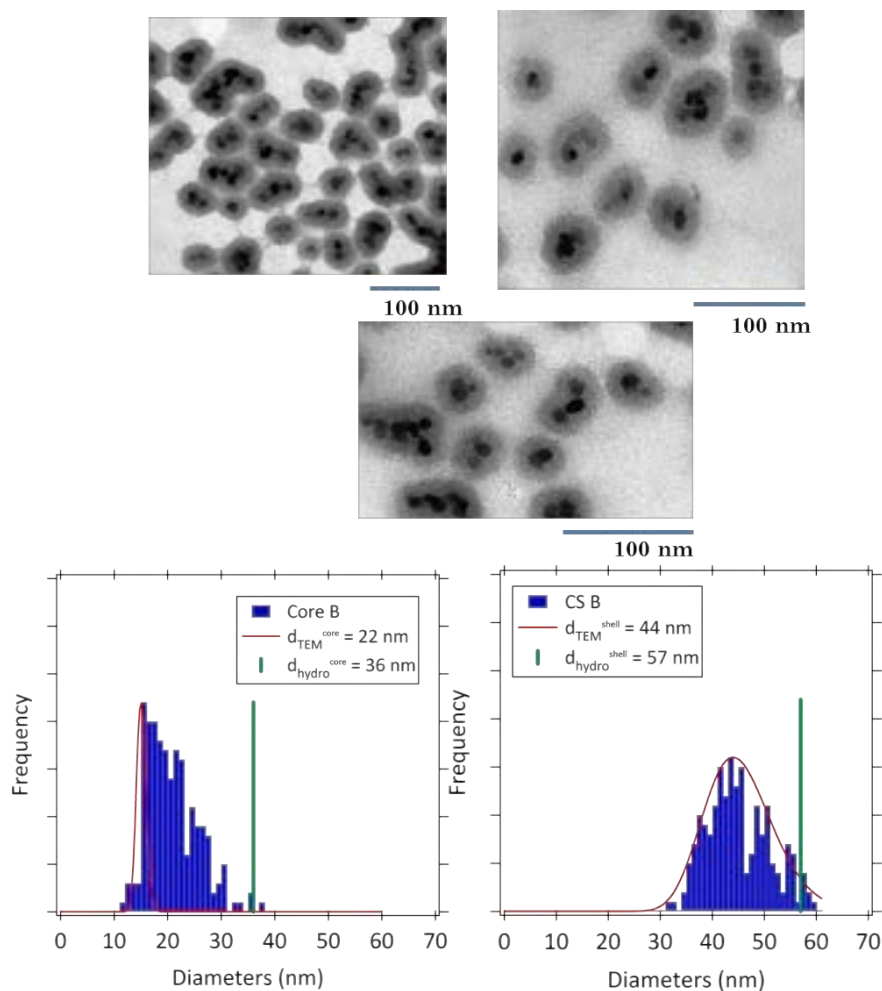


Figure 3.13: Transmission Electron Microscopy pictures of CS B. Size numbering fitted with the Langevin model and DLS measurements.

CS B are spherical particles as depicted on Figure 3.13. In average, three magnetic cores are encapsulated in a single silica shell.

Particles are yielding a physical diameter of $d_{phys}^{CS} = 44$ nm for the total core-shell ($\sigma = 0.22$) and 22 nm ($\sigma = 0.10$) for the cores. Particles counting was done by Image J on 200 particles. Particles are well-dispersed both as MNP and encapsulated particles indicated by their hydrodynamic diameters (36 and 57 nm respectively).

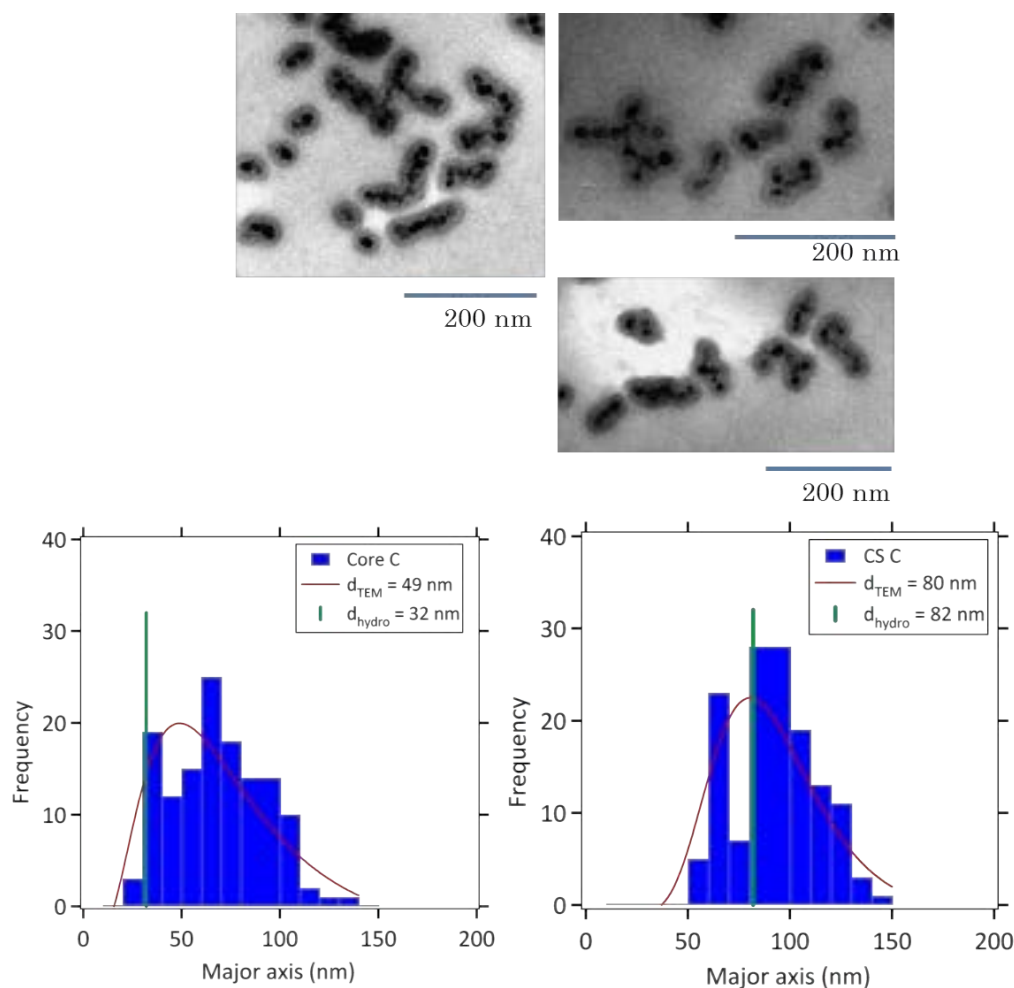


Figure 3.14: Transmission Electron Microscopy pictures of CS C. Size numbering fitted with the Langevin model and DLS measurements.

CS C have a more elliptical shape forming short chains as depicted on Figure 3.14. In average, five magnetic cores are encapsulated in a single silica shell.

Particles counting was done by Image J on 150 particles with an elliptical fitting. CS chains length is 80 nm in average and the length of the aggregated cores in their silica shell reaches 49 nm.

Particles are well-dispersed both as MNP and encapsulated particles indicated by their hydrodynamic diameters (32 and 82 nm respectively). One should note a smaller hydrodynamic diameter for the cores compared to the TEM diameter. DLS is measured on aggregated cores before encapsulation. Cores may have aggregated even more during the functionalization step.

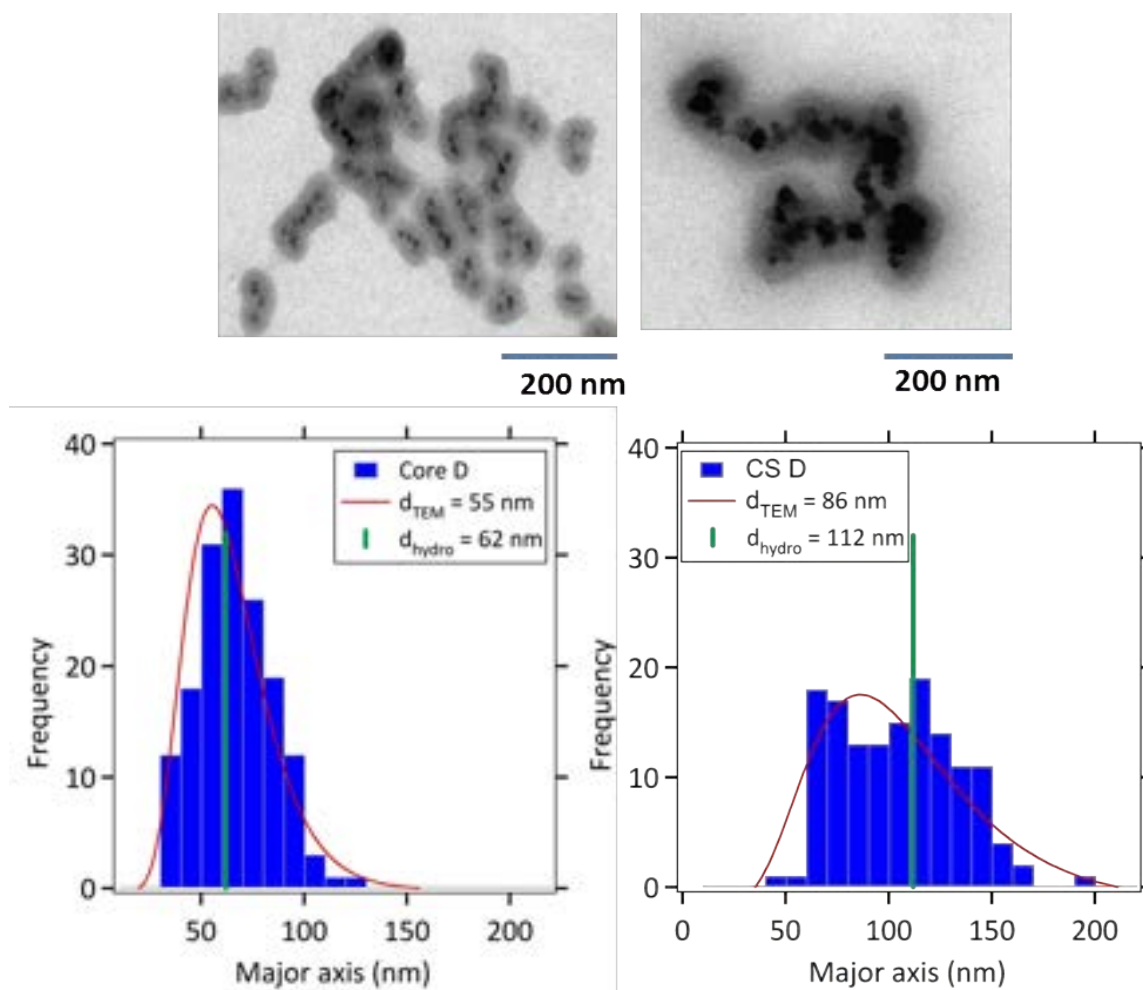


Figure 3.15: Transmission Electron Microscopy pictures of CS C. Size numbering fitted with the Langevin model and DLS measurements.

CS D show also elliptical shapes forming short chains as depicted on Figure 3.15. The shape are more blurry and its rather difficult to count the number of cores inside a shell, which is itself difficult to distinguish one from another.

Particles counting was done by Image J on 150 particles with an elliptical fitting. CS chains length is 86 nm in average and the length of the aggregated cores in their silica shell reaches ca. 55 nm.

Even if TEM images displays not well defined particles, DLS measurements are indicating well-dispersed particles both as MNP and encapsulated particles indicated by their hydrodynamic diameters (62 and 112 nm respectively) near from their physical diameters.

Obtained core-shell nanoparticles are to be seen on Figure 3.16. Table 3.3 summarizes the salt conditions used and the resulting TEM physical diameters.

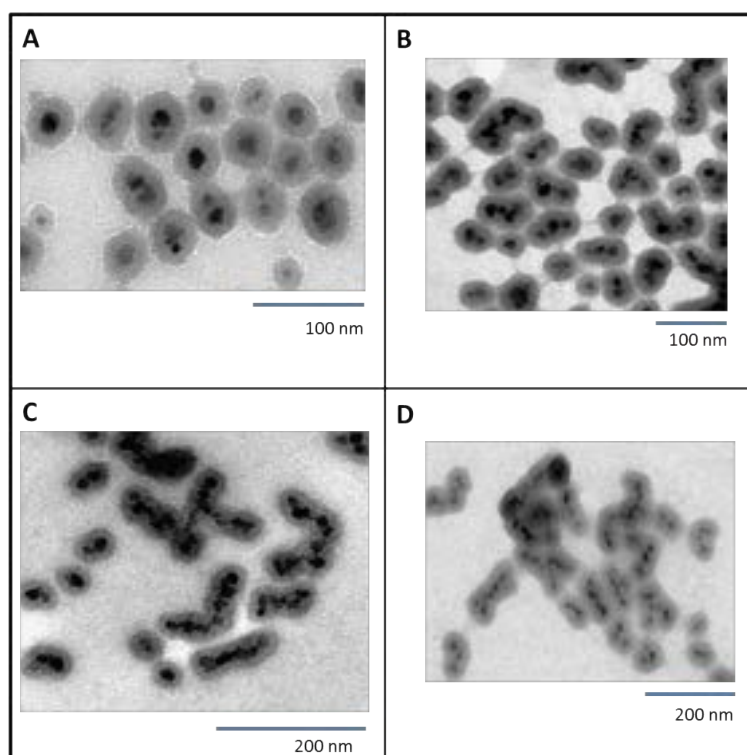


Figure 3.16: TEM images of A, B, C and D nanoparticles as their diameter increases.

Table 3.3: Particles and their TEM sizes.

| Particles | TEM diameters (nm) | | [NH ₄ Cl] (mM) |
|-----------|--------------------|-------------|---------------------------|
| | d_{core} | d_{total} | |
| Spheres | | | |
| A | 17 | 42 | 0 |
| B | 22 | 44 | 2.5 |
| Ellipses | | | |
| C | 49 | 80 | 4 |
| D | 55 | 86 | 5 |

The CS particles are characterized by a mean hydrodynamic diameter from 45 to 112 nm. Diffusion light scattering gives the dispersion state in the aqueous medium and the hydrodynamical size. The latter matches the size of the particles with their double layer solvated so increased compared to the physical TEM diameter.

The physical size range achieved is shifting from a spherical morphology (45 to 57 nm in diameter) to an elliptical morphology (up to 86 nm of the chain length) where maghemite sorted cores form short chain-like structures inside the silica shell. This property was attributed to an alignment of the magnetic domains during the synthesis and will be further discussed in Section 3.2.2.

For the biggest nanoparticles (C and D), a sampling has been done to test the robustness of our Image J counting especially in the case of elliptical particles where

the enumeration of each individual particle is a challenge (see 3.17 and 3.18). To do so, each list of size counting was divided into 3 and reorganized in an ascending order thanks to the generation of a random number. From each list, a size histogram was created and the Langevin model applied.

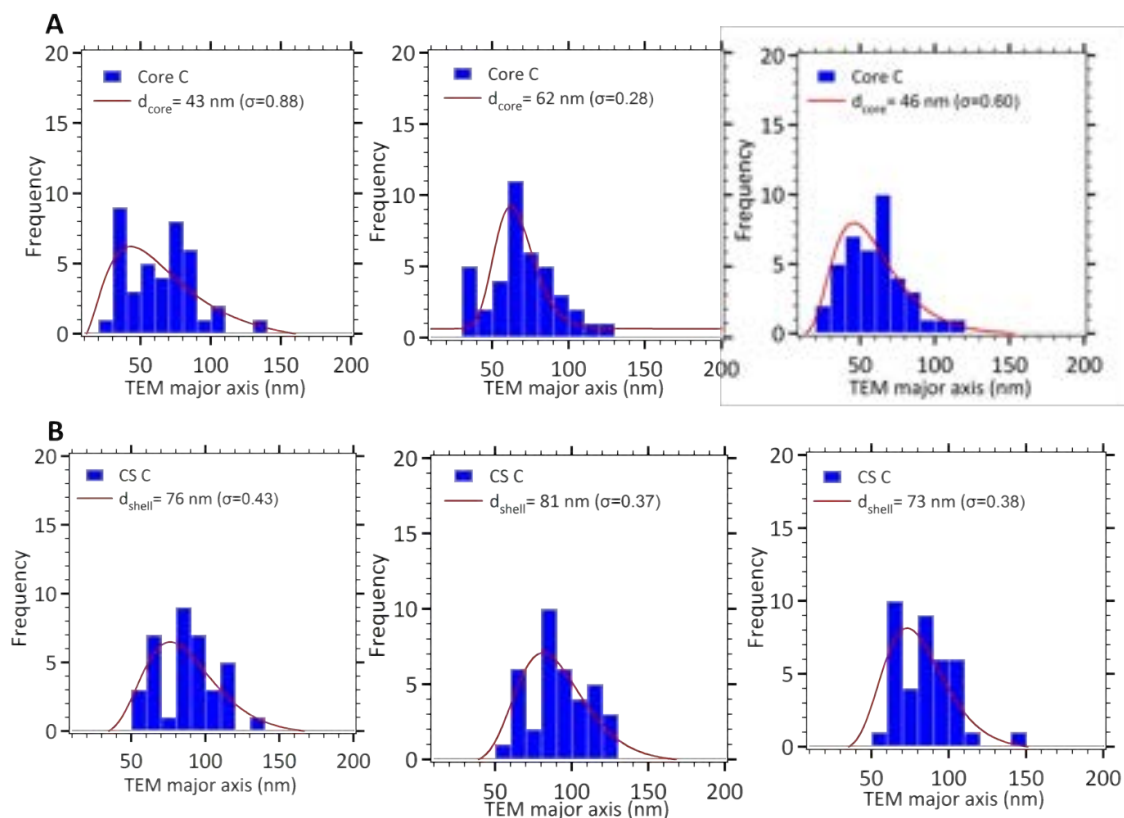


Figure 3.17: Sampling of core C (A) and CS C (B) on Transmission Electron Microscopy data and size numbering fitted with the Langevin model. Particles counting was done by Image J on 150 particles

The l_{core} , l_{total} and σ values are sum up in Table 3.4.

Table 3.4: Mean length l_0 and polydispersity index σ variations in sampling of C and D particles.

| Particles | TEM core diameters (nm) | | TEM shell diameters (nm) | |
|-----------|-------------------------|----------|--------------------------|----------|
| | l_{core} | σ | l_{total} | σ |
| C | 46 | 0.60 | 81 | 0.37 |
| | 62 | 0.28 | 73 | 0.38 |
| | 43 | 0.88 | 76 | 0.43 |
| D | 52 | 0.58 | 85 | 0.60 |
| | 51 | 0.50 | 91 | 0.39 |
| | 60 | 0.34 | 64 | 0.10 |

The l_{core} and l_{shells} values obtained for both C cores and shells respectively, matches the mean diameter of the global counting with consistent σ values validating our Image J counting. For CS D, it is rather unclear, mainly due to the fact

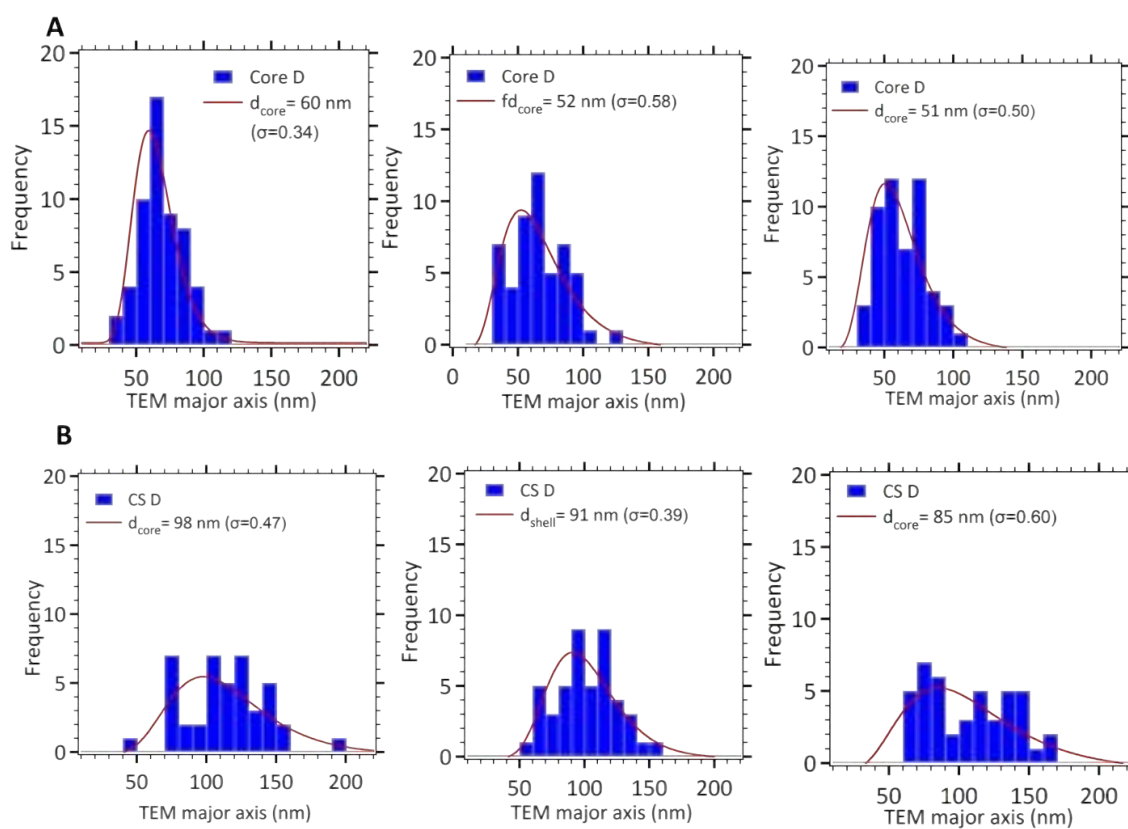


Figure 3.18: Sampling of core D (A) and CS D (B) on Transmission Electron Microscopy data and size numbering fitted with the Langevin model. Particles counting was done by Image J on 150 particles

that TEM images do not display well-defined particles.

To conclude, pre-aggregation of maghemite cores before encapsulation allows to play on the morphology and the size of the CS particles even if bigger particles (D) are not that well defined and TEM pictures show some polydispersity. Anyhow the synthesis is easy robust and efficient.

Magnetic characterization of the capture unit

When core-shell particles are composed of multiple magnetic cores they also exhibit a super paramagnetic behavior. In an initial approximation we assume magnetic cores have few interactions between them. The magnetic momentum of the particle consist in the vectorial sum of each magnetic momentum divided by the volume of the core-shell.

Magnetostatic behavior: SQUID measurements:

Figures 3.19 and 3.20 display the magnetostatic signature of each core-shell system (A, B, C and D compared to the bare MNP).

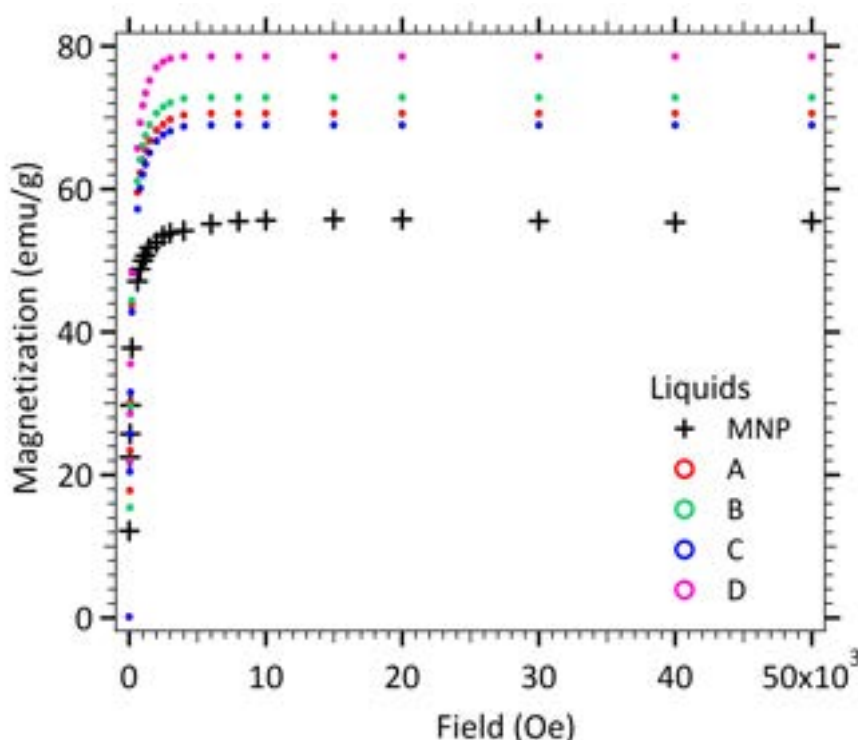


Figure 3.19: Magnetization of all particles in liquid state versus field. The M_{sat} values were corrected by calculating the mass of magnetic material from powder measurements.

The layout of the curves are indicating stable solutions in the liquid phase. Magnetization measurements are corrected with their iron content. Saturation magnetizations are reaching unexpectedly high values due to a under-estimation of the iron concentration in core-shells (under-estimation of iron concentration may come

from titration imprecision due to multiple dilutions). They should gather around the 60 emu g^{-1} value.

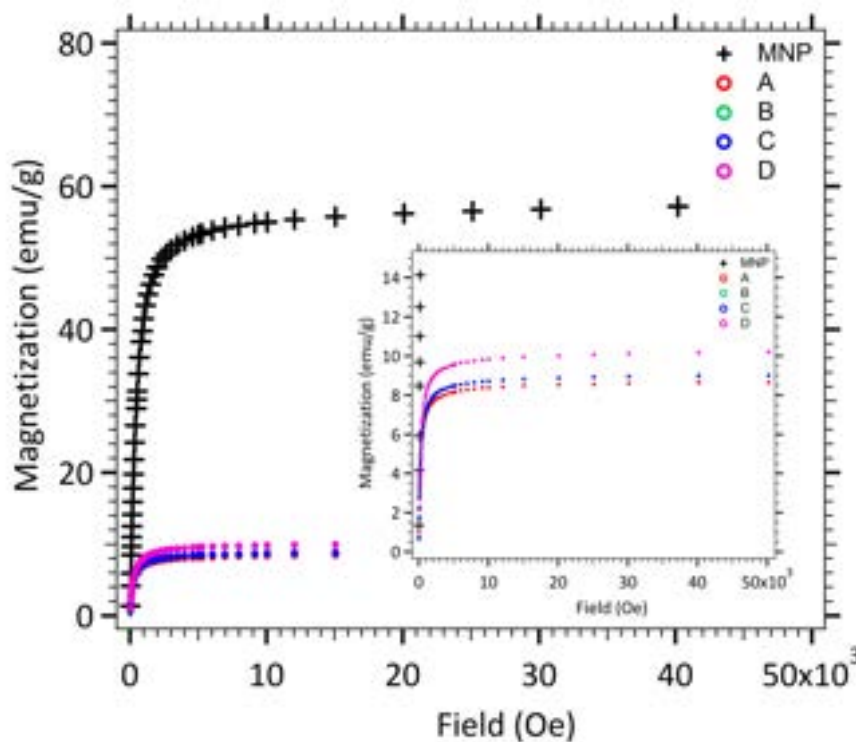


Figure 3.20: Magnetization of all particles in powder state versus field.

On Figure 3.20 magnetization measurements were corrected with samples' mass yielding small saturation magnetization values for core-shells mainly composed of silica (see ratio of magnetic material in Table 3.5).

Each core-shell type can be described with a magnetization at saturation value M_{sat} and a susceptibility value χ . The magnetic susceptibility correspond to the measure of how magnetizable a substance can become in the presence of a magnetic field. It is an intrinsic parameter of the material. The magnetization saturation $M_{sat} = m_s \cdot \phi$ is the maximum induced magnetic moment that can be obtained in a magnetic field. Beyond this field no further increase in magnetization occurs. The magnetization of the bulk maghemite of 85 emu g^{-1} is not reached, this means that the magnetic order is not perfect in the whole particle. This lack of magnetization may be supposed localized in the nonmagnetic surrounding layer (surface effect disorders) [142].

In combination with measurements in powder states (Figure 3.20), the fit of the theoretical expression (Langevin formalism [138]) to the experimental magnetization curve, weighted by the size distribution, allowed the determination of the characteristic magnetic diameter d_{mag} and the polydispersity index σ for each sample. The mean value of the magnetic diameters can be calculated in order to take into account the polydispersity with the following Equation 3.16 :

$$\bar{m} = d_{mag} \cdot e^{-\sigma^2/2} \quad (3.16)$$

The M_{sat} value of each A, B, C and D was divided by the saturation magnetization of the bare MNP (black crosses on 3.20) giving the ratio of maghemite (ms ratio). Details values can be found in Table 3.5.

Table 3.5: Magnetic diameters and magnetic materials ratio

| Particle | d_{mag} (nm) | σ | \bar{m} (nm) | M_{sat}^{powder} (emu g^{-1}) | ms ratio (%) |
|----------|----------------|----------|----------------|------------------------------------|--------------|
| MNP | 10.9 | 0.37 | 11.7 | 56.53 | ND |
| A | 9.4 | 0.30 | 9.83 | 8.63 | 15.3 |
| B | 10.3 | 0.42 | 11.2 | 8.98 | 15.9 |
| C | 8.5 | 0.41 | 9.25 | 8.99 | 15.9 |
| D | 8.3 | 0.30 | 8.68 | 10.15 | 18.0 |

\bar{m} is found to be roughly the same and independent of the particle's size (Table 3.5). σ values of polydispersity in magnetic domains were consistent with the values of standard laboratory-synthesized ferrofluids polydispersity index of about 0.35-0.4 [142]. Indeed as SQUID is a magnetostatic method there is no dissipation *e.g.* Néel mechanism. The data show an individual behavior.

The complexity of the magnetic behavior of SPION and the myriad of parameters (size, shape, aggregation, iron concentration, surface effects) affecting this behavior make their build for a precise goal complex. Papers detailing numeric computations and mathematical models have predicted with more or less efficiency the behavior of individual non interacting particles before synthesizing them [329, 330]. But silica plays a role and the existence of multiple SPION in a cluster can affect the field of nearby SPIONs constructively or destructively depending on their proximity (silica shield) and orientation.

Magnetic hyperthermia of CS particles:

In order to have a rough understanding of the effect of the core diameter on the heating efficiency of our particles we subjected them to a 535 kHz and 10.56 kA m^{-1} magnetic field for a few minutes in concentrated solutions. The description of the setup can be found in Section 3.1.3.

On Figure 3.21 is drawn the increase in temperature for particles C. The specific loss power is calculated by taking the dT/dt measure (straight line) on a 13 second linear portion of the increasing slope (50 points of measure, initial slope method [331]) and by deducing the slight increase of a pure water solution induced by the heating of the coil ("cor" in dotted line).

On Figure 3.22, SLP is drawn versus physical diameter of the core of particles. The SLP is first drawing a slightly rising plateau for maghemite cores, samples A, B and C between 60-80 $W g^{-1}$ then the SLP of D (TEM core size 55 nm and large size distribution) was increased by ca. 1.25 times reaching 100 $W g^{-1}$.

In order to be able to compare with commercial particles and AMF setups that don't use the same frequency f and magnetic field magnitude H the Intrinsic Loss Power (ILP) has been calculated according to Equation 3.17.

$$ILP = \frac{SLP}{H^2 \cdot f} \quad (3.17)$$

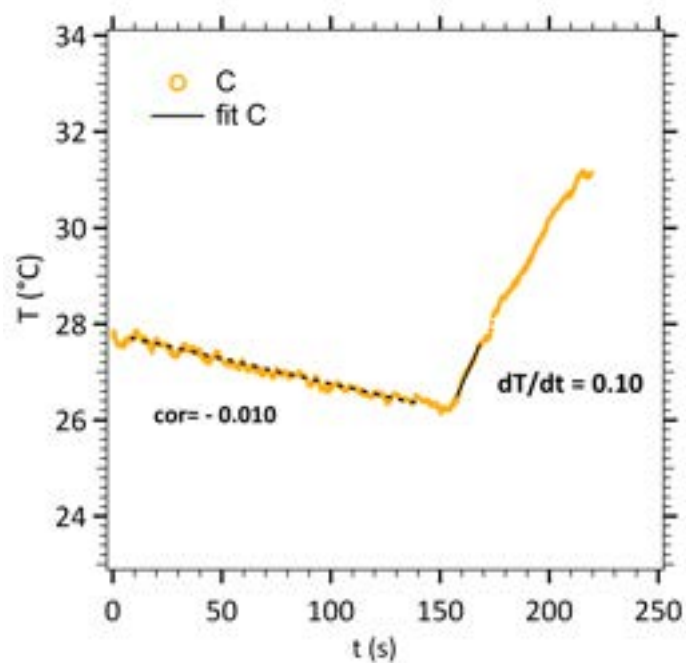


Figure 3.21: Example AMF measurements (increase of temperature vs time) and dT/dt calculation and correction for C.

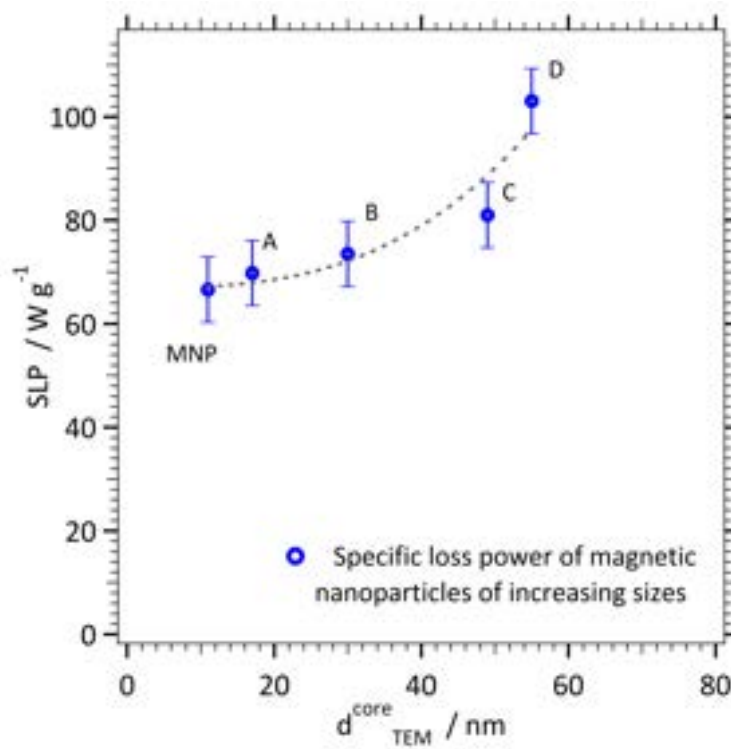


Figure 3.22: Heating power of the individual 11 nm cores (MNP) and 4-types synthesized core-shell nanoparticles versus their physical diameter

Table 3.6: Comparison with commercial intrinsic loss powers

| Particles | $d_{DLS}(\sigma)(nm)$ | \bar{m}^\dagger | [Fe] [¶] | ILP* |
|----------------|-----------------------|-------------------|-------------------|------|
| Nanomag-D-spio | 91 (0.13) | 13.8 | 5.9 | 3.12 |
| Resovist | 61 (0.19) | 13.1 | 27.8 | 3.1 |
| Fluidmag-D | 39 (0.08) | 14.3 | 14.7 | 2.67 |
| Nanomag-D-spio | 84 (0.15) | 13.3 | 6.0 | 2.31 |
| MNP | 26 | 11.7 | 6.16 | 1.1 |
| A | 48 | 9.83 | 5.54 | 1.1 |
| B | 63 | 11.2 | 5.49 | 1.2 |
| C | 80 | 9.25 | 5.36 | 1.4 |
| D | 100 | 8.68 | 2.96 | 1.7 |

[†] Mean magnetic diameter

[¶] (mg mL⁻¹)

* (m² nH kg⁻¹)

with SLP the specific loss power of particles in W g⁻¹, H the intensity of the magnetic field in A m⁻¹ and f its frequency in Hz.

Our home made nanoparticles are around the same order of magnitude of the commercial ones.

Our particles are composed of multiple single domain maghemite cores aggregated inside a silica shell forming more or less well defined short chain-like aggregates. In a liquid solution, both Neel and Brown relaxation occur, the dominant process being the shorter characteristic time ($1/\tau = 1/\tau_N + 1/\tau_B$). For a monodomain core the time necessary to jump over the magnetic anisotropy energy barrier K.V is governed by Neel relaxation time with τ_N in the order of magnitude of a few nanosecond. For bigger particles there is a contribution of Brown relaxation.

As discussed in Chapter 1 section 1.4.1, effective anisotropy is tunable through shape and surface modification. In answer to the yielded heating capacities of spherical magnetite or maghemite, Das *et. al.* designed Fe₃O₄ nanorods reporting a 0.68 m² nH kg⁻¹ [332] SAR value compared to particles with similar volume (0.11 m² nH kg⁻¹ for spheres, 0.25 m² nH kg⁻¹ for cubes). Their work pinpoints that SAR of iron oxides can be increased and tuned by playing on their aspect ratio and that the latter is crucial even if volumes are similar which is not obvious in Neel's description. Reported chainlike formation for nanocubes [333] or biomimicking magnetotactic bacteria chains [334] increases SAR compared to randomly oriented systems up to 2.7 m² nH kg⁻¹.

For short chain-like structures, the increase in SAR may come from two contributions. A major contribution from the chain geometry. Hysteresis loop is more rectangular for a chain than for a sphere, see Figure 3.23. And a minor contribution from texturization effect. The released energy by the spin relaxation is dependent on the anisotropy energy of the NP that is to say the energy that imposes the direction of the magnetic momenta against the crystalline network. The magnetic energy of a chain is dominated by anisotropic dipole-dipole interactions. The latter favors longitudinal alignment of the magnet to crystalline easy axes during chain formation. If the MNP magnetic anisotropy axes are aligned parallel to the chain axis it results

in higher effective anisotropy due to a magnetic order as depicted on scheme 3.24. Although these predictions cannot be strictly extrapolated to our case as magnetic cores are randomly brought together, the existence of a certain magnetic order between chains should not be discarded [335].

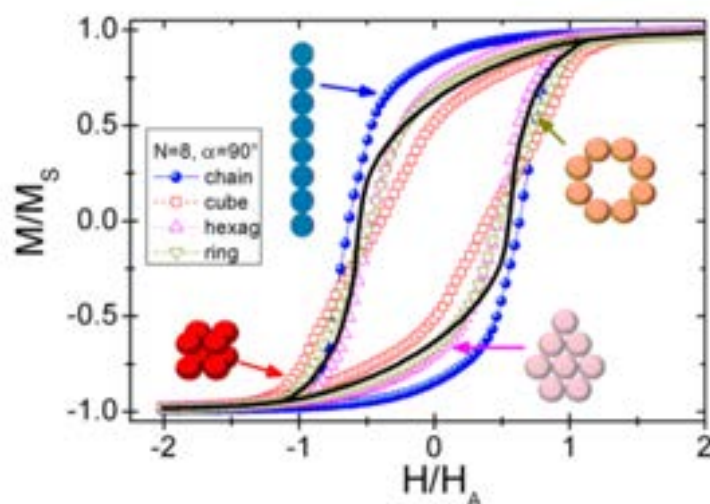


Figure 3.23: $M(H)$ hysteresis curves corresponding to different spatial arrangements (bidimensional chain, hexagonal lattice, and ring; 3D cube) of the same amount of particles, $N = 8$, and for the easy anisotropy axes randomly distributed into a cone of angle $\alpha = 90^\circ$. The black line stands for the case of noninteracting particles [334]

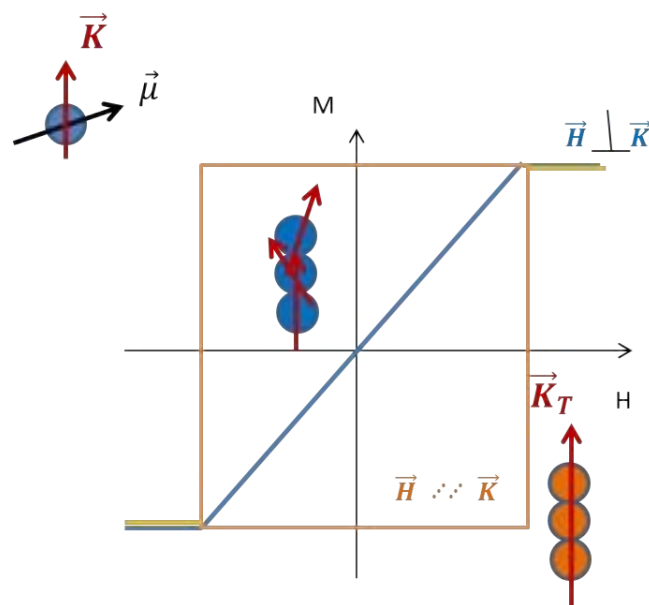


Figure 3.24: Effect of texturization: if crystalline easy axes of the chain is parallel to ac field hysteresis loop is rectangular (no texturization) whereas non colinear magnocrystalline axes result is a decrease in hysteresis losses and a magnetic signature without hysteresis.

Our synthesis combine easiness and efficiency. Indeed nanorods present a better cristalinity but the synthesis is a difficult hydrothermal process (in organic phase, controlled pressure, high temperature, and long time of synthesis. See Table 3.2.) [336, 332]. The increase of SLP with the core diameter in our case could be explained

by considering the magnetic order inside a nanoparticle when the morphology is shifting from spherical to elliptical with aligned chains.

In conclusion, nanoparticles appears to efficient nano-heaters under an AMF. Yet DNA strands, to dissociate, needs a substantial increase in temperature. As the objective of this work is to capture and release short DNA strands, iron oxide nanoparticles allow to consider a denaturation of DNA via magnetic hyperthermia. The A and C particles have been selected for DNA grafting to be able to compare between a "little" spherical particle and a "big" elliptical particle. CS D, even if the suspension is stable, needs to be redispersed with ultrasounds before usage. That's why we prefer to focus on CS C, more stable. All the more that the heating efficiency of magnetic nanoparticles in biological conditions remains poorly understood, especially regarding the influence of their dispersion state .

Post-functionalization: DNA grafting

It is necessary to characterize the surface state of particles after functionalization with $-\text{NH}_2$ and polymer chains and before DNA grafting. The presence of polarizable functions at the surface of nanoparticles can be characterized by a measurement of the effective charge e.g. the resulting charge of particles after condensation of counter-ions. For the structural charge, a quantification of the number of surfacic amine groups with a chemical titration is needed.

The effective charge is governing interactions with DNA and take part to the keeping of f stability. It is characterized by zetametry which is a measure of the eletrophoretic mobility and thus of the zeta potential (ζ). ζ is characterizing the charge state of particles at the shear plane of the electrical double layer that is to say between the compact layer and the diffuse layer. Laser zetametry is calculating the speed of the particles under an electrical field by characterizing the laser beam diffusion of nanoparticles under field. Their movement generates a frequency shift of diffused light of the incident wave (Doppler). This shift is linked to the electrophoretic mobility.

Quid of amine groups on the surface

From the concentration of NH_2 functions $[\text{NH}_2]$ in solution, the surfacic density of amine functions can be calculated.

These calculations do not go without an estimation of the number of objects in ferrofluids (N_{CS}) calculated from the volume filled by one nanoparticle (see section 3.2.2).

The number of amines groups per core-shell is obtained with Equation 3.18.

$$d = \frac{N_{amines}}{N_{CS}} = \frac{[\text{NH}_2] \cdot N_A \cdot V}{N_{CS}} \quad (3.18)$$

The number of amine functions per nm^2 can be written according to Equation 3.19.

$$d_{\text{NH}_2} = \frac{[\text{NH}_2] \cdot N_A \cdot V}{N_{CS} \cdot S_{CS}} \quad (3.19)$$

with N_A the avogadro number, V the volume of solution, S_{CS} the surface of the particle. Results are sum up in Table 3.7.

Table 3.7: TEM diameters, ζ potential measurements, density and number of amine groups on the surface of CS A, B, C and D.

| Particles | d_{TEM} (nm) | ζ (mV) | $-NH_2$ per nm^2 | $-NH_2$ per NP |
|-----------|----------------|--------------|--------------------|----------------|
| A | 42 | 13.1 | 1.1 | 6 000 |
| B | 44 | 14.4 | 2.6 | 16 800 |
| C | 80 | 13.3 | 1.8 | 25 000 |
| D | 86 | 12.7 | 2.3 | 45 000 |

Consistent with the increase in size of CS particles, the number of amine functions available for post-functionalization at the surface of each CS is increasing up to 45 000 amines functions per NP for CS D.

Zeta potential measurements

Zeta potential measurements at pH 7 as shown on Table 3.7 corroborated the presence of NH_2 functions (+13 mV vs -30 mV for non functionalized particles. The values of +30 mV and -10 mV can also be cited for particles functionalized with only $-NH_2$ and PEG respectively [312]) as the modification makes the ζ -potential of the functionalized nanoparticles more positive as expected. Without amine functions, only hydroxyl functions are present, deprotonated at pH 7.4. Primary amines possess a pK_a around 10 and are protonated at physiological pH.

Grafting of DNA

The grafting method and the matrix used for probe grafting to capture the molecule of interest are key parameters in the conception of a biosensor especially in the case where high sensibility selectivity and stability are sought.

The grafting of a DNA probe both on nanoparticles or electrodes ask for a strong bound while keeping intact DNA properties and integrity. Various methods are reported in literature: physical or electrochemical adsorption [337, 338, 74], electrochemical trapping [339], covalent grafting [215].

Covalent graftings and biotin/streptavidin bindings provide strong links to keep stability. Covalent grafting generally implies the use of functional groups to establish the link between the matrix and modified DNA. Among others succinimides [340], aldehydes [341] or maleides [125] should be cited.

DNA grafting on NP is widely done on gold NP as it allows to densely pack the surface with DNA-probes modified with a thiol end. Table 3.8 summarizes literature results on the loading of DNA on nanoparticles according to the type of beads and the functionalization process.

The probe number has a direct impact on the test time and the sensibility of the measure. In this optic Hurst *et al.* investigated the factors for the highest coverage percentage of a thiol modified DNA probe on gold. NaCl concentration (by decreasing particles interactions), spacer type and the size of NP are playing a leading role in DNA/NP interaction [343]. Ultimately they chose PEG spacers and a $[NaCl]=0.7$ M

Table 3.8: Loading efficiencies (number of DNA per NP) according to the type of beads, the modification of the probe and the type of grafting.

| NP type | DNA-probe | Grafting | DNA/np | Reference |
|-----------------------------|---------------------|----------------------------------|--------------------|-----------|
| Acrylic microspheres | DNA-NH ₂ | covalent | ND | [342] |
| Au (15 nm) | DNA-SH | N-acrilosuccinimid adsorption | 250 | [343] |
| Au (250 nm) | | | 25.10 ³ | |
| Au (16 nm) | DNA-SH | adsorption | 158 | [344] |
| Au@SiO ₂ (90 nm) | DNA-COHR | covalent | 10.10 ³ | [345] |
| Glass (μ m) | carboxy-DNA | covalent | 4x10 ¹² | [346] |

via UV-Vis measurements. Always keeping in mind the increase in the sensitivity of detection of OGN on NP Demers *et al.* tried maximizing hybridization with the complementary DNA strand. Only 4% of hybridization could be reached (against 33% on thin films[50]) due to sterical and electrostatical hampering, an order of magnitude also observed by Liu *et al.* on silver NPs. This hybridization efficiency can be increased up to 44% with co adsorbed molecules like mercaptoethanol and spacers [344, 347]. Walsh *et al.* reached a 90% efficiency on glass beads for immobilizing their 20 basis DNA probe and a 58% hybridization efficiency.

With -NH₂ functional groups on our surface an obvious covalent coupling imply the use of DNA modified with a carboxy end and a peptidic coupling with EDC/NHS. This kind of coupling is more complex than a classical chemical reaction. The kinetic parameters have to be considered together with the stability of the link biomolecule – nanoparticle. Buffer concentration, amount of reagents, time of reaction and morphology of the nanoparticles have to be kept in mind to avoid agglomeration.

EDC is a catalyzer very soluble in water. It stabilizes the reaction intermediates to increase the final yield. NHS increase even more the yield and maintain some links stable [348]. EDC reacts with carboxylate groups forming an activated ester intermediate. This latter react with primary amines to form a peptide bound and with water to hydrolyze the initial carboxylate.

Theoretical considerations

Prior to the use of NP in sensor format, the covalent immobilization of oligonucleotides to allow hybridization has to be optimized. To roughly get an order of magnitude of reactants to introduce, the maximum DNA probes that can be immobilized according to surfaces considerations was calculated.

All calculations are based on the nanoparticle TEM diameter. Calculation of the maximal loading of each class of NPs was done by considering steric repulsions. The average diameter of a base pair of DNA is 0.7 Å (d_{DNA}). So the maximum loading of the DNA probes on each nanoparticles is given by the following equation:

$$N_{DNAmax} = \frac{S_{CS}}{\pi \cdot d_{DNA}^2} \quad (3.20)$$

with S_{CS} the core-shell surface.

For C and D, the surface (S_{CS}) was calculated as an ellipse with

$$a = \frac{1}{2} \cdot \text{major axis}$$

and

$$b = \frac{1}{2} \cdot \text{minor axis}$$

The eccentricity is given by Equation 3.21.

$$e = \frac{\sqrt{a^2 - b^2}}{a} \quad (3.21)$$

Considering that the axis of rotation is the major axis, the area of the ellipse is given by Equation 3.22.

$$A = 2 \cdot \pi \cdot b^2 + 2 \cdot \frac{\pi \cdot a \cdot b}{e} \cdot \arcsin e \quad (3.22)$$

Table 3.9 shows the results of Equation 3.22 for CS A and C. Consistent with increasing TEM size, the number of DNA that can be grafted is substantially higher for CS C.

Table 3.9: Surfacic densities in -NH₂ groups and in probe DNA according to each TEM diameter

| Particle | d _{TEM} (nm) | -NH ₂ groups/NP | DNA-loading/NP |
|----------|-----------------------|----------------------------|----------------|
| A | 42 | 6 000 | 440 |
| C | 80 | 25 000 | 1 100 |

DNA grafting

Our DNA probe to be loaded has been modified with a carboxy tail in order to be coupled to the NH₂ NPs via a peptidic EDC/NHS coupling (see section 3.1.4 for protocol). Fluorescence detection was used to detect unbound DNA with the Oli-green kit (See Section 3.1.4 for protocol). As fluorescence is partly quenched on iron nanoparticles as reported in different studies [349], the quantitations were indirect measurements collected in the filtrate after magnetic separation process, Figure 3.25.

The rate of immobilization of A particles was tested with various DNA/NP ratios as displayed on Figure 3.26. The Table below details standard deviations.

The curve reaches quickly a plateau when introducing from 50% to 100% of the maximum steric number calculated with Equation 3.20 (200 to 400 DNA introduced). Apparently it is enough to saturate the nanoparticle's surface and to graft ca. 150 DNA per nanoparticle. This value is in good agreement with our theoretical calculations regarding the order of magnitude.

Even if a lot of -NH₂ groups are functionalized on the nanoparticles surface carboxy modified DNA can not occupy all of it due to sterical consideration. The number of DNA possible to couple is far below the number of amine groups available. To reach the highest efficiency for later hybridization DNA probes should not be too densely packed. Indeed both strands are negatively charged and enough space

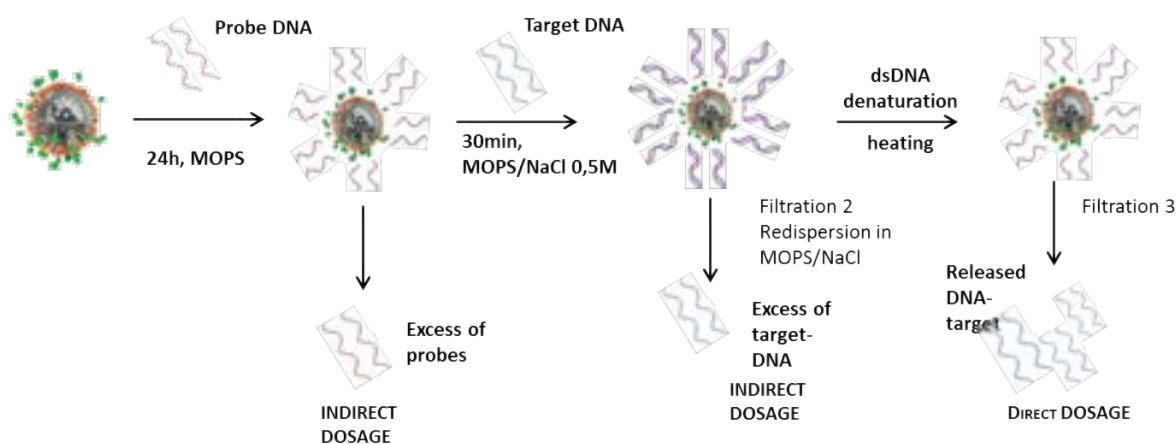


Figure 3.25: Single strand protocol scheme and subsequent fluorescence detection.

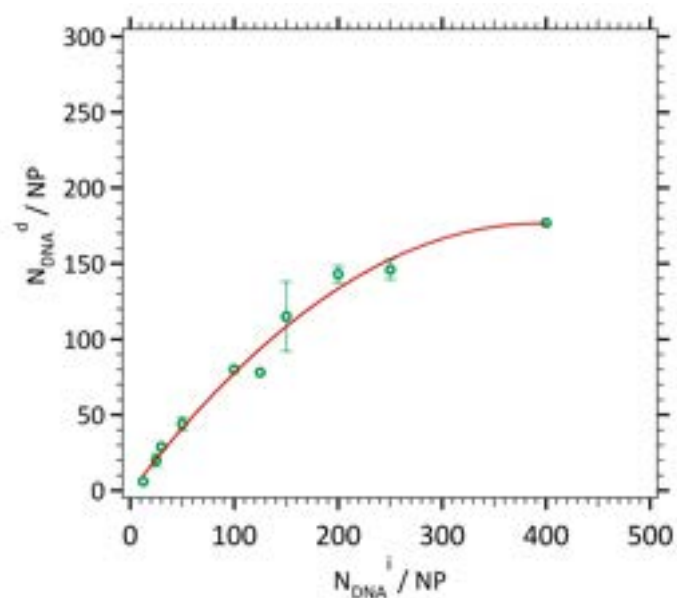


Figure 3.26: Number of DNA probe actually grafted on one nanoparticle (orange dots) versus number of DNA introduced per nanoparticles of 42 nm in diameter (A) and mean curve fitting (red line).

should be left to let the target come near the probe to be hybridized.

An efficiency and a rate of DNA-probe immobilization can be defined as follows:

$$E = \frac{N_{DNA}^d}{N_{DNA}^i} \quad (3.23)$$

$$R = \frac{N_{DNA}^d}{N_{DNA}^{max}} \quad (3.24)$$

with N_{DNA}^d the number of DNA per NP detected in fluorescence and N_{DNA}^i the number of DNA per NP introduced. N_{DNA}^{max} is referring to the maximal theoretical number of DNA that can be grafted on the surface on a nanoparticle given its size. See section 3.2.2 for computation. The efficiencies and rate of DNA-probe immobilization only for chosen values of introduced DNA are summarized in Table 3.10.

Table 3.10: Number, efficiency and rate of immobilization of DNA on A according to the ratio DNA per nanoparticles introduced.

| N_{DNA}^i/NP | 30 | 50 | 100 | 150 | 200 | 250 | 400 |
|---------------------------|-----|-------|-------|------|--------------|-------|------|
| $\overline{N_{DNA}^d}/NP$ | 29 | 44 | 80 | 128 | 143 | 146 | 177 |
| (σ) | (0) | (4.4) | (NA)* | (30) | (5.5) | (6.5) | (NA) |
| E^\dagger | 97 | 87 | 80 | 86 | 71 | 58 | 44 |
| R^\P | 7 | 10 | 18 | 29 | 32 | 33 | 40 |

† Efficiency of grafting %

¶ Rate of grafting % * Not applicable

The more DNA is introduced the more DNA-probes are grafted on the surface (R increases) until a 40% of surface saturation. The most reasonable value of DNA-probes to introduce, in terms of DNA modified -CO₂H consumption, an expensive reagent, is given by the plateau value. Rather than using 400 DNA/NP to graft 200DNA/NP, it is more reasonable to use 200 DNA/NP to graft around 150 DNA/NP (143 DNA/NP precisely). It corresponds to a better efficiency (70 % against 44%) and a reasonable consumption of DNA modified -CO₂H.

Our nanoplatform is now fully functionalized and characterized to proceed to the capture of DNA targets and their subsequent release.

3.3 Capture and release of DNA targets

Following the classical procedure grafting/hybridization/deshybridization we proceed once the probe grafted to the hybridization with the target and subsequent denaturation according to the steps described on Figure 3.25. Corresponding methods and calibration curves can be found in Section 1 under simple-strand protocol.

Classical road

Release of DNA, a T_m issue

DNA strands are attached in a reversibly way by hydrogen bonds between nucleotides DNA base-stacking interactions among aromatic nucleotide bases with a DNA strand that is covalently bound to the NP surface.

Be T_m the melting temperature of our complex e.g. the temperature when the half the targets are dissociated from their complementary probes. If $T > T_m$ the hydrogen bonds break brutally as it is a reaction from a cooperative nature (as a zipper).

Due to the dissociation-characteristics of double-stranded DNA during heating, the energy required to break the base-base-hydrogen bonding between two strands of DNA is dependent on their length l_{basis} , the saline concentration of the medium $[Na^+]$ and the composition in G and C bases %GC [350]. T_m is given by the following Equation 3.25:

$$T_m = 16.6 \cdot \log[Na^+] + 0.41(\%GC) + 81.5 - \frac{675}{l_{basis}} \quad (3.25)$$

With our target of 21 basis (7.14 nm in length) a saline buffer concentration of 0.5 M and a GC composition of 47.6 % the melting temperature of our complex should be 55°C but the melting temperature of immobilized double stranded DNA tends to be higher than melting temperature of DNA in solution [351] as the strands are less accessible. According to Dias *et. al.* calculations [189], the melting temperature on the surface should approach the melting temperature in solution by 5 to 8°C.

We subjected our particles A, grafted with 150 DNA/NP to decreasing concentrations of DNA targets followed by their deshybridization (20 min, 95°C).

The captured DNA amounts to be seen on Figure 3.27 are feeble compared to the one attached (around 150 DNA/NP) roughly 4% and subsequent deshybridization is quasi non existing. In order to check if the feeble hybridization noticed is due to an overgrafting of the probes on the surface and thus hindering the approach of the target (as reported in literature with feeble hybridization ratio and seen on UME in Chapter 1), we proceeded to the double-stranded protocol.

Proof of concept of DNA release on nano-heaters under an AMF

In order to optimize the DNA-probe loading on the nanoparticles a two-step protocol was performed (See section 3.1.4 and Figure 3.28) with a prior hybridization between probe and target. So the surface grafted will be saturated with duplexes

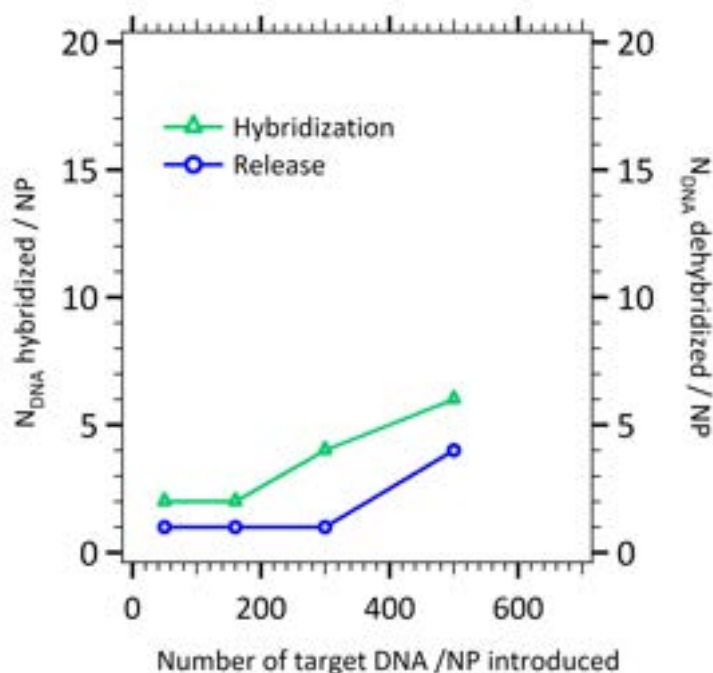


Figure 3.27: Hybridization with target on particles A and subsequent deshybridization by a global heating (20 min, 95C).

of DNA increasing the number of targets captured. The duplex will be grafted via the modified carboxy tail of the probes. As we are in presence of a mix of probe and target with different molar masses, subsequent fluorescence detection will not be possible. Thus the captured target will be assessed when deshybridized. In order to get the maximum duplexes grafted on the surface, 440 probes per particles for A and 1100 for C were left to hybridize with 10 equivalent of targets.

AMF measurements were done on nanoparticles loaded according to the double strand protocol. The goal is triple: reach the maximum loading of DNA duplex; avoid multiple filtrations and the loss of many nanoparticles in the Miltenyi columns.

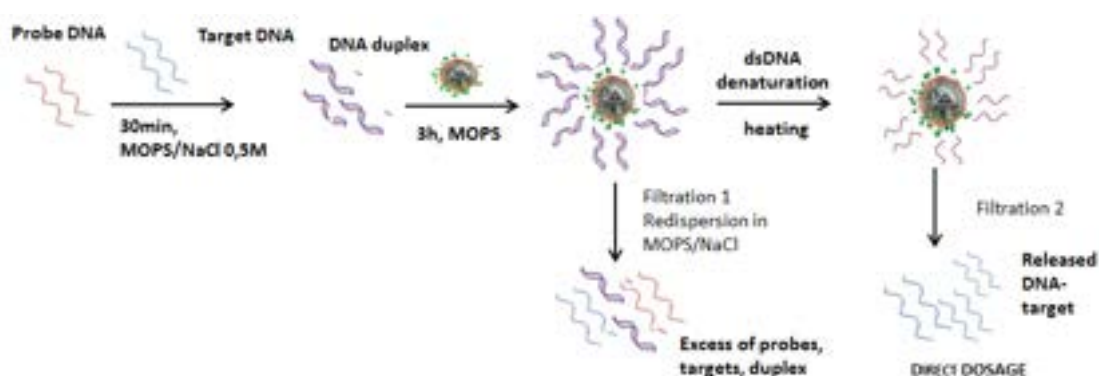


Figure 3.28: Double strand protocol scheme and subsequent fluorescence detection.

Check of double stranded protocol success, 95°C global heating

Before subjecting our loaded particles to an AMF, we wanted to be sure that DNA-duplex could be denatured by heat on the surface of particles. We thus subjected them to a global 95°C heating. Figure 3.29 shows the resulting amount of DNA released.

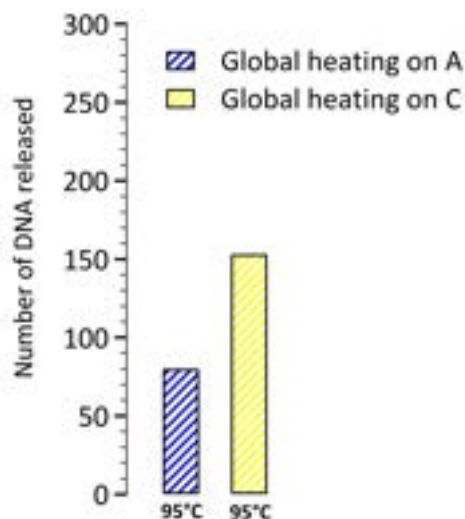


Figure 3.29: 95°C (20 minutes) global heating on particles A and C.

Ca. 100 DNA/NP could be detached for particles A and 140 for particles C. It is far from the introduced values (440 and 1100 respectively) but parameters such as electrostatic repulsions between both negatively charged DNA strands and rehybridation of DNA targets after denaturation could intervene. We took these values as references for further denaturation experiments.

DNA release under an AMF, a local heating

The release of DNA target rely on a local heating in the surroundings of the particle (e.g. a few nanometers [189]) while leaving the solution at room temperature. We subjected A and C to an AMF.

Figure 3.30 compares the release in an AMF on CS A with a global heating (layout A) while keeping the solution at 27°C (layout B). The AMF is only about half efficient than a global heating.

Figure 3.31 displays the release in an AMF on CS C and its comparison with a global heating. We assume that the 20 minutes 95°C heating is sufficient to release all hybridized DNA. One hour magnetic hyperthermia on the C NPs (local heating, solution is kept at 28°C) is 88% as efficient as a 95°C heating to release all hybridized DNA. 150 DNA per nanoparticle have been hybridized according to this deduction. This value seems consistent with the single strand grafting where the electrostatic

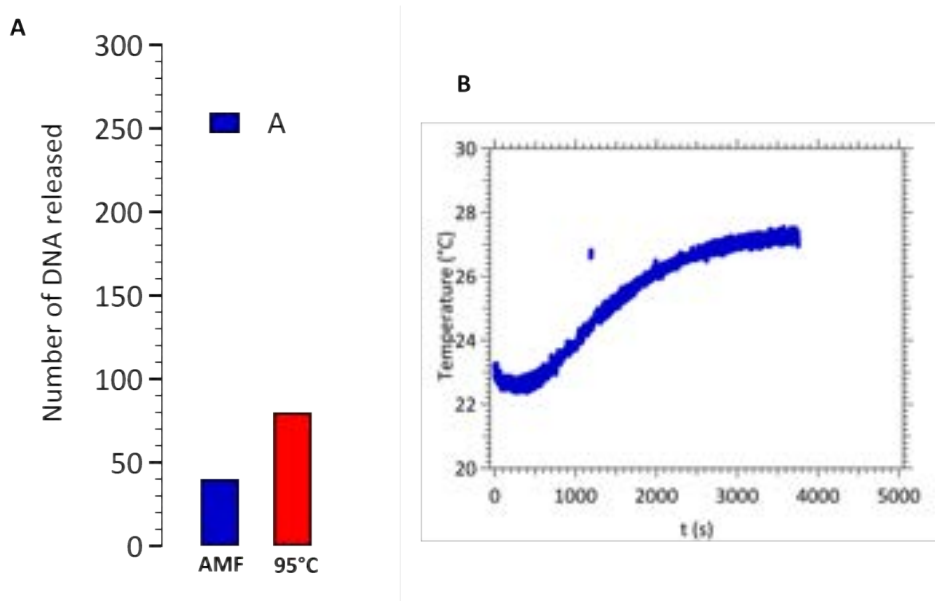


Figure 3.30: A. Number of released DNA by AMF on A compared to a macroscopic heating of 95°C and B. monitoring of the temperature during the magnetic hyperthermia experiment.

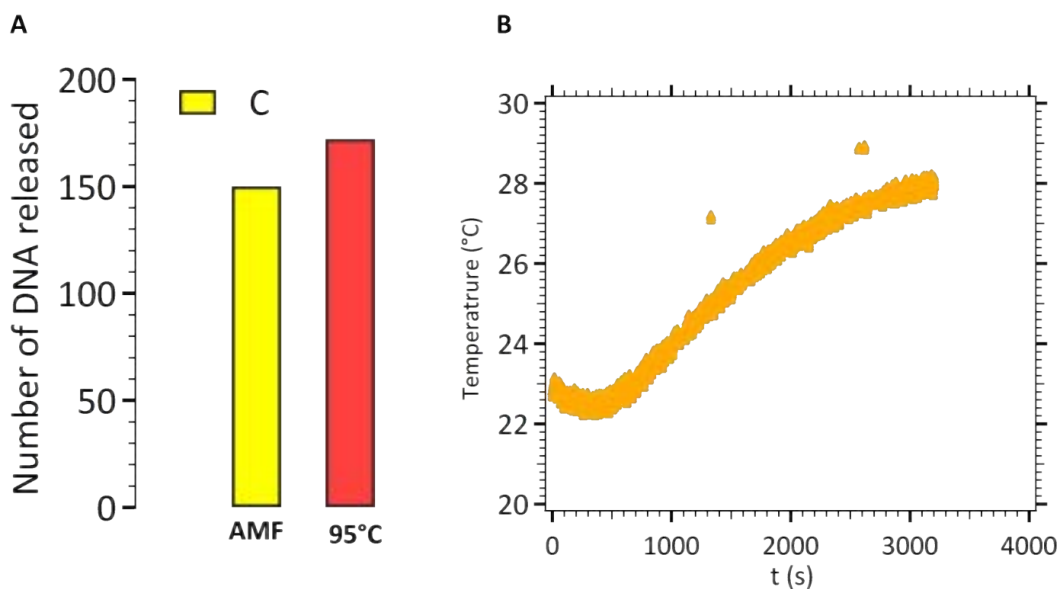


Figure 3.31: A. Number of released DNA by AMF on C compared to a macroscopic heating of 95°C and B. monitoring of the temperature during the magnetic hyperthermia experiment.

and steric interferences of a rigid double-strand structure[346] and the steric hindrance of the PEG chains kept strands from being too densely packed. Walsh *et al.* found up to 50% uptake divergence between OGN hybridized and OGN probes grafted.

We compared heating on both particles in Figure 3.32.

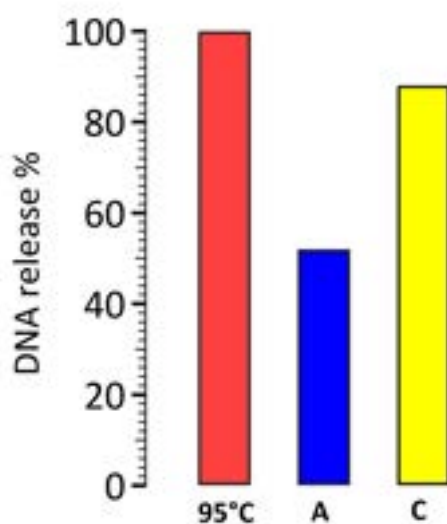


Figure 3.32: AMF heating on NPs measured by the corresponding fluorescence of the filtrates for particles A and C. Release efficiencies were calculated after determination of the total DNA denatured where the samples were heated up to 95°C for 20 min.

A local heating is 88% as efficient as a macroscopic heating at 95°C as shown on Figure 3.32 while keeping the temperature at 27°C with advantages in terms of temperature control (no feedback loop needed) and integrity of temperature sensible components. As a comparison AMF heating has also been done on A with an efficiency only reaching 50%. Figure 3.29 brings forward the impact of size as at 95°C, deshybridization is at its highest. CS C has a larger size resulting in increased DNA loading and thus increased DNA release. Figures 3.30 and 3.31 are showing the efficiency of magnetic hyperthermia. CS C is reaching the maximum deshybridization level and is 88% as efficient as a 95°C global heating whereas A is only reaching 50% of this value. Magnetic hyperthermia on CS C results in higher DNA release efficiencies due to both size increase and magnetic hyperthermia increase (related to their short-chain like structures).

Conclusion

The synthesized γ -Fe₂O₃@SiO₂ core-shell nanoplatform stable at biological pH bears novel and tunable properties. Synthesis and functionalization was done by direct condensation of organosilanes on citrated iron oxide nanoparticles. Playing on the shape of the particles via maghemite core aggregation allows to increase both core-shell size and heating power.

With physical diameters from 42 to 86 nm, synthesized core-shell particles possess a positive effective charge after functionalization with amines groups and PEG chains allowing both colloidal stability and coupling with biomolecules. 6 000 to 45 000 amines groups per NP were available for coupling.

A post-functionalization by DNA grafting was performed in order to capture with high specificity DNA targets complementary to the probe. With the steric hindrance of PEG chains and electrostatic repulsion between DNA strands a maximum of ca. 200 DNA probes were grafted per NP.

A modified protocol for grafting (immobilization of the DNA duplex instead of each separate strand) was conducted in order to optimize the DNA probe loading for hybridization. The subsequent release of DNA targets with a global heating was successful to release 100 to 150 DNA targets.

Subjected to an alternative magnetic field, 80 nm in TEM diameter CS particles were as efficient in local heating as a 95°C global heating while keeping the solution at 27°C crucial for biological media or energy efficiency. This work seeks to be a proof of concept for tunable DNA release at room temperature.

Our results should be applied in the future with a classical probe immobilization, target hybridization and target release scheme. In order to check the high specificity capture of our nanoplatform, capture should be done in a more complex biological solution with a mixture of various DNA sequences and length.

We successfully built a nanoplatform to efficiently capture and release DNA mimicking the miRNA-122. Transposing this system in microfluidics will allow to decrease reaction time and reactant used especially DNA. Indeed in a narrow channel collisions are increased increasing the rate of reactions. Moreover this capture module does not go without a detection module in order to reach sensitivities from the attomolar and avoid a fluorescent detection with limitations of losing nanoparticles through filtrations and obvious limited sensibility (10⁻⁶ M).

Chapter 4

Towards a complete Lab-On-Chip

In the previous chapter, it has been demonstrated that magnetic hyperthermia could be used to release a DNA target attached to its probe immobilized on a magnetic nanoparticle. Microfluidics needs no introduction. The aim of this chapter is, through the transposition of magnetic hyperthermia on a chip, on one hand to reduce analysis time devoted to extraction, purification and on the other hand, which goes with it, to couple on the same microfluidic chip the module of target manipulation and the detection module.

Miniaturization and coupling of various process of molecular biology on the same device was reported to decrease analysis time, reduce the volume of reactants and decrease contamination by reducing the number of human manipulation steps that may lead to an optimized LOD. Ferrigno *et al.* decreased experimental time frame by conducting serial dilutions and parallel potentiometric titrations on chip [352]. On the same note, Stephan *et al.* chose a parallel approach for amperometric quantifications with on chip calibration curves and on chip addition method with networks of sensors [353]. Saliba *et al.* combined an efficient 94% magnetic trapping with functionalized beads on magnetic arrays with cell culture and typing with ten times less volume than without the use of microfluidics [354].

The module of target manipulation presented herein focus on the release of the target by thermal denaturation of DNA strands with magnetic hyperthermia on chip. The changeover to microfluidics allow to confine the nanoparticles in a 200 nanoliter volume hence increasing the efficiency of the thermal exchanges. Magnetic field amplitudes can be reduced as can be the volume of the samples. It opens also the door to a direct detection of the released DNA targets on the same chip.

4.1 Materials and Methods

4.1.1 Microfluidic chip fabrication

Glass/Glass setup

The glass/glass setup bearing only the fluidic channel was comprised of a lower glass part with a 50 μm high channel etched in the glass. First glass was cleaned with $\text{H}_2\text{O}_2/\text{H}_2\text{SO}_4$ (1:1) prior to Plasma Enhanced Chemical Vapor Deposition (PECVD) deposit (20 sccm SiH_4 , 10 W, 40 minutes) of a thick, 600 nm layer of amorphous silicium (aSi), the mask for the etching. The aSi deposit was followed by a 400°C annealing for 4 hours to decrease mechanical constraints (notching effects). UV photolithography with AZ4214 was used to draw the mask pattern. Two different channel geometries are used, see Figure 4.1. The pattern was transferred to the aSi layer with Reactive Ion Etching (RIE, 10 W RF, 10 mTorr, 10 sccm SF_6 , 2'30). Finally the obtained substrate is exposed to a solution with a low dilution of HF ($\text{HF}/\text{HCl}/\text{H}_2\text{O}$, 10:3:20, 27 min). HCl input allows to reduce microchannel's floor rugosity [355]. The upper glass part served as cover bounded hermetically to the lower part (glass/glass bounding patent [356]). The total thickness of the device did not exceed 1 mm.

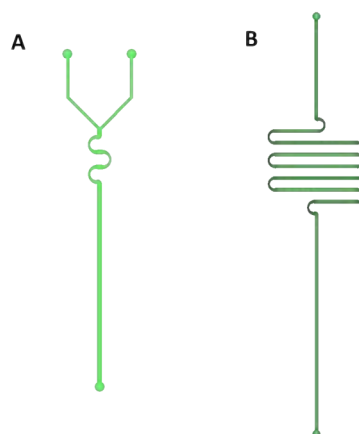


Figure 4.1: L-edit masks of the two channel geometries A and B used.

Glass/PDMS setup

Two design of microfluidic setup were tested. One with a microfluidic channel etched into the glass substrate, electrodes patterned inside and a thin PDMS layer as cover. The second with electrodes patterned on a flat glass substrate and a thin PDMS layer bearing the microfluidic channel as cover.

Electrodes insertion

Embedded electrodes

The first layer of electrodes was photolithographed with a change in resin (AZ-NLOF 2070, 36 s UV3 insolation, 1 min development in MF26 A) followed by a RIE clean (60 s, 10 W). Electrodes were then metallized on a Plassys 550S (C2N, Orsay) in a tilted way. First, the deposition platform was tilted at a 30° angle for titanium

(20 nm) and platinum (100 nm) sputtering then the substrate was tilted at a -30° angle for a second platinum layer (100 nm) followed by lift-off to remove the metal outside the patterns.

Classical electrodes' patterning

For the setup without embedded electrodes, electrodes were obtained according to the process detailed in Chapter 2.

Before the cover bonding, a-CN_x WE were inserted on top of the Ti/Pt electrodes according to the same process detailed in Chapter 2. The L-edit masks are shown on Figure 4.2 (geometry B*).

Thin PDMS layers with or without the fluidic channel were obtained by pouring a small amount of mixed base and curing agents on a silicium wafer, degased under vacuum and at 70°C . Obtained layers were about $400\text{-}600\ \mu\text{m}$ thin. Both the PDMS layer and the glass slides were subjected to an oxygen plasma for bounding.

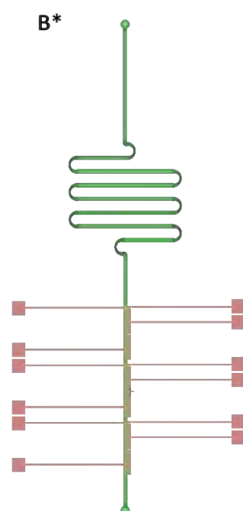


Figure 4.2: L-edit masks for the fluidic channel (green, geometry B) and the network of electrodes (red, geometry B*).

4.1.2 Setup for performing on chip magnetic hyperthermia

The setup was inspired from Lacroix *et al.* [357]. A picture can be seen on Figure 4.3. The microfluidic setup was connected to a programmable syringe pump allowing flow rates from 0.01 to $5\ \mu\text{L s}^{-1}$. In this homemade set-up, the homogeneous radiofrequency magnetic field is produced inside a $1.5\ \text{mm}$ gap (in which the chip is inserted), cut in a low loss ferrite ring on which 55 turns of Litz wire are wound. This magnetizing coil is coupled to a $1\ \text{nF}$ capacitor to form a series LC circuit whose resonance frequency is about $180\ \text{kHz}$. The resonant circuit is excited at the resonance frequency by a signal generator coupled to a RF power amplifier and produces magnetic field amplitude of $370\ \text{Oe}$ (measured using a single turn pick-up coil).



Figure 4.3: Picture of the setup composed of the microfluidic chip with an inset and outlet of solution inserted in the gap of a magnetic core with ferrite.

4.1.3 DNA grafting, release and detection

Double-strand protocol

80 nm in diameter (TEM) nanoparticles functionalized with the DNA-probe were used.

The protocol is detailed in Chapter 3. After DNA duplex immobilization on magnetic nanoparticles, they were introduced in the microfluidic chip at a specific flow with the use of a programmable syringe pump.

Fluorescence detection

After the passage in the microfluidic channel, the output solution was collected and filtrated on magnetic columns prior to fluorescence detection. The fluorescence detection is the same as in Chapter 3 on a Cary Eclipse fluorimeter ($\lambda_{excitation}=480$ nm, $\lambda_{emission}=520$ nm) with the Quant-iT Oligreen ss-DNA Assay Kit from Invitrogen [317].

Electrochemical detection

a-CN_x electrodes were screened in our two-electrode setup (a-CN_x 30 μ m working electrode and platinum 2 mm counter electrode) in an equimolar (3 mM) mixture of Fe(II) and Fe(III) in NaCl 0.5 M and 10^{-8} M in MB with the use of Electrochemical Impedance Spectroscopy (EIS) (Gamry). The WE are functionalized with DNA-probes (1 g L^{-1}) thanks to an EDC/NHS two-step protocol (Chapter 2).

4.2 Results and discussion

The originality of this LOC comes from the design of a microfluidic device adapted to its insertion into the millimetric gap of a toric inductance with a ferrite core. The

device takes thus advantage of an optimal field (field magnitude increases with the inverse of the gap size) and an increase of the reaction due to confinement. However, in order to be able to fit into the ca. 1 mm gap of the torus generating the field, the microfluidic chip fabrication has to be modified. Indeed, the chip with its PDMS slab bounded used in Chapter 2 has a total thickness of ca. 3 cm. A glass/glass setup was needed with glass slides ca. 500 μm thick each. The glass/glass bounding was performed by the Klearia start-up [356].

Two different devices were used in this chapter. In a first instance, a microfluidic chip, composed of two glass slides bounded with a channel of geometry A was used (See Figure 4.4) to transfer the magnetic hyperthermia technology of Chapter 3 on a microfluidic chip.

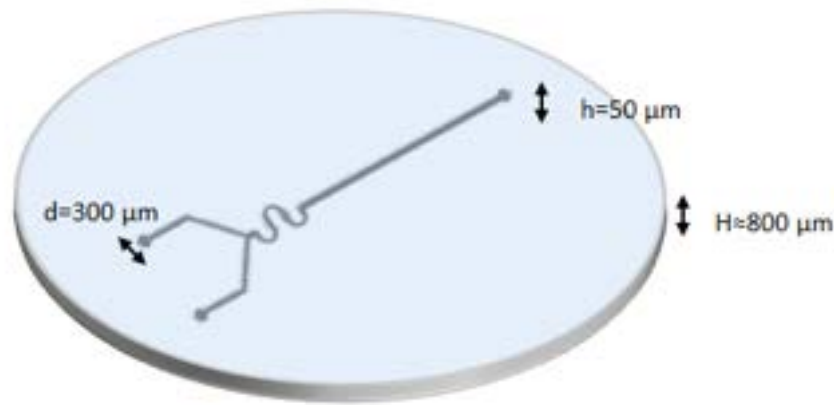


Figure 4.4: Scheme of the first setup used: two glass slides bounded together with an engraved 50 μm deep fluidic channel.

4.2.1 Magnetic hyperthermia on chip

Inductance with a gap, induced magnetization

The setup is taking advantage of the use of an electromagnet with a millimetric gap (ca. 1 mm) with a winding composed of n spires in which is flowing a current I . The gap can be seen as a layer of thin air perpendicular to the median line of the circuit and with a thickness far below the mean perimeter of the tore. In these conditions edge effect can be neglected and it is commonly admitted that the magnetic lines are parallel to the median line of the torus.

The field, H_e , in the gap, e , can be written as:

$$H_e = \frac{n \cdot I}{e} \quad (4.1)$$

with n , the number of spires, I the current intensity in the spires. The magnetic flux, Φ , transiting through the circuit, especially in the gap, is given by:

$$\Phi = \frac{\mu_0 \cdot n \cdot I \cdot S}{e} \quad (4.2)$$

with μ_0 the vacuum permeability and S , the spires surface.

Equation 4.2 shows the possibility to get a high field by focusing in a small gap the field produced by an inductance with dimensions far above the one of the gap [131].

First, nanoparticles used are the core-shell nanoparticles synthesized and characterized in Chapter 3. As a reminder their TEM physical diameter is 80 nm with a core of 49 nm (See Figure 4.5). Their heating power is $1.3 \text{ m}^2 \text{ nH kg}^{-1}$. After submission to the double-stranded protocol and filtration on magnetic columns outside the microfluidic chip, nanoparticles are introduced in the microfluidic device with a chosen flow. The nanoparticles are subjected to the alternative magnetic field on their journey under the inductance, bathing in an homogeneous field of 370 G. Then, the obtained solution at the output of the microfluidic device is filtrated on magnetic columns and analyzed by fluorescence. See section 3.1.4 for complete description of the detection.

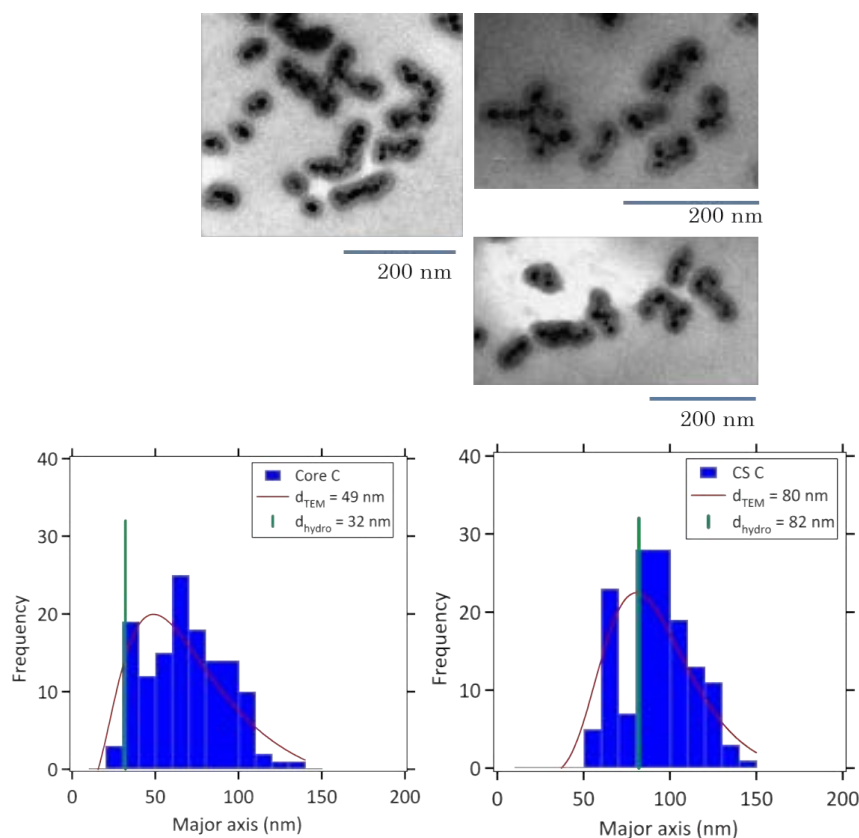


Figure 4.5: TEM pictures of core-shell nanoparticles C and size distributions.

Figure 4.6 is describing the key steps of the protocol.

Optimization of NPs' residence time under AC field

Two flow rates (0.11 and $0.01 \mu\text{L s}^{-1}$) with channel A geometry were used to investigate the NP residence time under the AC magnetic field thus the time of DNA

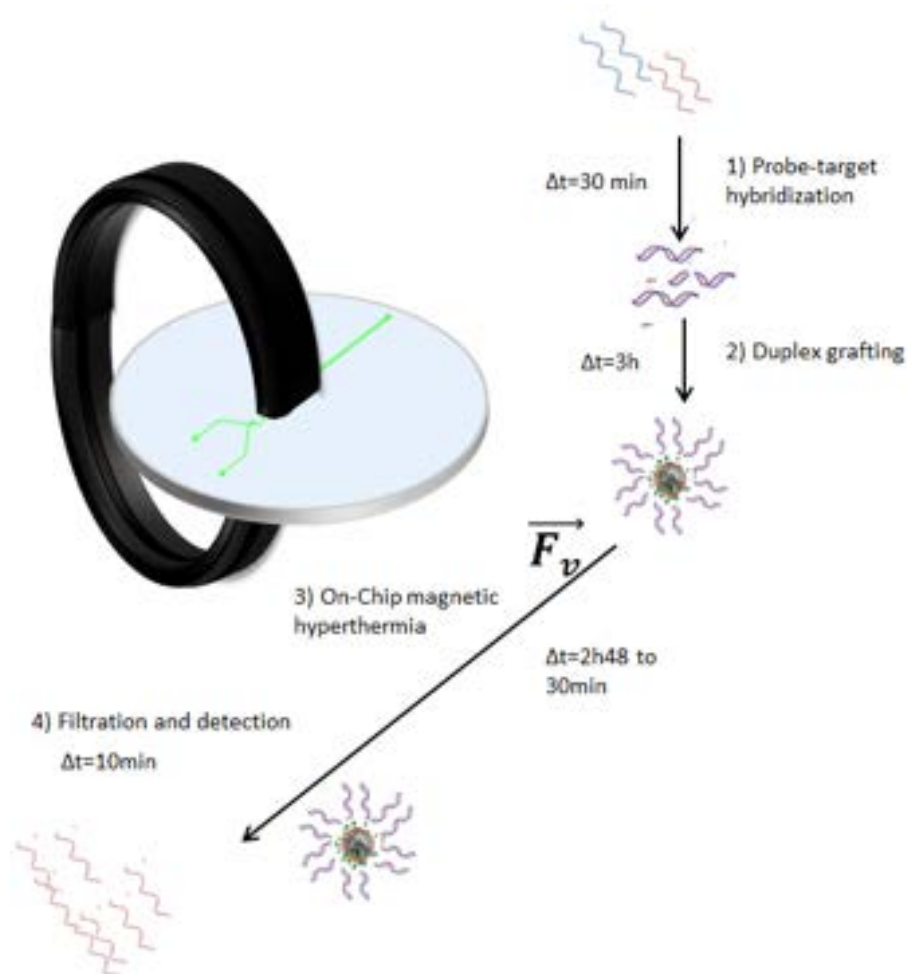


Figure 4.6: Hyperthermia protocol to release target DNA on magnetic nanoparticles. 1. MNP were synthesized and functionalized with DNA duplex outside the chip. 2. Grafting of double-strand DNA via peptidic coupling on NPs (outside the chip). 3. Introduction of functionalized NP in the microfluidic device for magnetic hyperthermia. 4. Filtration step on Miltenyi columns previous to fluorimetric detection (outside the chip).

heating. Table 4.1 summarizes the experimental condition used in terms of flow rates, time of residence, volume of detection and time of experiment. Flow rates and time of experiment were calculated so that the final volume recovered after Δt contains enough single-strand DNA to perform a reliable fluorimetric detection. The tore has a 1 cm^2 section. The path length of a NP under the tore in the serpentine configuration of geometry A is thus 1 cm. Residence time is given by Equation 4.3, as follows:

$$t = \frac{d \cdot h \cdot w}{v} \quad (4.3)$$

where t is the residence time of the suspension of nanoparticles under the magnetic field, $w \cdot d$ the section of the channel under the electromagnet (w , the width of the channel, d , the length under the magnet), v the flow rate, h the height of the channel.

Table 4.1: Comparison of optimized parameters for flow rates and residency time under AC field with fluidic geometry A for on-chip magnetic hyperthermia and fluorimetric detection.

| Optical detection | v ($\mu\text{L s}^{-1}$) | Residence time | Volume of detection μL | Δt^\dagger |
|-------------------|------------------------------|----------------|-----------------------------------|--------------------|
| Geometry A | 0.11 | 3 s | 400 | 2h48 |
| Geometry A | 0.01 | 12 s | 100 | 2h48 |

[†] minimum time of experiment to get a sufficient volume V for fluorimetric detection.

Figure 4.7 shows the results in terms of released DNA targets according to the two flow rates used in geometry A. The maximum number of released DNA is determined by a global heating at 95°C during 20 minutes (100%).

Blanks are made as control experiments without the magnetic hyperthermia heating to quantify the noise background. With a $0.11 \mu\text{L s}^{-1}$ the amount of released DNA is in the blank level range. The amount of released DNA with an optimized flow is comparable both to a global heating, and to magnetic hyperthermia outside the chip or on-chip. Proposed mechanism involves the heating of the vicinity of nanoparticles submitted to an homogeneous alternative magnetic field in the gap of the electromagnet. The heating induces a denaturation of double-stranded DNA, releasing the target single-stranded DNA collected at the output of the setup. The difference between experiments with flow rates 0.11 and $0.01 \mu\text{L s}^{-1}$ lies in the time while the nanoparticles are subjected to the alternative field (see Table 4.1). Indeed the time needed to the denaturation of the DNA duplex to take place (diffusion and zipping) is within a time scale of tens of seconds consistent with an increased release of target DNA with a lower flow and thus a longer residence time under field.

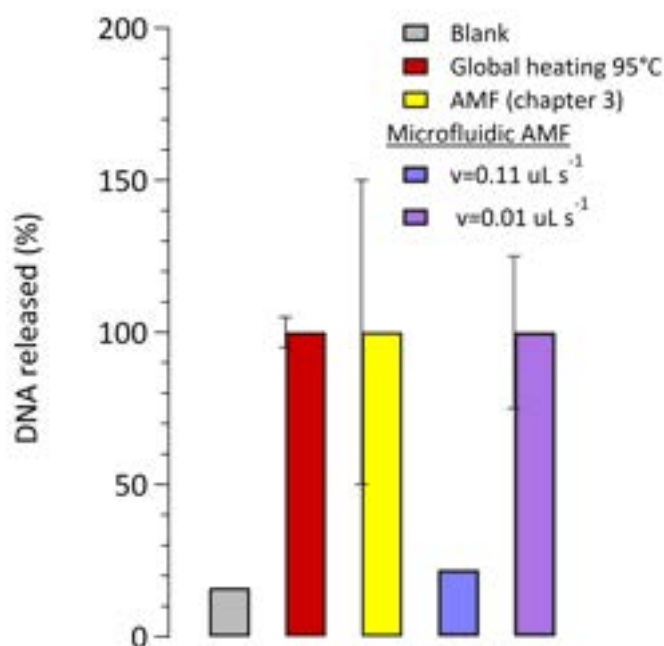


Figure 4.7: Comparison of the results with fluorimetric detection of released targets according to the two flow rates used in geometry A.

The transfer of magnetic hyperthermia on chip was successful yielding as efficient levels of DNA release as in the setup outside microfluidics and as a global heating.

The magnetic hyperthermia technology transfer on a microfluidic chip and the optimization of flow rates in order to get target DNA released amounts comparable to other heating protocol global or local are subjected to a CNRS invention declaration.

4.2.2 Coupling of magnetic hyperthermia on chip and electrochemical detection

Microfabrication of the fluidic device

In a second phase, the technology of fabrication had to evolve from a whole glass setup to a PDMS/glass setup with a thin layer of PDMS [358]. Indeed the electric connections for electrodes (pads) has to be apparent and the fluidic channel has to be closed. The width of the cover slide is thus reduced to ca. 1.5 mm. A glass bounding may be difficult to provide an hermetic covering as edge effect are more important than for the PDMS. So a thin layer of PDMS (<500 μm) has to be bound to the glass slide with the fluidic channel engraved and the two levels of electrodes metallized.

The microfabrication of the engraved channel with a wet etching, the electrodes lithography and metallization and PDMS bounding are detailed in section 4.1.1.

Embedded electrodes

A change in the photoresist was needed to get a thicker layer of resist that could cover the sides of the channel. The photoresist used was the NLOF with a thickness of $5\ \mu\text{m}$ instead of $e=1.4\ \mu\text{m}$ for AZ5214. A picture of the enducted glass slide can be seen of Figure 4.8. Even with NLOF resin, covering all sides of the channel to avoid an unwanted metallization that could short-circuit all electrodes constitute a first technological knock down. A thin layer of uncovered glass slide around channel geometry can be seen on Figure 4.8.



Figure 4.8: Picture of the glass substrate after channel engraving and enduction, development lithography steps.

PDMS

The advantage of using PDMS over a whole glass setup are, beyond the easier bounding procedure with less edge effects, the reduce adsorption of biomolecules on its surface due to its low surface energy and its capacity to adsorb variations in highs particularly pertinent with structures surfaces and metalized electrodes. The whole PDMS/glass setup, that will be used in following experiments is shown on Figure 4.10. The network of electrodes, the engraved microfluidic channel with the geometry B*, the thin PDMS cover and PDMS layer for inlet and outlet can be seen.

Before performing magnetic hyperthermia and electrochemical detection, electrodes were screened with an equimolar (3 mM) mixture of Fe(II) and Fe(III) in 0.5 M NaCl with 10^{-8} M MB. Currents for these embedded electrodes are smaller compared to the ones obtained on electrodes fabricated with classic techniques (Chapter 2) but still measurable. Out of six couple of electrodes manufactured only two (WE, CE) couples are working (e.g. not short-circuited). This may come from the thin layer of uncovered glass slide on the edge of the channel, visible on Figure 4.8.

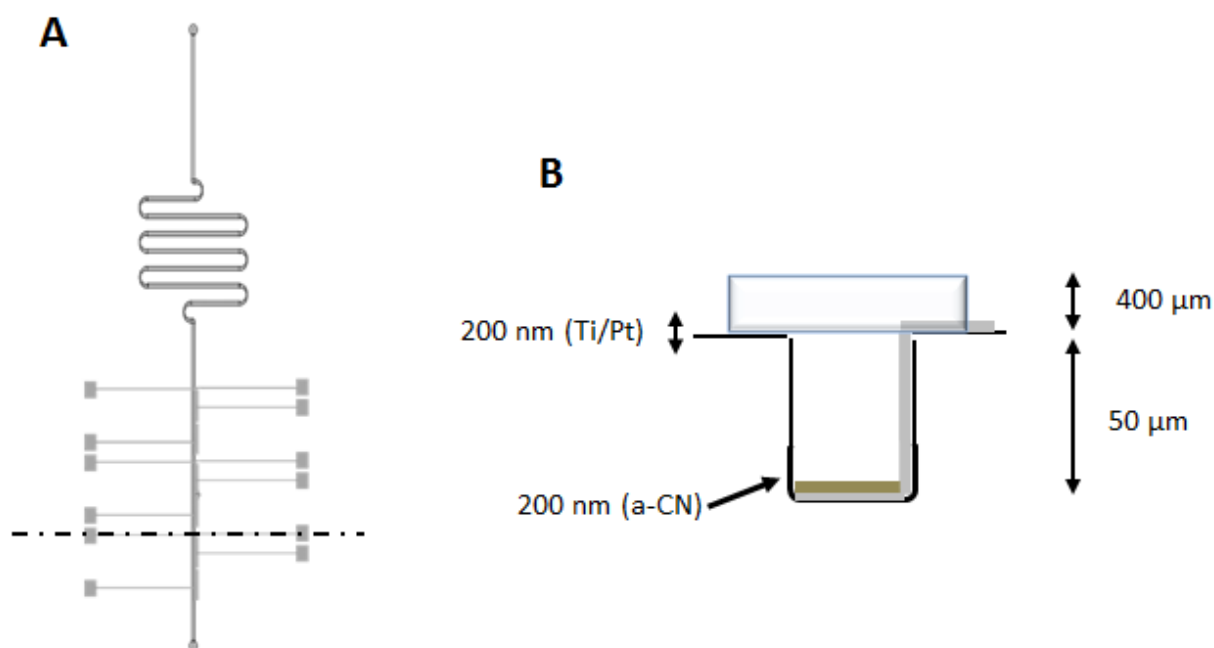


Figure 4.9: Scheme of the final setup in side view. **A.** Schematic top view of the device. **B.** Cross section view (along the dotted line on A) with PDMS cover over Ti/Pt and a-CN_x layers on top of the engraved channel.



Figure 4.10: Picture of the final PDMS/glass microfluidic setup for magnetic hyperthermia and electrochemical detection coupling. Microfluidic channel is colored in lightred.

Optimization of the time of experiment by playing on the geometry of the fluidic channel

In order to reduce the time of experiment, one way is to play on the geometry of the channel notably by increasing the volume under the AC field. We chose to increase the path length of the serpentine giving rise to geometry B with a serpentine of 5.7 cm in length instead of 1 cm. Table 4.3 shows the updated parameters.

Table 4.2: Comparison of optimized parameters depending on the different geometries of the fluidic channel for on-chip magnetic hyperthermia and fluorimetric detection.

| Optical detection | $v^\dagger(\mu\text{L s}^{-1})$ | Δt^\ddagger |
|-------------------|---------------------------------|---------------------|
| Geometry A | 0.01 | 2h48 |
| Geometry B | 0.056 | 30 min |

[†] maximum flow speed so that DNA undergo a T temperature during 15 s.

[‡] minimal time of experiment to get a sufficient volume V (100 μL) for fluorimetric detection.

A 0.01 $\mu\text{L s}^{-1}$ flow was chosen for geometry A to get a 12 s time of heating. Concerning geometry B, to get a 12 s time of heating, to compare with geometry A, a flow of 0.056 $\mu\text{L s}^{-1}$ is needed.

The time of experiment Δt should be estimated, in order to collect a sufficient volume for fluorescence detection ca 100 μL according to Equation 4.3. The calculation times were found to be 2h48min for geometry A and 30 minutes for geometry B.

Coupling with the electrochemical on-chip detection

Figure 4.11 is describing the key steps of the modified protocol integrating electrochemical detection.

The intrinsic limit of detection of fluorescence cannot reach below the 10^{-6} M with standards of our target DNA.

Table 4.3 gives the flow used, the total reaction time Δt (release and detection) and the limits of detection (LOD) according to the detection technique.

The advantage of electrochemical on-chip detection compared to fluorescence is easily pinpointed in Table 4.3. The LOC of such a device with Ultramicroelectrodes in microfluidics with a quasi-static flow is 10^{-16} M on gold (Chapter 2) whereas it is 10^{-6} M for fluorescence. The channel geometry used is the one optimized (geometry B) so that the NPs sees the magnetic field during 12 s (flow of 0.056 $\mu\text{L s}^{-1}$). Ultramicroelectrodes in carbon were added to perform electrochemistry (geometry B*, see section 2.1.4 and 4.1.3). Thus, contrary to fluorescence detection where the solution has to be retrieved at the outset of the chip, filtrated and diluted in cuvettes, the electrochemical detection is direct. As soon as target DNA strands are detached due to the magnetic hyperthermia heating of the NPs, they are captured

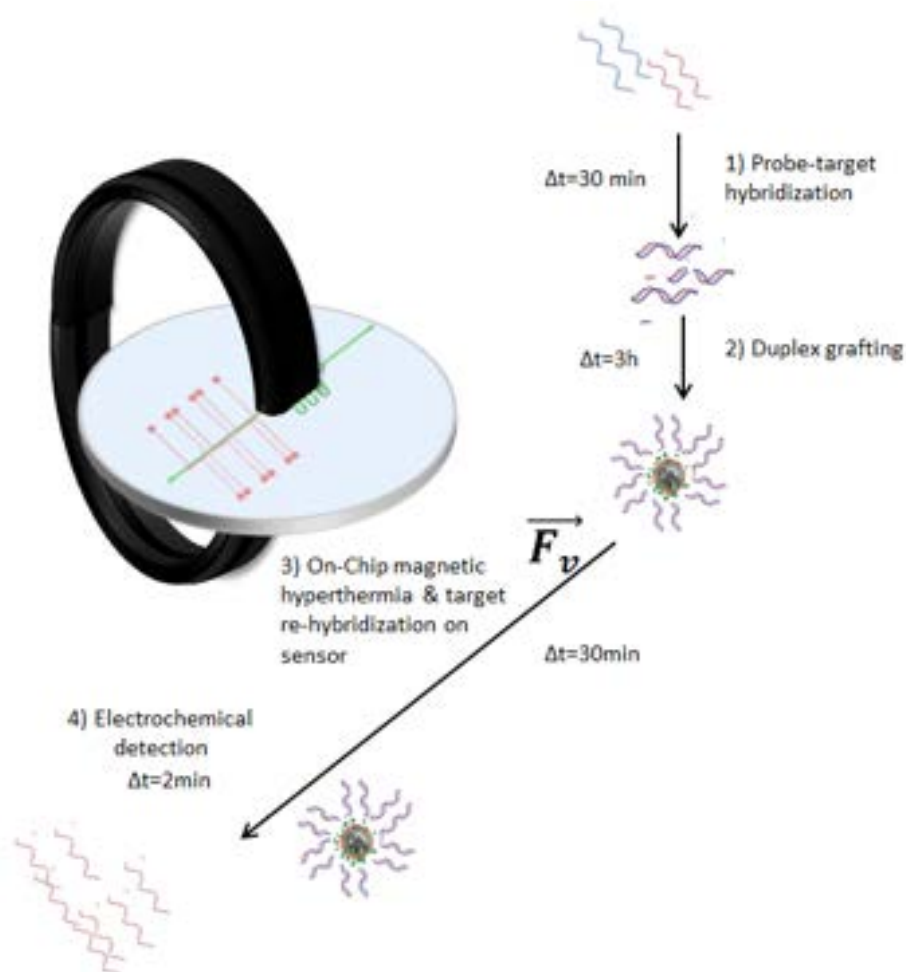


Figure 4.11: Hyperthermia protocol to release target DNA on magnetic nanoparticles and their electrochemical detection. **1.** MNP were synthesized and functionalized with DNA duplex outside the chip. **2.** Grafting of double-strand DNA via peptidic coupling on NPs (outside the chip). **3.** Introduction of functionalized NP in the microfluidic device for magnetic hyperthermia and release under alternative magnetic field. Released targets hybridize on the sensor functionalized with complementary probes **4.** Electrochemical detection in $\text{Fe}^{III}\text{CN}_6^{3-}/\text{Fe}^{II}\text{CN}_6^{4-}$, MB, 0.5 M NaCl electrolyte.

Table 4.3: Comparison of optimized parameters depending on the technique of detection for on-chip magnetic hyperthermia.

| Detection | $v(\mu\text{L s}^{-1})$ | Δt | LOD (M) |
|-------------------------------|-------------------------|---------------------|------------|
| Optical (geometry B) | 0.056 | 30 min [¶] | 10^{-6} |
| Electrochemical (geometry B*) | 0.056 | 30 min [†] | 10^{-16} |

[¶] minimal time of experiment to get a sufficient volume V ($100 \mu\text{L}$) for fluorimetric detection.

[†] time to perform the electrochemical hybridization detection protocol.

by the probe-functionalized microelectrodes downstream according to the protocol detailed in section 4.1.3. So, the same flow is used for hyperthermia protocol and electrochemical detection. The protocol corresponding to the 10^{-16} M LOD is the one for a hybridization step of 30 minutes e.g. the time for which a sufficient amount of targets is reaching and hybridizing on the UME. This hybridization time can be decreased but will impact the LOD as the latter is flow dependent.

Figure 4.12 is a picture of the experimental setup to perform both hyperthermia and electrochemical detection. The microfluidic chip (A) is inserted in the gap of an electro-magnet (C) coupled to a signal generator (D) coupled to a RF power amplifier producing an homogeneous radiofrequency magnetic field. The microfluidic setup was connected to a programmable syringe pump allowing flow rates from 0.01 to $5 \mu\text{L s}^{-1}$ (B). Global temperature in the vicinity of the electromagnet was checked with a thermic camera (E). The microfluidic device was connected to a Gamry potentiostat (F) to perform electrochemical measurements (CV and EIS).

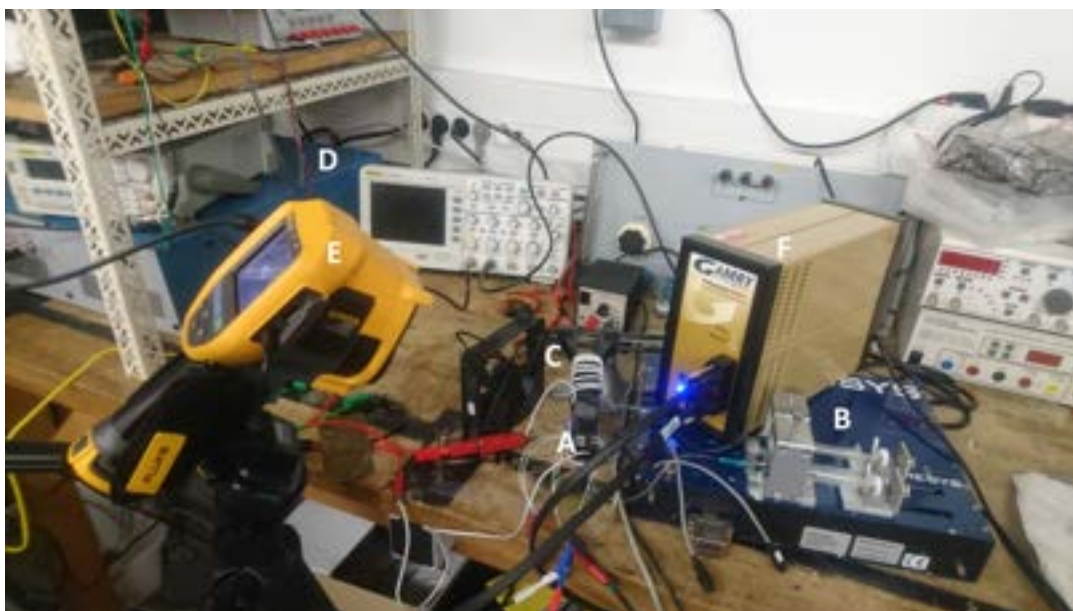


Figure 4.12: Picture of the final instrumental setup for magnetic hyperthermia and electrochemical detection on a chip.

Magnetic hyperthermia conjugated with electrochemical detection was performed according to the scheme depicted on Figure 4.11, in a 30 minutes protocol ($0.056 \mu\text{L/s}$ flow). Results for electrochemical detection after probe immobilization (blue curve) and after target hybridization (green curve) on a a-CN_x working electrode screened by EIS in $\text{Fe}^{\text{III}}\text{CN}_6^{3-}/\text{Fe}^{\text{II}}\text{CN}_6^{4-}$, MB, 0.5 M NaCl electrolyte are showed on Figure 4.13 for the first microfabricated setup (embedded electrodes).

Although a small current was visible before DNA probe immobilization, after single-stranded DNA grafting an impedance component of high resistivity can be seen. A high resistivity curve is consistent with probe grafting as it inhibits redox complex diffusion towards electrodes. After target hybridization, electrochemical conductivity is increasing, resistivity is decreased indicating the success of both the magnetic hyperthermia protocol in geometry B* and the subsequent target hybridization on a-CN_x electrodes in 30 minutes. However, resistivity is too large to be able to quantify the amount of target DNA and to compare it with previous results

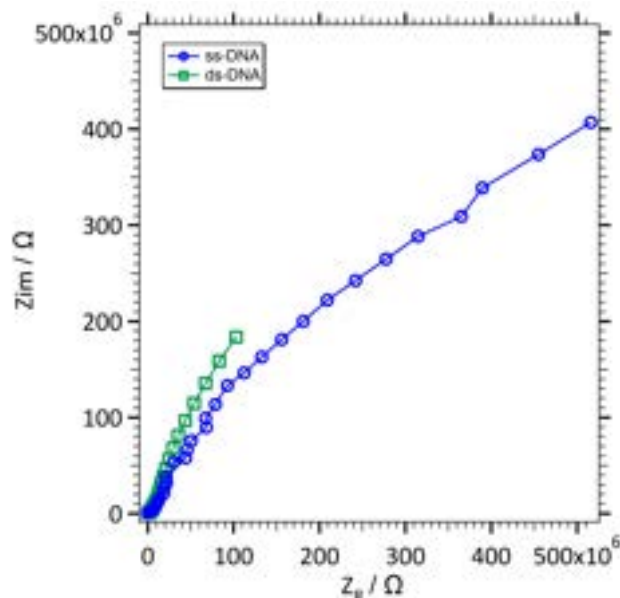


Figure 4.13: EIS graph of electrochemical behavior of a-CNx electrodes after probe immobilization (blue curve) and after target hybridization (green curve) from 1 MHz to 0.1 mHz.

(Chapter 2).

This high resistivity may come from the fabrication of embedded electrodes. Due to the depth of the microfluidic channel, the edges and the floor of the channel are less accessible to metal deposition resulting in poorly adhesive platinum layer and thus less conductive electrodes. In order to perform quantitative measurements, a switch to the previous working technology is necessary, that is to say, a flat substrate bearing electrodes on one hand and a PDMS layer bearing the microfluidic channel on the other hand. The key point here lies in the realization of a microfluidic channel inside a 500 μm thick PDMS layer.

Results are shown on Figure 4.14. On frame A the success of activation and functionalization with DNA probes can be seen with a respective decrease down to 13 cm^2 and increase up to 30 cm^2 of the impedance. On frame B, the coupled sequences of hyperthermia and hybridization with target DNA released from the nanoparticles lead to a decrease of impedance down to 14 cm^2 indicating the success of hybridized DNA targets and thus their detection. These results consist a proof of concept of the technique, repeated experiments have to be done to check the repeatability.

4.3 Perspectives

4.3.1 Optimizations

For now on some optimizations have already been done:

- The flow has been optimized according to the channel geometry so that NPs are under the field influence for ca 12 s, the time necessary for the molecular phenomenon of duplex deshybridization may take place efficiently,

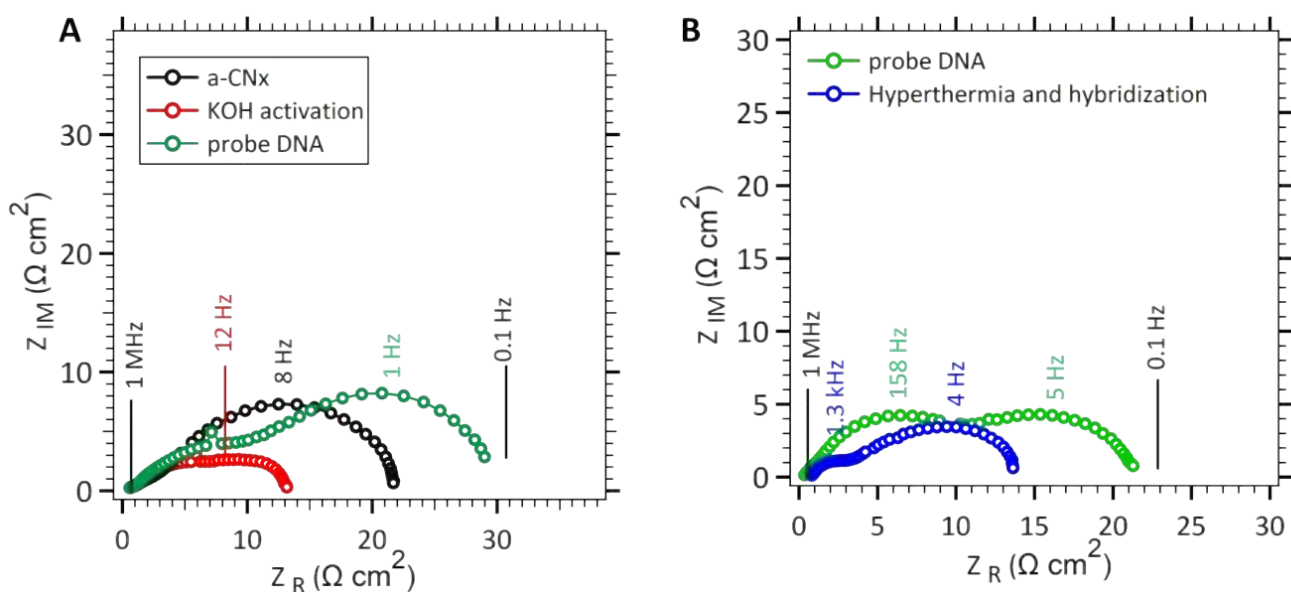


Figure 4.14: EIS graph of electrochemical behavior of a-CNx electrodes after probe immobilization (blue curve) and after hybridization (green curve) from 1 MHz to 0.1 mHz according to the second microfabricated setup. A. One experiment of a-CNx activation followed by functionalization with probe DNA. B. Second experiment of fonctionnalization with probe DNA followed by magnetic hyperthermia and electrochemical detection.

- the microchannel geometry was optimized so that a maximum of fluidic volume stays a maximum time under the field decreasing to 30 minutes the time of experiment,
- Magnetic hyperthermia was coupled to electrochemical detection.

Some more optimization could further increase efficiency:

- Decreasing sensor's resistivity to perform quantitative measurements,
- Move toward a miniaturized setup to meet clinical criteria of portability.

4.3.2 Miniaturization toward a portable equipment

Our device is well adapted to biological samples, with volumes of a few microliters even nanoliters. Micro and nanofabrication techniques for the realization of microdevices are well mastered. Our device could be entirely miniaturized and portable. Indeed, the power needed for heating (17 W, measured on the RF amplifier) is as powerful as a portable phone transducer. For electrochemical detection a portable ammeter could be enough (see Chapter 2). The generation of the flow remains. Only a small flow is needed (around $0.01 \mu\text{L s}^{-1}$). A residual flow by serynge injection could be enough or the introduction of a plug progressing by capillarity and gravity [352, 359] in the microfluidic channel.

4.3.3 Towards a capture/denaturation setup

The current setup is only performing magnetic hyperthermia on chip. For future application such as, pre-concentration, purifications, there is a need of capturing and immobilizing nanoparticles while a solution is passing through.

With one eletromagnet, in the current geometry (2D), it is rather compromised. A 1D geometry should be needed, in order to perform capture along one direction and release along the other. For capture aims, the field has to be static and the optimized form for the electromagnet should be a tip. But we can take advantage of the geometry of the fluidic channel and its serpentine by playing on the magnetic gradients induced by the field. Three pulses will be needed : 1 pulse for a capture and purification (long quadratic pulse) in an area of the channel where the magnetic force (e.g. $\vec{B} \cdot \text{grad} \cdot \vec{B}$) is at its highest, 1 pulse for magnetic hyperthermia release (sinusoidal signal, where the magnetic field is maximum) and the last pulse for further confinement on the detection area, as pictured on Figure 4.15.

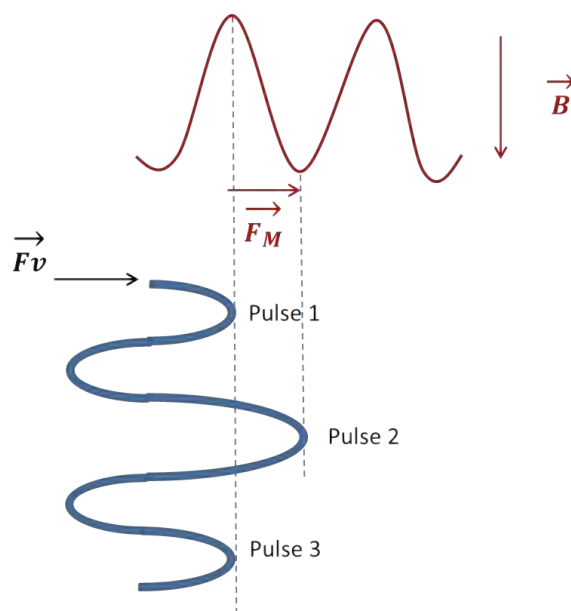


Figure 4.15: Pulse 1 : confinement (static), pulse 2 : release (AC field, alignment with the area of higher magnetic field)., pulse 3 : confinement (static).

For the capture pulse, the confinement has to be done in the are of higher magnetic force (static field), for the release if it is done by focusing the field of an electromagnet in its millimetric gap.

The need for local heating is everywhere

Many systems could use local heating. Indeed the heating of a biologic solution is a crucial point in an amplification process or detection of a biological target. A global heating asks for a feedback loop to compensate thermal losses and can induce a denaturation of components, non compatible with a high temperature.

Local heating in or outside a chip was already used in literature whether it is for a cellular or molecular process. Chen et al. analyze with cellular imaging the direct

effect of a thermosensible inhibitor on cell division [360]. Their biocompatible microfluidic setup is coupled to a temperature controller module.

There is also the issue of the PCR protocol used to amplify DNA strands before detection. A precise control of temperature over a large range is needed for each step and cycle of the amplification procedure (90°C, 55°C, 70°C and 37°C [208]), which is time consuming and quantification errors can be made notably for short sequences [5]. It is important to stress that the direct detection of DNA sequences without PCR is a major challenge for *in vitro* molecular diagnosis.

Currently PCR in droplets, isothermal PCR (LAMP, NASMA, RCA [39]) are alternatives to the classical PCR. Houssin et al. have demonstrated a molecular amplification of a non isothermal chip with an ultra rapid thermalization speed [361]. Cheng and Houssin are quoting the temperature controller Cherry Biotech, the "the fastest heat cooler worldwide for microscopy" in the 5 to 45°C temperature range [362]. But all these technologies need a heating system with a thermalization chamber and a feedback loop for temperature whether it is a heating via Joule effect (nanoheaters), Peltier, infrared or microwaves [39].

Our device is consistent with previous innovations. It allows easy manipulation of biological fluids without interference (no leakage through materials and reduced adsorption). Glass is biocompatible and transparent and non porous. Microfluidics allows a fine and dynamic tuning of the microsystem environment (concentrations, flow, time of residency) while keeping a reduce volume of reaction well adapted to the used of biological precious samples. The use of on-chip magnetic hyperthermia is a major step in the way it avoid the use of a complex external temperature module (complex chain of system calibration between water inset, heating induced by imaging devices and temperature compensation). With magnetic hyperthermia thermic inertia is no more the limiting parameter allowing to further reduce times of reactions.

Our device can adapt to the above-mentioned technologies: nanoparticles are small enough to be up-taken by cells and the PCR protocol can be made on nanoparticles. PCR protocol for nucleic acids amplification is well established, extracted amount of nucleic acids are small, all current detection system commercialized or soon to be need an extraction and amplification module. Our LOC is thus a response to the issue raised. Biocompatibility and chemical surface functionalization are assured. The use of magnetic nanoparticles with a flexible functionalization optimally integrate in the device and contribute to its efficiency.

Conclusion

In this chapter, the knock down of several technological barriers is presented:

- The transposition of magnetic hyperthermia on chip with an optimization of the residence time of magnetic nanoparticles for an increased DNA release,
- A microfabricated fluidic setup to perform magnetic hyperthermia coupled to an electrochemical detection with several technological key points: electrodes embedded in an engraved channel, thin PDMS bounding.

These achievements constitute building blocks towards a complete on chip medical diagnosis. The designed LOC device is thus an answer to the issue of fully integrated LOC. The fluidic device will allow a selective extraction of targets thanks to the specific DNA hybridization. Integration of an on chip electrochemical detection below the release of the targets is possible. Biocompatibility and functionalization of surface chemistry are provided. The use of magnetic nanoparticles with a flexible functionalization can be optimally integrated for extraction of specific targets and their further release.

On chip magnetic hyperthermia is thus paving the way for many adjustments in terms of extraction module and cellular and molecular focus. Finally, miniaturization allow the integration of an *in situ* technique of detection near the released species avoiding both a macroscopic heating of the medium and by reducing experimental time frames of separation outside the chip. All of that will increase even more the interest and efficiency for magnetic hyperthermia and microfluidic detection. Regarding this part, the integration of planar microelectrode in the fluidic system will allow a direct titration of released species via on chip electrochemistry [363].

General conclusion

This thesis work focus on DNA biosensors and laboratories on chip for the detection of the miARN122's sequence for an early diagnosis. The aim is to challenge its current detection through PCR, long lasting with multiple steps of heating and inducing quantification errors. This work seek to meet molecular clinic diagnosis specifications of rapidity, portability, specificity and sensitivity and relying on a Whitesides' quote:

"In the future, it is certainly possible that healthcare will move from treating to anticipating disease." Whitesides, 2006

The originality and the strength of this work thesis lie on the pooling of skills from four laboratories : Laboratoire Interfaces et Systèmes Electrochimiques LISE (UMR 8235 CNRS/UPMC Paris) with Jean Gamby for the expertise in Electrochemistry and microfluidic, Laboratoire Physico-Chimie des colloïdes et Nanosystèmes Interfaciaux PHENIX (UMR 8234 CNRS/ UPMC Paris) with Vincent Dupuis for the expertise in magnetism and Jean-Michel Siaugue for the expertise in design and fabrication of magnetic nanoparticles, l'Unité de Technologie Chimiques et Biologiques pour la santé UTCBS (Chimie ParisTech, INSERM, Université Paris Descartes) with Mathieu Lazerges for the expertise in DNA biosensors and le Centre de Nanosciences et de Nanotechnologies C2N (UMR 9001 CNRS Univ. Paris-Sud) for micro and nanofabrication skills in clean room.

This work relied on a consequent bibliographic review to better define advantages and drawbacks of already existing techniques and show the relevance of microfluidics for molecular detection. Several technological and process barriers were knock down, building blocks towards a complete LOC for medical diagnosis:

- the transposition in microfluidics of an electrochemical biosensor in a two-electrode configuration and the subsequent DNA detection through the characterization of hydrodynamics and mass-transport toward an electrode in microchannels. It also permitted to see the influence of the electrode material used and probe density issues on the efficiency of hybridization detection,
- the application of magnetic hyperthermia to DNA deshybridation and its transposition on a microfluidic chip,
- the manufacture of a device coupling magnetic hyperthermia specifications and electrochemical detection.

We will sum up here each achievement according to the above mentioned key points.

DNA hybridization detection on Ultra-microelectrode (UME)

In order to get a device easy to set up, the focus is on simplicity: hybridization based biosensors compared to direct sequencing and electrochemical transduction as it is the simplest way to convert a biological recognition event into a readable electrical signal. More precisely, the detection is amperometric with a faradic signal proportional to the concentration of the specie of interest.

The sensitivity of the detection relies on the use of a planar UME. A temporal and spatial resolution allow this local probe of concentration to measure small currents (ohmic drop and S/N decreased) and study fast process due to planar diffusion regime. Three key step are mastered for an optimized detection: 23-base DNA probe immobilization on gold via thiol adsorption in two hours, target hybridization in a 30-minutes protocol, transduction into an electrical signal in cyclic voltammetry with an electroactive specie $[\text{Fe}^{\text{III}}(\text{CN})_6]^{3-} / [\text{Fe}^{\text{II}}(\text{CN})_6]^{4-}$ redox couple thanks to long-range electron transfer through the double strand DNA. The sensor is able to differentiate between a single strand and a double strand DNA thanks to Methylene Blue, DNA intercalant, and redox specie.

Quantification of the target was deduced from the resulting electrical signal characterized by cyclic voltammetry. The limit of detection for DNA hybridization was 10^{-9} - 10^{-10} M consistent with previous works. The transposition into a microfluidic channel composed of a glass slide with photolithographed array of electrodes and a PDMS cover bearing the fluidic channel allowed to couple electrochemistry with microfluidics. With the decrease in dimensions, the reactions are confined for increased performances tuned by the hydrodynamical control of the flow on diffusion and convection layers. The geometry of electrodes, working electrode in generator position and counter-electrode in collector position, allows to reach a behavior compatible with Levich prediction. The limit of detection for DNA hybridization was 0.1 fM in stopped flow experiments, where it can reach 1 aM over a $0.5 \mu\text{L s}^{-1}$ flow rate, a value 10^4 -fold lower than the one measured with a conventional UME dipped into an electrolyte droplet under the same analytical conditions. An explanation was that forced convection drives more biomolecules to the area of detection even if a balance between the speed of collection and the number of biomolecules collected has been found.

SAM probe coverage was found to be 80% of the electrodes' surface. These close packed DNA probe layers are yielding low rates of hybridization (10% hybridization). These results supported the decision to find a easier and better way to control the surface fonctionnalization instead of playing on the dilution of the SAM, by switching to nitrogenated amorphous carbon. a-CN_x electrodes provide an improved electrochemical reactivity and amines anchoring groups for covalent grafting of the probes. By playing on the amount of DNA probe grafted, the efficiency of hybridization can be tuned.

To conclude, gold and a-CN_x electrodes in microfluidics can play the role of detection system of our molecule of interest with a 0.1 aM limit of detection. It is important to note that our choice of electrodes was rather driven by the stability of the probe layer and its robustness rather than on a maximal decrease of limit of detection.

γ -Fe₂O₃@SiO₂ core-shell nanoparticles, nanocarriers for DNA capture and release

In order to manufacture a fully integrated lab on chip, a module of extraction of the molecule of interest is needed. The first step towards that module is the design of a platform, a nanoplateform that may capture, manipulate and release DNA. Magnetic hyperthermia on core-shell nanoparticles bears promising achievements in biotargeting especially. Here, we take advantage of the γ -Fe₂O₃ cores and the loading capacity of the submicrometer diameter particles to release by a local heating a DNA target mimicking the liver specific oncotarget miRNA-122. The synthesized γ -Fe₂O₃@SiO₂ core-shell nanoplateform stable at biological pH bears novel and tunable properties by playing on the shape of the particles via maghemite core aggregation yielding a 1.3 to 1.7 m² nH kg⁻¹ high ILP compared to the ILP reported with magnetite nanorods 0.68 m² nH kg⁻¹ [332]. A range of diameters from 42 to 86 nm was achieved, with a positive effective charge after functionalization with amines groups and PEG chains allowing both colloidal stability and coupling with biomolecules allowed up to 150 DNA probes to be grafted per NP.

Probe density is a constant problem for hybridization efficiency. By comparing the pseudo optimized probe density on the surface of UME and nanoparticles, it appears to be quite the same as the number of probes introduced in the case of double strand protocol for NP e.g. 1.5x10⁻⁸ mol for nitrogenated amorphous carbon UME and 1.8x10⁻⁸ mol for 80 nm NP (TEM diameter). The study of this nanoplateform allowed to better grasp the dynamics of hybridization especially the influence of electrostatic repulsion due to densely packed DNA strands.

A modified protocol for grafting (immobilization of the DNA duplex instead of each separate strand) was developed in order to optimize the DNA probe loading for hybridization. The subsequent release of DNA targets with a local heating was successful to release 100 to 150 DNA targets. Subjected to an alternative magnetic field, 80 nm in TEM diameter CS particles were as efficient in local heating as a 95°C global heating (while keeping the solution at 27°C), crucial for biological media or energy efficiency.

Towards a complete Lab-On-Chip

The transposition of magnetic hyperthermia on chip takes again advantage of microfluidics, the common thread of this thesis work with confined nanoparticles under magnetic alternative radiofrequency field. By playing on hydrodynamics parameters, the influence of magnetic particles' residence time was highlighted, pinpointing what may be the limiting reaction in this system, the denaturation process of DNA happening in a few dozen seconds.

The microsystem to perform magnetic hyperthermia on chip successfully released DNA strands in an amount comparable to global heating and AMF outside a microfluidic chip. Following these results, a CNRS patent application was filed.

A complete lab on chip seeks to couple its various modules on the same chip. Several technological barriers had to be overcome to couple a microfabricated fluidic

setup to perform magnetic hyperthermia and an electrochemical detection : electrodes have to be embedded in an engraved channel and the bounding of thin layers of PDMS has to be mastered.

These achievements constitute building blocks towards a complete on chip medical diagnosis. The designed LOC device is thus an answer to the issue of fully integrated LOC. The fluidic device will allow a selective extraction of targets thanks to the specific pairing of Watson and Cricks. Integration of an on chip electrochemical detection below the release of the targets is possible. Biocompatibility and functionalization of surface chemistry are provided. The use of magnetic nanoparticles with a flexible functionalization can be optimally integrated for extraction of specific targets and their further release.

On chip magnetic hyperthermia is thus paving the way for many adjustments in terms of extraction module and cellular and molecular focus. Finally, miniaturization allow the integration of an *in situ* technique of detection near the released species avoiding both a macroscopic heating of the medium and by reducing experimental time frames of separation and purification outside the chip. All of that will increase even more the interest and efficiency for magnetic hyperthermia and microfluidic detection. For that part, the integration of planar microelectrode in the fluidic system will allow a direct titration of released species via on-chip electrochemistry.

Conclusion

The aim of this wide thesis work was obviously not to optimize each section but rather to show that the transposition in microfluidics could lead to optimized limits of detection and decreased experiment time towards increased performances. Chapter 4 intends to be a proof of concept for magnetic hyperthermia on chip and should be further confronted to a more complex biological solution with a mixture of various DNA sequences and length. One should note that the process bears a double barrier of specificity, the first one through hybridization on nanoparticles and the second one while hybridizing on probes coupled to the UME.

Strategies have been proposed to build a fully operational capture module coupling a fluidic geometry with bends and magnetic pulses to immobilize tagged magnetic nanoparticles bearing the target of interest and retrieving it from its biological matrix prior to magnetic hyperthermia. However in serum and plasma miRNAs are encapsulated in the Argonaute protein leaving only 7 nucleotides visible out of 23 for hybridization on the probe. It may not be sufficient for specific binding even more that a large proportion of miRNAs have similar sequences. The solution should be to functionalize nanoparticles with an antibody specific to the argonaute protein of the miRNA to detect, but this kind of antibody wasn't engineered yet. For now on, serum and plasma have to be treated with the Qiagen kit mentioned in chapter 1 and the mix of RNAs could be injected to the fully integrated Lab-On-Chip.

Appendix A

Capture kinetics: Ultra-microelectrode vs Nanoparticles

Here, we compare the efficiency uptake of our assembly of nanoparticles of 40 nm in radius in experimental conditions compared to the uptake on a planar Ultra microelectrode of 30 μm .

An aqueous solution contains DNA targets with a concentration $C_{bulk}(t)$ and a diffusion coefficient D ($1.0 \times 10^{-11} \text{ m}^2 \text{ s}^{-1}$). The UME and the nanoparticles are functionalized with the complementary probe as depicted on Figure A.1.

A.1 Diffusion dynamics of DNA targets on an Ultra-microelectrode

The computation of the diffusion on a planar microelectrode does not have any analytical solution. The spherical microelectrode is the best approaching analytical method. The time constant is depending on the width of the band against its radius for a spherical electrode which is sensibly the same value.

The molar number of DNA targets that collides with a spherical UME of radius r_1 per unit of time at stationary state is:

$$\frac{\partial n}{\partial t_s} = 4.D.C_{bulk}(t).r_1 \quad (\text{A.1})$$

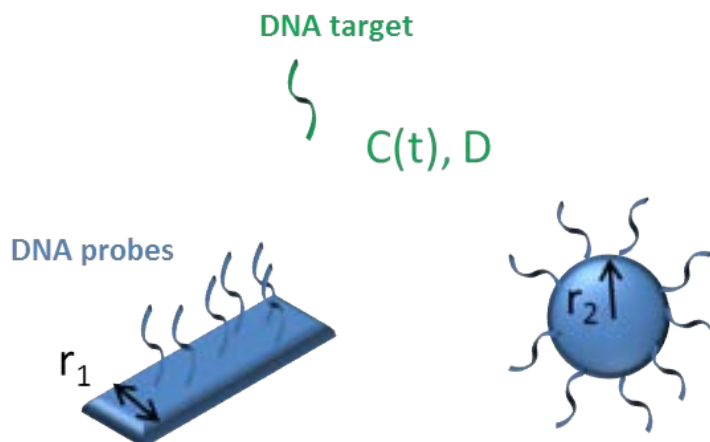


Figure A.1: Modeling of the capture dynamics of DNA targets (green) on an UME and on nanoparticles (blue).

In our case, concentrations of DNA targets are feeble (from 10^{-12} M to 10^{-18} M) giving a rate of hybridization on probes grafted negligible. Equation A.1 becomes:

$$\frac{\partial n}{\partial t_s} = 4.D.C^0.r_1 \quad (\text{A.2})$$

As the layer of diffusion and the electrode are around the same size diffusion is spherical in the vicinity of the electrode. According to Nernst approximation the concentration gradient induced by the perturbation remain mainly restricted to a distance near their radius.

The flux is defined according to Fick laws:

$$J(r, t) = -D.\frac{\partial C(r, t)}{\partial r}$$

along with the bulk concentration:

$$\frac{\partial C(r, t)}{\partial t} = D.\left[\frac{\partial^2 C(r, t)}{\partial r^2} + \frac{2}{r}.\frac{\partial C(r, t)}{\partial r}\right]$$

UME are reaching rapidly (around a millisecond) a stationary current proportional to r_1 and is not affected by what happens inside the solution giving a stationary solution for the bulk concentration:

$$C(r, t_\infty) = C^0.\left[1 - \frac{r_0}{r}\right]$$

And for $r=r_1$

$$\frac{\partial C(r)}{\partial r}_{r=r_1} = -\frac{C^0}{r_1}$$

To continue with the molar number of DNA targets reaching the UME ($r=r_1$)

$$dn = J_{r=r_1}.S.dt = D.\frac{C^0}{r_1}.4.r_1^2.dt$$

Finally

$$dC_{bulk} = \frac{dn}{V} = \frac{4.r_1.D}{V}.C^0.dt$$

With

$$k_1 = \frac{4.r_1.D}{V}$$

giving

$$\frac{dC}{C} = k_1.dt$$

The solution is

$$C_{bulk}(t) = C^0.e^{k_1.t}$$

To finish a multiplication by Avogadro number N_a gives the number of target DNA reaching and hybridizing on the UME:

$$N_{target} = N_a.V.C^0.e^{k_1.\Delta t} \quad (\text{A.3})$$

with

$$k_1 = \frac{4.r_1.D}{V}$$

where r_1 , is the radius of the UME, D , the diffusion coefficient of DNA in aqueous media and V , the volume of the solution.

A.2 Nanoparticles, nanomagnets for DNA capture

The molar number of target DNA that collide with a spherical nanoparticle with a radius r_2 at stationary state per unit of time is:

$$\frac{\partial n}{\partial t_s} = 4.\pi.D.C(t).r_2 \quad (\text{A.4})$$

For N nanoparticles in solution, we assume that the volume V in solution is way bigger than the total volume of nanoparticles. The expression $(dn/dt)_s$ becomes:

$$\frac{\partial n^N}{\partial t_s} = N.4.\pi.D.C(t).r_2 \quad (\text{A.5})$$

The second Fick law in spherical coordinates gives:

$$\frac{\partial C(r, t)}{\partial t} = D. \left[\frac{\partial^2 C(r, t)}{\partial r^2} + \frac{2}{r} \cdot \frac{\partial C(r, t)}{\partial r} \right] \quad (\text{A.6})$$

And

$$J(r, t) = -D. \frac{\partial C(r, t)}{\partial r}$$

Concerning the boundary conditions, at the surface of the nanoparticle $C(r = r_2, t=0)$ as we assume that all target hybridize as it collides with a probe. Far from the nanoparticle the bulk concentration is the initial concentration such as

$$\lim_{r \rightarrow \infty} C(r, t) = C^0$$

and at $t=0$ the concentration is C^0 everywhere.

The concentration in the bulk change significantly more slowly than the concentration in the vicinity of the nanoparticle as the diffusion is spherical the stationary time is around one millisecond. So the solution is given by:

$$C(r, t_\infty) = C^0. \left[1 - \frac{r_2}{r} \right] \quad (\text{A.7})$$

So

$$\frac{\partial C(r)}{\partial t} = -\frac{C^0.r_2}{r^2} \quad (\text{A.8})$$

And at $r=r_2$

$$\frac{\partial C(r)}{\partial t} \Big|_{r=r_2} = -\frac{C^0}{r_2} \quad (\text{A.9})$$

dn is given by

$$dn = J.S.dt = 4.\pi.C^0.r_2.D.dt \quad (\text{A.10})$$

Following Equation A.5

$$dn^N = 4.\pi.C(t).r_2.D.N.dt \quad (\text{A.11})$$

To continue with the concentration

$$dC = \frac{dn}{V} = \frac{4\pi \cdot r_2 \cdot D \cdot N}{V} \cdot C \cdot dt \quad (\text{A.12})$$

We set

$$k_2 = \frac{4\pi \cdot r_2 \cdot D \cdot N}{V} \quad (\text{A.13})$$

leading to

$$\frac{dC}{C} = k_2 \cdot dt \quad (\text{A.14})$$

The solution is

$$C_{bulk}(t) = C^0 \cdot e^{k_2 \cdot t} \quad (\text{A.15})$$

To finish Equation A.5 multiplied by Avogadro number N_a gives the number of target DNA reaching and hybridizing on N nanoparticles:

$$N_{target} = N_a \cdot V \cdot C^0 \cdot e^{k_2 \cdot \Delta t} \quad (\text{A.16})$$

with

$$k_2 = \frac{4\pi \cdot r_2 \cdot D \cdot N}{V}$$

where r_2 is the radius of the nanoparticle D the diffusion coefficient of DNA in aqueous media, N the number of nanoparticles and V the volume of the solution. This expression is only valid for a variation of $C_{bulk}(t)$ negligible and a rate of hybridized probe negligible. This is the case as the diffusion is spherical and the concentration of DNA targets feeble (from 10^{-12} M to 10^{-18} M).

The following Figure A.2 compares different reaction times Δt according to each initial target concentration C^0 in our experimental conditions. That is to say a microchannel volume of 440 nL and a number of nanoparticles N of 3.7×10^{13} .

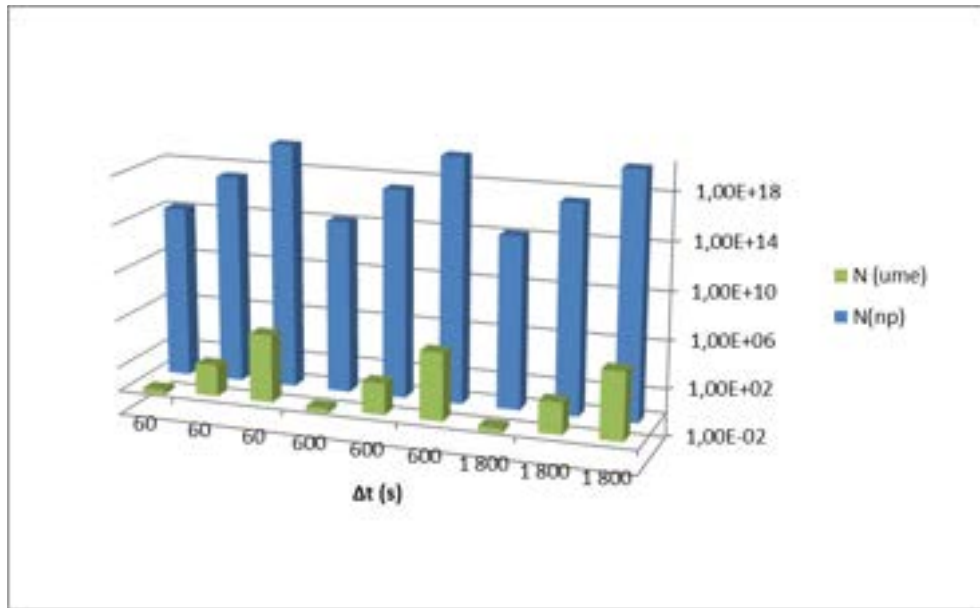


Figure A.2: Comparison between the number of DNA captured by a $30 \mu\text{m}$ wide UME and N nanoparticles of 80 nm in diameter.

Table A.1: Number of target DNA captured on an UME and N nanoparticles

| Δt | C^0 | N_{target}^{UME} | N_{target}^{NP} |
|------------|------------|----------------------|----------------------|
| 30 min | 10^{-12} | 4.1×10^5 | 1.7×10^{20} |
| | 10^{-15} | 4.1×10^2 | 1.7×10^{17} |
| | 10^{-18} | 4.1×10^{-1} | 1.7×10^{14} |
| 10 min | 10^{-12} | 4.1×10^5 | 1.7×10^{20} |
| | 10^{-15} | 4.1×10^2 | 1.7×10^{17} |
| | 10^{-18} | 4.1×10^{-1} | 1.7×10^{14} |
| 1 min | 10^{-12} | 4.1×10^5 | 1.7×10^{20} |
| | 10^{-15} | 4.1×10^2 | 1.7×10^{17} |
| | 10^{-18} | 4.1×10^{-1} | 1.7×10^{14} |

Nanoparticles of 80 nm in diameter appear to be outstanding assets in order to capture small unit of DNA. Thus it seems trivial to use an assembly of nanoparticles upstream of a module of DNA detection via an Ultra-microelectrode. The factor between the respective efficiencies is r' times N , with r' the difference between the two radius and N the number of nanoparticles, $N = 3.7 \times 10^{13}$ in our case.

Bibliography

- [1] Eva Van Rooij. The art of MicroRNA research. *Circ. Res.*, 108:219–234, 2011.
- [2] Allan M. Gurtan and Phillip a. Sharp. The role of miRNAs in regulating gene expression networks. *J. Mol. Biol.*, 425(19):3582–3600, 2013.
- [3] Xin Wei Wang, Niels H H Heegaard, and Henrik Orum. MicroRNAs in liver disease. *Gastroenterology*, 142(7):1431–1443, 2012.
- [4] Terry T. Goodrich, Hye Jin Lee, , and Robert M. Corn*. Enzymatically Amplified Surface Plasmon Resonance Imaging Method Using RNase H and RNA Microarrays for the Ultrasensitive Detection of Nucleic Acids. 2004.
- [5] Leni Moldovan, Kara E. Batte, Joanne Trgovcich, Jon Wisler, Clay B. Marsh, and Melissa Piper. Methodological challenges in utilizing miRNAs as circulating biomarkers. *J. Cell. Mol. Med.*, 18(3):371–390, 2014.
- [6] Amaia Lujambio and Scott W. Lowe. The microcosmos of cancer. *Nature*, 482:347–355, 2012.
- [7] Adrien Plecis. *Etude Et Controle De La Charge De Surface Dans Les Dispositifs Micro/Nanofluidiques : Nouveaux Outils Pour Les Sciences Separatives*. PhD thesis, 2008.
- [8] JA Benn, J Hu, BJ Hogan, RC Fry, and LD Samson. Comparative modeling and analysis of microfluidic and conventional DNA microarrays. *Anal. Biochem.*, 348:284–293, 2006.
- [9] J Melin and SR Quake. Microfluidic large-scale integration: the evolution of design rules for biological automation. *Annu. Rev. Biophys. Biomol. Struct.*, 36:213–231, 2007.
- [10] Todd M Squires, Robert J Messinger, and Scott R Manalis. Making it stick: convection, reaction and diffusion in surface-based biosensors. *Nat. Biotechnol.*, 26(4):417–426, 2008.
- [11] Carla P Concepcion, Ciro Bonetti, and Andrea Ventura. The microRNA-17-92 family of microRNA clusters in development and disease. *Cancer J.*, 18(3):262–7, 2012.
- [12] V Narry Kim, Jinju Han, and Mikiko C Siomi. Biogenesis of small RNAs in animals. *Nat. Rev. Mol. Cell Biol.*, 10(fEBRuARy):126–139, 2009.
- [13] Ross C Wilson and Jennifer a Doudna. Molecular mechanisms of RNA interference. *Annu. Rev. Biophys.*, 42:217–39, 2013.
- [14] B Czech and GJ Hannon. Small RNA sorting: matchmaking for Argonautes. *Nat. Rev. Genet.*, 2011.

- [15] M. P. Hunter, N. Ismail, Xi. Zhang, Baltazar D. Aguda, Eun Joo Lee, Lianbo Yu, Tao Xiao, Jeffrey Schafer, Mei-Ling Ting Lee, Thomas D. Schmittgen, S. Patrick Nana-Sinkam, David Jarjoura, and Clay B. Marsh. Detection of microRNA Expression in Human Peripheral Blood Microvesicles. *PLoS One*, 3(11):e3694, nov 2008.
- [16] Jason D Arroyo, John R Chevillet, Evan M Kroh, Ingrid K Ruf, Colin C Pritchard, Donald F Gibson, Patrick S Mitchell, Christopher F Bennett, Era L Pogossova-Agadjanyan, Derek L Stirewalt, Jonathan F Tait, and Muneesh Tewari. Argonaute2 complexes carry a population of circulating microRNAs independent of vesicles in human plasma. *Proc. Natl. Acad. Sci. U. S. A.*, 108(12):5003–8, mar 2011.
- [17] S. Bellingham, B. Coleman, and A. Hill. Small RNA deep sequencing reveals a distinct miRNA signature released in exosomes from prion-infected neuronal cells. *Nucleic Acids Res.*, 40(21):10937–10941, 2012.
- [18] X Chen, H Liang, J Zhang, K Zen, and CY Zhang. Horizontal transfer of microRNAs: molecular mechanisms and clinical applications. *Protein Cell*, 2012.
- [19] J Kim, A Krichevsky, and Y Grad. Identification of many microRNAs that copurify with polyribosomes in mammalian neurons. *Proc. Natl. Acad. Sci.*, 101(1):360–365, 2004.
- [20] P Xu, SY Vernooy, M Guo, and BA Hay. The *Drosophila* microRNA Mir-14 suppresses cell death and is required for normal fat metabolism. *Curr. Biol.*, 13(9):790–795, 2003.
- [21] J Brennecke, DR Hipfner, A Stark, and RB Russell. bantam encodes a developmentally regulated microRNA that controls cell proliferation and regulates the proapoptotic gene hid in *Drosophila*. *Cell*, 113(1):23–36, 2003.
- [22] Jean-Claude. Kaplan and Marc Delpech. *Biologie moléculaire et médecine*. Flammarion médecine-sciences, 1989.
- [23] R. C. Lee, R. L. Feinbaum, and V. Ambros. The *C. elegans* heterochronic gene lin-4 encodes small RNAs with antisense complementarity to lin-14. *Cell*, 75(5):843–854, 1993.
- [24] Zhihua Qiu and Yimin Dai. Roadmap of miR-122-related clinical application from bench to bedside. *Expert Opin. Investig. Drugs*, 23(3):347–55, 2014.
- [25] Yi Zhang, Yin Jia, Ruiying Zheng, Yingjun Guo, Yue Wang, Hui Guo, Mingyu Fei, and Shuhan Sun. Plasma MicroRNA-122 as a Biomarker for Viral-, Alcohol-, and Chemical-Related Hepatic Diseases. *Clin. Chem.*, 56(12), 2010.
- [26] Qiang Shi, Xi Yang, and Donna L Mendrick. Hopes and challenges in using miRNAs as translational biomarkers for drug-induced liver injury. *Biomark. Med.*, 7(Dili):307–15, 2013.
- [27] Kenji Takahashi, Irene Yan, Hui-Ju Wen, and Tushar Patel. microRNAs in liver disease: from diagnostics to therapeutics. *Clin. Biochem.*, 46(10-11):946–52, jul 2013.

- [28] J Xu, C Wu, X Che, L Wang, and D Yu. Circulating MicroRNAs, miR21, miR122, and miR223, in patients with hepatocellular carcinoma or chronic hepatitis. *Mol. Carcinog.*, 50(2):136–142, 2011.
- [29] George Adrian Calin, Calin Dan Dumitru, Masayoshi Shimizu, Roberta Bichi, Simona Zupo, Evan Noch, Hansjuerg Aldler, Sashi Rattan, Michael Keating, Kanti Rai, Laura Rassenti, Thomas Kipps, Massimo Negrini, Florencia Bullrich, and Carlo M Croce. Frequent deletions and down-regulation of micro-RNA genes miR15 and miR16 at 13q14 in chronic lymphocytic leukemia. *Proc. Natl. Acad. Sci. U. S. A.*, 99(24):15524–9, 2002.
- [30] Jinghua Chen, Jing Zhang, Qian Zhuang, Jing Chen, and Xinhua Lin. Hybridization biosensor using sodium tanshinone IIA sulfonate as electrochemical indicator for detection of short DNA species of chronic myelogenous leukemia. *Electrochim. Acta*, 53(6):2716–2723, feb 2008.
- [31] X. Ji, R. Takahashi, Y. Hiura, G. Hirokawa, Y. Fukushima, and N. Iwai. Plasma miR-208 as a Biomarker of Myocardial Injury. *Clin. Chem.*, 55(11):1944–1949, 2009.
- [32] Shlomit Gilad, Eti Meiri, Yariv Yogev, Sima Benjamin, Danit Lebanony, Noga Yerushalmi, Hila Benjamin, Michal Kushnir, Hila Cholakh, Nir Melamed, Zvi Bentwich, Moshe Hod, Yaron Goren, and Ayelet Chajut. Serum MicroRNAs Are Promising Novel Biomarkers. *PLoS One*, 3(9):e3148, sep 2008.
- [33] Jessica A. Weber, David H. Baxter, Shile Zhang, David Y. Huang, Kuo How Huang, Ming Jen Lee, David J. Galas, and Kai Wang. The MicroRNA Spectrum in 12 Body Fluids. *Clin. Chem.*, 56(11):1733–1741, 2010.
- [34] Qiagen. Purification of total RNA, including small RNAs, from serum or plasma using the miRNeasy Mini Kit. 2011; available at: <http://www.qiagen.com/products/rnastabilizationpurification/microrna/mirneasyminikit> - Recherche Google.
- [35] AA Aboobaker, P Tomancak, and N Patel. Drosophila microRNAs exhibit diverse spatial expression patterns during embryonic development. *Proc. Natl. Acad. Sci.*, 102(50):18017–18022, 2005.
- [36] EM Small, RJA Frost, and EN Olson. MicroRNAs add a new dimension to cardiovascular disease. *Circulation*, 121(8):1022–1032, 2010.
- [37] AJ Tijssen, EE Creemers, and PD Moerland. MiR423-5p as a circulating biomarker for heart failure. *Circulation*, 106(6):1035–1039, 2010.
- [38] H Wang, R Ach, A Tsalenko, and B Curry. Direct miRNA profiling from low-input total RNA: Stepping towards quantitative measurements. 2007.
- [39] Chen-Min Chang, Wen-Hsin Chang, Chih-Hung Wang, Jung-Hao Wang, John D Mai, and Gwo-Bin Lee. Nucleic acid amplification using microfluidic systems. *Lab Chip*, 13(7):1225–42, 2013.
- [40] K-A Kreuzer, A Bohn, U Lass, U R Peters, and C A Schmidt. Influence of DNA polymerases on quantitative PCR results using TaqMan TM probe format in the LightCycler TM instrument. *Mol. Cell. Probes*, 14:57–60, 2000.

- [41] CA Heid, J Stevens, KJ Livak, and PM Williams. Real time quantitative PCR. *Genome Res.*, 6(10):986–994, 1996.
- [42] CT Wittwer, MG Herrmann, and CN Gundry. Real-time multiplex PCR assays. *Methods*, 25(4):430–442, 2001.
- [43] Daniel Thevenot, Klara Toth, Richard Durst, George Wilson, and George Wilson Electrochemical. Electrochemical biosensors: recommended definitions and classification. *Pure Appl. Chem.*, 71(12):2333–2348, 1999.
- [44] Veeradasan Perumal and Uda Hashim. Advances in biosensors: Principle, architecture and applications. *J. Appl. Biomed.*, 12:1–15, 2014.
- [45] CED Chidsey and DN Loiacono. Chemical functionality in self-assembled monolayers: structural and electrochemical properties. *Langmuir*, 1990.
- [46] T Wink, SJ Van Zuilen, A Bult, and WP Van Bennekom. Self-assembled monolayers for biosensors. *Analyst*, 122(4):43R–50R, 1997.
- [47] NK Chaki and K Vijayamohanan. Self-assembled monolayers as a tunable platform for biosensor applications. *Biosens. Bioelectron.*, 17(1):1–12, 2002.
- [48] C D Bain, J Evall, G M Whitesides, D T Ic, and George M Whitesides. Formation of monolayers by the coadsorption of thiols on gold: variation in the head group, tail group, and solvent. *J. Am. Chem. Soc.*, 111(18):7164–7175, 1989.
- [49] HO Finklea, S Avery, M Lynch, and T Furttsch. Blocking oriented monolayers of alkyl mercaptans on gold electrodes. *Langmuir*, 3(3):409–413, 1987.
- [50] AB Steel, TM Herne, and MJ Tarlov. Electrochemical quantitation of DNA immobilized on gold. *Anal. Chem.*, 70(22):4670–4677, 1998.
- [51] TM Herne and MJ Tarlov. Characterization of DNA probes immobilized on gold surfaces. *J. Am. Chem. Soc.*, 119(38):8916–8920, 1997.
- [52] Rastislav Levicky, Tonya M. Herne, Michael J. Tarlov, and Sushil K. Satija. Using Self-Assembly To Control the Structure of DNA Monolayers on Gold: A Neutron Reflectivity Study. *J. Am. Chem. Soc.*, 120(38):9787–9792, 1998.
- [53] Shana O. Kelley, Nicole M. Jackson, Michael G. Hill, and Jacqueline K. Barton. Long-range electron transfer through DNA films. *Angew. Chemie - Int. Ed.*, 38(7):941–945, 1999.
- [54] Shanlin Pan and Lewis Rothberg. Chemical control of electrode functionalization for detection of DNA hybridization by electrochemical impedance spectroscopy. *Langmuir*, 21(17):1022–1027, 2005.
- [55] Elicia L. S. Wong and J. Justin Gooding. Electronic Detection of Target Nucleic Acids by a 2,6-Disulfonic Acid Anthraquinone Intercalator. *Anal. Chem.*, 75(15):3845–3852, aug 2003.
- [56] Maël Manesse, Valerie Stambouli, Rabah Boukherroub, and Sabine Szunerits. Electrochemical impedance spectroscopy and surface plasmon resonance studies of DNA hybridization on gold/SiO_x interfaces. *Analyst*, 133:1097–1103, 2008.

- [57] Fausto Lucarelli, Giovanna Marrazza, Anthony P.F Turner, and Marco Mascini. Carbon and gold electrodes as electrochemical transducers for DNA hybridisation sensors. *Biosens. Bioelectron.*, 19(6):515–530, jan 2004.
- [58] Joseph Wang, Emil Palecek, Peter E Nielsen, Gustavo Rivas, Xiaohua Cai, Haruki Shiraishi, Narasaiah Dontha, Denbai Luo, and Percio A M Farias. Peptide Nucleic Acid Probes for Sequence-Specific DNA Biosensors. 7863(10):7667–7670, 1996.
- [59] J Wang, AN Kawde, and E Sahlin. Renewable pencil electrodes for highly sensitive stripping potentiometric measurements of DNA and RNA. *Analyst*, 125(1):5–7, 2000.
- [60] G Marrazza, G Chiti, and M Mascini. Detection of human apolipoprotein E genotypes by DNA electrochemical biosensor coupled with PCR. *Clin. Chem.*, 46(1):31–37, 2000.
- [61] DJ Caruana and A Heller. Enzyme-amplified amperometric detection of hybridization and of a single base pair mutation in an 18-base oligonucleotide on a 7- μ m-diameter microelectrode. *J. Am. Chem. Soc.*, 121(4):769–774, 1999.
- [62] KM Millan, AJ Spurmanis, and SR Mikkelsen. Covalent immobilization of DNA onto glassy carbon electrodes. *Electroanalysis*, 4(10):929–932, 1992.
- [63] G Marrazza, I Chianella, and M Mascini. Disposable DNA electrochemical sensor for hybridization. 14:43–51, 1999.
- [64] Arzum Erdem, Kagan Kerman, Burcu Meric, Ulus Salih Akarca, and Mehmet Ozsoz. DNA Electrochemical Biosensor for the Detection of Short DNA Sequences Related to the Hepatitis B Virus. *Electroanalysis*, 11(8):586–587, jun 1999.
- [65] Joseph. Wang, Xiaohua. Cai, Jianyan. Wang, Colleen. Jonsson, and Emil. Palecek. Trace Measurements of RNA by Potentiometric Stripping Analysis at Carbon Paste Electrodes. *Anal. Chem.*, 67(22):4065–4070, nov 1995.
- [66] J Wang, JR Fernandes, and LT Kubota. Polishable and renewable DNA hybridization biosensors. *Anal. Chem.*, 1998.
- [67] Kelly M. Millan and Susan R. Mikkelsen. Sequence-selective biosensor for DNA based on electroactive hybridization indicators. *Anal. Chem.*, 65(17):2317–2323, sep 1993.
- [68] KM Millan, A Saraullo, and SR Mikkelsen. Voltammetric DNA biosensor for cystic fibrosis based on a modified carbon paste electrode. *Anal. Chem.*, 66(18):2943–2948, 1994.
- [69] T. de Lumley-Woodyear, C. N. Campbell, and A. Heller*. Direct Enzyme-Amplified Electrical Recognition of a 30-Base Model Oligonucleotide. *J. Am. Chem.Soc.*, 118(23):5504–5505, 1996.
- [70] H Bünemann. Immobilization of denatured DNA to macroporous supports: II. Steric and kinetic parameters of heterogeneous hybridization reactions. *Nucleic Acids Res.*, 10(22):7181–7196, 1982.

- [71] BD Hames and SJ Higgins. *Nucleic acid hybridisation: a practical approach*. Oxford, 1985.
- [72] J Wang, G Rivas, C Parrado, X Cai, and MN Flair. Electrochemical biosensor for detecting DNA sequences from the pathogenic protozoan *Cryptosporidium parvum*. *Talanta*, 1997.
- [73] J Wang, G Rivas, and X Cai. Screenprinted electrochemical hybridization biosensor for the detection of DNA sequences from the *Escherichia coli* pathogen. *Electroanalysis*, 1997.
- [74] Fausto Lucarelli, Giovanna Marrazza, Ilaria Palchetti, S. Cesaretti, and Marco Mascini. Coupling of an indicator-free electrochemical DNA biosensor with polymerase chain reaction for the detection of DNA sequences related to the apolipoprotein E. *Anal. Chim. Acta*, 469:93–99, 2002.
- [75] L Authier, C Grossiord, and P Brossier. Gold nanoparticle-based quantitative electrochemical detection of amplified human cytomegalovirus DNA using disposable microband electrodes. *Anal. Chem.*, 2001.
- [76] Jahan Bakhsh Raoof, Reza Ojani, Seyed Mahdi Golabi, Ezat Hamidi-Asl, and Mohammad Saeid Hejazi. Preparation of an electrochemical PNA biosensor for detection of target DNA sequence and single nucleotide mutation on p53 tumor suppressor gene corresponding oligonucleotide. *Sensors Actuators B Chem.*, 157(1):195–201, sep 2011.
- [77] M. Lazerges, V.T. Tal, P. Bigey, D. Scherman, and F. Bedioui. Electrochemical DNA-biosensors: Two-electrode setup well adapted for miniaturized devices. *Sensors Actuators B Chem.*, 182:510–513, jun 2013.
- [78] M Lazerges and F Bedioui. Analysis of the evolution of the detection limits of electrochemical DNA biosensors. *Anal. Bioanal. Chem.*, 2013.
- [79] Hui Peng, Christian Soeller, Nickolas Vigar, Paul a Kilmartin, Mark B Cannell, Graham a Bowmaker, Ralph P Cooney, and Jadranka Travas-Sejdic. Label-free electrochemical DNA sensor based on functionalised conducting copolymer. *Biosens. Bioelectron.*, 20(9):1821–8, mar 2005.
- [80] Carla Dos Santos Riccardi, Hideko Yamanaka, Mira Josowicz, Janusz Kowalik, Boris Mizaikoff, and C Kranz. Label-free DNA detection based on modified conducting polypyrrole films at microelectrodes. *Anal. Chem.*, 78(4):1139–45, 2006.
- [81] Kavita Arora, Nirmal Prabhakar, Subhash Chand, and B. D. Malhotra. Immobilization of single stranded DNA probe onto polypyrrole-polyvinyl sulfonate for application to DNA hybridization biosensor. *Sensors Actuators, B Chem.*, 126:655–663, 2007.
- [82] Esmaeel Alipour, Mohammad Hossein Pournaghi-Azar, Mojtaba Parvizi, Sayed Mahdi Golabi, and Mohammad Saeid Hejazi. Electrochemical detection and discrimination of single copy gene target DNA in non-amplified genomic DNA. *Electrochim. Acta*, 56(5):1925–1931, 2011.
- [83] Chin Pei Chen, Abhijit Ganguly, Ching Ying Lu, Ting Yu Chen, Chun Chiang Kuo, Reui San Chen, Wen Hsun Tu, Wolfgang B. Fischer, Kuei Hsien Chen,

- and Li Chyong Chen. Ultrasensitive in situ label-free DNA detection using a GaN nanowire-based extended-gate field-effect-transistor sensor. *Anal. Chem.*, 83(6):1938–1943, 2011.
- [84] Jian Weng, Jianfeng Zhang, Hui Li, Liping Sun, Chenghong Lin, and Qiqing Zhang. Label-free DNA sensor by boron-doped diamond electrode using an ac impedimetric approach. *Anal. Chem.*, 80(18):7075–7083, 2008.
- [85] V Dharuman, E Nebling, T Grunwald, J Albers, L Blohm, B Elsholz, R Wörl, and R Hintsche. DNA hybridization detection on electrical microarrays using coulometric pulse technique. *Biosens. Bioelectron.*, 22(5):744–51, dec 2006.
- [86] Shufeng Liu, Jing Liu, Li Wang, and Feng Zhao. Development of electrochemical DNA biosensor based on gold nanoparticle modified electrode by electrodeless deposition. *Bioelectrochemistry*, 79(1):37–42, aug 2010.
- [87] Omotayo a. Arotiba, Anna Ignaszak, Rehana Malgas, Amir Al-Ahmed, Priscilla G.L. Baker, Selwyn F. Mapolie, and Emmanuel I. Iwuoha. An electrochemical DNA biosensor developed on novel multinuclear nickel(II) salicylaldimine metallodendrimer platform. *Electrochim. Acta*, 53(4):1689–1696, dec 2007.
- [88] Shafiquzzaman Siddiquee, Nor Azah Yusof, Abu Bakar Salleh, Soon Guan Tan, Fatimah Abu Bakar, and Lee Yook Heng. DNA hybridization based on *Trichoderma harzianum* gene probe immobilization on self-assembled monolayers on a modified gold electrode. *Sensors Actuators B Chem.*, 147(1):198–205, may 2010.
- [89] Yang Bo, Weiqi Wang, Junfei Qi, and Shasheng Huang. A DNA biosensor based on graphene paste electrode modified with Prussian blue and chitosan. *Analyst*, 136(9):1946–51, may 2011.
- [90] Jing Zhang, Jing Hua Chen, Rong Chun Chen, Guo Nan Chen, and Feng Fu Fu. Sequence-specific detection of trace DNA via a junction-probe electrochemical sensor employed template-enhanced hybridization strategy. *Biosens. Bioelectron.*, 25(4):815–9, dec 2009.
- [91] Elicia L S Wong and J Justin Gooding. Charge transfer through DNA: A selective electrochemical DNA biosensor. *Anal. Chem.*, 78(7):2138–44, apr 2006.
- [92] V. Dharuman and Jong Hoon Hahn. Effect of short chain alkane diluents on the label free electrochemical DNA hybridization discrimination at the HS-ssDNA/diluent binary mixed monolayer in presence of cationic intercalators. *Sensors Actuators B Chem.*, 127(2):536–544, nov 2007.
- [93] A Erdem, K Kerman, B Meric, US Akarca, and M Ozsoz. Novel hybridization indicator methylene blue for the electrochemical detection of short DNA sequences related to the hepatitis B virus. *Anal. Chim. Acta*, 2000.
- [94] B Meric, K Kerman, D Ozkan, P Kara, and S Erensoy. Electrochemical DNA biosensor for the detection of TT and Hepatitis B virus from PCR amplified real samples by using methylene blue. *Talanta*, 2002.
- [95] Xiaojun Chen, Somenath Roy, Yanfen Peng, and Zhiqiang Gao. Electrical sensor array for polymerase chain reaction-free messenger RNA expression profiling. *Anal. Chem.*, 82(14):5958–64, jul 2010.

- [96] PE Sheehan and LJ Whitman. Detection limits for nanoscale biosensors. *Nano Lett.*, 2005.
- [97] G Zheng, F Patolsky, Y Cui, and WU Wang. Multiplexed electrical detection of cancer markers with nanowire sensor arrays. *Nature*, 2005.
- [98] Berta Esteban Fernández de Ávila, Herschel M. Watkins, José M. Pingarrón, Kevin W. Plaxco, Giuseppe Palleschi, and Francesco Ricci. Determinants of the Detection Limit and Specificity of Surface-Based Biosensors. *Anal. Chem.*, 85(14):6593–6597, jul 2013.
- [99] Berg and Howard C. *Random Walks in Biology*. Princeton University Press, Princeton, 1993.
- [100] R Byron Bird, Warren E Stewart, and Edwin N Lightfoot. *Transport Phenomena Revised Second Edition*. New York, 2 edition, 2002.
- [101] MT Record Jr and W Zhang. Analysis of effects of salts and uncharged solutes on protein and nucleic acid equilibria and processes: a practical guide to recognizing and interpreting polyelectrolyte. *Adv. Protein Chem.*, 51:281–305, 1998.
- [102] Yuri Belosludtsev, Inna Belosludtsev, Bonnie Iverson, Sergey Lemeshko, Rick Wiese, Michael Hogan, and Tom Powdrill. Nearly Instantaneous, Cation-Independent, High Selectivity Nucleic Acid Hybridization to DNA Microarrays. *Biochem. Biophys. Res. Commun.*, 282(5):1263–1267, apr 2001.
- [103] SK Yoon, GW Fichtl, and PJA Kenis. Active control of the depletion boundary layers in microfluidic electrochemical reactors. *Lab Chip*, 2006.
- [104] DJ Laser and JG Santiago. A review of micropumps. *J. Micromech. Microeng.*, 14(04):35–64, 2004.
- [105] Duffy, Heather L. Gillis, Joe Lin, Jr. Norman F. Sheppard, Kellogg, and Gregory J. Microfabricated Centrifugal Microfluidic Systems: Characterization and Multiple Enzymatic Assays. *Anal. Chem.*, 1999.
- [106] AJP Martin and RLM Syngé. A new form of chromatogram employing two liquid phases: A theory of chromatography. 2. Application to the micro-determination of the higher monoamino-acids in. *Biochem. J.*, 1941.
- [107] HG Kunkel and A Tiselius. Electrophoresis of proteins on filter paper. *J. Gen. Physiol.*, 1951.
- [108] DJ Harrison, A Manz, Z Fan, and H Luedi. Capillary electrophoresis and sample injection systems integrated on a planar glass chip. *Analytical*, 1992.
- [109] HP Le. Progress and trends in ink-jet printing technology. *J. Imaging Sci. Technol.*, 1998.
- [110] LJ Thomas Jr and SP Bessman. Prototype for an implantable micropump powered by piezoelectric disk benders. *ASAIO J.*, 1975.
- [111] KF Buechler. Diagnostic devices for the controlled movement of reagents without membranes. *US Pat. 5,458,852*, 1995.

- [112] Luc Gervais, Nico de Rooij, and Emmanuel Delamarche. Microfluidic Chips for Point-of-Care Immunodiagnosics. *Adv. Mater.*, 23(24):H151–H176, jun 2011.
- [113] E Verpoorte and NF De Rooij. Microfluidics meets MEMS. *Proc. IEEE*, 2003.
- [114] JC McDonald and GM Whitesides. Poly (dimethylsiloxane) as a material for fabricating microfluidic devices. *Acc. Chem. Res.*, 2002.
- [115] J S Rossier, M A Roberts, R Ferrigno, and H H Girault. Electrochemical Detection in Polymer Microchannels. *Anal. Chem.*, 71:4294–4299, 1999.
- [116] Jean Gamby, Mathieu Lazerges, Christine Pernelle, Hubert Perrot, Hubert H. Girault, Bernard Tribollet, B. Liu, P. Yang, Y. Xu, and H. Wang. Electroacoustic miniaturized DNA-biosensor. *Lab Chip*, 7(11):1607, oct 2007.
- [117] Peter A. Willis, Brian D. Hunt, Victor E. White, Michael C. Lee, Michael Ikeda, Sam Bae, Michael J. Pelletier Grunthanera, and Frank J. Monolithic Teflon1 membrane valves and pumps for harsh chemical and low-temperature use. *Lab Chip*, 2007.
- [118] KLA Chan, X Niu, AJ de Mello, and SG Kazarian. Rapid prototyping of microfluidic devices for integrating with FT-IR spectroscopic imaging. *Lab Chip*, 2010.
- [119] AW Martinez, ST Phillips, GM Whitesides, and E Carrilho. Diagnostics for the developing world: microfluidic paper-based analytical devices. 2009.
- [120] C Zhang, J Xu, W Ma, and W Zheng. PCR microfluidic devices for DNA amplification. *Biotechnol. Adv.*, 2006.
- [121] J Wang, G Rivas, JR Fernandes, JLL Paz, and M Jiang. Indicator-free electrochemical DNA hybridization biosensor. *Anal. Chim. Acta*, 375:197–203, 1998.
- [122] R. M. Umek, S. W. Lin, and J. Vielmetter. Electronic Detection of Nucleic Acids. *J. Mol. Diagnostics*, 3(2):74–84, 2001.
- [123] K Hashimoto, K Ito, and Y Ishimori. Microfabricated disposable DNA sensor for detection of hepatitis B virus DNA. *Sensors Actuators B Chem.*, 1998.
- [124] D Xu, K Huang, Z Liu, Y Liu, and L Ma. Microfabricated disposable DNA sensors based on enzymatic amplification electrochemical detection. *Electroanalysis*, 2001.
- [125] Wayne U Wang, Chuo Chen, Keng-hui Lin, Ying Fang, and Charles M Lieber. Label-free detection of small-molecule-protein interactions by using nanowire nanosensors. *Proc. Natl. Acad. Sci. U. S. A.*, 102(9):3208–12, mar 2005.
- [126] RS Foote, J Khandurina, and SC Jacobson. Preconcentration of proteins on microfluidic devices using porous silica membranes. *Analytical*, 2005.
- [127] D Wu and AJ Steckl. High speed nanofluidic protein accumulator. *Lab Chip*, 2009.
- [128] CW Price, DC Leslie, and JP Landers. Nucleic acid extraction techniques and application to the microchip. *Lab Chip*, 2009.

- [129] Jong Wook Hong, Vincent Studer, Giao Hang, W French Anderson, and Stephen R Quake. A nanoliter-scale nucleic acid processor with parallel architecture. *Nat. Biotechnol.*, 22(4):435–439, apr 2004.
- [130] A Guinier and R Jullien. *La Matière à l'état solide: des supraconducteurs aux superalliages*. Hachette, 1987.
- [131] EDT de Lacheisserie. Magnétisme, Tome 1: Fondements (Coll. Grenoble sciences). *EDP Sci.*, 2000.
- [132] R Dreyfus, J Baudry, ML Roper, M Fermigier, and HA Stone. Microscopic artificial swimmers. *Nature*, 2005.
- [133] RM Cornel and U Schwertmann. The Iron Oxides. Structure, Properties, Reactions and Uses. *VCH Weinheim*, 1996.
- [134] Farkhad G. Aliev, Miguel A. Correa-Duarte, Arif Mamedov, John W. Ostrander, Michael Giersig, Lius M. Liz-Marzán, and Nicholas A. Kotov. Layer-By-Layer Assembly of Core-Shell Magnetite Nanoparticles: Effect of Silica Coating on Interparticle Interactions and Magnetic Properties. *Adv. Mater.*, 11(12):1006–1010, aug 1999.
- [135] R Perzynski, YL Raikher, and D Fiorani. Surface effects in magnetic nanoparticles. *Springer Sci. New York*, 2005.
- [136] S Bedanta and W Kleemann. Supermagnetism. *J. Phys. D. Appl. Phys.*, 2008.
- [137] J. L. Dormann. Le phénomène de superparamagnétisme. *Rev. Phys. Appl.*, 16:275–301, 1981.
- [138] J.-C. BACRI, R. PERZYNSKI, and D. SALIN. Magnetic colloidal properties of ionic ferrofluids. *J. Magn. Magn. Mater.*, 62(1):36–46, 1986.
- [139] R Kaiser and G Miskolczy. Magnetic properties of stable dispersions of sub-domain magnetite particles. *J. Appl. Phys.*, 1970.
- [140] R E Rosensweig. Heating magnetic fluid with alternating magnetic field. *J. Magn. Magn. Mater.*, 252:370–374, 2002.
- [141] MI Shliomis. Magnetic fluids. *Physics-Uspokhi*, 1974.
- [142] J. P. Fortin, C. Wilhelm, J. Servais, C. Ménager, J. C. Bacri, and F. Gazeau. Size-Sorted Anionic Iron Oxide Nanomagnets as Colloidal Mediators for Magnetic Hyperthermia. *J. Am. Chem. Soc.*, 129(9):2628–2635, 2007.
- [143] LH Reddy, JL Arias, J Nicolas, and P Couvreur. Magnetic nanoparticles: design and characterization, toxicity and biocompatibility, pharmaceutical and biomedical applications. *Chem. Rev.*, 2012.
- [144] R. Lawaczeck, H. Bauer, T. Frenzel, M. Hasegawa, and H. J. Ito, Y., Kito, K., ... & Weinmann. Magnetic iron oxide particles coated with carboxydextran for parenteral administration and liver contrasting: pre-clinical profile of SH U555A. *Acta radiol.*, 38(4):584–597, 1997.
- [145] Frank K. Wacker, Klaus Reither, Wolfgang Ebert, Michael Wendt, Jonathan S. Lewin, and Karl-Juergen Wolf. MR Image-guided Endovascular Procedures with the Ultrasmall Superparamagnetic Iron Oxide SH U 555 C as an Intravascular Contrast Agent: Study in Pigs. *Radiology*, 226(2):459–464, feb 2003.

- [146] V Dousset, C Gomez, KG Petry, and C Delalande. Dose and scanning delay using USPIO for central nervous system macrophage imaging. *Reson. Mater. ...*, 1999.
- [147] SCA Michel, TM Keller, JM Frohlich, D Fink, and R Caduff. Preoperative Breast Cancer Staging: MR Imaging of the Axilla with Ultrasmall Superparamagnetic Iron Oxide Enhancement 1. *Radiology*, 2002.
- [148] RC Semelka and TKG Helmberger. Contrast Agents for MR Imaging of the Liver. *Radiology*, 218(1):27–38, 2001.
- [149] WS Enochs, G Harsh, and F Hochberg. Improved delineation of human brain tumors on MR images using a longcirculating, superparamagnetic iron oxide agent. *J. Magn.*, 1999.
- [150] JWM Bulte, M De Cuyper, and D Despres. Short- vs. long-circulating magnetoliposomes as bone marrow-seeking MR contrast agents. *J. Magn.*, 1999.
- [151] KJ Widder and AE Senyei. Magnetic microspheres: a model system for site specific drug delivery in vivo. *Exp. Biol.*, 1978.
- [152] C Alexiou, W Arnold, RJ Klein, FG Parak, and P Hulin. Locoregional cancer treatment with magnetic drug targeting. *Cancer Res.*, 2000.
- [153] Andreas S. Lübbe, Christian Bergemann, Jeffery Brock, and David G. McClure. Physiological aspects in magnetic drug-targeting. *J. Magn. Magn. Mater.*, 194(1):149–155, 1999.
- [154] JP Stevenson, M Rutnakornpituk, and M Vadala. Magnetic cobalt dispersions in poly (dimethylsiloxane) fluids. *J. Magn.*, 2001.
- [155] Mehta. Direct binding of protein to magnetic particles. *Biotechnology*, 1997.
- [156] ML Hans and AM Lowman. Biodegradable nanoparticles for drug delivery and targeting. *Opin. Solid State Mater. Sci.*, 2002.
- [157] EE Carpenter. Iron nanoparticles as potential magnetic carriers. *J. Magn. Magn. Mater.*, 225(1):17–20, 2001.
- [158] F. C. Cabrera, A. F. Melo, J. C. de Souza, A. E. Job, and F. N. Crespilho. A flexible lab-on-a-chip for the synthesis and magnetic separation of magnetite decorated with gold nanoparticles. *Lab Chip*, 15(8):1835–1841, 2015.
- [159] UO Häfeli, GJ Pauer, WK Roberts, and JL Humm. Magnetically targeted microspheres for intracavitary and intraspinal Y-90 radiotherapy. *Sci. Clin.*, 1997.
- [160] C. Mah, I. Zolotukhin, T. J. Fraitas, J. Dobson, C. Batich, and B. J. Byrne. Microsphere-mediated delivery of recombinant AAV vectors in vitro and in vivo. *Mol Ther*, page S239, 2000.
- [161] R. Molday and D. Mackenzie. Immunospecific ferromagnetic iron-dextran reagents for the labeling and magnetic separation of cells. *J. Immunol. Methods*, 52(3):353–367, 1982.
- [162] C. Sangregorio, J. K. Wiemann, C. J. O'Connor, and Z. Rosenzweig. A new method for the synthesis of magnetoliposomes Bio/Chemical Magnetism A new method for the synthesis of magnetoliposomes. *J. Appl. Phys.*, 85(8):5699–5701, 1999.

- [163] Jon Dobson Heath Pardoe, Wanida Chua-anusorn, Timothy G. St. Pierre*. Structural and magnetic properties of nanoscale iron oxide particles synthesized in the presence of dextran or polyvinyl alcohol. *J. Magn. Magn. Mater.*, 225:41–46, 2001.
- [164] Q A Pankhurst, J Connolly, S K Jones, and J Dobson. Applications of magnetic nanoparticles in biomedicine. *J. Phys. D Appl. Phys.*, 36(03):167–181, 2003.
- [165] M Zborowski. *Physics of magnetic cell sorting*. Springer, 1997.
- [166] Lee R. Moore, Alexander R. Rodriguez, P. Stephen Williams, Kara McCloskey, Brian J. Bolwell, Masayuki Nakamura, Jeffrey J. Chalmers, and Maciej Zborowski. Progenitor cell isolation with a high-capacity quadrupole magnetic flow sorter. *J. Magn. Magn. Mater.*, 225:277–284, 2001.
- [167] T Rheinländer, D Roessner, W Weitschies, and W Semmler. Comparison of size-selective techniques for the fractionation of magnetic nanospheres. *Front. Magn.*, 1999.
- [168] P Todd, RP Cooper, JF Doyle, and S Dunn. Multistage magnetic particle separator. *J. Magn.*, 2001.
- [169] Bruno Teste, Bruno Teste, M Jean-louis Marty, M Christophe Marquette, and M Vincent Studer. *Développement d'un microsysteme diagnostique de l'allergie*. PhD thesis, 2011.
- [170] H. Thurman Henderson (Jin-Woo Choi), Chong H. Ahn, Shekhar Bhansali. A new magnetic bead-based, filterless bio-separator with planar electromagnetic surfaces for integrated bio-detection systems. *Sensors Actuators B*, 68:34–39, 2000.
- [171] A. Rida and M. Gijs. Dynamics of magnetically retained supraparticle structures in a liquid flow. *Appl. Phys. Lett.*, 85(2004):4986–4988, 2004.
- [172] F. Lacharme, C. Vandevyver, and M. Gijs. Full On-Chip Nanoliter Immunoassay by Geometrical Magnetic Trapping of Nanoparticle Chains. *Anal. Chem.*, 80:2905–2910, 2008.
- [173] Kristian Smistrup, Torsten Lund-Olesen, Mikkel F. Hansen, and Peter T. Tang. Microfluidic magnetic separator using an array of soft magnetic elements. *J. Appl. Phys.*, 99:100–102, 2006.
- [174] Qasem Ramadan, Victor Samper, Daniel Poenar, and Chen Yu. On-chip microelectromagnets for magnetic-based bio-molecules separation. *J. Magn. Magn. Mater.*, 281:150–172, 2004.
- [175] Sanae Tabnaoui. Magnetic fluidized bed for sample preconcentration and immunoextraction in microfluidic systems. 2012.
- [176] Kyu Sung Kim and Je-Kyun Park. Magnetic force-based multiplexed immunoassay using superparamagnetic nanoparticles in microfluidic channel. *Lab Chip*, 5:657–664, 2005.

- [177] R G Digigow, J-F Dechézelles, J Kaufmann, D Vanhecke, H Knapp, M Latuada, B Rothen-Rutishauser, and a Petri-Fink. Magnetic microreactors for efficient and reliable magnetic nanoparticle surface functionalization. *Lab Chip*, 14(13):2276–86, 2014.
- [178] F Paul, D Melville, and S Roath. A bench top magnetic separator for malarial parasite concentration. *IEEE Trans.*, 1981.
- [179] C Del Gratta, S Della Penna, and P Battista. Detection and counting of specific cell populations by means of magnetic markers linked to monoclonal antibodies. *Phys. Med.*, 1995.
- [180] WK Hofmann, S de Vos, M Komor, and D Hoelzer. Characterization of gene expression of CD34+ cells from normal and myelodysplastic bone marrow. *Blood*, 2002.
- [181] Arjan G J Tibbe, Bart G De Grooth, Jan Greve, Paul A Liberti, Gerald J Dolan, and Leon W M M Terstappen. Optical tracking and detection of immunomagnetically selected and aligned cells. *Nat. Biotechnol.* VOL, 17, 1999.
- [182] M Kala, K Bajaj, and S Sinha. Magnetic bead enzyme-linked immunosorbent assay (ELISA) detects antigen-specific binding by phage-displayed scFv antibodies that are not detected with. *Anal. Biochem.*, 1997.
- [183] J Van der Zee. Heating the patient: a promising approach? *Ann. Oncol.*, 2002.
- [184] R. K. Gilchrist, Richard Medal, William D. Shorey, Russell C. Hanselman, John C. Parrott, and C. Bruce Taylor. Selective Inductive Heating of Lymph Nodes *. *Ann. Surg.*, 146(4):596–606, 1957.
- [185] Andreas Jordan, Regina Scholz, Peter Wust, Horst Fähling, and Roland Felix. Magnetic fluid hyperthermia (MFH): Cancer treatment with AC magnetic field induced excitation of biocompatible superparamagnetic nanoparticles. *J. Magn. Magn. Mater.*, 201(1-3):413–419, 1999.
- [186] Bert Hildebrandt, Peter Wust, Olaf Ahlers, Annette Dieing, Geetha Sreenivasa, Thoralf Kerner, Roland Felix, and Hanno Riess. The cellular and molecular basis of hyperthermia. *Crit. Rev. Oncol. Hematol.*, 43(1):33–56, 2002.
- [187] Akira Ito, Kour Tanaka, Hiroyuki Honda, Shigeru Abe, Hideyo Yamaguchi, and Takeshi Kobayashi. Complete regression of mouse mammary carcinoma with a size greater than 15 mm by frequent repeated hyperthermia using magnetite nanoparticles. *J. Biosci. Bioeng.*, 96(4):364–369, 2003.
- [188] Klaus Maier-Hauff, Ronny Rothe, Regina Scholz, Uwe Gneveckow, Peter Wust, Burghard Thiesen, Annelie Feussner, Andreas von Deimling, Norbert Waldoefner, Roland Felix, and Andreas Jordan. Intracranial Thermotherapy using Magnetic Nanoparticles Combined with External Beam Radiotherapy: Results of a Feasibility Study on Patients with Glioblastoma Multiforme. *J. Neurooncol.*, 81(1):53–60, jan 2007.
- [189] Jorge T. Dias, Mar??a Moros, Pablo Del Pino, Sara Rivera, Valeria Graz??, and Jesus M. De La Fuente. DNA as a molecular local thermal probe for the analysis of magnetic hyperthermia. *Angew. Chemie - Int. Ed.*, 52(44):11526–11529, 2013.

- [190] Y Rabin. Is intracellular hyperthermia superior to extracellular hyperthermia in the thermal sense? *Int. J. Hyperth.*, 2002.
- [191] S. Mornet. Synthèse et modification chimique de la surface de nanoparticules de maghémite à des fins d'applications biomédicales. *PhD*, 2002.
- [192] M.I. Shliomis, A.F. Pshenichnikov, K.I. Morozov, and I.Yu. Shurubor. Magnetic properties of ferrocolloids. *J. Magn. Magn. Mater.*, 85(1-3):40–46, apr 1990.
- [193] A Jordan, R Scholz, P Wust, and H Fähling. Magnetic fluid hyperthermia (MFH): Cancer treatment with AC magnetic field induced excitation of bio-compatible superparamagnetic nanoparticles. *J. Magn. Magn. Mater.*, 201:413–19, 1999.
- [194] A Jordan, P Wust, H Fähling, and W John. Inductive heating of ferrimagnetic particles and magnetic fluids: physical evaluation of their potential for hyperthermia. *Int. J. Hyperth.*, (9):51–58, 2009.
- [195] N F Borrelli, A A Luderer, and J N Panzarino. Hysteresis heating for the treatment of tumours. *Phys. Med. Biol.*, 29, 1984.
- [196] SK Jones, BN Gray, and MA Burton. Evaluation of ferromagnetic materials for low-frequency hysteresis heating of tumours. *Phys. Med. Biol.*, 37, 1992.
- [197] R Hergt, W Andra, CG D'Ambly, and I Hilger. Physical limits of hyperthermia using magnetite fine particles. *IEEE Trans.*, 1998.
- [198] James P. Butler Ning Wang, Donald E. Ingber, and Science. *Mechanotransduction Across the Cell Surface and Through the Cytoskeleton on JSTOR*. American Association for the Advancement of Science, 1993.
- [199] J Dobson, A Keramane, and AJ El Haj. Theory and applications of a magnetic force bioreactor. *Eur. Cells Mater*, 2002.
- [200] Wei Wu, Quanguo He, and Changzhong Jiang. Magnetic iron oxide nanoparticles: Synthesis and surface functionalization strategies. *Nanoscale Res. Lett.*, 3:397–415, 2008.
- [201] D Kato and M Oishi. Ultrasensitive detection of DNA and RNA based on enzyme-free click chemical ligation chain reaction on dispersed gold nanoparticles. *ACS Nano*, 8(10):9988–999, 2014.
- [202] J Wang, AN Kawde, A Erdem, and M Salazar. Magnetic bead-based label-free electrochemical detection of DNA hybridization. *Analyst*, 2001.
- [203] E Paleček, M Fojta, and F Jelen. New approaches in the development of DNA sensors: hybridization and electrochemical detection of DNA and RNA at two different surfaces. *Bioelectrochemistry*, 2002.
- [204] PS Dittrich, K Tachikawa, and A Manz. Micro total analysis systems. Latest advancements and trends. *Anal. Chem.*, 2006.
- [205] Christian Amatore, Nicolas Da Mota, Catherine Sella, and Laurent Thouin. General Concept of High-Performance Amperometric Detector for Microfluidic (Bio)Analytical Chips. *Anal. Chem.*, 80:4976–4985, 2008.

- [206] C Sella and L Thouin. Electrochimie et microsystèmes fluidiques. Concepts et performances issus de la miniaturisation. *Actual. Chim.*, 2017.
- [207] Jonathan A. Cooper and Richard G. Compton. Channel Electrodes — A Review. *Electroanalysis*, 10(3):141–155, 1998.
- [208] BS Ferguson and SF Buchsbaum. Integrated Microfluidic Electrochemical DNA Sensor. *Anal. ...*, 81(15):7341–7346, 2009.
- [209] J Wang, R Polsky, and D Xu. Silver-enhanced colloidal gold electrochemical stripping detection of DNA hybridization. *Langmuir*, 2001.
- [210] E Paleček. Past, present and future of nucleic acids electrochemistry. *Talanta*, 2002.
- [211] Maurizio Callari, Matteo Dugo, Valeria Musella, Edoardo Marchesi, Giovanna Chiorino, Maurizia Mello Grand, Marco Alessandro Pierotti, Maria Grazia Daidone, Silvana Canevari, and Loris De Cecco. Comparison of Microarray Platforms for Measuring Differential MicroRNA Expression in Paired Normal/Cancer Colon Tissues. *PLoS One*, 7(9):e45105, sep 2012.
- [212] Katarina Cuk, Manuela Zucknick, Dharanija Madhavan, Sarah Schott, Michael Golatta, J?rg Heil, Frederik Marm?, Andrey Turchinovich, Peter Sinn, Christof Sohn, Hans Junkermann, Andreas Schneeweiss, and Barbara Burwinkel. Plasma MicroRNA Panel for Minimally Invasive Detection of Breast Cancer. *PLoS One*, 8(10):e76729, oct 2013.
- [213] Sara Pizzamiglio, Stefano Bottelli, Chiara Maura Ciniselli, Susanna Zanutto, Claudia Bertan, Manuela Gariboldi, Marco Alessandro Pierotti, and Paolo Verderio. A normalization strategy for the analysis of plasma microRNA qPCR data in colorectal cancer. *Int. J. Cancer*, 134(8):2016–2018, apr 2014.
- [214] Benoit Dubertret, Michel Calame, and Albert J. Libchaber. Single-mismatch detection using gold-quenched fluorescent oligonucleotides. *Nat. Biotechnol.*, 19, 2001.
- [215] Xi Chun Zhou, Li Qun Huang, and Sam Fong Yau Li. Microgravimetric DNA sensor based on quartz crystal microbalance: comparison of oligonucleotide immobilization methods and the application in genetic diagnosis. *Biosens. Bioelectron.*, 16(1-2):85–95, jan 2001.
- [216] J. D. Watson and F. H. C. Crick. A structure for deoxyribose nucleic acid, 1953.
- [217] Karel Štulík, Christian Amatore, Karel Holub, Vladimír Mareček, and Włodzimierz Kutner. Microelectrodes. Definitions, characterization, and applications (Technical report). *Pure Appl. Chem. Republic South Africa I. R. Gutz (Brazil)*, 72(8):1483–1492, 2000.
- [218] Christian Amatore, Stéphane Arbault, Cécile Bouton, Karen Coffi, Jean Claude Drapier, Hala Ghandour, and Yuehong Tong. Monitoring in real time with a microelectrode the release of reactive oxygen and nitrogen species by a single macrophage stimulated by its membrane mechanical depolarization. *Chem-BioChem*, 7(4):653–661, 2006.

- [219] Ian Streeter, Nicole Fietkau, Javier Del Campo, Roser Mas, Francesc Xavier, M Noz, and Richard G Compton. Voltammetry at Regular Microband Electrode Arrays: Theory and Experiment. *J. Phys. Chem. C*, 111(12058-12066), 2007.
- [220] Danu Suwatchara, Martin C Henstridge, Neil V Rees, and Richard G Compton. Experimental Comparison of the Marcus-Hush and Butler-Volmer Descriptions of Electrode Kinetics. The One-Electron Oxidation of 9,10-Diphenylanthracene and One-Electron Reduction of 2-Nitropropane Studied at High-Speed Channel Microband Electrodes. *J. Phys. Chem. C*, 115:14876–14882, 2011.
- [221] Jie Wang, Shuping Li, and Yuzhong Zhang. A sensitive DNA biosensor fabricated from gold nanoparticles, carbon nanotubes, and zinc oxide nanowires on a glassy carbon electrode. *Electrochim. Acta*, 55(15):4436–4440, jun 2010.
- [222] Mathilde Faure, Bruno Sotta, and Jean Gamby. Investigating the kinetics of paramagnetic-beads linked alkaline phosphatase enzyme through microchannel resistance measurement in dielectric microchip. *Biosens. Bioelectron.*, 58:61–67, 2014.
- [223] A. Nassi, F.-X. Guillon, A. Amar, B. Hainque, S. Amriche, D. Maugé, E. Markova, C. Tsé, P. Bigey, M. Lazerges, and F. Bedioui. Electrochemical DNA-biosensors based on long-range electron transfer: optimization of the amperometric detection in the femtomolar range using two-electrode setup and ultramicroelectrode. *Electrochem. Acta*, 209:269–277, 2016.
- [224] RJ Marcus. RW Lumry See the Marcus treatment in the Experimental *J. Chem. Phys.*, 24, 1956.
- [225] VG Levich and RR Dogonadze. Theory of non-radiation electron transitions from ion to ion in solutions. *Dokl. Akad. Nauk SSSR*, 124(1):123–126, 1959.
- [226] Jay R Winkler and Harry B Gray. Long-Range Electron Tunneling. *J. Am. Chem. Soc.*, 136:2930–2939, 2014.
- [227] BR Crane, AJ Di Bilio, and JR Winkler. Electron Tunneling in Single Crystals of *Pseudomonas aeruginosa* Azurins. *Chem. Soc.*, 6:4250–4266, 2001.
- [228] Yoshio Okahata, Takuya Kobayashi, Kentaro Tanaka, and Masatsugu Shimomura. Anisotropic Electric Conductivity in an Aligned DNA Cast Film. *J. Am. Chem. Soc.*, 120(6165-6166), 1998.
- [229] Anthony Harriman. Electron tunneling in DNA. *Angew. Chemie - Int. Ed.*, 38(7):945–949, 1999.
- [230] Shana O. Kelley, R. Erik Holmlin, Eric D. A. Stemp, and Jacqueline K. Barton. Photoinduced Electron Transfer in Ethidium-Modified DNA Duplexes: Dependence on Distance and Base Stacking. *J. Am. Chem. Soc.*, 119(41):9861–9870, oct 1997.
- [231] Frederick D Lewis, Jianqin Liu, Wilfried Weigel, Wolfgang Rettig, Igor V Kurnikov, and David N Beratan. Donor-bridge-acceptor energetics determine the distance dependence of electron tunneling in DNA. *Proc. Natl. Acad. Sci. U. S. A.*, 99(20):12536–41, 2002.

- [232] Shana O Kelley, Elizabeth M Boon, Jacqueline K Barton, Nicole M Jackson, and Michael G Hill. Single-base mismatch detection based on charge transduction through DNA. *27(24):4830–4837*, 1999.
- [233] Wei Sun, Peng Qin, Hongwei Gao, Guicun Li, and Kui Jiao. Electrochemical DNA biosensor based on chitosan/nano-V₂O₅/MWCNTs composite film modified carbon ionic liquid electrode and its application to the LAMP product of *Yersinia enterocolitica* gene sequence. *Biosens. Bioelectron.*, 25(6):1264–70, feb 2010.
- [234] S O Kelley and J K Barton. DNA-mediated electron transfer from a modified base to ethidium: pi-stacking as modulator of reactivity. *Chem. Biol.*, 5(8):413–25, 1998.
- [235] Shana O Kelley, R Erik Holmlin, Eric D A Stemp, and Jacqueline K Barton. Photoinduced Electron Transfer in Ethidium-Modified DNA Duplexes: Dependence on Distance and Base Stacking. *J. Am. Chem. Soc.*, 119:9861–9870, 1997.
- [236] Xingyan Sun, Pingang He, Shenghui Liu, Jiannong Ye, and Yuzhi Fang. Immobilization of single-stranded deoxyribonucleic acid on gold electrode with self-assembled aminoethanethiol monolayer for DNA electrochemical sensor applications. *47:487–495*, 1998.
- [237] M Fleischmann, S Pons, DR Rolison, and PP Schmidt. Ultramicroelectrodes. *Datatech Syst. Morgant.*, 1987.
- [238] RM Wightman. Microvoltammetric electrodes. *Anal. Chem.*, 53(9):1125–1134, 1981.
- [239] P. N. Swan. *Ph.D. Dissertation*. PhD thesis, of Southampton, 1980.
- [240] M Gouy. *Sur la constitution de la chargé électrique a la surface d'u electrolyte*. PhD thesis, 1910.
- [241] David Leonard Chapman. A contribution to the theory of electrocapillarity. *Philos. Mag. Ser. 6*, 25(148):475–481, apr 1913.
- [242] Osamu Niwa, Hisao Tabei, Bruce P. Solomon, Fuming Xie, and Peter T. Kissinger. Improved detection limit for catecholamines using liquid chromatography-electrochemistry with a carbon interdigitated array microelectrode. *J. Chromatogr. B Biomed. Sci. Appl.*, 670(1):21–28, aug 1995.
- [243] RS Nicholson and I Shain. Theory of stationary electrode polarography. Single scan and cyclic methods applied to reversible, irreversible, and kinetic systems. *Anal. Chem.*, 1964.
- [244] Jean Michel. Saveant. *Elements of molecular and biomolecular electrochemistry : an electrochemical approach to electron transfer chemistry*. Wiley-Interscience, 2006.
- [245] Mark E. Orazem and Bernard. Tribollet. *Electrochemical Impedance Spectroscopy*. Wiley, 2011.
- [246] Petr Vanýsek. Electrochemical Series. In *CRC Handb. Chem. Phys.*, chapter 5, pages 80–89. 92th editi edition.

- [247] M.-C. Horny, M. Lazerges, J.-M. Siaugue, A. Pallandre, A.-M. Haghiri-Gosnet, and J. Gamby. DNA Electrochemical Hybridization Detection in Droplets Using Gold Ultramicroelectrodes in a Two-Electrode Configuration. *ECS Trans.*, 72(31):1–6, sep 2016.
- [248] Mathilde Faure. *Elaboration et études des propriétés de films minces de carbone amorphe azoté (a-CN_x) sur verre conducteur : vers l'élaboration de support en verre polarisable pour la détection électrochimique et / ou optique en puce microfluidique*. PhD thesis, Université Pierre et Marie Curie, 2013.
- [249] Christian Amatore, Cécile Pebay, Laurent Thouin, and Aifang Wang. Cyclic voltammetry at microelectrodes. Influence of natural convection on diffusion layers as characterized by in situ mapping of concentration profiles. *Electrochem. commun.*, 11(6):1269–1272, jun 2009.
- [250] L. Philip Reiss and Thomas J. Hanratty. An experimental study of the unsteady nature of the viscous sublayer. *AIChE J.*, 9(2):154–160, 1963.
- [251] Richard G. Compton, Adrian C. Fisher, R. Geoffrey Wellington, Peter J. Dobson, and Peter a. Leigh. Hydrodynamic voltammetry with microelectrodes: channel microband electrodes; theory and experiment. *J. Phys. Chem.*, 97:10410–10415, 1993.
- [252] Richard G. Compton, Adrian C. Fisher, R. Geoffrey Wellington, Peter J. Dobson, and Peter a. Leigh. Hydrodynamic voltammetry with microelectrodes: channel microband electrodes; theory and experiment. *J. Phys. Chem.*, 97:10410–10415, 1993.
- [253] Olga Ordeig, Neus Godino, Javier Del Campo, Francesc Xavier Muñoz, Fredrik Nikolajeff, and Leif Nyholm. On-chip electric field driven electrochemical detection using a poly(dimethylsiloxane) microchannel with gold microband electrodes. *Anal. Chem.*, 80(10):3622–3632, 2008.
- [254] Layal L. Rouhana, Maroun D. Moussallem, and Joseph B. Schlenoff. Adsorption of short-chain thiols and disulfides onto gold under defined mass transport conditions: Coverage, kinetics, and mechanism. *J. Am. Chem. Soc.*, 133(40):16080–16091, 2011.
- [255] M. Lazerges, H. Perrot, E. Antoine, A. Defontaine, and C. Compere. Oligonucleotide quartz crystal microbalance sensor for the microalgae *Alexandrium minutum* (Dinophyceae). *Biosens. Bioelectron.*, 21(7):1355–1358, 2006.
- [256] M. Lazerges, H. Perrot, N. Zeghib, E. Antoine, and C. Compere. In situ QCM DNA-biosensor probe modification. *Sensors Actuators, B Chem.*, 120(1):329–337, 2006.
- [257] Gerald D McEwen, Fan Chen, and Anhong Zhou. Immobilization, hybridization, and oxidation of synthetic DNA on gold surface: electron transfer investigated by electrochemistry and scanning tunneling microscopy. *Anal. Chim. Acta*, 643(1-2):26–37, jun 2009.
- [258] Nikin Patel, Martyn C Davies, Mark Hartshorne, Richard J Heaton, Clive J Roberts, Saul J B Tendler, and Philip M Williams. Immobilization of Protein Molecules onto Homogeneous and Mixed Carboxylate-Terminated Self-Assembled Monolayers. *Langmuir*, 13(24):6485–6490, 1997.

- [259] C. E. Porter, M. D., Bright, T. B., Allara, D. L., & Chidsey. Spontaneously organized molecular assemblies. 4. Structural characterization of n-alkyl thiol monolayers on gold by optical ellipsometry, infrared spectroscopy, and electrochemistry. *J. Am. Chem. Soc.*, 109(12):3559–3568, 1987.
- [260] Pablo Ramírez, Rafael Andreu, Juan José Calvente, Carmen J. Calzado, and Germán López-Pérez. Electrochemical formation and electron transfer through self-assembled monolayers of 4-mercaptophenol on mercury. *J. Electroanal. Chem.*, 582(1):179–190, 2005.
- [261] M. Steichen, Th. Doneux and Cl. Buess-Herman A. De Rache. Influence of the Crystallographic Orientation on the Reductive Desorption of Self-Assembled Monolayers on Gold Electrodes. *J. Electroanal. Chem.*, 649:164–170, 2015.
- [262] D.-F Yang, C P Wilde, and M Morin. Electrochemical Desorption and Adsorption of Nonyl Mercaptan at Gold Single Crystal Electrode Surfaces. *Final Form*, 1996.
- [263] C Vericat, M E Vela, G Andreasen, R C Salvarezza, L Vázquez, and J A Martín-Gago. Sulfur-Substrate Interactions in Spontaneously Formed Sulfur Adlayers on Au(111). *Langmuir*, 17(16):4919–4924, 2001.
- [264] Casanova-Moreno, Jannu R, and Dan Bizzotto. What Happens to the Thiolates Created by Reductively Desorbing SAMs? An in Situ Study Using Fluorescence Microscopy and Electrochemistry. *Langmuir*, 29(6):2065–2074, 2013.
- [265] RL McCreery. Advanced carbon electrode materials for molecular electrochemistry. *Chem. Rev.*, 2008.
- [266] S Ababou-Girard, H Sabbah, and B Fabre. Covalent grafting of organic layers on sputtered amorphous carbon: Surface preparation and coverage density. *J. Phys. Chem. C*, 111(7):3099–3108, 2007.
- [267] A. Lagrini, C. Deslouis, H. Cachet, M. Benlahsen, and S. Charvet. Elaboration and electrochemical characterization of nitrogenated amorphous carbon films. *Electrochem. commun.*, 6(3):245–248, 2004.
- [268] G Adamopoulos, C Godet, C Deslouis, H Cachet, A Lagrini, and B Saidani. The electrochemical reactivity of amorphous hydrogenated carbon nitrides for varying nitrogen contents: the role of the substrate. *Diam. Relat. Mater.*, 12:613–617, 2003.
- [269] R A Medeiros, A Benchick, R C Rocha-Filho, O Fatibello-Filho, B Saidani, C Debiemme-Chouvy, and C Deslouis. Simultaneous detection of ascorbic acid and dopamine with electrochemically pretreated carbon nitride electrodes: Comparison with boron-doped diamond electrodes. *Electrochem. commun.*, 24:61–64, 2012.
- [270] H. Cachet, C. Debiemme-Chouvy, C. Deslouis, A. Lagrini, and V. Vivier. Correlation between electrochemical reactivity and surface chemistry of amorphous carbon nitride films. *Surf. Interface Anal.*, 38(4):719–722, apr 2006.
- [271] ZR Wu, M Zhang, and FZ Cui. Adhesion and growth of smooth muscle cells on CN x coatings. *Surf. Coatings Technol.*, 2007.

- [272] T Katsuno, S Nitta, D Ohsawa, and Y Sato. Detection of heavy ions for cancer therapy using amorphous carbon nitride a-CN X films prepared by a nitrogen radical sputter method. *Diam. Relat. Mater.*, 2003.
- [273] Serigne Massamba Seck, Stéphane Charvet, Modou Fall, Emmanuel Baudrin, Michal Lejeune, and Mohammed Benlahsena. Detection of Cadmium and Copper Cations Using Amorphous Nitrogenated Carbon Thin Film Electrodes. *Electroanalysis*, 24(9):1839–1846, 2012.
- [274] A. C. Ferrari, S. E. Rodil, and J. Robertson. Resonant Raman spectra of amorphous carbon nitrides: The G peak dispersion. *Diam. Relat. Mater.*, 12(3-7):905–910, 2003.
- [275] SH Kim, CM Choi, KM Lee, and YB Hahn. Optical, mechanical and etch properties of amorphous carbon nitride films grown by plasma enhanced chemical vapor deposition at room temperature. *Synth. Met.*, 2010.
- [276] F. Demichelis, X.F. Rong, S. Schreiter, A. Tagliaferro, and C. De Martino. Deposition and characterization of amorphous carbon nitride thin films. *Diam. Relat. Mater.*, 4(4):361–365, apr 1995.
- [277] XH Zheng, JP Tu, and RG Song. Microstructure and tribological behavior of pulsed laser deposited a-CN x films. *Appl. Surf. Sci.*, 2010.
- [278] S. Jribi, S. I. Cordoba De Torresi, T. Augusto, H. Cachet, C. Debiemme-Chouvy, C. Deslouis, and A. Pailleret. Determination of surface amine groups on amorphous carbon nitride thin films using a one step covalent grafting of a redox probe. *Electrochim. Acta*, 136:473–482, 2014.
- [279] P Tamiasso-Martinhon, H Cachet, C Deslouis, and V Vivier. Amorphous carbon nitride a-CN x microelectrode: Fabrication and characterization. *Electrochem. commun.*, 12:1074–1076, 2010.
- [280] M. Benlahsen, H. Cachet, S. Charvet, C. Debiemme-Chouvy, C. Deslouis, A. Lagrini, and V. Vivier. Improvement and characterization of the electrochemical reactivity of amorphous carbon nitride electrodes. *Electrochem. commun.*, 7(5):496–499, 2005.
- [281] P. Tamiasso-Martinhon, H. Cachet, C. Debiemme-Chouvy, and C. Deslouis. Thin films of amorphous nitrogenated carbon a-CNx: Electron transfer and surface reactivity. *Electrochim. Acta*, 53(19):5752–5759, 2008.
- [282] Roberta A Medeiros, Roberto Matos, Abdelkader Benchikh, Boualem Saidani, Catherine Debiemme-Chouvy, Claude Deslouis, Romeu C Rocha-Filho, and Orlando Fatibello-Filho. Amorphous carbon nitride as an alternative electrode material in electroanalysis: Simultaneous determination of dopamine and ascorbic acid. *Anal. Chim. Acta*, 797:30–39, 2013.
- [283] Michael V Mirkin and Allen J Bard. Simple Analysis of Quasi-Reversible Steady-State Voltammograms. *Anal. Chem.*, 64:2293–2302, 1992.
- [284] Hugo B Suffredini, Valber A Pedrosa, Lúcia Codognoto, Sérgio A S Machado, Romeu C Rocha-Filho, and Luis A Avaca. Enhanced electrochemical response of boron-doped diamond electrodes brought on by a cathodic surface pre-treatment. *Electrochim. Acta*, 49:4021–4026, 2004.

- [285] S Ferro and A De Battisti. Electron transfer reactions at conductive diamond electrodes. *Electrochim. Acta*, 2002.
- [286] T Kondo, K Honda, DA Tryk, and A Fujishima. AC impedance studies of anodically treated polycrystalline and homoepitaxial boron-doped diamond electrodes. *Electrochim. Acta*, 2003.
- [287] Ichizo Yagi, Hideo Notsu, Takeshi Kondo, Donald A Tryk, and Akira Fujishima. Electrochemical selectivity for redox systems at oxygen-terminated diamond electrodes. *J. Electroanal. Chem.*, 473:173–178, 1999.
- [288] S. Sam, L. Touahir, J. Salvador Andresa, P. Allongue, J.-N. Chazalviel, A. C. Gouget-Laemmel, C. Henry de Villeneuve, A. Moraillon, F. Ozanam, N. Gabouze, and S. Djebbar. Semiquantitative Study of the EDC/NHS Activation of Acid Terminal Groups at Modified Porous Silicon Surfaces. *Langmuir*, 26(2):809–814, jan 2010.
- [289] Sarra Bouden, Antoine Dahi, Fanny Hauquier, Hyacinthe Randriamahazaka, and Jalal Ghilane. Multifunctional Indium Tin Oxide Electrode Generated by Unusual Surface Modification. *Nat. Publ. Gr.*, 2016.
- [290] Viatcheslav Jouikov and Jacques Simonet. Graphene: Large scale chemical functionalization by cathodic means. *Electrochem. commun.*, 46:132–136, 2014.
- [291] Artur Ciesielski, Sébastien Haar, Mohamed El Garah, Mathieu Surin, Stefano Masiero, and Paolo Samorì. Supramolecular engineering of guanine-based self-assembled architectures at surfaces and interfaces. *Actual. Chim.*, 399, 2015.
- [292] R. Szunerits, S., Jama, C., Coffinier, Y., Marcus, B., Delabouglise, D., & Boukherroub. Direct amination of hydrogen-terminated boron doped diamond surfaces. *Electrochem. commun.*, 8(7):1185–1190, jul 2006.
- [293] C. S. Lu, C. W., Hung, Y., Hsiao, J. K., Yao, M., Chung, T. H., Lin, Y. S., ... & Yang. Bifunctional Magnetic Silica Nanoparticles for Highly Efficient Human Stem Cell Labeling. *Nano Lett.*, 7(1):149–154, 2007.
- [294] ME Davis and DM Shin. Nanoparticle therapeutics: an emerging treatment modality for cancer. *Nat. Rev. Drug Discov.*, 2008.
- [295] Ruth Duncan. Polymer conjugates as anticancer nanomedicines. *Nat. Rev.*, 6:688–701, 2006.
- [296] M. Ferrari. Cancer nanotechnology: opportunities and challenges. *Nat. Rev.*, 5(3):161–171, 2005.
- [297] DA LaVan, T McGuire, and R Langer. Small-scale systems for in vivo drug delivery. *Nat. Biotechnol.*, 2003.
- [298] Kristina Riehemann, Stefan W Schneider, Thomas A Luger, Biana Godin, Mauro Ferrari, Harald Fuchs, K Riehemann, and H Fuchs. Diagnostics and Drug Delivery Nanomedicine—Challenge and Perspectives. *Angew. Chem. Int. Ed*, 48:872–897, 2009.
- [299] Stuart C McBain, Humphrey HP Yiu, and Jon Dobson. Magnetic nanoparticles for gene and drug delivery. *Int. J. Nanomedicine*, 2:169–180, 2008.

- [300] Jung Jun Min Mi Kyung Yu, Yong Yeon Jeong, Jinho Park, Sangjin Park, Jin Woong Kim, Kyuwon Kim, and Sangyong Jon. Drug-Loaded Superparamagnetic Iron Oxide Nanoparticles for Combined Cancer Imaging and Therapy In Vivo. *Angew. Chem. Int. Ed.* 2, 47:5362–5365, 2008.
- [301] Donald E Owens Iii and Nicholas A Peppas. Opsonization, biodistribution, and pharmacokinetics of polymeric nanoparticles. *Int. J. Pharm.*, 307:93–102, 2006.
- [302] M. M. van Vlerken, L. E., & Amiji. Multi-functional polymeric nanoparticles for tumour-targeted drug delivery. *Expert Opin. Drug Deliv.*, 3(2):205–216, 2006.
- [303] Kazunori Kataoka c , Hidenori Otsuka , Yukio Nagasaki. PEGylated nanoparticles for biological and pharmaceutical applications. *Adv. Drug Deliv. Rev.*, 55:403–419, 2003.
- [304] Monica Dettin, Davide Silvestri, Roberta Danesin, Erica Cretaio, Gianluca Picariello, Elisabetta Casarin, Agnese Sonato, Filippo Romanato, and Margherita Morpurgo. Synthesis and chromatography-free purification of PNA-PEO conjugates for the functionalisation of gold sensors. *Molecules*, 17(9):11026–11045, 2012.
- [305] Tae-Jong Yoon, Kyeong Nam Yu, Eunha Kim, Jun Sung Kim, Byung Geol Kim, Sang-Hyun Yun, Byeong-Hyeok Sohn, Myung-Haing Cho, Jin-Kyu Lee, and Seung Bum Park. Specific Targeting, Cell Sorting, and Bioimaging with Smart Magnetic Silica Core–Shell Nanomaterials**. *Small*, 2(2):209–215, 2006.
- [306] Yong-Hui Deng, Chang-Chun Wang, Jian-Hua Hu, Wu-Li Yang, and Shou-Kuan Fu. Investigation of formation of silica-coated magnetite nanoparticles via sol–gel approach. *Colloids Surfaces A Physicochem. Eng. Asp.*, 262(1):87–93, 2005.
- [307] Gunnar Glöckl, Rudolf Hergt, Matthias Zeisberger, Silvio Dutz, Stefan Nagel, and Werner Weitschies. The effect of field parameters, nanoparticle properties and immobilization on the specific heating power in magnetic particle hyperthermia. *J. Phys. Condens. Matter*, 18(38):S2935–S2949, 2006.
- [308] Andreas Jordan. Thermotherapy and Nanomedicine. In *Hyperth. Cancer Treat. A Prim.*, pages 60–63. Springer US, Boston, MA, 2006.
- [309] Eduardo Ruiz-Hernández, Alejandro Baeza, and María Vallet-Regí. Smart drug delivery through DNA/magnetic nanoparticle gates. *ACS Nano*, 5(2):1259–1266, 2011.
- [310] Juyao Dong and Jeffrey I. Zink. Taking the temperature of the interiors of magnetically heated nanoparticles. *ACS Nano*, 8(5):5199–5207, 2014.
- [311] Jae-Hyun Lee¹, Jung-tak Jang¹, Jin-sil Choi¹, Seung Ho Moon¹, Seung-hyun Noh¹, Ji-wook Kim¹, Kook In Park³, Jin-Gyu Kim², Il-Sun Kim³, Jinwoo Cheon¹, and *. Exchange-coupled magnetic nanoparticles for efficient heat induction. *Nat. Nanotechnol.*, 6:418–422, 2011.
- [312] V. Maurice, V., Georgelin, T., Siaugue, J. M., & Cabuil. Synthesis and characterization of functionalized core–shell gFe₂O₃–SiO₂ nanoparticles. *J. Magn. Mater.*, 321:1408–1413, 2009.

- [313] Thomas Georgelin, Sophie Bombard, Jean-Michel Siaugue, and Valørie Cabuil. Nanoparticle-Mediated Delivery of Bleomycin. *Angew. Chem. Int. Ed*, 49:8897–8901, 2010.
- [314] R. Massart, E. Dubois, V. Cabuil, and E. Hasmonay. Preparation and properties of monodisperse magnetic fluids. *J. Magn. Magn. Mater.*, 149(1-2):1–5, aug 1995.
- [315] S Lefebure, E Dubois, V Cabuil,) S Neveu, and R Massart. Monodisperse magnetic nanoparticles: Preparation and dispersion in water and oils. *J. Mater. Res.*, 13(10), 1998.
- [316] M. Etoc, F. Vicario, C., Lisse, D., Siaugue, J. M., Piehler, J., Coppey, M., & Dahan. Magnetogenetic Control of Protein Gradients Inside Living Cells with High Spatial and Temporal Resolution. *Nano Lett.*, 15(5):3487–3494, 2015.
- [317] O Catalog. Quant-iT™ OliGreen® ssDNA Reagent and Kit. pages 1–7, 2008.
- [318] Shouheng Sun, Hao Zeng, David B. Robinson, Simone Raoux, Philip M. Rice, Shan X. Wang and Guanxiong Li. Controlled Synthesis of MFe₂O₄ (M = Mn , Fe , Co , Ni and Zn) Nanoparticles. *J. Am. Chem. Soc.*, 126(1):273–279, 2004.
- [319] AK Gupta and M Gupta. Synthesis and surface engineering of iron oxide nanoparticles for biomedical applications. *Biomaterials*, 2005.
- [320] L. Poul, S. Ammar, N. Jouini, F. Fievet, and F. Villain. Synthesis of Inorganic Compounds (Metal, Oxide and Hydroxide) in Polyol Medium: A Versatile Route Related to the Sol-Gel Process. *J. Sol-Gel Sci. Technol.*, 26(1/3):261–265, 2003.
- [321] Haiyan Sun, Bo Chen, Xiuling Jiao, Zhen Jiang, Zhenhua Qin and Dairong Chen. Solvothermal Synthesis of Tunable Electroactive Magnetite Nanorods by Controlling the Side Reaction. *J. Phys. Chem. C*, 116:5476–5481, 2012.
- [322] Victor K. LaMer and Robert H. Dinegar. Theory, Production and Mechanism of Formation of Monodispersed Hydrosols. *J. Am. Chem. Soc.*, 72(11):4847–4854, nov 1950.
- [323] JC Bacri and R Perzynski. *Magnetic Fluids and Applications Handbook*. Begell House Inc. Pubs., 1996.
- [324] B. M. Berkovskii and V. G. Bashtovoy. *Magnetic fluids and applications handbook*. Begell House, 1996.
- [325] W Stöber, A Fink, and E Bohn. Controlled growth of monodisperse silica spheres in the micron size range. *J. Colloid Interface Sci.*, 1968.
- [326] Swadeshmukul Santra, Rovelyn Tapeç, Theodoropoulou, Nikoleta, † Jon Dobson, Arthur Hebard and, and Weihong Tan. Synthesis and Characterization of Silica-Coated Iron Oxide Nanoparticles in Microemulsion: The Effect of Non-ionic Surfactants. *Langmuir*, 17(10):2900–2906, 2001.
- [327] Peter M. Price, James H. Clark, Duncan J. Macquarrie, J. C. Moreira, W. L. Polito, P. Moreau, F. Di Renzo, A. Galarneau, F. Fajula, S. B. McCullen, J. B. Higgins, and J. L. Schlenker. Modified silicas for clean technology. *J. Chem. Soc. Dalton Trans.*, 9(2):101–110, jan 2000.

- [328] EJ Verwey and JT Overbeek. *Theory of the Stability of Colloidal Dispersions*. Amsterdam, elsevier edition, 1948.
- [329] T. D. Ortega, R. A., & Giorgio. A mathematical model of superparamagnetic iron oxide nanoparticle magnetic behavior to guide the design of novel nanomaterials. *J. Nanoparticle Res.*, 14(12):1282, 2012.
- [330] A. Millan, A. Urtizberea, N.J.O. Silva, F. Palacio, V.S. Amaral, E. Snoeck, and V. Serin. Surface effects in maghemite nanoparticles. 2007.
- [331] Irene Andreu and Eva Natividad. Accuracy of available methods for quantifying the heat power generation of nanoparticles for magnetic hyperthermia. *Int. J. Hyperth.*, 29(8):739–751, dec 2013.
- [332] H. Das, R., Alonso, J., Nemati Porshokouh, Z., Kalappattil, V., Torres, D., Phan, M. H., ... & Srikanth. Tunable High Aspect Ratio Iron Oxide Nanorods for Enhanced Hyperthermia. *J. Phys. Chem. C*, 120(18):10086–10093, 2016.
- [333] Carlos Martinez-Boubeta, Konstantinos Simeonidis, Antonios Makridis, Makis Angelakeris, Oscar Iglesias, Pablo Guardia, Andreu Cabot, Lluís Yedra, Sonia Estradé, Francesca Peiró, Zineb Saghi, Paul A Midgley, Iván Conde-Leborán, David Serantes, and Daniel Baldomir. Learning from Nature to Improve the Heat Generation of Iron-Oxide Nanoparticles for Magnetic Hyperthermia Applications. 2013.
- [334] C. Serantes, D., Simeonidis, K., Angelakeris, M., Chubykalo-Fesenko, O., Marciello, M., Morales, M. D. P., ... & Martinez-Boubeta. Multiplying magnetic hyperthermia response by nanoparticle assembling. *J. Phys. Chem. C*, 118(11):5927–5934, 2014.
- [335] I Andreu, E Natividad, L Solozábal, and O Roubeau. Nano-objects for addressing the control of nanoparticle arrangement and performance in magnetic hyperthermia. *ACS Nano*, 2015.
- [336] J. Y. Bao, L., Low, W. L., Jiang, J., & Ying. Colloidal synthesis of magnetic nanorods with tunable aspect ratios. *J. Mater. Chem.*, 22(15):7117–7120, 2012.
- [337] Kavita Arora, Subhash Chand, and B. D. Malhotra. Recent developments in bio-molecular electronics techniques for food pathogens. *Anal. Chim. Acta*, 568(1-2):259–274, 2006.
- [338] Kavita Arora, Asha Chaubey, Rahul Singhal, Ravindra P. Singh, M. K. Pandey, S. B. Samanta, B. D. Malhotra, and Subhash Chand. Application of electrochemically prepared polypyrrole-polyvinyl sulphonate films to DNA biosensor. *Biosens. Bioelectron.*, 21(9):1777–1783, 2006.
- [339] M. Jiang and J. Wang. Recognition and detection of oligonucleotides in the presence of chromosomal DNA based on entrapment within conducting-polymer networks. *J. Electroanal. Chem.*, 500(1-2):584–589, 2001.
- [340] Lisa Muñoz-Serrano, Ana R. Guadalupe, and Esther Vega-Bermudez. Morphological studies of oligodeoxyribonucleotides probes covalently immobilized at polystyrene modified surfaces. *J. Biotechnol.*, 118(3):233–245, 2005.

- [341] N Zammateo, L Jeanmart, S Hamels, S Courtois, P Louette, L Hevesi, and J Remacle. Comparison between different strategies of covalent attachment of DNA to glass surfaces to build DNA microarrays. *Anal. Biochem.*, 280(1):143–150, 2000.
- [342] Alizar Ulianas, Lee Yook Heng, Sharina Abu Hanifah, and Tan Ling Ling. An electrochemical DNA microbiosensor based on succinimide-modified acrylic microspheres. *Sensors (Switzerland)*, 12(5):5445–5460, 2012.
- [343] Sarah J. Hurst, Abigail K. R. Lytton-Jean and Chad A. Mirkin. Maximizing DNA Loading on a Range of Gold Nanoparticle Sizes. *Anal Chem.*, 78(24):8313–8318, 2008.
- [344] Linette Demers, Chad Mirkin, Robert Mucic, Robert Reynolds, Robert Letsinger, Robert Elghanian, and Garimella Viswanadham. Based Method for Determining the Surface Coverage and Hybridization Efficiency of Thiol - Capped Oligonucleotides Bound to Gold Thin Films and Nanoparticles. 72(22):5535–5541, 2000.
- [345] Shuhua Liu, Zhihua Zhang, and Mingyong Han. Gram-scale synthesis and biofunctionalization of silica-coated silver nanoparticles for fast colorimetric DNA detection. *Anal. Chem.*, 77(8):2595–2600, 2005.
- [346] M. K. Walsh, X. Wang, and B. C. Weimer. Optimizing the immobilization of single-stranded DNA onto glass beads. *J. Biochem. Biophys. Methods*, 47:221–231, 2001.
- [347] B C Yin, Y M Guan, and B C Ye. An ultrasensitive electrochemical DNA sensor based on the ssDNA-assisted cascade of hybridization reaction. *Chem. Commun.*, 48(35):4208–4210, 2012.
- [348] Dorota Bartczak and Antonios G. Kanaras. Preparation of peptide-functionalized gold nanoparticles using one pot EDC/Sulfo-NHS coupling. *Langmuir*, 27(16):10119–10123, 2011.
- [349] Joseph R. Lakowicz. Principles of Fluorescence Spectroscopy Principles of Fluorescence Spectroscopy. *Princ. Fluoresc. Spectrosc. Springer, New York, USA, 3rd edn, 2006.*, page 362, 2006.
- [350] Rita Meunier-Prest, Suzanne Raveau, Eric Finot, Guillaume Legay, Mustapha Cherkaoui-Malki, and Norbert Latruffe. Direct measurement of the melting temperature of supported DNA by electrochemical method. *Nucleic Acids Res.*, 31(23):e150, 2003.
- [351] Dongbiao Ge, Xin Wang, Keeshan Williams, and Rastislav Levicky. Thermostable DNA Immobilization and Temperature Effects on Surface Hybridization. *Langmuir*, 28:8446–8455, 2012.
- [352] Rosaria Ferrigno, Jessamine Ng Lee, Xingyu Jiang, and George M Whitesides. Potentiometric Titrations in a Poly(dimethylsiloxane)-Based Microfluidic Device. *Anal. Chem.*, 76:2273–2280, 2004.
- [353] Khaled Stephan, Patrick Pittet, Monique Sigaud, Louis Renaud, Olivier Vitori, Pierre Morin, Naim Ouaini, and Rosaria Ferrigno. Amperometric quantification based on serial dilution microfluidic systems. *Analyst*, 134:472–477, 2009.

- [354] Antoine-Emmanuel Saliba, Laure Saias, Eleni Psychari, Nicolas Minc, Damien Simon, François-Clément Bidard, Claire Mathiot, Jean-Yves Pierga, Vincent Fraisier, Jean Salamero, Véronique Saada, Françoise Farace, Philippe Vielh, Laurent Malaquin, and Jean-Louis Viovy. Microfluidic sorting and multimodal typing of cancer cells in self-assembled magnetic arrays. *Proc. Natl. Acad. Sci. U. S. A.*, 107(33):14524–9, aug 2010.
- [355] Ciprian Iliescu, Ji Jingb, Francis E.H. Taya, Jianmin Miaoc, and Tietun Sun. Characterization of masking layers for deep wet etching of glass in an improved HF/HCl solution. *Surf. Coat. Technol.*, 198:314–318, 2005.
- [356] C. Nanteuil and A.-M. Gosnet-Haghiri. Method for manufacturing a microfluidic chip, and related chip and plate, 2011.
- [357] L. M. Lacroix, R. Bel Malaki, J. Carrey, S. Lachaize, M. Respaud, G. F. Goya, and B. Chaudret. Magnetic hyperthermia in single-domain monodisperse FeCo nanoparticles: Evidences for Stoner-Wohlfarth behavior and large losses. *J. Appl. Phys.*, 105(2), 2009.
- [358] Abel L. Thangawng, Rodney S. Ruoff, Melody A. Swartz, and Matthew R. Glucksberg. An ultra-thin PDMS membrane as a bio/micro–nano interface: fabrication and characterization. *Biomed Microdevices*, 9:587–595, 2007.
- [359] Christian Amatore, Nicolas Da Mota, Catherine Sella, and Laurent Thouin. Theory and Experiments of Transport at Channel Microband Electrodes Under Laminar Flow. 3. Electrochemical Detection at Electrode Arrays under Steady State. *Anal. Chem.*, 82:2434–2440, 2010.
- [360] Tong Chen, Blanca Gomez-Escoda, Javier Munoz-Garcia, Julien Babic, Laurent Griscom, Pei-Yun Jenny Wu, and Damien Coudreuse. A drug-compatible and temperature-controlled microfluidic device for live-cell imaging. *Open Biol.*, 6(8):160156, 2016.
- [361] Timothée Houssin, Jérémy Cramer, Rébecca Grojsman, and Lyes Bellahsene. Ultrafast, sensitive and large-volume on-chip real-time PCR for the molecular diagnosis of bacterial and viral infections. *Lab Chip*, 16(8):1401–1411, 2016.
- [362] Heater Cooler for Microscopy | Cherry Biotech
<http://www.cherrybiotech.com/heater-cooler-for-microscopy>.
- [363] M.-C. Horny, M. Lazerges, J.-M. Siaugue, A. Pallandre, D. Rose, F. Bedioui, C. Deslouis, A.-M. Haghiri-Gosnet, and J. Gamby. Electrochemical DNA biosensors based on long-range electron transfer: investigating the efficiency of a fluidic channel microelectrode compared to an ultramicroelectrode in a two-electrode setup. *Lab Chip*, 7:307, 2016.

*Abstract***Electrochemistry & magnetic nanoparticles on a microfluidic Lab-On-Chip for medical diagnosis. Detection of the microRNA-122.**

by Marie-Charlotte HORNY

English version

Here we report on an experimental study of a microfluidic Lab-on-Chip composed of two modules for the detection of a 23 basis DNA sequence mimicking the miRNA-122. The downstream module is devoted to highly sensitive, highly specific and rapid diagnosis. Gold and a-CN_x Ultra-microelectrodes were characterized in a [Fe(CN)₆]³⁻ / [Fe(CN)₆]⁴⁻ / MB / NaCl electrolyte in a two-electrode configuration to reduce congestion of the channel. Hybridization schemes were performed yielding a 1 10⁻¹⁸ M limit of detection, in a 30-minutes protocol under a 0.5 μL s⁻¹ flow. The surprisingly low LOD was attributed to the shrinking of the diffusion layer under forced convection that allowed bringing more biomolecules on the sensor. The input of a-CN_x layers provided covalent grafting and a probe density compatible with hybridization efficiency. The upstream module is a target-DNA release module. It operates in magnetic hyperthermia, transposed in microfluidics to increase performances through confinement. The obtained results on the magnetic nanoplat-form that carries DNA showed an increase in target release arising from the superparamagnetic nature of the particles due to both heating efficiencies under an alternative magnetic field and increased loading consistent with short-chain like structures and larger dimensions respectively.

French version

Nous présentons ici, une étude expérimentale d'un laboratoire sur puce microfluidique composé de deux modules pour la détection d'une séquence courte d'ADN, modèle du miARN-122. Le module en aval est un module hautement sensible et spécifique, pour un diagnostic précoce et rapide. Les ultra-microélectrodes d'or et de a-CN_x utilisées comme électrodes de travail sont caractérisées avec une électrolyte composée de [Fe(CN)₆]³⁻ / [Fe(CN)₆]⁴⁻ / MB / NaCl en configuration à deux-électrodes afin de diminuer l'encombrement du canal. Des schémas d'hybridation sont effectués menant à une limite de détection de 1 10⁻¹⁸ M en 30 minutes sous flux de 0.5 μL s⁻¹. Cette LOD très basse est attribuée à la réduction de la couche de diffusion sous convection forcée, permettant à un plus grand nombre de molécules d'atteindre le capteur. L'apport des couches de a-CN_x permet un greffage covalent et une densité en sondes compatible avec une hybridation efficace. Le module en amont, est un module de relargage de cibles par hyperthermie magnétique. Ce module a été transposé en microfluidique pour augmenter les performances par confinement. Les résultats obtenus concernant la nanoplateforme magnétique transportant l'ADN montrent un relargage augmenté de cible, provenant d'une part d'une efficacité plus grande sous champ magnétique alternatif et de nanoparticules pouvant capturer plus de cibles ; résultats cohérents avec, respectivement, des structures en courte-chaînes et des diamètres de particules plus élevés.